

Table of Contents

Introduction	1
Chapter 1	State of the art for the design of footbridges.....3
1.1	Scientific papers4
1.1.1	Footbridge Dynamics4
1.1.2	Human Induced Vibration (HIV)8
1.2	Recommendations and prescriptions8
1.3	References 15
Chapter 2	Design requirements and performance satisfaction 19
2.1	Dynamics of the footbridges design and structural health monitoring20
2.1.1	Governing relations20
2.1.2	Structural Health Monitoring32
2.2	Comfort for footbridges: codes and literature overview39
2.3	Pedestrian Timber Bridge: a new construction way. Introduction to the structures under study44
2.4	References50
Chapter 3	Experimental campaign and numerical modeling.....55
3.1	Experimental campaign55
3.1.1	“Tesa” footbridge experimental campaign56
3.1.2	“Trasaghis” footbridge experimental campaign64
3.2	Cable-stayed system: “Tesa” footbridge FE Model..... 70
3.2.1	Design data and numerical model definition..... 70
3.2.2	FE Model refinement and validation..... 76
3.3	FE Model of the “Trasaghis” footbridge 78
3.3.1	Project data and numerical model definition..... 78
3.3.2	FE Model refinement and validation.....85
3.4	References93

Chapter 4	Modeling the main actions.....	97
4.1	Wind action.....	98
4.2	Human induced vibration source	106
4.2.1	Crowd Load Model (CLM)	107
4.3	Time-histories simulation	114
4.3.1	Wind velocity field	114
4.3.2	Crowd Load Model: numerical simulation and validation	118
4.4	References.....	124
Chapter 5	Model order reduction (MOR).....	127
5.1	MOR background	128
5.2	Structural response.....	133
5.3	MOR accuracy	142
5.4	References.....	144
Chapter 6	Control solutions.....	147
6.1	Passive control solutions.....	149
6.2	Semiactive control solutions	165
6.3	Active control solutions	180
6.4	References.....	191
Chapter 7	Conclusions.....	193
Appendix A:	Technical details for the two footbridges used as case studies.....	195
A.1	Trasaghis footbridge	195
A.2	Tesa footbridge	208
A.3	References.....	219
Appendix B:	A standard model for the single pedestrian walking and running	221
B.1	Dynamic behaviour of a single pedestrian	221
B.2	References.....	229
Appendix C:	Overview of some existing codes and guidelines.....	231
C.1	ISO 10137.....	231

C.2	Fib-buletin 32	233
C.3	BS 5400	236
C.4	Sétra-AFGC	237
C.5	The comfort level in existing recommendations	242
C.6	References	244
Appendix D: Crowd Load Model (CLM): experimental data set		247
D.1	Time-Frequency analysis of the signals: theoretical background	247
D.2	Experimental data analysis	251
D.3	References	266
Acknowledgements		269

Table of Figures and Tables

Figure 1.1. The Millennium Bridge.....	3
Figure 1.1.1. Vibration comfort criteria for footbridges in case of human induced vibrations [8].	5
Figure 1.1.2. Monitoring system of the <i>Pedro Gómez Bosque</i> footbridge [12].	6
Figure 1.1.3. On the left: general view of the footbridge. On the right: testing under human induced vibration [13].	6
Figure 1.1.4. Active control scheme [19].	7
Figure 1.2.1. Peak of tolerable acceleration for high range of frequencies ($f \gg 1$ Hz) ([27] and [28]).	10
Figure 1.2.2. Peak of tolerable acceleration for low range of frequencies ($f < 1$ Hz). Values are plotted in terms of root-mean-square of the acceleration. To compare these result with the ones proposed in Figure 1.2.1, multiply these values by $2^{0.5}$ ([29]-[31]).	10
Figure 1.2.3. Summary of human exposure to acceleration. Peak accelerations versus frequencies [32].	11
Figure 1.2.4. Peak acceleration criteria proposed by [35] and [26].	12
Figure 1.2.5. Structural safety criteria for frequencies range up to 50 Hz [41].	13
Figure 1.2.6. General peak acceleration criteria [43].	14
Figure 2.1.1. Schematic representation of a 1 -DOF system.	21
Figure 2.1.2. Dynamic parameter trend for specific value of the critical damping.	23
Figure 2.1.3. Free oscillation of a 1 -DOF system with different value of damping.	24
Figure 2.1.4. Oscillation of a 1 -DOF system – divergences induced by a “negative” damping	25
Figure 2.1.5. Representation of the “logarithmic decrement method”.	26
Figure 2.1.6. Representation of the “bandwidth method”.	26
Figure 2.1.7. Schematic representation of a n -DOF system.	26
Figure 2.1.8. Modal superposition approach applied to a 2 -DOF system.	32
Figure 2.1.9. SHM architecture applied to a bridge [12].	34
Figure 2.1.10. Example of proposed rehabilitation planning based on the Ultimate Limit Strength [13].	34
Figure 2.1.11. SHM for bridge. Typical flowchart [16].	36
Figure 2.1.12. SHM for bridge. Typical flowchart [25].	37
Figure 2.2.1. Building vibration z-axis base curve for acceleration (foot-to-head vibration direction) [33].	41

Figure 2.2.2. Building vibration z-axis base curve for acceleration (foot-to-head vibration direction) [33].	42
Figure 2.2.3. Methodology flowchart proposed by Sétra-AFGC [36].	44
Figure 2.3.1. “Trasaghis” footbridge.	45
Figure 2.3.2. “Trasaghis” footbridge. View of the pillars.	45
Figure 2.3.3. View from the bottom of the “Trasaghis” footbridge on the left. Zoom on the structural resistant scheme of the deck on the right.	46
Figure 2.3.4. General view of the “Tesa” footbridge.	46
Figure 2.3.5. “Tesa” footbridge. Satellite view of the location.	46
Figure 2.3.6. View of the pillar on the left; detail of the connection between cable and deck on the right.	47
Figure 2.3.7. View of the structural scheme of the “Tesa” footbridge deck.	47
Figure 2.3.8. Tynset bridge, Norway [40].	48
Figure 2.3.9. Cosumnes River Bridge, California (USA) [41].	48
Figure 2.3.10. Goodpasture Covered Bridge. Lane County, Oregon (USA) [42]. a) lateral view; b) frontal view.	49
Figure 2.3.11. Goodpasture Covered Bridge. Lane County, Oregon (USA) [43].	49
Figure 2.3.12. Lejonstroms Bridge. Skelleftea, Sweden [44].	50
Figure 3.1.1. Example of the tri-axial accelerometer posed over the deck.	56
Figure 3.1.2. Example of the wireless station unit (WSU) employed for the data acquisition-transmission.	57
Figure 3.1.3. Sensors equipment configuration during the in situ tests.	57
Figure 3.1.4. Sensors WSA1 during the in situ tests.	58
Figure 3.1.5. Sensors WSA2 during the in situ tests.	58
Figure 3.1.6. Sensors WSA3 during the in situ tests.	58
Figure 3.1.7. “Tesa” footbridge – picture during test <i>B2</i> .	59
Figure 3.1.8. Acceleration along the Z axis recorded by WSA2 – duration 25 sec – sampling rate 100 Hz – November 7, 2013 @ 2.12 pm – air temperature 15°C.	60
Figure 3.1.9. Acceleration along Z axe recorded (160 sec) by WSA2 – sampling rate 100 Hz – November 7, 2013 @ 2.55 pm – air temperature 15°C.	60
Figure 3.1.10. Data processing – acceleration acquired by WAA1 during the <i>test A</i> along Y transversal axis. a) FFT; b) STFFT.	61
Figure 3.1.11. Data processing – acceleration acquired by WAA1 during the <i>test A</i> along Y transversal axis. a) WA.	62
Figure 3.1.12. Data processing by using SSI – acceleration acquired by WAA1 during the <i>test A</i> along Y transversal axis. a) mode I ($f=1.30$ Hz); b) mode III ($f=2.85$ Hz).	63
Figure 3.1.13. The tri-axial accelerometer connected with a wireless sensor unit (WSU) posed over the deck.	64

Figure 3.1.14. Example of the Kinematic EPISSENSOR uni- and tri- axial accelerometer employed during the experimental campaigns.	65
Figure 3.1.15. Sensors configuration for the two experimental campaign (November 30, 2012 and May 12, 2013).....	66
Figure 3.1.16. Periodograms of the signals recorded at position 3 (P#3): from the top to bottom, one sees the elaboration of the signals (along direction Y) collected in November, in the early morning of May 12, 2013 and in the late morning of the same day. The number of points in the temporal window of the signal is 2170.	67
Figure 3.1.17. Periodograms of the signals recorded at position 3 (P#3): from the top to bottom, one sees the elaboration of the signals (along direction Z) collected in November, in the early morning of May 12, 2013 and in the late morning of the same day. The number of points in the temporal window of the signal is 2170.	68
Figure 3.1.18. Periodograms of the signals recorded at position 7 (P#7): FFT along direction Y.....	69
Figure 3.1.19. Periodograms of the signals recorded at position 7 (P#7): FFT along direction Z - data collected in May 12, 2013.....	70
Figure 3.2.1. View of the numerical model implemented in MARC Mentat2010.	71
Figure 3.2.2. Detail of the kinematics boundary condition below the mains GLT beams. On the left picture from field; on the right the implemented boundary on the numerical model.....	73
Figure 3.2.3. Detail of the kinematics boundary condition at the base of the pillars. On the left picture from field; on the right the implemented boundary on the numerical model.....	74
Figure 3.2.4. Detail of the kinematics boundary condition at the base of the pillars. On the left picture from field; on the right the implemented boundary on the numerical model.....	74
Figure 3.2.5. Above: lateral view of the numerical model; below: view from the above.	75
Figure 3.2.6. Frontal view of the numerical model.	75
Figure 3.2.7. 3-D view of the numerical model.....	75
Figure 3.2.8. View of the deck. On the left 3-D view; on the right cross-section view..	76
Figure 3.2.9. FFT – acceleration acquired by WAa1 during the <i>test A</i> along the Y axis.	77
Figure 3.2.10. Mode I – prevalent motion along the transversal direction Y. FEM dynamic modal analysis performed in MARC Mentat2010 – $f = 1.28$ Hz.....	77
Figure 3.3.1. View of the numerical model implemented in MARC Mentat2010.	79
Figure 3.3.2. Detail of the kinematics boundary condition at the base of the pillars. On the left picture from field; on the right the implemented boundary on the numerical model.....	81

Figure 3.3.3. Detail of the kinematics boundary condition at the base of the stays. On the left picture from field; on the right the implemented boundary on the numerical model.	81
Figure 3.3.4. Detail of the kinematics boundary condition for the GLT beams. On the left picture from field; on the right the implemented boundary on the numerical model.	82
Figure 3.3.5. Above: lateral view of the numerical model; below: view from the above.	83
Figure 3.3.6. Frontal view of the numerical model.	83
Figure 3.3.7. 3-D view of the numerical model.	84
Figure 3.3.8. View from the bottom of the deck. On the left picture from field; on the right the implemented boundary on the numerical model.	84
Figure 3.3.9. View of the deck. On the left 3-D view; on the right cross-section view.	84
Figure 3.3.10. View of the steel pillars and stays systems. On the left 3-D view; on the right cross-section view.	85
Figure 3.3.11. Partial numerical of the steel pillars and stays implemented in MARC Mentat2010.	85
Figure 3.3.12. Mode I – local mode related to the prevalent vertical motion of the stays. a) FFT of the experimental data (Campaign of May, 2013 – position $P\#7$) – $f = 1.08 \pm 1.11$ Hz; b) FEM dynamic modal analysis performed in MARC Mentat2010 – $f = 1.06$ Hz.	88
Figure 3.3.13. Mode II – local mode related to the prevalent horizontal/transversal motion of the stays. a) FFT of the experimental data along Y (Campaign of May, 2013 – position $P\#7$) – $f = 1.31 \pm 1.43$ Hz; b) FFT of the experimental data along Y (Campaign of May, 2013 – position $P\#1$) – $f = 1.37$ Hz.	89
Figure 3.3.14. Mode II – local mode related to the prevalent horizontal/transversal motion of the stays. a) FFT of the experimental data along Z (Campaign of May, 2013 – position $P\#1$) – $f = 1.5$ Hz; b) FEM dynamic modal analysis performed in MARC Mentat2010 – $f = 1.41$ Hz.	90
Figure 3.3.15. Mode III – global “pseudo” torsional mode of the deck. a) FFT of the experimental data along Y (Campaign of May, 2013 – position $P\#7$) – $f = 1.95$ Hz; b) FFT of the experimental data along Y (Campaign of May, 2013 – position $P\#1$) – $f = 1.97$ Hz.	91
Figure 3.3.16. Mode III – global “pseudo” torsional mode of the deck. a) FFT of the experimental data (Campaign of May, 2013 – position $P\#3$) – $f = 1.74 \pm 1.95$ Hz; b) FFT of the experimental data along Y (Campaign of May, 2013 – position $P\#3$) – $f = 1.74 \pm 1.95$ Hz.	92
Figure 3.3.17. Mode III – global “pseudo” torsional mode of the deck. FEM dynamic modal analysis performed in MARC Mentat2010 – $f = 1.96$ Hz.	93

Figure 4.1.1. Global reference frame.....	99
Figure 4.1.2. Example of “mean” wind velocity (U) trend for three different case of roughness [8].	99
Figure 4.1.3. Flowchart for the wind velocity field simulation.	106
Figure 4.2.1. Grid of nodes for the simulation.	108
Figure 4.2.2. Local frame system for the k -th node.....	110
Figure 4.2.3. Spatial configuration of the crowd model implemented.	111
Figure 4.2.4. Classical model of moving loads. Deterministic approach. An example of two consecutive time steps.	111
Figure 4.2.5. Flowchart for the CLM simulation.....	112
Figure 4.2.6. Above: experimental set-up; below: walking test of six person configuration.	113
Figure 4.3.1. Grid of nodes for wind velocity field simulation.	114
Figure 4.3.2. Wind velocity components along the x_1 and x_3 axes as simulated for node: a) $n1$, b) $n19$	115
Figure 4.3.3. Force components along the x_1 and x_3 axes for node: a) $n8$, b) $n22$ and c) $n23$	117
Figure 4.3.4. a) Grid of nodes for the simulation; b) example of the deck nodal grid implemented in MARC Mentat2010.	118
Figure 4.3.5. Steady component of the force over the simulation grid.	119
Figure 4.3.6. 3-D plot of the “barrel dented” function over the nodes of the simulation grid.	119
Figure 4.3.7. Step 1 – simulated force files by the proposed CLM model.	120
Figure 4.3.8. Step 2 – simulated force files by the proposed CLM model.	120
Figure 4.3.9. Step 3 – simulated force files by the proposed CLM model.	121
Figure 4.3.10. Example of the simulated forces implemented in MARC Mentat2010.	122
Figure 4.3.11. Time-frequency plots from the data taken by sensor WSa2 along axis Y (transversal). a) data acquired in situ; b) data from the numerical simulation.	122
Figure 4.3.12. Time-frequency plots from the data taken by sensor WSa2 along axis Z (gravity) a) data acquired in situ and filtered at 2.50 Hz; b) data from the numerical simulation.	123
Figure 5.1. MOR: graphical representation [4].	128
Figure 5.1.1. MOR: visual representation [11].	132
Figure 5.2.1. “Light” FEM implemented in MARC Mentat2010 environment.	133
Figure 5.2.2. Dynamic modal comparison of the “Trasaghis” footbridge FEM: mode I. a) “Light” FEM $f = 1.22$ Hz; b) “Full” FEM $f = 1.06$ Hz.	134
Figure 5.2.3. Dynamic modal comparison of the “Trasaghis” footbridge FEM: mode II. a) “Light” FEM $f = 1.32$ Hz; b) “Full” FEM $f = 1.41$ Hz.	135

Figure 5.2.4. Dynamic modal comparison of the “Trasaghis” footbridge FEM: mode III. a) “Light” FEM $f = 2.40$ Hz; b) “Full” FEM $f = 1.96$ Hz.....	136
Figure 5.2.5. Dynamic modal comparison of the “Trasaghis” footbridge FEM: mode IV. a) “Light” FEM $f = 1.87$ Hz; b) “Full” FEM $f = 2.83$ Hz.....	137
Figure 5.2.6. Dynamic modal comparison of the “Trasaghis” footbridge FEM: mode V. a) “Light” FEM $f = 3.47$ Hz; b) “Full” FEM $f = 3.07$ Hz.....	138
Figure 5.2.7. Hankel Singular Values – State Contributions.	139
Figure 5.2.8. Gird of nodes for the “light” numerical model of the “Trasaghis” footbridge.....	139
Figure 5.2.9. Fluctuating part of the simulated wind velocity for the <i>node 5</i> . a) Y component; b) Z component.	140
Figure 5.2.10. Wind forces for the <i>node 5</i> . a) Y component; b) Z component.	141
Figure 5.2.11. Dynamic response of the “light” FEM under the simulated wind loads – <i>node 3</i> . Displacement along Y and Z axes.....	141
Figure 5.2.12. Dynamic response of the “light” FEM under the simulated wind loads – <i>node 3</i> . Accelerations along Y and Z axes.....	142
Figure 5.3.1. Comparison among “light” FEM and the implemented MOR models in terms of displacements along Y and Z axes – <i>node 3</i> . a) MOR 145 states; b) MOR 114 states.	143
Figure 5.3.2. Comparison among “light” FEM and the implemented MOR models in terms of displacements along Y and Z axes – <i>node 3</i> - MOR 84 states.....	144
Figure 6.1. Scheme of a Passive Control System [2].....	148
Figure 6.2. Scheme of an Active Control System [2].	148
Figure 6.1.1. 3-D view of the numerical model of the “Trasaghis” footbridge implemented in Marc MENTAT2010.	153
Figure 6.1.2. View of the implemented TMDs solution on “Trasaghis” footbridge. In particular TMD1 and TMD3 hung on the tubular elements in the l.h.s. of the footbridge, while TMD2 and TMD4 are hanged on the tubular elements in the r.h.s.....	154
Figure 6.1.3. Above: Lateral view of the location of the <i>i</i> -th TMD. Below: cross-section of the <i>i</i> -th TMD.....	157
Figure 6.1.4. Grid of nodes.....	158
Figure 6.1.5. Time histories response before and after mounting the passive control system (“TMD_A”) designed. Acceleration responses for the <i>node n22</i> along x_1 (a) and x_3 (b), respectively.	160
Figure 6.1.6. Time histories response before and after mounting the passive control system (“TMD_A”) designed. Acceleration responses along x_1 at the <i>node n8</i>	161
Figure 6.1.7. Time histories response before and after mounting the passive control system (“TMD_A”) designed. Displacement responses for the <i>node n22</i> along x_1 (a)	

and x_3 (b), respectively. The response of the node n8 is meaningful due to the stiffness of the deck.	162
Figure 6.1.8. Response spectra as obtained from the acceleration responses along x_1 (a) and x_3 (b) at the node n22; and (c) from the acceleration response along x_1 at the node n8, before and after the installation of the passive control system (TMD_A).	164
Figure 6.1.9. Response spectra as obtained from the acceleration responses along x_1 (a) and x_3 (b) at the node n22, before and after the installation of the passive control system (TMD_A).	165
Figure 6.2.1. Time history of the relative displacement for the node of TMD2 along x_1 direction a), and x_3 direction b).	168
Figure 6.2.2. View of the TMD_C of the “Trasaghis” footbridge.	169
Figure 6.2.3. Time histories of the accelerations (a) along direction x_1 and (b) along direction x_3 obtained for node n22 under the semiactive control scheme TMD_As3.	172
Figure 6.2.4. Time histories of the displacements (a) along direction x_1 and (b) along direction x_3 obtained for node n22 under the semiactive control scheme TMD_As3.	173
Figure 6.2.5. Time histories of the accelerations (a) along direction x_1 and (b) along direction x_3 obtained for node n8 under the semiactive control scheme TMD_As3.	174
Figure 6.2.6. Time histories of the displacements (a) along direction x_1 and (b) along direction x_3 obtained for node n8 under the semiactive control scheme TMD_As3.	175
Figure 6.2.7. Time histories of the accelerations (a) along direction x_1 and (b) along direction x_3 obtained for node n22 under the semiactive control scheme TMD_Bs1.	176
Figure 6.2.8. Time histories of the displacements (a) along direction x_1 and (b) along direction x_3 obtained for node n22 under the semiactive control scheme TMD_Bs1.	177
Figure 6.2.9. Time histories of the accelerations (a) along direction x_1 and (b) along direction x_3 obtained for node n8 under the semiactive control scheme TMD_Bs1.	178
Figure 6.2.10. Time histories of the displacements (a) along direction x_1 and (b) along direction x_3 obtained for node n8 under the semiactive control scheme TMD_Bs1.	179
Figure 6.3.1. Scheme of the control forces implemented for the “Trasaghis” footbridge.	183
Figure 6.3.2. Time history of the control forces – node 3. a) MOR 145 states; b) MOR 114 states; c) MOR 84 states.	184
Figure 6.3.3. Active control solution for the “Trasaghis” footbridge - model MOR 145 states: comparison of uncontrolled vs. controlled. Response of: a) Displacements along Y and Z axes – node 3; b) Accelerations along Y and Z axes (zoom between 10 to 20 sec) – node 3.	185
Figure 6.3.4. Active control solution for the “Trasaghis” footbridge - model MOR 145 states: comparison of uncontrolled vs. controlled. Response of: a) Displacements along Y and Z axes – node 5; b) Accelerations along Y and Z axes (zoom between 10 to 20 sec) – node 5.	186

Figure 6.3.5. Active control solution for the “Trasaghis” footbridge - model MOR 114 states: comparison of uncontrolled vs. controlled. Response of: a) Displacements along Y and Z axes – <i>node 3</i> ; b) Accelerations along Y and Z axes (zoom between 10 to 20 sec) – <i>node 3</i>	187
Figure 6.3.6. Active control solution for the “Trasaghis” footbridge - model MOR 114 states: comparison of uncontrolled vs. controlled. Response of: a) Displacements along Y and Z axes – <i>node 5</i> ; b) Accelerations along Y and Z axes (zoom between 10 to 20 sec) – <i>node 5</i>	188
Figure 6.3.7. Active control solution for the “Trasaghis” footbridge - model MOR 84 states: comparison of uncontrolled vs. controlled. Response of: a) Displacements along Y and Z axes – <i>node 3</i> ; b) Accelerations along Y and Z axes (zoom between 10 to 20 sec) – <i>node 3</i>	189
Figure 6.3.8. Active control solution for the “Trasaghis” footbridge - model MOR 84 states: comparison of uncontrolled vs. controlled. Response of: a) Displacements along Y and Z axes – <i>node 5</i> ; b) Accelerations along Y and Z axes (zoom between 10 to 20 sec) – <i>node 5</i>	190
Figure A.1.1. Chorography at scale 1:25000: the map shows the lake and the emissary channel. The red circle indicates the bridge location.	196
Figure A.1.2. A general view of the “Trasaghis footbridge”.	196
Figure A.1.3. Technical drawings of the footbridge.	197
Figure A.1.4. Details of the main GLT beams: a) view during the construction stage; b) details of the joint connection.	198
Figure A.1.5. Details of the deck cross-section resistant scheme.	199
Figure A.1.6. View from above of the structural scheme of the deck.....	199
Figure A.1.7. Detail of the walking table during the construction stage.....	200
Figure A.1.8. Example of the structural joint connection: detail of the joint.....	200
Figure A.1.9. Example of the structural joint connection: connection of the lateral section in correspondence of the steel oblique tubular element.....	201
Figure A.1.10. Construction stage: assembling the central section of the footbridge. a) before the assembly; b) during the stage.....	201
Figure A.1.11. A detail of the tubular steel oblique elements (left). A lateral view of the antenna (right).....	202
Figure A.1.12. View of the upper protection system of the beam made by copper (left). A detail of the external larch cladding (right).....	202
Figure A.1.13. View of the neoprene support.....	203
Figure A.1.14. Load test stage. a) Load configuration (measure in <i>m</i>); b) during the test (below).....	204
Figure A.1.15. Measurement during the load test stage carried out.....	204
Figure A.1.16. Lateral view of the Trasaghis footbridge.....	205

Figure A.1.17. Frontal view of the Trasaghis footbridge.	205
Figure A.1.18. Detail of the structural joint between the GLT curved beam and the oblique steel tubular element.	205
Figure A.1.19. View of the reinforced concrete foundation system.	206
Figure A.1.20. View from above of the walkway. Detail of the H-shape steel element connection with the GLT curved beam.	207
Figure A.1.21. Detail of the connection between the GLT curved beam and the concrete foundation system.	207
Figure A.2.1. a) Map of the location. The red circle indicates the bridge location. b) Satellite view of the area where the footbridge is located. The red line indicates the footbridge.	208
Figure A.2.2. Lateral view of the timber footbridge.	209
Figure A.2.3. Technical drawings of the footbridge.	210
Figure A.2.4. Steel cables.	211
Figure A.2.5. Detail of the joint connection with the steel cables. Connection with antenna (left); connection with the deck (right).	211
Figure A.2.6. Details of the deck cross-section resistant scheme.	212
Figure A.2.7. View from the bottom of the deck.	212
Figure A.2.8. Detail of the <i>neoprene</i> support.	213
Figure A.2.9. Detail of the joints connection.	213
Figure A.2.10. Construction stage: assembling the central section of the footbridge. a) Before the assembly; b) during the stage.	214
Figure A.2.11. Survey operations during the load test.	215
Figure A.2.12. Lateral view of the footbridge.	216
Figure A.2.13. Frontal view of the footbridge.	216
Figure A.2.14. Detail of the upper protection of the main GLT arcuate beams.	217
Figure A.2.15. Detail of the internal support made by reinforced concrete.	217
Figure A.2.16. Cross-section of the deck.	217
Figure A.2.17. Detail of the connection of the cable with the ground.	218
Figure A.2.18. View of the walking deck.	218
Figure B.1.1. Force trend due to different types of step [1].	222
Figure B.1.2. Schematic representation of the lateral forces during the motion [2].	223
Figure B.1.3. Time history of the human induced force: vertical component [3].	223
Figure B.1.4. Time history of the human induced force: lateral component [3].	224
Figure B.1.5. Time history of the human induced force: longitudinal component [3].	224
Figure B.1.6. Walking force: vertical component. Differences between three harmonics representation for walking step frequency $f=2\text{Hz}$ [3].	225

Figure B.1.7. Walking force. a) lateral component; b) longitudinal component. Differences between four harmonics representation for walking step frequency $f=2\text{Hz}$ [3].	226
Figure B.1.8. Running force. vertical component. Differences between three harmonics representation for running step frequency $f=3\text{Hz}$ [3].	227
Figure C.1.1. Building vibration z-axis base curve for acceleration (foot-to-head vibration direction) [1].	232
Figure C.1.2. Building vibration x- and y-axis base curve for acceleration (side-to-side and back-to-chest vibration direction) [1].	233
Figure C.2.1. Different scenarios of pedestrian densities [2].	234
Figure C.2.2. Velocity versus density of pedestrian [2].	234
Figure C.2.3. Dynamic amplification factor for resonant response due to sinusoidal force moving across simple span [2].	235
Figure C.3.1. Methodology flowchart proposed by Sétra-AFGC [7].	237
Figure C.3.2. Example of loads application: mode shape versus load direction [7]. ...	241
Figure C.3.3. factor ψ for vertical and longitudinal vibrations on the left, and for lateral vibrations on the right [7].	242
Figure C.3.1. Vertical critical accelerations (m/s^2) versus natural frequency (Hz) by various codes [7].	244
Figure D.1.1. Six persons walking. Time-frequency plots from the data recorded by sensor WSa2 along transversal (Y) axis. a) data from right-to-left crossing; b) data from left-to-right crossing.	249
Figure D.1.2. Six persons walking. Time-frequency plots from the data recorded by sensor WSa2 along gravity (Z) axis. a) data from right-to-left crossing; b) data from left-to-right crossing.	250
Figure D.2.1. Time-frequency plot from the data taken by sensor WSa2 along Y transversal axis during <i>test Ia</i> . a) <i>RtoL</i> data ; b) <i>LoR</i> data	252
Figure D.2.2. Time-frequency plots from the data taken by sensor WSa2 along Z gravity axis during <i>test Ia</i> . a) <i>RtoL</i> data ; b) <i>LtoR</i> data	253
Figure D.2.3. Configuration of the walking <i>test B2</i>	255
Figure D.2.4. Time-frequency plots from the data recorded by sensor WSa2 along the Y transversal axis during <i>test Ib</i> . a) <i>RtoL</i> data ; b) <i>LtoR</i> data.	257
Figure D.2.5. Time-frequency plots from the data recorded by sensor WSa2 along Z gravity axis during <i>test Ib</i> . a) <i>RtoL</i> data ; b) <i>LtoR</i> data.	258
Figure D.2.6. Configuration of the walking <i>test B3</i>	259
Figure D.2.7. Time-frequency plots from the data recorded by sensor WSa2 along Y transversal axis during <i>test Ic</i> . a) <i>RtoL</i> data ; b) <i>LtoR</i> data.	261
Figure D.2.8. Time-frequency plots from the data recorded by sensor WSa2 along Z gravity axis during <i>test Ic</i> . a) <i>RtoL</i> data ; b) <i>LtoR</i> data.	262

Figure D.2.9. Time-frequency plots from the data recorded by sensor WSa2 along Y transversal axis during <i>test II</i> . a) <i>RtoL</i> data ; b) <i>LtoR</i> data.....	264
Figure D.2.10. Time-frequency plot - WSa2 along Z gravity axis - <i>test II</i> . a) <i>RtoL</i> data ; b) <i>LtoR</i> data.	265
Figure D.2.11. Zoom between 1.00 Hz and 5.00 Hz of the singular value of spectral density matrix. Comparison between acquisitions along transversal Y axis from WSa1 during the test B1 (solid black line) and test B2 (dashed black line) and test B3 (solid red line).	266

Table 1.2.1. Acceleration limits in Eurocode 0 [24].	9
Table 1.2.2. German Standard DIN 4150 [40].	13
Table 1.2.3. Structural criteria: overall acceptance.	14
Table 2.1.1. Typical sensors employed during a SHM [12].	38
Table 3.1.1. “Tesa” footbridge – frequencies range from data analysis.	63
Table 3.1.2. Frequency ranges “Trasaghis” footbridge – main results.	69
Table 3.2.1. “Tesa” footbridge - numerical model: mains features.	72
Table 3.2.2. “Tesa” footbridge - numerical model: main features.	72
Table 3.2.3. “Tesa” footbridge - numerical model: materials properties.	72
Table 3.2.4. “Tesa” footbridge – frequencies comparison.	77
Table 3.3.1. “Trasaghis” footbridge - numerical model: geometry of the structural elements.	79
Table 3.3.2. “Trasaghis” footbridge - numerical model: materials properties.	80
Table 3.3.3. “Trasaghis” footbridge - numerical model: main features.	80
Table 3.3.4. Partial FEM - Frequency ranges for different boundary conditions for the deck-stay link.	86
Table 3.3.5. Frequency ranges for the lowest modes of the “Trasaghis” footbridge.	87
Table 3.3.6. Frequencies percentage error. Comparison between “field” and “FEM” results.	87
Table 4.2.1. Walking (round trip) of six persons.	113
Table 4.3.1. Coordinates of the nodes for the simulation grid.	114
Table 5.2.1. Frequencies percentage error. Comparison between “light” and “full” FEM.	134
Table 5.3.1. Time consuming	142
Table 6.1.1. Masses of the structural and non-structural elements for the “Trasaghis” footbridge.	153
Table 6.1.2. Frequency ranges for the lowest modes of the “Trasaghis” footbridge.	153
Table 6.1.3. Optimum absorber parameters for TMD design [15].	155
Table 6.1.4. Main features of the TMD_A solution.	156
Table 6.1.5. Root-mean-square values computed on the whole duration (120 sec) of the acceleration and displacement time histories obtained from the numerical analyses. The peak values are also reported in italic, and they are expressed in m/s^2 for the accelerations, and in mm for the displacements.	158
Table 6.1.6. Root- mean-square values computed on the tails (the first 15 sec after the event) of the of the response time histories obtained from the numerical analyses. The peak values are also reported in italic, and they are expressed in m/s^2 for the accelerations, and in mm for the displacements.	159
Table 6.2.1. Root-mean-squares on the whole duration (120 sec) of the response time histories computed from the numerical analyses carried out in a semi-active	

environment. The value in italic in each cell gives the peak value (with its sign) expressed as m/s^2 for the accelerations, and as mm for the displacements.	170
Table 6.2.2. Root-mean-squares on the tail (the first 15 sec after the event) of the time histories computed as response from the numerical analyses carried out. The value in italic in each cell gives the starting point (with its sign) of the decay, expressed as m/s^2 for the accelerations, and as mm for the displacements.	171
Table B.1.1. Range of activities (top table). Typical values for step frequency (f_s), velocity (v_s) and step length (l_s) (bottom table) [1].	222
Table B.1.2. Different Fourier coefficients for walking and running [4].	228
Table C.1.1. Coordination factor $C(N)$ suggested by ISO 10137 [1].	233
Table C.3.1. Acceleration ranges (in m/s^2) for vertical vibrations proposed by Sétra-AFGC [7].	239
Table C.3.2. Acceleration ranges (in m/s^2) for horizontal vibrations proposed by Sétra-AFGC. The acceleration is limited in any case to $0.10 m/s^2$ to avoid lock-in effect [7].	239
Table C.3.3. Frequency ranges (Hz) of the vertical and longitudinal vibrations [7][36].	239
Table C.3.4. Frequency ranges (Hz) of the transversal vibrations [7].	239
Table C.3.5. Typical critical damping ratio [7].	240
Table C.3.6. Case 1 - Loads per unit of area proposed by Sétra-AFGC. Below: factor ψ for vertical and longitudinal vibrations on the left, and for lateral vibrations on the right [7].	240
Table C.3.7. Case 2 - Loads per unit of area proposed by Sétra-AFGC. Below: factor ψ for vertical and longitudinal vibrations on the left, and for lateral vibrations on the right [7].	241
Table C.3.1. Overview of the limit value of the acceleration according to the main international codes [7].	243
Table C.3.2. Overview of the critical frequencies according to the main international codes [7].	244
Table D.2.1. Walking (round trip) of one person.	251
Table D.2.2. Walking (round trip) of four persons.	255
Table D.2.3. Walking (round trip) of six persons.	259
Table D.2.4. Running (round trip) of one person.	263

Introduction

In recent years the use of timber as construction material has become quite common in all Europe. This is in general a preferred choice in all those applications where the structure has to fit well in the surrounding landscape. Moreover different studies demonstrated that wood in general has a good thermal and acoustic properties. Moreover timber elements are eco-friendly: they fit very well in all those applications where the issues of pollution are sensitive or needs an *ad hoc* design approach. Thus, there is a lot of application of timber all around the world for the so called “green constructions”.

In this work a particular branch of timber constructions is discussed and analyzed: the pedestrian bridges. The motivations behind this work can be summarized in two main aspects:

- 1) this research field is quite young and different research groups are working within the footbridges area. In particular several works in the literature are focused on comfort, vibrations control, and so forth...;
- 2) the design of pedestrian bridges is analyzed in this work to better identify the dynamics of these structures, trying to identify a new design scheme for those loads that affect the behaviour of these particular structures, the so called Human Induced Loads (HIL).

The development of new techniques and construction materials, as for example the glued laminated timber (GLT) within the field of timber bridges, allows the designers to conceive footbridges with span of 100 m long or more, “without” problems in terms of safety but leading to specific performance considerations.

In this thesis, the *in situ* measured structural responses of two existing timber footbridges are reported, analyzed and discussed. These records are used in order to better understand the dynamic behaviour of this type of structures. An attempt to

develop a numerical model able to simulate the interaction among the structure and the human induced loads in a realistic manner is the next step. Finally different vibrations control solutions, under wind and pedestrian loads, are numerically implemented and their performance is discussed.

The thesis is organized in seven chapters plus four appendixes. The topics of the single chapters are:

Chapter 1 – State of the art for the design of footbridges: the main recommendations and prescriptions within the field of the pedestrian bridge are also considered;

Chapter 2 – Design requirements and performance satisfaction: code and literature reviews concerning the dynamic of the bridge and the comfort of the footbridges are provided;

Chapter 3 – Numerical modelling: the numerical models of the case studies are reported;

Chapter 4 – Action modelling: the loads assigned in the numerical simulations are presented;

Chapter 5 – Model order reduction (MOR): the theory behind MOR is briefly presented and discussed. Moreover the main results achieved by applying this technique are emphasized;

Chapter 6 – Control solutions: the vibration control solutions implemented are introduced and their effect evaluated;

Chapter 7 – Conclusions.

Chapter 1 State of the art for the design of footbridges

In last years, developments of new high strength materials and construction technology, have introduced a growing trend towards the construction of lightweight and slender pedestrian bridges (see [1]-[3] among others). This slenderness pointed out how these structures are quite sensitive to dynamic aspects. This is mainly due to their reduced mass that, during the action of the dynamic forces, can increase the amplitude of the vibrations.

Probably the most world-wide famous case, within the footbridges in which the vibrations caused several to the users, is the “Millennium Bridge” in London (Figure 1.1).



Figure 1.1. The Millennium Bridge.

As well documented, during the opening celebration day, the bridge was crossed by about 90000 people, with up to 2000 people simultaneously on the bridge (resulting in a maximum density between 1.3 and 1.5 persons per square metre) [4]. Unexpected excessive lateral vibrations of the bridge occurred showing as this structure was suffering a lack of stiffness. Excessive vibration did not occur continuously, but built up when a large number of pedestrians were on the affected spans of the bridge and

decayed when the number of people on the bridge reduced, or the persons stopped their walking. This can be explained by a phenomenon known as *lock-in* effect: that pedestrian(s), disturbed by the vibration of the footbridge, tends to synchronize its (their) step with the natural frequency of the bridge. In the case of the Millennium bridge the problem was solved by a retrofit adopting 37 fluid-viscous dampers to control the horizontal movements and 52 tuned mass dampers to control the vertical movement.

The increase of vibration problems in modern footbridges shows that footbridges should be no longer designed for static loads only (as required by the Italian code [5]), but their dynamic behaviour has also to be accounted by the designer. Indeed the lateral vibration problems of the Millennium Bridge is not so unusual; in fact recent studies (see [6]-[7] among others) showed as any bridge with lateral frequency modes of less than 1.3 Hz, and sufficiently low mass have the same phenomenon with sufficient pedestrian loading¹.

1.1 Scientific papers

Different research group all around the world are currently working in one or more fields related with footbridges: design, monitoring of existing structures, serviceability evaluation (comfort evaluation), structural control, Human Induced Vibration and/or Loads (HIV – HIL) and so forth...

The purpose of this section is to give a general review, but it is worth noticing that the attention is only focused on recent reviews and contributions on this theme to international conferences. From the references lists of them it is possible to find all the precedent literature in this field.

1.1.1 Footbridge Dynamics

With reference to the structural opportunities offered by the use of timber as a construction material, an overview is in [6]. In this paper the authors analyses the main typologies of structural scheme for timber footbridges giving a general review of the traditional past applications and suggestions for possible developments in this field.

For the evaluation of the serviceability conditions for a pedestrian bridge, the reader is referred to reference [7]. The authors of this review give an evaluation of the

¹ The greater the number of people, the greater the amplitude of the vibrations

methodology proposed by the recent European guidelines HiVoSS (for steel structures) and the French guidelines Sétra, widely applied in practice for comfort assessment: the discussion is based on a selection of eight slender footbridges. As a result, the above guidelines are highly sensitive to small variations in the predicted natural frequencies. Based on a series of in situ experimental investigations, the author of [8] presents a new vibration comfort criteria for footbridges (Figure 1.1.1).

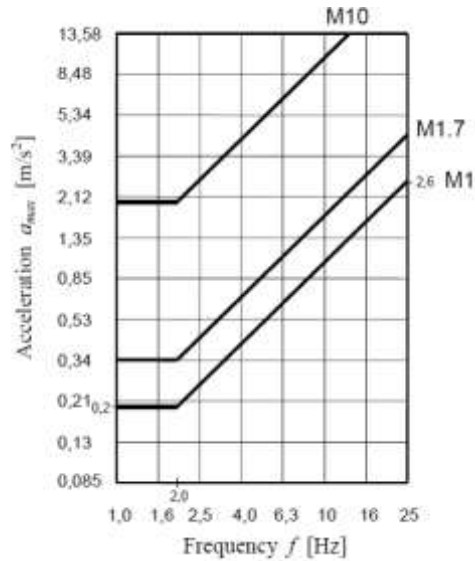


Figure 1.1.1. Vibration comfort criteria for footbridges in case of human induced vibrations [8].

Moving to the monitoring of timber bridges, different papers have been published. Indeed timber is very sensitive to the environmental changes, e.g. humidity, temperature and so on (see [9] and [10] among others). In reference [11] an *ad hoc* system of devices for the monitoring of the footbridge is designed with the intent of evaluating how the changes in the environment conditions can affect the modal response of the structure. The duration of the data acquisition (1 year) and the number of sensors employed are significant aspects of the report in [12]. In particular the monitoring system is made of 18 tri-axial accelerometers, 9 at each side of the deck, a temperature sensor and an anemometer located along the deck (Figure 1.1.2). From these data the changes of the dynamic properties due to the temperature variation were analyzed. Moreover different studies on the comfort were developed on the basis of real data.

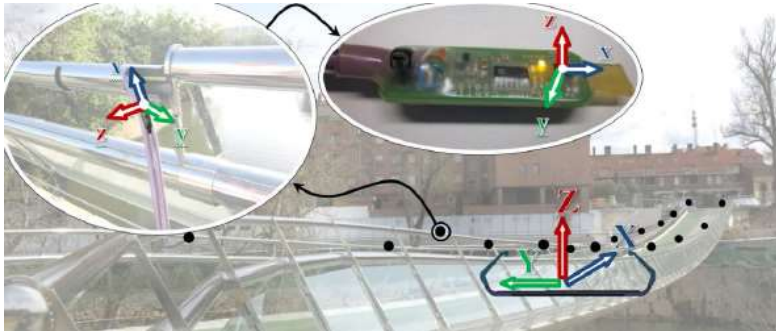


Figure 1.1.2. Monitoring system of the *Pedro Gómez Bosque* footbridge [12].

The investigation of the aspects related to the particular shape of the footbridge, is reported in [13]. The footbridge shows a ring form with outer radius of about 40 m, service width of 4 m, raised about 5,5 m over the crossroad level (Figure 1.1.3).



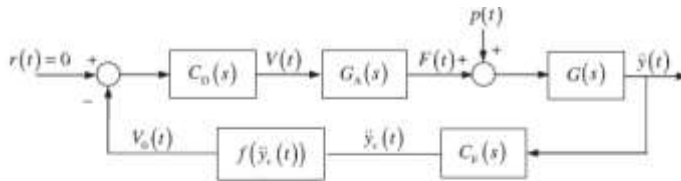
Figure 1.1.3. On the left: general view of the footbridge. On the right: testing under human induced vibration [13].

The proper design of the monitoring system is investigated in [14]. The authors addresses the layout optimization of a Wireless Sensors Network for a footbridge monitoring system considering both the network energy consumption and the sensor placement quality, in order to best capture the footbridge properties. This work shows as a proper design (calibrated for that particular structure) is needed in order to achieve the best result from a monitoring campaign.

Moving to the structural control of footbridges, several papers can be found in the literature (see [15] and [16] among others). An example of passive control is presented in [17]. This paper describes a study of the human induced dynamic effects on the new footbridge over the Ave River, in Santo Tirso, Portugal. The study outlines the need of installing a system of two tuned mass dampers (TMD), with total mass of 2100kg, in order to mitigate the induced vibrations. A new set of tests on the system mounting the devices assess the effectiveness of the mitigation system in increasing the comfort level.

This experience pointed out as the role of the damping is essential to mitigate the vibration; in particular shows as the measured damping ratio is usually below the one theoretically estimated. Thus, it is important to be very carefully in the estimation of the damping. In [18] the authors implemented five MR-TMD control devices at the middle span of the footbridge to be controlled under wind pressure. In particular a semi-active strategy is adopted. The controllable Coulomb force is adjusted in a manner that its value does not exceed the nominal maximum force of the MR damper but it is higher than the nominal minimum force of the MR damper. The results show that the semi-active control have a better control, in terms of acceleration performance, compared with the classical passive control solution.

A further paper covers the active structural control is reported in [19]. The design and experimental implementation of a passive tuned mass damper (TMD) and of an active mass damper (AMD) to mitigate human induced vibrations on an in-service footbridge is discussed. The TMD is designed based on the H_∞ control theory. The AMD consists of a proof - mass actuator controlled by a strategy based on acceleration feedback with a phase-lag network. The main features of the control strategy are summarized in Figure 1.1.4. As shown in this scheme the output of the system is the structural acceleration since it is convenient to measure it. The authors conclude with one remark: compared with passive control solutions, the cost of an active solution is much higher. In the particular case of the two strategies studied in [19], the authors estimated that the implementation of the AMD solution (i.e. AVC hardware and installation) costs about three or four times more than the passive solution (TMD).



$r(t)$	Reference command	$\ddot{y}(t)$	Acceleration response
$V(t)$	Control voltage	$\ddot{y}_c(t)$	Compensated acceleration
$F(t)$	Actuator force	$V_0(t)$	Initial control voltage
$p(t)$	Plant disturbance	$f(\ddot{y}_c)$	Nonlinear element
$C_0(s)$	Transfer function of the direct compensator		
$G_A(s)$	Transfer function of the proof-mass actuator		
$G(s)$	Transfer function of the structure		
$C_f(s)$	Transfer function of the feedback compensator		

Figure 1.1.4. Active control scheme [19].

1.1.2 Human Induced Vibration (HIV)

Consider now the topic of the Human Induced Vibration (HIV) [20]. The paper [21] deals with the possibility of introducing simplified procedures to evaluate the maximum dynamic response of footbridges due to a realistic loading scenario. Thus, a new non-dimensional approach is introduced to identify the essential non-dimensional parameters governing the dynamic behaviour under different loadings. Finally two simplified procedures based on the definition of two coefficients, the Equivalent Amplification Factor (EAF) and the Equivalent Synchronization Factor (ESF), are proposed with the aim of assessing the vibration serviceability of a footbridge without the need of numerical analyses. The coefficient EAF is defined as the ratio between the maximum dynamic response to a realistic loading scenario and the maximum dynamic response to a single resonant pedestrian, while ESF is the ratio between the maximum dynamic response to a realistic loading scenario and the maximum dynamic response to uniformly-distributed resonant pedestrian loadings. Moreover in [22], the human walking is modelled using the random nature of the dynamic load due to pedestrians walk. The probabilistic approach allows the designer to account for the variation of the human walking force, due to the variation of the pedestrian weight, the step frequency, the step length and the dynamic load factors (DLF), and so forth..., on the dynamic response of the footbridges.

1.2 Recommendations and prescriptions

Timber footbridges with long span, and more generally all slender bridges, are sensitive to vibrations, thus dynamic considerations have to be taken into account during the design [12].

These sources of vibrations can be due to pedestrian traffic, and in particular by a crowd of pedestrians walking along the deck in resonance with the bridge, or in extreme case by rescue vehicles (e.g. ambulance) that may cross the bridge in emergency cases [22]. The general design rules regarding vibrations in timber footbridges reported in Eurocode 5 ([23]), state that a bridge should be designed in a such a way that the loads acting on the bridge do not result in uncomfortable vibrations for the pedestrian.

The basic question is: “*how is possible to define a level of vibration comfortable or uncomfortable?*” As an example in Eurocode 0 ([24]) acceleration limits (Table 1.2.1) regarding pedestrian induced vibrations are proposed, but no methods are given for the evaluation of the dynamic behaviour. The code states that it is a designer’s

responsibility to make reasonable assumptions during the design stage and analysis to guarantee that the proposed limits are fulfilled.

Table 1.2.1. Acceleration limits in Eurocode 0 [24].

<i>Acceleration limit [m/s²]</i>	<i>Direction and occurrence</i>
0.7	Vertical acceleration
0.2	Lateral acceleration, normal use
0.4	Lateral acceleration, exceptional crowd conditions

The experience of vibrations is highly individual because it is difficult to specify suitable regulations for vibrations in lightweight bridges (see [25] among others). In fact the perception of the vibration depends on visual and acoustic cues, individual's position (moving, standing, sitting or lying), preoccupation and knowledge, health conditions on that particular day, and so on. All these aspects can modify the occupant awareness about vibration perception increasing/decreasing the whole comfort level. Moreover the perception seems to be related to the human's activities, in particular as pointed out in [26] for tall buildings, "*the least tolerant appears to be those people doing officework, with apartment dwellers seemingly more tolerant and tower-top diners even more*".

The studies carried out in [27] and [28] show the peak of tolerable acceleration for people in function of the frequency. In particular these studies cover only the frequency range above to 1Hz (Figure 1.2.1).

In Figure 1.2.2 the tolerable peak of accelerations in function of low value of frequency ($f < 1\text{Hz}$) is reported following the experiences reported in [29]-[31].

Similar conclusions are achieved in [32] and summarized in Figure 1.2.3.

In the particular case of wind-induced motion of tall buildings, the study reported in [33] suggested that the root-mean-square acceleration should not exceed 5 mg for a return period of 6 years to avoid significant vacancy of an office building.

The research carried out by [34] found that the difference between individuals' perception tends to be more significant than the effects of body positions, indicating the acceleration value of 4 mg for a perception level, and 2 mg as a disturbing level for the frequency of 0.13 Hz.

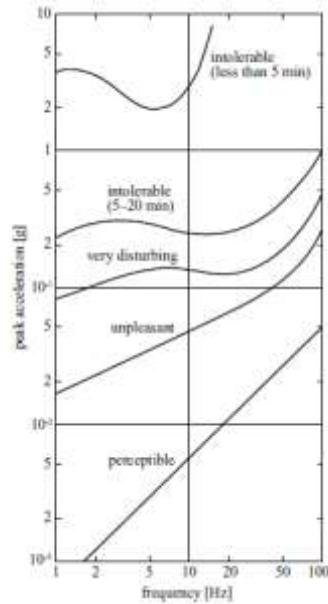


Figure 1.2.1. Peak of tolerable acceleration for high range of frequencies ($f \gg 1$ Hz) ([27] and [28]).

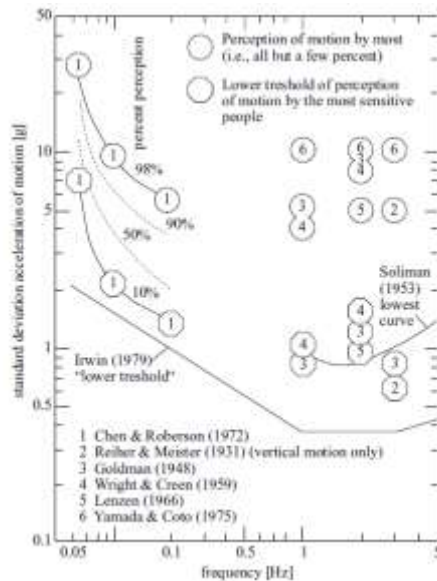


Figure 1.2.2. Peak of tolerable acceleration for low range of frequencies ($f < 1$ Hz). Values are plotted in terms of root-mean-square of the acceleration. To compare these result with the ones proposed in Figure 1.2.1, multiply these values by $2^{0.5}$ ([29]-[31]).

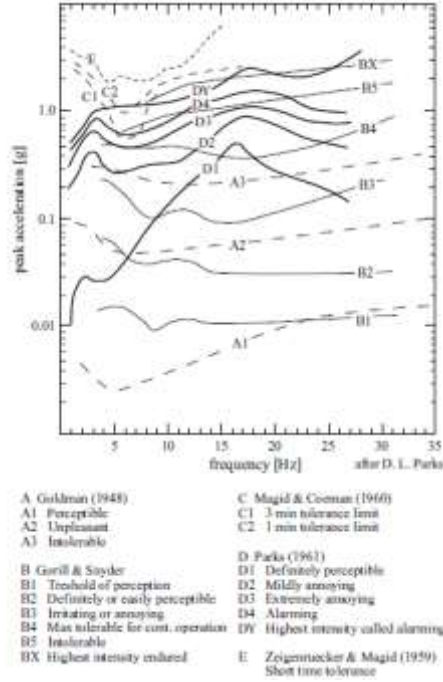


Figure 1.2.3. Summary of human exposure to acceleration. Peak accelerations versus frequencies [32].

Based on the experience matured by [35], the standard ISO6897 [36] proposes the following expression to indicate the level of human occupancy comfort in terms of the root-mean-square acceleration [m/s^2]:

$$\sigma_a = e^{-3.56-0.41\ln(n)}, \quad (1.1)$$

n being the frequency with an approximately normal distribution [Hz], as a satisfactory magnitude indicating a level of acceleration at which “*about 2% of the occupants will comment adversely*”.

Further studies summarized in [26] develop a formulation to evaluate the peak acceleration in the horizontal plane a_h [m/s^2] for the return period R [year] (less than 10 years), due to wind loads as:

$$a_h = \sqrt{2\ln(nT)} \left[0.68 + \frac{\sqrt{\ln(R)}}{5} \right] e^{-3.5-0.41\ln(n)}, \quad (1.2)$$

where n is the frequency [Hz] and T the period of wind storm ($T=600$ sec as suggested in [26]).

Equations (1.1) and (1.2) are graphically presented in Figure 1.2.4.

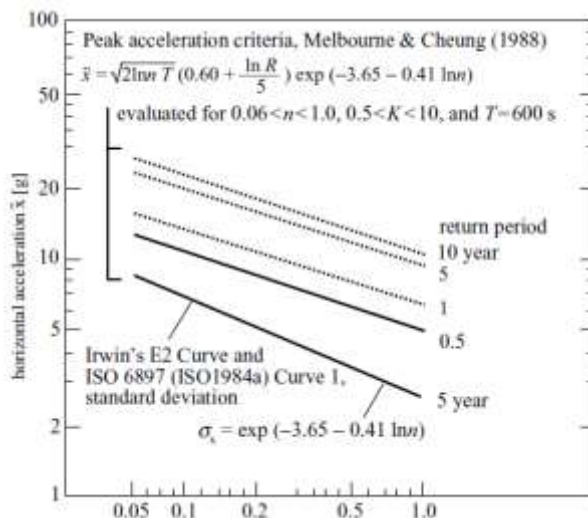


Figure 1.2.4. Peak acceleration criteria proposed by [35] and [26].

The above acceptable criteria regarding the human tolerable vibrations (comfort) may be classified as “physiological” criteria. More details about this topics, in particular related to how evaluate the comfort level of footbridges, will be presented and deeply analyzed in section 2.2.

More in general for all the structures the acceptance criteria for vibrations of civil engineering structures should be considered from various aspects. Indeed the structure should, or better must not collapse maintain its structural integrity during the “vibration”. Secondly the vibration could produce any mechanical problems such as overstressing, malfunctioning and so forth..., that sometimes could be produce future troubles (e.g. fatigue problems) or worst hide problems that compromise the global structural safety. As for the comfort criteria is not so easy produce an unified code (see [37]-[39] among others), anyway different guidelines and/or code are proposed in literature. An example as given in Table 1.2.2 [40].

Table 1.2.2. German Standard DIN 4150 [40].

Acceleration limit [m/s^2]	Peak velocity limits	
	Frequency range [Hz]	Velocity [mm/s]
Industrial buildings	$f \leq 10$	20
Residential buildings	$10 < f \leq 50$	$15 + f/2$
Vulnerable buildings	$50 < f \leq 100$	$30 + f/5$

Another chart showing the safety limits of structural vibration, and based on the study by [41], is presented in Figure 1.2.5.

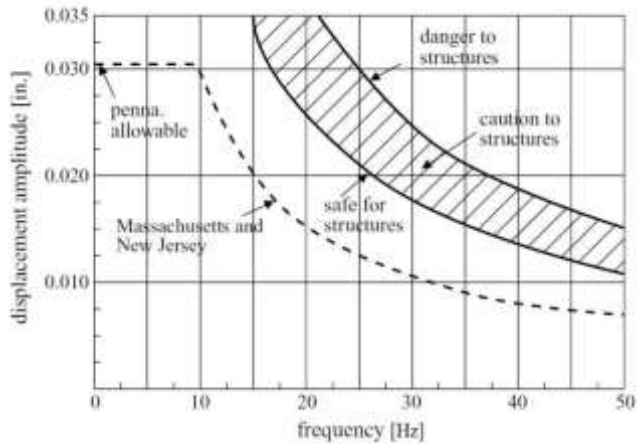


Figure 1.2.5. Structural safety criteria for frequencies range up to 50 Hz [41].

A general review of the existing criteria is proposed in [42] and summarized in Table 1.2.3.

An unified peak acceleration criteria taking account all the above presented study, is introduced by [43] and summarized² in Figure 1.2.6. This discomfort criterion approximately corresponds to the curve labelled as “unpleasant” in Figure 1.2.1, the

² As specified by the author the proposed criteria is only a rough approach in order to evaluate the discomfort of the structure, and cannot be applied blindly to all structures.

peak acceleration criteria for $R = 5$ years in Figure 1.2.4 and about the middle line of the “Chen and Robertson bounds” (Figure 1.2.2) for the lower frequency range.

Table 1.2.3. Structural criteria: overall acceptance.

<i>Structures</i>	<i>Acceptance acceleration/velocity level</i>	<i>Comments</i>
Pedestrian structures	$a \leq 5 - 10\% \text{ g}$	Normally the lower value does not produce discomfort
Office buildings	$a \leq 2\% \text{ g}$	DIN and BS may yield quite different values
Gymnasia (sport halls)	$a \leq 5 - 10\% \text{ g}$	Gymnasia $a \leq 5 - 10\% \text{ g}$ The higher value recommended only if the acoustic effect is small, and only participants are on or near the vibrating floor
Dancing and concert halls	$a \leq 5 - 10\% \text{ g}$	The same as for gymnasia
Factory floors	$v \leq 10\text{mm/s}$	Stricter bounds required for high-quality production factories

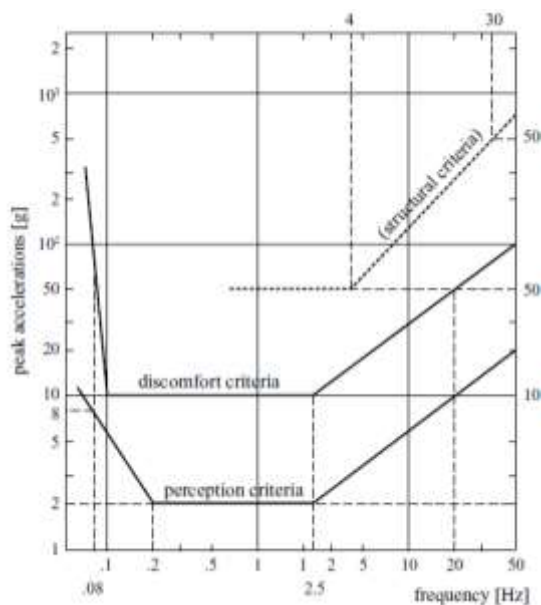


Figure 1.2.6. General peak acceleration criteria [43].

Concluding, usually the discomfort criteria are much stricter than the structural criteria and hence become more critical for structural design purposes. Thus, great care should be taken when the required services of the structure are particularly sensitive.

1.3 References

- [1] Giacosa L.M.; A. De Stefano, 2007. Long-Term Structural Health Monitoring of the 2006 Torino's Olympic Pedestrian Cabled-Stayed Bridge. In: SMSST'07, Chonqing, Naijing - Cina, 19-27 Maggio 2007.
- [2] Bursi, O. S., Ussia, A., Kumar, A., 2013. Structural health monitoring of a complex cable-stayed footbridge and reliability assessment. On the Proceeding of the 11th International Conference on Structural Safety & Reliability - ICOSSAR 2013, New York, USA, June 16-20, 2013.
- [3] Bonelli A, Bursi, O. S. , Ceravolo R., Santini S., Tondini N., Zasso A., 2010. Dynamic Identification and Structural Health Monitoring of a Twin Deck Curved Cable-Stayed Footbridge: The “Ponte Del Mare” of Pescara in Italy”. On the Proceeding of the Fifth European Workshop on Structural Health Monitoring, Sorrento, Naples, Italy, 29 June - 02 July, 2010.
- [4] P. Dallard et al. 2001. The London Millennium Footbridge. The Structural Engineer Volume 79/No 22.
- [5] Norme tecniche per le costruzioni - D.M. 14 Gennaio 2008 (NTC2008) [In Italian].
- [6] Zobel H., Alkhafaji T., 2011. Contemporary Structural Solutions Of Timber Pedestrian Bridges On the Proceeding of the 4th International Conference Footbridge - Wrocław (Poland) on July 6th – 8th, 2011.
- [7] K. Van Nimmen, G. Lombaert, G. De Roeck, P. Van den Broeck, 2014. Vibration serviceability of footbridges: Evaluation of the current codes of practice. *Engineering Structures* **59**, pp. 448–461.
- [8] M. Pańtak, 2012. Elaboration of the vibration comfort criteria for footbridges during vibrations induced by pedestrians. *Bridge Maintenance, Safety, Management, Resilience and Sustainability – Biondini & Frangopol (Eds) - Taylor & Francis Group, London, ISBN 978-0-415-62124-3.*
- [9] Bortoluzzi D., Casciati F., Casciati S., Faravelli L., Chen Z., 2013. Reporting the results of two experimental campaigns on a pedestrian timber bridge - 9th International Workshop on Structural Health Monitoring 2013 – IWSHM - Stanford University, Stanford, CA – USA, September 10-2, 2013.
- [10] Bortoluzzi D., Casciati F., Casciati S., Faravelli L., 2013. Comparison of accelerometric response records on a timber footbridge. On the Proceeding of

- 2nd International Conference on Timber Bridges 2013 – ICTB2013, Las Vegas, Nevada USA, September-October, 2013.
- [11] Iván M. Díaz, José M. Soria, Norberto Ibán, Mariano Cacho Pérez, Jaime García-Palacios, 2014. Vibration Monitoring of a Steel-plated Stress-ribbon Footbridge: Effects of Environmental and Operational Factors on Modal Properties. On the Proceeding of the 6th World Conference on Structural Control and Monitoring - 6WCSCM, Barcellona, Spain, 15-17 July, 2014.
- [12] Antolín Lorenzana et al., 2014. One year of the structural health monitoring of Pedro Gómez Bosque footbridge. On the Proceeding of the 6th World Conference on Structural Control and Monitoring - 6WCSCM, Barcellona, Spain, 15-17 July, 2014.
- [13] Siwowski T., Janas L., 2014. Numerical and experimental assessment of the dynamic behaviour of a circular footbridge. On the Proceeding of the 9th International Conference on Structural Dynamics, EURODYN 2014 Porto, Portugal, 30 June - 2 July 2014.
- [14] K. Jalsan, K. Flouri & G. Feltrin, 2012. Bi-Objective Layout Optimization of a Wireless Sensor Network for Footbridge Monitoring. Bridge Maintenance, Safety, Management, Resilience and Sustainability – Biondini & Frangopol (Eds) - Taylor & Francis Group, London, ISBN 978-0-415-62124-3.
- [15] Bortoluzzi, D., Casciati, S., Elia, L., Faravelli, L. 2013. Semi-Active Control for the Mitigation of the Vibration on a Footbridge. On the Proceeding of XXI Congresso dell'Associazione Italiana di Meccanica Teorica ed Applicata – AIMETA2013 – Torino , Italy, September, 17-20, 2013.
- [16] Bortoluzzi, D., Casciati, F., Faravelli, L. 2014. Vibration mitigation in a “cable-stayed-like” timber footbridge. On the Proceeding of the 6th World Conference on Structural Control and Monitoring - 6WCSCM, Barcellona, Spain, 15-17 July, 2014.
- [17] Rodrigo Falcão Moreira, Elsa Caetano, Álvaro Cunha, 2014. Vibration control and monitoring on the new footbridge over the Ave River in Santo Tirso, Portugal. On the Proceeding of the 9th International Conference on Structural Dynamics, EURODYN 2014 Porto, Portugal, 30 June - 2 July 2014.
- [18] J. Liu, L. Jiang, S.J. Li, Q. Zhou, and R.C. Zhang, 2014. Smart control for responses of footbridge induced by wind pressure due to high speed train using MR-TMD system. On the Proceeding of the 6th World Conference on

Structural Control and Monitoring - 6WCSCM, Barcellona, Spain, 15-17 July, 2014.

- [19] Carlos M. Casado et al., 2013. Implementation of passive and active vibration control on an in-service footbridge. *Journal of Structural Control And Health Monitoring*; 20, pp. 70–87.
- [20] Casciati S., Faravelli L., Bortoluzzi D., 2013. Human Induced Vibrations In A Pedestrian Timber Bridge. On the Proceeding of the 4th International Conference on Computational Methods in Structural Dynamics & Earthquake Engineering - COMPDYN2013, Kos Island (GR), 12-14 Jun 2013.
- [21] Piccardo G., Tubino F., 2009. Simplified procedures for vibration serviceability analysis of footbridges subjected to realistic walking loads. *Journal of Computers and Structures* 87, pp. 890-903.
- [22] José Guilherme Santos da Silva, Jorge Maurício dos Santos de Souza, 2014. Dynamic analysis of pedestrian footbridges based on probabilistic modelling. On the Proceeding of the 9th International Conference on Structural Dynamics, EURODDYN 2014 Porto, Portugal, 30 June - 2 July 2014.
- [23] Eurocode 5 - EN 1995-2:2004. Design of timber structures - Part2: Bridges, 1st edition.
- [24] Eurocode 0 - EN 1990. Basis of structural design, 1st edition.
- [25] Kliger R., Svensson T. , J. and I. Svensson, 2013. Vibration response of long cable-stayed timber footbridge – case study. On the Proceeding of 2nd International Conference on Timber Bridges 2013 – ICTB2013, Las Vegas, Nevada USA, September-October, 2013.
- [26] Melbourne W. and Cheung J., 1988. Designing for serviceable accelerations in tall buildings. *Proceedings of the 4th International Conference on Tall Buildings*, pp. 148–155, Hong Kong and Shanghai.
- [27] Harris C., 1976. *Shock and Vibration Handbook*, 2nd edn. McGraw-Hill.
- [28] Wiss F. and Parmelee R., 1974. Human perception of transient vibrations *Proceedings of the American Society of Civil Engineers*, 100 (ST4), 773–787.
- [29] Chen P. and Robertson L., 1973. Human perception thresholds of horizontal motion. *Proceedings of the American Society of Civil Engineers*, 98, 1681–1695.

- [30] Irwin P., 1979. Human response to dynamic motion of structures. *The Structural Engineer* 9(56A), pp. 237–244.
- [31] Melbourne W., 1998. Comfort criteria for wind-induced motion in structures. *Structural Engineering International* 8(1), pp. 40–44.
- [32] Chang F (1973) Human response to motions in tall buildings. *Proceedings of the American Society of Civil Engineers*, 98, pp. 1259–1272.
- [33] Hansen R., Reed J. and Vannarcke E., 1974. Human response to wind-induced motion on buildings. *Proceedings of the American Society of Civil Engineers*, 99, 1589–1605.
- [34] Khan F. and Parmelee R., 1971. Service criteria for tall buildings for wind loading. *Proceedings of the 3rd International Conference Wind Effects on Buildings and Structures*, pp. 401–408, Tokyo.
- [35] Irwin P., 1986. Motion in tall buildings. *Proceedings of the Conference on Tall Bridges and Urban Habitat*, pp. 759–778, Chicago.
- [36] ISO 6897, 1984. Guidelines for the Evaluation of the Response Occupants of Fixed Structures, Especially Buildings and Off-shore Structures, to Low Frequency Horizontal Motion (0.063 to 1 Hz). ISO, International Standards Organization.
- [37] ISO/DIS 4866, 1984. Mechanical Vibrations and Shock Measurement and Evaluation of Vibration Effects on Buildings. International Standards Organization.
- [38] ISO 2373, 1987. Mechanical vibration of certain rotating electrical machinery with shaft heights between 80 and 400 mm - Measurement and evaluation of the vibration severity. International Standards Organization.
- [39] ISO 10816, 1995. Mechanical vibration -- Evaluation of machine vibration by measurements on non-rotating parts. International Standards Organization.
- [40] German Standard DIN 4150 [41].
- [41] Leet L., 1960. *Vibrations from Blasting Rocks*. Harvard University Press.
- [42] Bachmann H. and Ammann W., 1987. Vibrations in structures – induced by man and machines. In *Structural Engineering Documents*, 3rd edn, IABSE, Zurich (Switzerland).
- [43] Wenzel H., 2009. *Health Monitoring of Bridges*. John Wiley & Sons Ltd, The Atrium, Southern Gate, Chichester, West Sussex PO19 8SQ, England.

Chapter 2 Design requirements and performance satisfaction

As already observed in the previous chapter, one of the main problems when one works on footbridges, is not the safety aspect, but rather the limitation of the vibration in order to achieve a good result in term of comfort for the user.

This means that footbridges should be no longer designed for static loads only, but also accounting for the dynamic behaviour during the design stage, without forgetting the rule of thumb: *“the more slender structures become, the more attention must be paid to vibration phenomena”*.

One of the main and simplest way if one wants to take into control the vibration of a given footbridge is that one has to keep the natural frequency within a suitable range as will be better analyzed and discussed in section 2.2 (see [1]-[2] among others). To fulfil such a requirements, one could be forced to a special footbridge design; in fact very slender and/or lightweight structures, suspension bridges and so forth... could be unable to satisfy these requirements. Not only natural frequencies but also mass, damping, deck loading (pedestrian loads) determines the dynamic behaviour of the footbridge.

These bridges are usually characterized by the lowest value of the natural frequencies very close to the external excitations like that of the pedestrian loads; thus the risk of resonance is quite great. Vibrations of footbridges may occur in vertical and horizontal directions. Even the torsion of the bridge deck is sometimes excited.

Vibrations of footbridges may lead to serviceability problems, affecting the comfort of the crossing pedestrians. Collapse or even damage due to human induced dynamic forces are quite unlikely to occur. For these kinds of structures, the pedestrian induced load³ is probably the main source of vibration of footbridges, together with the wind loads.

³ Pedestrian loading is by nature unsteady, transient and waddling in a small range of excitation frequency.

Another dynamic loading on footbridges is intentional excitation by people that are jumping on the spot, bouncing, swaying body horizontally, shaking stay cables etc... In that case, the comfort is certainly not fulfilled but the structure should preserve its integrity under these extreme loads must be considered.

Summarizing, in general the assessment of human-induced vibrations needs to be considered by the designer during the design to evaluate that:

- 1) vibrations due to pedestrian traffic are acceptable for the users (comfort aspects),
- 2) the footbridge does not collapse when subjected to intentional excitation (safety aspects due to extreme loads).

Once proved that the dynamic behaviour of the bridge due to expected loads is evaluated and fulfilled the required comfort, the footbridge can be designed and constructed. If the vibration behaviour does not satisfy some comfort criteria, changes in the design or damping devices should be considered.

Concluding, a well done footbridge design should consider all these factors in order to match together structural (both from static and dynamic point of view) and architectural aspects with the comfort requirements.

2.1 Dynamics of the footbridges design and structural health monitoring

The purpose of this section is to recall the main features and concepts within the dynamic of the structures (see [3]-[5] among others) and the structural health monitoring (see [6]-[8] among others).

2.1.1 Governing relations

For the general formulation of the dynamic problem the reader will be referred to [9]-[14] among others.

Most of the structural dynamic properties can be highlighted studying the so called simple oscillator. The simple oscillator (discrete system) consists of mass m , connected to a support by a linear spring of stiffness k and a linear damper of viscosity c , on which is acting an external force $F(t)$. It is supposed that the device moves only in one direction; therefore one has only one degree of freedom (1-DOF) defined by the position $x(t)$ of its mass (Figure 2.1.1).

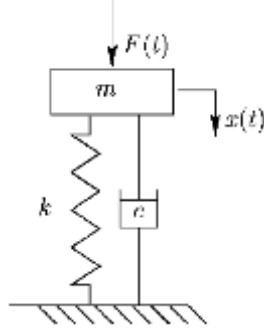


Figure 2.1.1. Schematic representation of a 1-DOF system.

The dynamic equation of equilibrium can be written as [9]:

$$m\ddot{x}(t) + c\dot{x}(t) + kx(t) = F(t), \quad (2.1)$$

or, introducing the following quantities:

$$\omega_0 = \sqrt{\frac{k}{m}} = 2\pi f_0 \quad (2.2)$$

$$\xi = \frac{c}{2\sqrt{km}}$$

in the new form:

$$\ddot{x} + 2\xi\omega_0\dot{x} + \omega_0^2 x = \frac{F}{m}. \quad (2.3)$$

where the dependence on the time is made implicit for simplicity, f_0 is the natural frequency of the oscillator (Hz)⁴ and ξ the (non-dimensional) critical damping ratio. It is important to underline that the following developments are based on the hypothesis of linear damping: $F_{damping}(x, \dot{x}) \propto \dot{x}(t)$ (viscous, with a damping force proportional to speed [14]). This is the assumption selected by most footbridge designers and engineers.

Assume that the external excitation can be represented as a harmonic function expressed as:

$$F(t) = F_s \sin(\omega t). \quad (2.4)$$

⁴ Or equivalently ω_0 the natural pulsation of the oscillator (rad/sec).

Then it is possible to evaluate the “static” response of the oscillator under the action of an equivalent force of amplitude equal to F_s ; that is:

$$x_{static} = \frac{F_0}{k} = \frac{F_0/m}{\omega_0^2}. \quad (2.5)$$

From this it is possible to determine the maximum dynamic response of the system by simply multiplying the static response by the dynamic amplification parameter $A(\Omega)$:

$$x_{max} = x_{static} A(\Omega), \quad (2.6)$$

where $\Omega = \omega/\omega_0$ is the relative pulsation (or reduced pulsation), and the dynamic amplification parameter can be represented as a function of the relative pulsation and the critical damping ratio:

$$A(\Omega) = \frac{1}{\sqrt{(1-\Omega^2)^2 + 4\xi^2\Omega^2}}. \quad (2.7)$$

These parameter may be represented by a set of curves parameterized by ξ as reported in Figure 2.1.2.

These curves show a peak for the value of $\Omega_R = \sqrt{1-2\xi^2}$ characterising the resonance⁵ and therefore corresponding to the resonance frequency:

$$f_R = \omega_R/2\pi \Leftrightarrow \omega_R = \omega_0 \sqrt{1-2\xi^2}. \quad (2.8)$$

It is worth underlining that the resonance phenomena for a damped structure occurs when the frequency of the external excitation equals the resonance frequency; that is $\omega = \omega_R$.

Since the structural damping for the usual civil structures is weak ([9] and [13]), i.e. $\xi \ll 1$, one may consider that resonance occurs when:

$$\omega = \omega_0 \approx \omega_R \Leftrightarrow \Omega_R = 1 \rightarrow A(\Omega_R = 1) \approx \frac{1}{2\xi}. \quad (2.9)$$

⁵ Resonance is the tendency of a system to oscillate with greater amplitude at some frequencies than at others. At these frequencies, even small periodic driving forces can produce large amplitude oscillations.

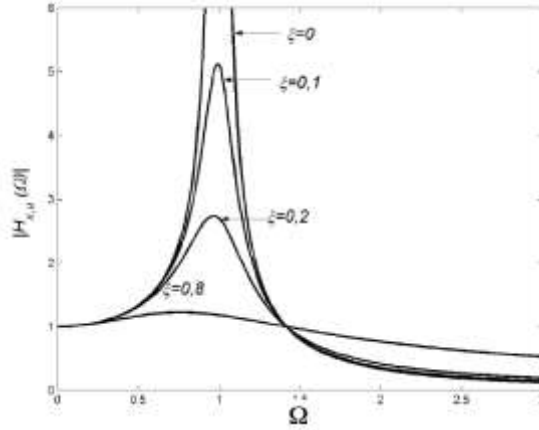


Figure 2.1.2. Dynamic parameter trend for specific value of the critical damping.

The above properties, even if introduced for a 1-DOF, show that designing the structures only taking into account the maximum intensity (F_s) of the acting load can result to be unsatisfactory. In fact the resonance phenomenon can generate higher displacements/ stresses even if the intensity of the loads is lower. Thus, for example, the force $F_1(t) = F_s \sin(\omega_1 t)$ can generate displacements or stresses much lower than a load with an amplitude 10 times weaker, $F_2(t) = [F_s/10] \sin(\omega_2 t)$, only because $F_2(t)$ has a frequency much closer to the resonance frequency of the structure. Moreover the resonance amplification is directly related to damping.

The most common sources of damping are:

- 1) the internal damping linked with the material itself; its value is mainly linked to the temperature and the frequency of excitation;
- 2) the damping by friction (Coulomb) $F_{damping}(x, \dot{x}) = \mu [sign(\dot{x})]$: it is mainly linked to the construction joints between different elements.

Just to illustrate how the damping acts on the response of the oscillator, consider the so called free vibration: assume that the external force is equal to zero over the time ($F(t)=0$). Thus, re-writing equation (2.3) one achieves:

$$\ddot{x} + 2\xi\omega_0\dot{x} + \omega_0^2 x = 0. \quad (2.10)$$

The generic solution of the above differential equation can be expressed as:

$$x(t) = X_0 e^{rt}, \quad (2.11)$$

being r the solution of the characteristic equation:

$$r^2 + (2\xi\omega_0)r + \omega_0^2 = 0. \quad (2.12)$$

$\xi \geq 0$ characterized the so called dissipative system. The different rates are so classified depending on the damping ratio as:

- 1) $0 \leq \xi < 1$ (the typical case for civil structures);
- 2) $\xi = 1$;
- 3) $\xi > 1$.

The response of the 1 -DOF system is summarized in Figure 2.1.3.

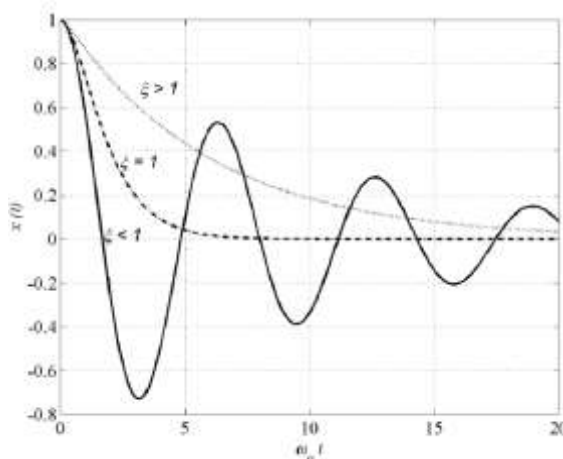


Figure 2.1.3. Free oscillation of a 1 -DOF system with different value of damping.

For the applications of this thesis damping is modelled by viscous damping. This may be physically interpreted as a force that opposes the velocity of the structure. It is interesting to note that sometimes (as for some models of the pedestrian load), the forces "agree" with the velocity. This "agreement" generates "negative" value of damping, which leads to oscillations of the pedestrian bridges that become greater and greater (Figure 2.1.4). Thus, instability problems could appear and could lead, in the worst hypothesis, to the collapse of the construction.

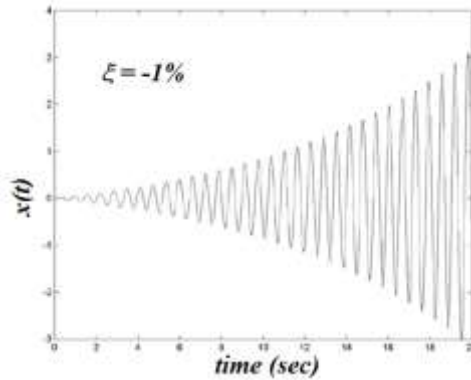


Figure 2.1.4. Oscillation of a 1-DOF system – divergences induced by a “negative” damping.

A properly evaluation of the damping is therefore a key point ([15] and [16]).

Two methods are here briefly presented ([9], [14] and [16]):

- 1) *logarithmic decrement method*: the damping may be evaluated knowing the period T_a corresponding the interval between two distinct peaks, and the

$$\text{decrement } \delta = \log \left(\frac{x(t_1)}{x(t_2)} \right) \approx \frac{2\pi\xi}{\sqrt{1-\xi^2}}. \text{ Assuming } \xi \ll 1, \text{ one obtains: } \xi \approx \frac{\delta}{2\pi}$$

(Figure 2.1.5).

- 2) *bandwidth method*: the damping may be evaluated by the equation $\Delta\Omega = \Omega_1 - \Omega_2 \approx 2\xi\sqrt{1-\xi^2} \approx 2\xi$ when $\xi \ll 1$, where the bandwidth $\Delta\Omega$ is such that $|A(\Omega_{1,2})| = \frac{|A(\Omega)|_{\max}}{\sqrt{2}}$ (Figure 2.1.6).

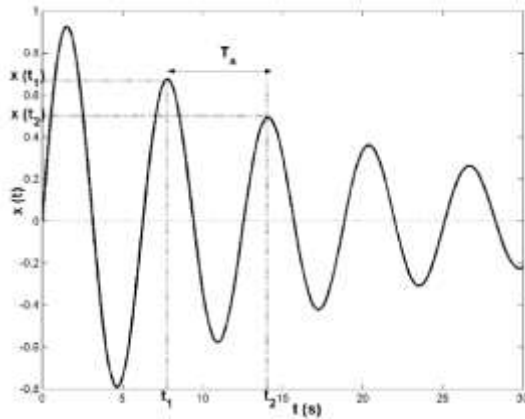


Figure 2.1.5. Representation of the “logarithmic decrement method”.

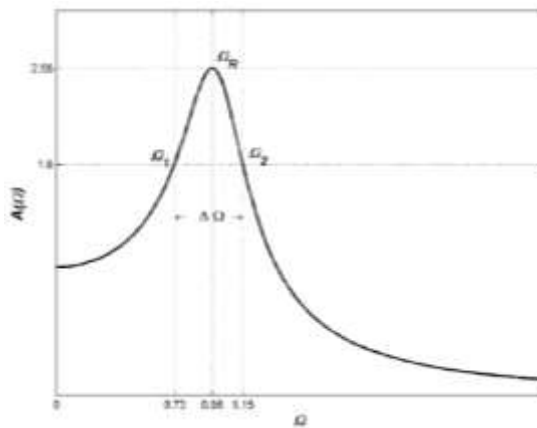


Figure 2.1.6. Representation of the “bandwidth method”.

In order to generalize the problem to the case of a discrete n -DOF system, system in Figure 2.1.7 is considered. It sees n masses connected in series by springs and dampers. The displacement of the generic mass is then dependent on the displacement of another mass; in other word one can say that the n masses are coupled through springs and dampers.

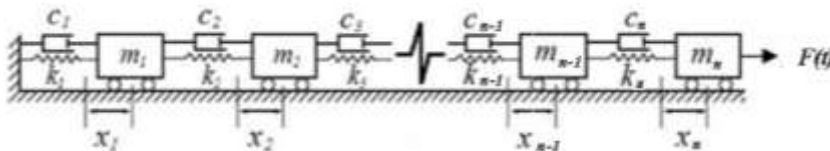


Figure 2.1.7. Schematic representation of a n -DOF system.

Let's $x_i(t)$ the position of the n -th mass where $i=1,2,\dots,n$. Then, the dynamic equation of equilibrium becomes [9]:

$$\mathbf{M}\ddot{\mathbf{X}} + \mathbf{C}\dot{\mathbf{X}} + \mathbf{K}\mathbf{X} = \mathbf{F}, \quad (2.13)$$

where:

- $\mathbf{X} = [X_1 \quad X_2 \quad \dots \quad X_n]^{-1}$ is the vector of DOFs (size n);
- $\mathbf{M} = \begin{bmatrix} m_1 & \dots & 0 \\ \vdots & \ddots & \vdots \\ 0 & \dots & m_n \end{bmatrix}$ is the mass matrix (size n by n). Dealing with the hypothesis of lumped masses (discrete approach) this matrix assumes the classical diagonal form because the accelerations of a lumped mass produces inertial forces only in correspondance of the concentration points;
- $\mathbf{C} = \begin{bmatrix} c_{11} & \dots & c_{1n} \\ \vdots & \ddots & \vdots \\ c_{n1} & \dots & c_{nn} \end{bmatrix}$ is the damping matrix (size n by n);
- $\mathbf{K} = \begin{bmatrix} k_{11} & \dots & k_{1n} \\ \vdots & \ddots & \vdots \\ k_{n1} & \dots & k_{nn} \end{bmatrix}$ is the stiffness matrix (size n by n);
- $\mathbf{F} = [f_1 \quad f_2 \quad \dots \quad f_n]^{-1}$ is the vector of the external forces acting on the system (size n).

in which the dependence on the time is neglected for simplicity.

The mass and stiffness matrices can be evaluated starting from energy considerations [9] as follows:

- the mass matrix is associated with the kinetic energy T of the system, as the sum of the kinetic energies of each mass; that is:

$$T = \frac{1}{2} \sum_{i=1}^n (m_i \dot{x}_i^2) = \frac{1}{2} \dot{\mathbf{X}}^T \mathbf{M} \dot{\mathbf{X}}; \quad (2.14)$$

- the stiffness matrix is associated with the strain energy J of the system, that is the sum of the elastic potential energy of each spring:

$$J = \frac{1}{2} \left[k_{11} x_1^2 + k_{12} (x_2 - x_1)^2 + \dots + k_{mm} x_{n-1}^2 \right] = \frac{1}{2} X^T \mathbf{K} X; \quad (2.15)$$

These two matrices are both symmetric, moreover the mass matrix is positive definite (because the kinetic energy is always positive by definition), while the stiffness matrix is positive semi-definite because of definition.

For n -DOF systems it is useful to introduce the *modal superposition* approach [14]. Consider the free movement case, thus the equation of motion (2.13) can be re-written as:

$$\mathbf{M} \ddot{X} + \mathbf{K} X = 0, \quad (2.16)$$

where the generic vector solution may be represented as:

$$X = \phi_0 e^{rt}, \quad (2.17)$$

in which ϕ_0 is a vector of constant to be determinate, of size n . Substituting (2.17) into (2.16) one reach:

$$(\mathbf{K} + r^2 \mathbf{M}) \phi_0 = 0. \quad (2.18)$$

The above equation admits advantageous solutions only if the determinant of the system is equal to zero; that is only if:

$$\det(\mathbf{K} + r^2 \mathbf{M}) = 0. \quad (2.19)$$

For a classical n -DOF system the above system has $2n$ solutions: $\pm i\omega_k$, $k = 1, 2, \dots, n$ where ω_k represents the k -th natural pulsation of the system. With each index k , there is an associated vector called modal vectors of the system ϕ_k such that the response of the whole system can be re-written as:

$$X(t) = \sum_{k=1}^n \phi_k \left(\alpha_k e^{-i\omega_k t} + \beta_k e^{+i\omega_k t} \right). \quad (2.20)$$

The components of the vector ϕ_k are linked, thus usually these modal vectors are defined after normalization. The most frequent choices are here summarized:

- one of the components is made equal to 1.
- each mode is unitary; i.e. $|\phi_i| = 1$;

- satisfy the requirement: $\phi_i^T \mathbf{M} \phi_j = 1$.

Summarizing, the natural pulsations ω_i are the square roots of the natural positive values of the matrix $\mathbf{M}^{-1}\mathbf{K}$ evaluable solving the equation $\det(\mathbf{K} - \omega_i^2 \mathbf{M}) = 0$. The natural forms of a discrete system are the natural vectors ϕ_i associated with it. The couple (ω_i, ϕ_i) is called a natural vibration mode where $i=1,2,\dots,n$. In other words for a linear system a mode is one particular solution of the free non-damped vibration, in which all the DOFs components are synchronous⁶:

$$X(t)_{\text{mode}0} = \phi_0 e^{i\omega_0 t}. \quad (2.21)$$

The above natural vibration modes are orthogonal in relation to the mass matrix and in relation to the stiffness matrix [9]; that is:

$$\begin{aligned} \phi_i^T \mathbf{M} \phi_j &= m_i \delta_{ij}, \\ \phi_i^T \mathbf{K} \phi_j &= k_i \delta_{ij}, \end{aligned} \quad \forall i, j \quad (2.22)$$

in which δ_{ij} is the classical Kronecker symbol, while m_i and k_i represent, respectively, the so called generalised mass and stiffness associated to i -th mode. Their values will depend on the normalization used to define the natural vectors as described above.

To the case of non-damped forced vibration, the dynamic equilibrium (2.13) become as:

$$\mathbf{M}\ddot{\mathbf{X}} + \mathbf{K}\mathbf{X} = \mathbf{F}. \quad (2.23)$$

To solve directly the above equation needs to evaluate the inverse of the mass matrix that could be costly, from the calculation point of view, if the number of DOFs is high. Thus, it is standard practice to apply the modal superposition approach. This way is quite useful because it is able to unlinks the equations of motion that compose the general equations, significantly reducing the calculation operations. The principle behind this approach is to introduce a reference change re-writing the equation of motion in the new base system obtained by a linear combination of the natural vectors ϕ_i the so called modal base. Thus, the response $X(t)$ of the system represented by equations (2.23) may be expressed as:

$$X(t) = \Phi q(t) = \sum_{i=1}^n \phi_i q_i(t), \quad (2.24)$$

⁶ That is they reach their maxima and their minima at the same time.

in which:

- $\phi = [\phi_1 \quad \phi_2 \quad \cdots \quad \phi_n]$ is a matrix (size n by n) where each columns contain the natural vector ϕ_i ;
- $q(t)$ is the vector the modal variables, the new variables obtained re-writing the problem in the new reference system.

Having in mind the orthogonality of the modes, see (2.22), and the generic solution in (2.24), pre-multiplying equation (2.23) by ϕ^T one obtains:

$$\phi^T \mathbf{M} \phi \ddot{q}(t) + \phi^T \mathbf{K} \phi q(t) = \phi^T F(t) \rightarrow \tilde{\mathbf{M}} \ddot{q}(t) + \tilde{\mathbf{K}} q(t) = \phi^T F(t) \quad (2.25)$$

or in extended form:

$$\begin{bmatrix} \ddots & 0 & 0 \\ 0 & m_i & 0 \\ 0 & 0 & \ddots \end{bmatrix} \ddot{q}(t) + \begin{bmatrix} \ddots & 0 & 0 \\ 0 & k_i & 0 \\ 0 & 0 & \ddots \end{bmatrix} q(t) = \phi^T F(t). \quad (2.26)$$

where $\tilde{\mathbf{M}}, \tilde{\mathbf{K}}$ are respectively the diagonalized mass and stiffness matrices. This allows one to get a system of unlinked differential equations as:

$$\ddot{q}(t) + \omega_i^2 q(t) = p_i(t), \quad (2.27)$$

where the vector $p_i(t) \triangleq \frac{\phi^T F}{m_i}$ contain the component per unit of generalized mass of the force vector $F(t)$, and it is called the modal contribution factors of the applied force vector.

The possibility of writing the general problem expressed by equation (2.23) in diagonalized form should be achieved in order to decrease the computational cost as observed. The presence of damping matrix \mathbf{C} makes the problem a little bit more complicated. In fact, as far as the damping matrix \mathbf{C} is a general matrix, it is not possible to state that this matrix will also be diagonalized by the modal superposition approach. However, there are some cases where this property does apply. The most remarkable case when a matrix \mathbf{C} is transformed into a diagonal matrix by the modal approach is the one called “proportional damping”. In fact when the structure under study is not too much dissipative and the natural frequencies are clearly separated, it can be shown that is reasonable ([9] and [14]) to define the damping matrix as a linear combination of the mass and stiffness matrices; that is:

$$\mathbf{C} = \sum_{j=1}^N \alpha_j \mathbf{M} (\mathbf{M}^{-1} \mathbf{K})^{j-1}, \quad \alpha_j \in \mathbb{R}. \quad (2.28)$$

Assuming in the above equation $N=2$ one achieves:

$$\mathbf{C} = \alpha_1 \mathbf{M} + \alpha_2 \mathbf{K}, \quad (2.29)$$

the so called Rayleigh's damping matrix, where α_1 and α_2 are two constant parameters called Rayleigh's coefficients, whose values define the entity of damping actions in the system, that in the International System have the physical dimension of s^{-1} and s respectively.

Since both the mass and stiffness matrices may be diagonalized applying the modal approach (see equation (2.23)), is simple to observe as the damping matrix expressed by will also be diagonalized by following the same approach; indeed:

$$\boldsymbol{\phi}^T \mathbf{C} \boldsymbol{\phi} = \boldsymbol{\phi}^T (\alpha_1 \mathbf{M} + \alpha_2 \mathbf{K}) \boldsymbol{\phi} = \dots = \alpha_1 \tilde{\mathbf{M}} + \alpha_2 \tilde{\mathbf{K}}. \quad (2.30)$$

Thus, the n equations of motion of the generic system described in (2.23) are decoupled. Then one considers each single equation as represented by a 1-DOF system as follows⁷:

$$\ddot{q}(t) + 2\xi_i \omega_i \dot{q}(t) + \omega_i^2 q(t) = p_i(t), \quad (2.31)$$

where $\xi_i = \gamma_i / 2\omega_i m_i$ in which $\gamma_i = \alpha_1 m_i + \alpha_2 k_i$. In practice, each critical damping ratio ξ_i must be experimentally recalibrated and/or evaluated. By the way it is usual to consider that the value of the critical damping ratio does not depend on the mode under consideration. This allows one to assume $\xi_i = \xi$, where the constant value ξ is fixed experimentally or by the regulations [36].

In conclusion the principle of modal superposition allows one to treat the generic n -DOF system as the "sum" of n simple oscillators (Figure 2.1.8), once a new reference frame has been introduced.

⁷ This formulation can be seen as a generalization of equation (2.27).

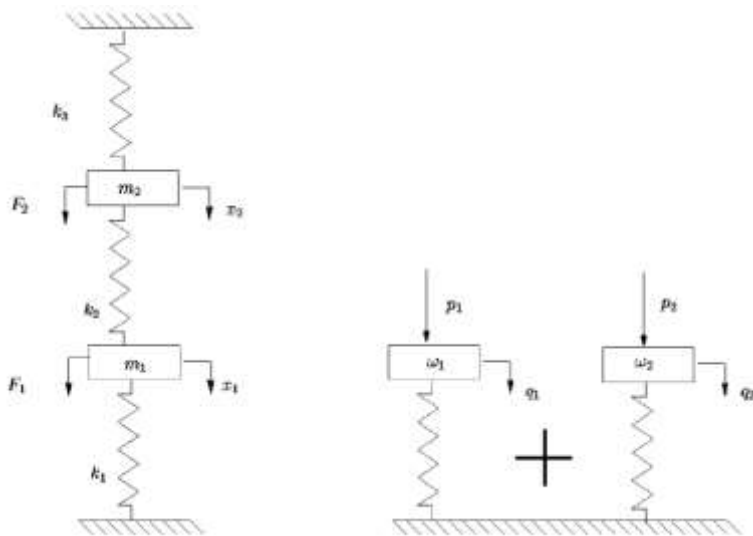


Figure 2.1.8. Modal superposition approach applied to a 2-DOF system.

2.1.2 Structural Health Monitoring

Another important aspect for civil engineering structures (e.g. bridges, strategic buildings and so forth... but in particular footbridges), is the maintenance, and/or the health monitoring issue. It is important indeed to maintain at least, and when possible improve, the quality and the level of serviceability of the structural system for the user. To achieve this purpose one needs to “know” the lifecycle performance of the structure to ensure long service life and durability. A useful tool to be used for this scope is the so called **Structural Health Monitoring** (SHM). The SHM process involves the observation of a system over time using sampled dynamic response measurements from several sensors installed along sensitive points of the structure. From the analysis and study of these measurements, or in other words from the study of the on field dynamic behaviour of the structure, the health of the system can be evaluated, pointing out any eventual damage or problem for the safety.

As proposed by [17] five axioms may be formulated for structural health monitoring that are:

- **Axiom 1.** The assessment of damage requires a comparison between two system states.

- **Axiom 2.** The identification of the existence and location of damage can be done in an unsupervised learning mode, but the type of damage and the damage severity can only be identified in a supervised learning mode.
- **Axiom 3.** Without intelligent feature extraction, the more sensitive a measurement is to damage, the more sensitive it is to changing operational and environmental conditions.
- **Axiom 4.** There is a trade-off between the sensitivity to damage of an algorithm and its noise rejection capability.
- **Axiom 5.** The size of damage that can be detected from changes in system dynamics is inversely proportional to the frequency range of excitation.

In the civil engineering area SHM requires to take account for numerous non linearity and not well known “boundary” condition of the problem, as in the case of soil structure interaction. Thus, the SHM key of success is enclosed in the possibility to collect high quality data combined with realistic identified models and deterioration laws [12]. The final output of a SHM could be the reliability index, the safety level, a graphic symbol or any other output depending on the owner [18]. An example of a SHM architecture applied to a bridge case is reported in Figure 2.1.9. Another example can be found in [19].

In the last years different approaches were proposed for health monitoring (see [20]-[24] among others). It is important that the data collected during the experimental campaign be accurately stored in order to, first of all, create a database for the structure, and apply new future algorithms when available to compare the structural behaviour between the “old” and “new” data analysis approach. By the way, it is important to note that to achieve a whole computerized SHM system able to make decision about the structural health monitoring by itself is far away.

It is clear now as SHM provides the opportunity to quantify the condition of the structure and gives the guidelines for making decisions about the structure (Figure 2.1.10), since the dynamic characteristic contains information on the global structural condition as well as on local phenomena [13].

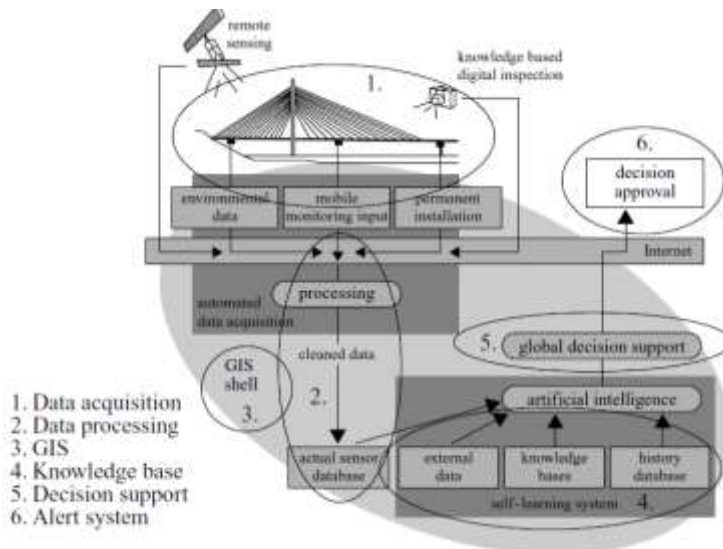


Figure 2.1.9. SHM architecture applied to a bridge [12].

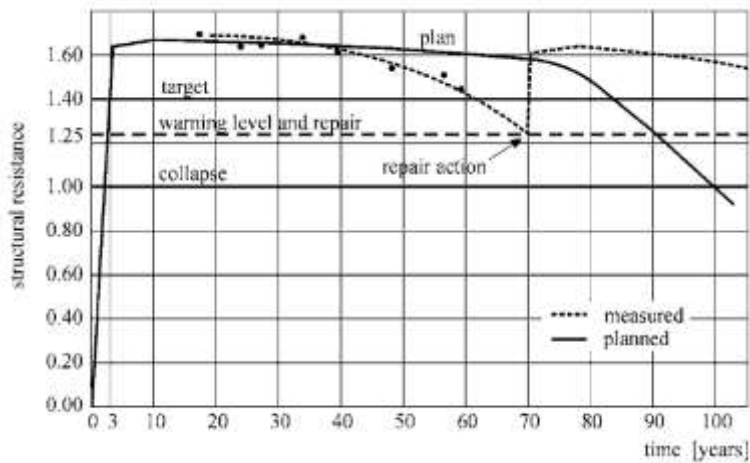


Figure 2.1.10. Example of proposed rehabilitation planning based on the Ultimate Limit Strength [13].

Three different main topics could be taken into account when one wants to perform a SHM:

- 1) responsibility;
- 2) economy;
- 3) curiosity.

From the above-mentioned motivations it is necessary to offer services on increasing quality levels depending on the structure under study and so to the depths of investigation that one wants to perform. Usually five level of investigation (Figure 2.1.11) are introduced within bridges field according to [12]:

- **Level 1 - Rating:** this represents the basic/conventional assessment of the structure starting with a visual field inspection that provides a subjective impression of the condition of the structure.
- **Level 2 - Condition assessment:** rough visual field inspection after which is possible to decide whether the conventional approach is satisfactory or an extended one is needed. Moreover this inspection will determine the type and quantity of instrumentation that will be used on field.
- **Level 3 - Performance assessment:** provides additional indicators for the assessment and will demonstrate the performance of the structure. It requires several synchronous devices to perform the monitoring.
- **Level 4 - Detail assessment and rating:** establish an analytical model representing the structure. The numerical model will be compared with the result collected during the monitoring campaign(s).
- **Level 5 - Lifetime prediction:** the last step regards the lifetime evaluation (see Figure 2.1.12 as proposed in [25]). To achieve a serious lifetime prediction the records available have to be long enough to cover, at least, three relevant cycles for the structure (e.g. usually at least three years).

To achieve the above purpose, a selection of suitable data has to be made. In particular one can have four different levels of monitoring., that are:

- 1) *spot monitoring*: should comprise a very quick measurement campaign with a few simple to handle sensors only. It provides only general condition information of the structure in order to create a ranking;
- 2) *periodic monitoring*: repeated campaigns on a structure after a specified time interval (e.g. seasonal, monthly campaign and so forth...);
- 3) *permanent monitoring*: continuously monitoring over the time. This approach allows a very detailed assessment about the structure;

- 4) *online monitoring*: observation and assessment allows warning through electronic media⁸. Decisions might be taken by the computer based on the measurement data.

With reference to above classifications the monitoring carried out in this work, and related to the two footbridges object of study, can be defined as **periodic monitoring – level 3**.

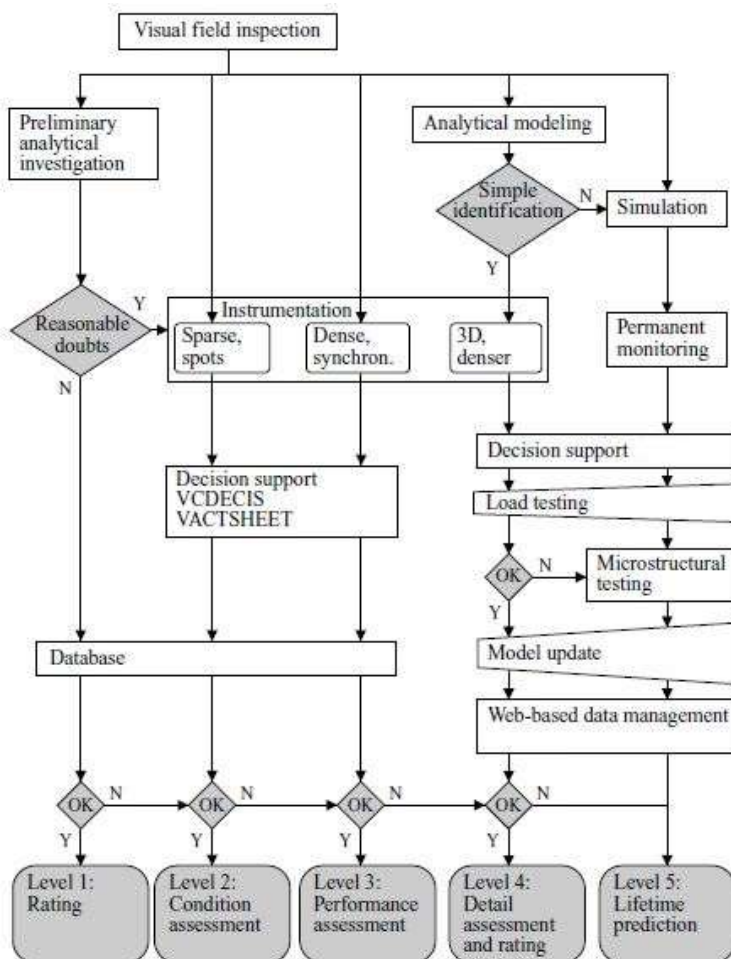


Figure 2.1.11. SHM for bridge. Typical flowchart [16].

⁸ These alert systems will only be applied at extremely critical structures.

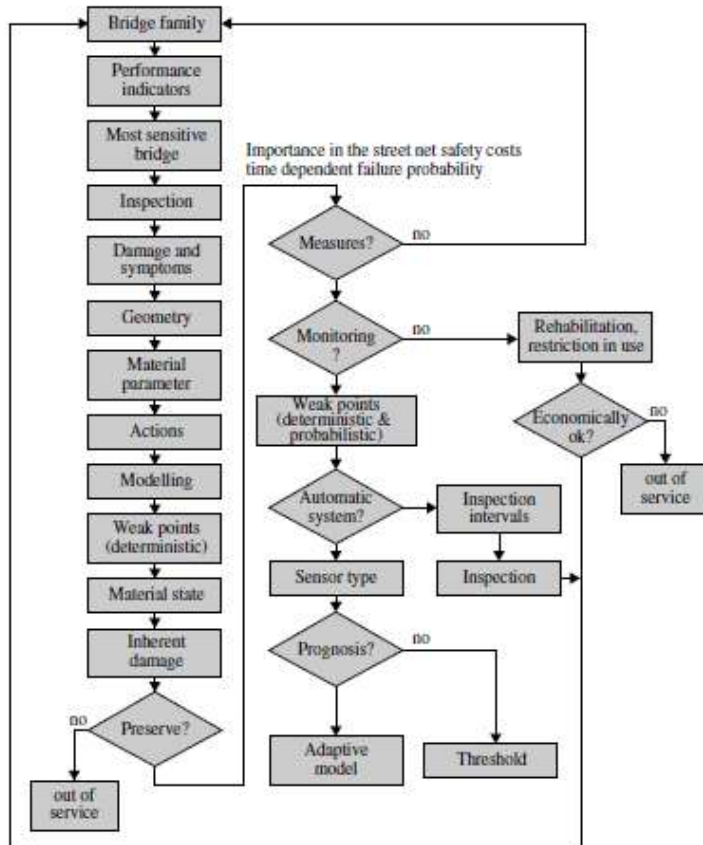


Figure 2.1.12. SHM for bridge. Typical flowchart [25].

Different typologies of devices/sensors may be used to acquire data from field as summarised in Table 2.1.1 [12], while usually the transmission of the data is entrusted to two technologies: either wired or wireless solution [26].

In conclusion, the monitoring system [27] should be considered and implemented by the designer at the design stage. Indeed the designer knows very well which could be the sensitive cross-sections of the structure, so he/she can suggest the best position for the sensors along the structure in order to optimize the quality cost trade-off. When the SHM is implemented within the design stage, all the infrastructures (e.g. power supply devices, cable, and so on) necessary to perform the monitoring may be located in an optimal position reducing once again the global operational cost.

Table 2.1.1. Typical sensors employed during a SHM [12].

Measured Value	Sensor Type	Measurement Range (MR)	Resolution	Linearity	Supply	Frequency Range	Influences
Displacement	LVDT	1-50 mm	1 % MR	0.1% MR	AC/DC	0-100 Hz	cross forces
	LVDT caliper	1-50 mm	1 % MR	0.1% MR	AC/DC	0-50 Hz	measurement frequency
	Triangulation sensor	2-200 mm	1 % MR	0.3% MR	DC	0-10 kHz	reflecting surfaces, soil
	Cable extension transducer	50-10000 mm	1 % MR	0.05% MR	DC	0-500 Hz	cross forces
Inclination	Bubble level	±10 grade	1 % MR	0.1 grade	DC	0.5Hz	vibrations
	Pendulum	±1 grade	1 % MR	0.05% MR	DC	0.5Hz	
Settlement	Hydrostatic leveling system	0-60 mm	0.01 mm		DC	static	atmosph. press., temp
	PSD	0-90 mm	< 0.05 mm	< 1% MR	DC	0-500 Hz	gradients moisture
Strain	Strain gauges	1-10000 µm/m	1 µm/m	< 1%	DC/AC	0-1000 kHz	ΔT, bucklage
	Fiber Bragg gratings	±10000 µm/m	1 µm/m	< 1%	Laser light	0-100 kHz	
	Fabry-Perot fiber sensor	±5000 µm/m	1 µm/m		Broadband white light	0-1 kHz	ΔT
	SOFD system	0.5% sensor length	2 µm/m	< 1%	Laser light	static	transverse stress
Acceleration	Optical string	0.5% sensor length			Laser light	0-100 Hz	fixing
	Piezoelectric sensors	±100 g	10 µg	< 1%	DC	0.1-2000 Hz	
	MEMS-A040 B12 (differential choke)	±1g ±20 g	5 µg	< 1% 1%	DC AC	0-250 Hz 0-100 Hz	
Vibrating velocity	Geophone	100 mm/s	5 µm/s	< 1%	DC/AC	4-1000 Hz	fixing
	Laser vibrometer	10 m/s	1 µm/s	< 1%	DC/AC	1-20000 Hz	
Temperature	Thermocouples	-185 to 300°C	50 µV/K	1%			leads
	PT100	-200 to 600°C	400 µV/K	< 1%	DC		temperature gradients

2.2 Comfort for footbridges: codes and literature overview

The classical design of the pedestrian bridges allows to work within a static context. It is therefore quite frequent, that after the construction of the bridge, the crossing pedestrians feel vibrations. In other words these structures tend to be more sensitive to dynamic forces induced by pedestrians, resulting in vibrations of the bridge deck. These vibrations can reach high levels, especially when the walking step of the pedestrians is close to the natural frequency of the bridge, resulting in situations in which the users feel uncomfortable or even unsafe. This aspect is very important for the Serviceability Limit State (SLS) evaluation of footbridges. As above suggested, the classical static approach is not enough to guarantee an adequate degree of comfort, and a more sophisticated dynamical approach seems to be more effective during the design stage.

Within the contest of the comfort evaluation for the footbridges (and in general for all those structures sensitive to vibrations problems), different approaches or guidelines are proposed in the last years (see [28]-[30] among others). But an unified code that establishes “how” to evaluate these aspects has not yet been coded, and these topics are still in a developing stage. This lack of regulation gives to the designers a sort of freedom during the design. Nevertheless it is of vital importance that the bridge has to get a minimum level of comfort in agreement at least with the client or owner requirements. Thus the question “Will the footbridge meet the comfort criteria when vibrating?” plays an important role in the design process.

As observed in section 1.2 the concept of comfort is directly correlated to human perception and so it is not so simple to identify a general and unified definition of “comfort level”.

In the following the more interesting guidelines and codes which could be taken into account during the design stage, are presented and discussed. More details are reported in *Appendix C*.

The first code to be proposed is the **Eurocode** [31]. The criteria on which this code is based, is to provide the maximum level of acceleration to ensure the minimum level of comfort. In all those cases in which this minimum level is no longer satisfied, the code prescribes the installation of *ad hoc* devices (e.g. dampers, TMD and so forth...) to reduce the level of vibration on the bridge. More in detail Eurocode 0 - Appendix 2 [31], states that the pedestrian comfort criteria must be defined in terms of maximum acceleration in any part of the bridge. The maximum values of acceleration recommended are:

- 0.7 m/s² for the vertical vibrations;

- 0.2 m/s² for horizontal vibration, in conditions of normal use;
- 0.4 m/s² for horizontal vibration, in exceptional conditions of the crowd.

In addition, the code states that the comfort assessment must be carried out if the natural frequencies of the bridge are less than:

- 5 Hz for vertical vibrations;
- 2.5 Hz for the horizontal transverse and torsional vibrations.

In Eurocode 1 - Part 2 [32] the traffic load models for the design of road bridges, rail and pedestrian walkways are defined. In particular in Section 5.7, the dynamic models to be applied for pedestrian loads are discussed. Moreover it is underlined as, depending on the dynamic characteristics of the structure, the main natural frequencies of the bridge should be evaluated by an appropriate numerical model. Furthermore in the SLS verification of vibration must be considered those forces exerted by pedestrians which have a frequency equal to a natural frequencies of the structure. *Ad hoc* model of these forces should be proposed by the designer, while the code does not give more details about “how” to evaluate the human induced loads. Eurocode 5 – Part 2 deals with the design of wooden structures [2], and in particular covers the design of timber bridges. This code requires the calculation of the maximum acceleration in the presence of small groups or crowds of persons both in the vertical and horizontal (i.e. in transversal direction compared with the deck axis) direction, where the maximum acceptable accelerations are the same reported in Eurocode 0 and above summarized. The code states once again that the assessment should be made for those structures that have natural frequencies lower than 5 Hz and 2.5 Hz, respectively, for the vertical and horizontal modes.

Another code is the **ISO 10137** [33]. This code provides a series of principles for the prediction of the vibrational characteristics of a structure during the design stage. To assess the effects of the vibrations is important to refer to the type of vibration source, its location and the receiving element. The assessment of the response is evaluated by a numerical model is needed. The code gives to the designer the choice of the comfort of level to be considered, but states that the pedestrian bridges must be so that the amplitude of the vibrations do not cause discomfort to users. In the absence of more definitive data, the code suggests the following maximum level of vibrations:

- in the vertical direction (z-axis): the vibrations should not exceed those obtained by a multiplying factor of 60 to the relevant base curve represented in Figure 2.2.1 when one or more persons still standing on the walkway have

to be accounted for (such as the first scenario), in which case a multiplying factor of 30 should be applied.

- horizontal vibrations induced by pedestrian traffic or wind should not exceed 60 times the base curve for the horizontal direction (x and y- axis), see Figure 2.2.2.

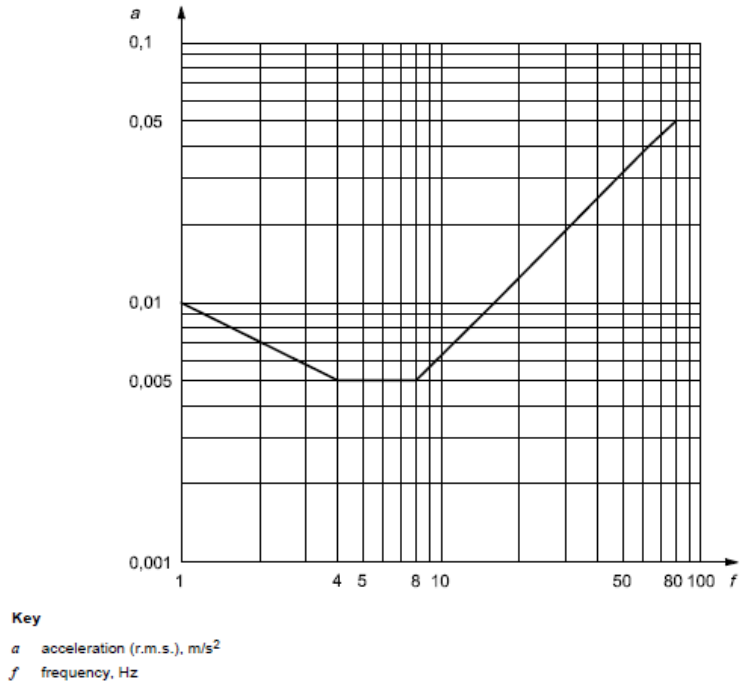


Figure 2.2.1. Building vibration z-axis base curve for acceleration (foot-to-head vibration direction) [33].

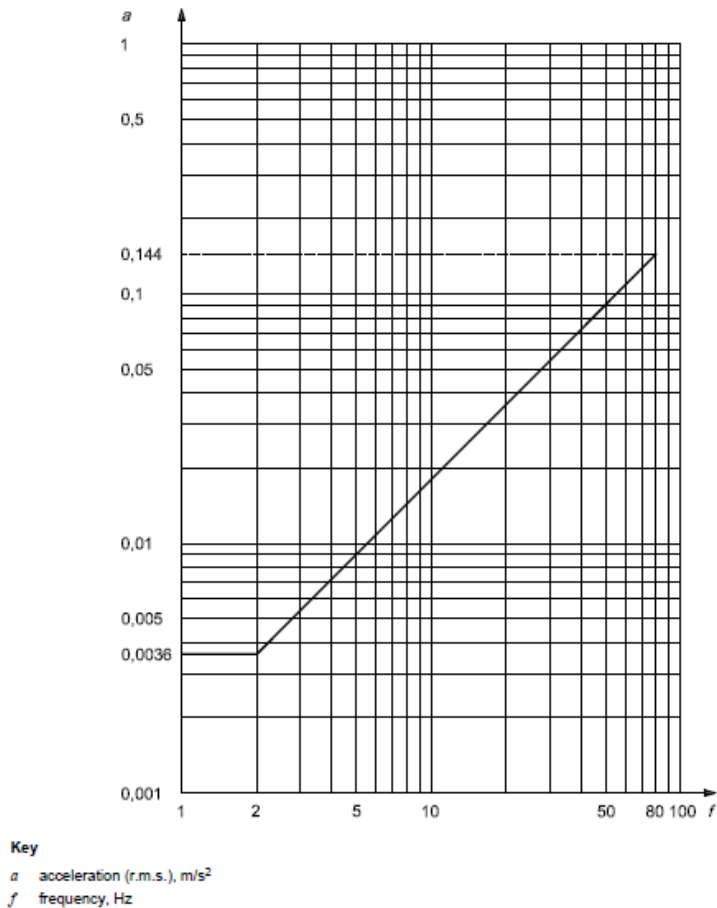


Figure 2.2.2. Building vibration z-axis base curve for acceleration (foot-to-head vibration direction) [33].

The **British Standard** BS5400, BD 29/04 and BD 37/01 [34] state that all the footbridges should satisfy the following minimum requirements:

- in the vertical direction the natural frequencies of the structure must have a value greater than 5 Hz;
- in the transverse horizontal direction the minimum frequency is fixed at 1.5 Hz.

If the fundamental frequency of vertical vibration, said f_0 , however, is less than or equal to 5 Hz, the maximum vertical acceleration a_v (expressed as m/s^2) of any part of the bridge has to be limited to:

$$a_v \leq 0.5\sqrt{f_0}. \quad (2.32)$$

The maximum vertical acceleration may be calculated either by simplified method or by rigorous method. For complex structures, the maximum vertical acceleration must be calculated assuming that the dynamic load induced by a single pedestrian is that due to a concentrated force F , which moves through the span of the bridge at a constant speed $v_t = 0.9f_0$ [m/s], where:

$$F = 180\sin(2\pi f_0 t). \quad (2.33)$$

If the fundamental frequency of the horizontal vibration is less than 1.5 Hz, great attention has to be paid to avoid the possibility to activate the lateral movement of the deck (the so called *lock-in* effects). The codes, however, do not propose any method to evaluate the maximum horizontal (transversal) acceleration.

The guidelines published by the **Fib** [35] provide an available tool for the design of the footbridges, in particular with reference to the assessment of the maximum acceleration to be compared with the comfort limit value. Following this guideline the maximum acceleration in [m/s^2] is defined as:

$$a = 0.6 \frac{\alpha G}{0.5M} \frac{\pi}{\delta} (1 - e^{-n\delta}), \quad (2.34)$$

where G is the dead load of an ideal pedestrian (0.7 kN), M the mass in [t] of the equivalent 1 -DOF oscillator for single span, δ the logarithmic decrement and n the number of cycles per span (span over step length).

The last document here analyzed is the **Technical guide Sétra-AFGC** [36]. Several aspects have to be considered by the designer during the design of the footbridge to avoid resonant phenomena in order to improve, or guarantee, an adequate level of comfort. Moreover this guideline can be used in order to evaluate the comfort of existing bridges. Operationally the proposed method can be summarized in the following five steps:

- 1) *step 1*: determination of the footbridge class;
- 2) *step 2*: choice of comfort level;
- 3) *step 3*: evaluation of the dynamic footbridge properties (if needed);

- 4) *step 4*: dynamic evaluation (if needed);
- 5) *step 5*: modification of the structural design to fulfil the comfort requirement (if needed).

The methodology of working is summarized in the flowchart in Figure 2.2.3.

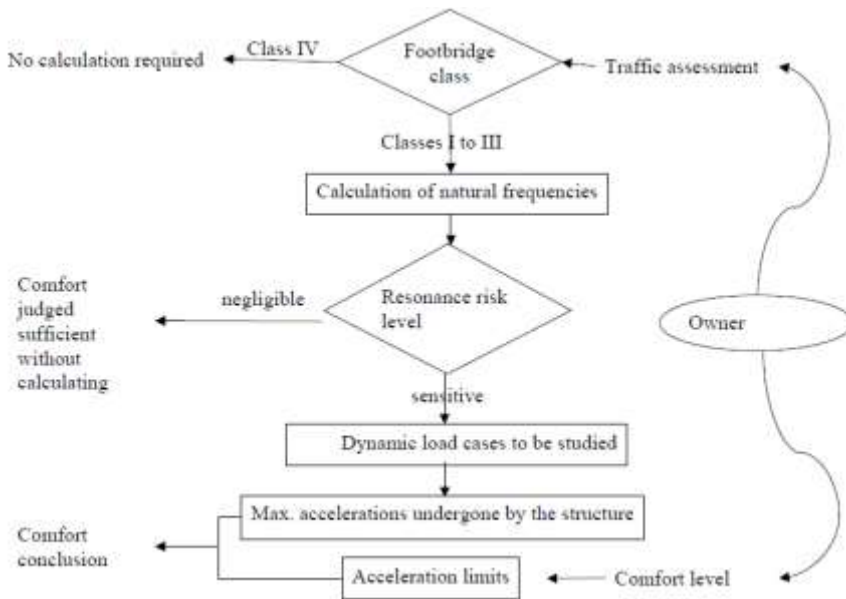


Figure 2.2.3. Methodology flowchart proposed by Sétra-AFGC [36].

2.3 Pedestrian Timber Bridge: a new construction way. Introduction to the structures under study

Pedestrian bridges are becoming a common trend in the design. In particular in the last years thanks to the developments of new [37] high strength materials within the field of wood (e.g. Glue Laminated Timber (GLT) elements), in many installations regarding the construction of footbridge, timber is selected as main resistant material.

Part strictly structural reasons based on the strength of wooden materials, timbers elements are valuable for both economics and environmental aspects because they are eco-friendly materials. For this reason they are very appreciated in all those installation where the bridge as to fit well with the surrounding environment.

In this work two footbridges located in two different Alpine villages are considered as case studies.

The first one, called “Trasaghis” footbridge (Figure 2.3.1), is located in the Trasaghis Municipality not far Udine city (North-east of Italy). Even if the bridge looks like the cable-stayed type, in this structural solution the cables are replaced by oblique steel tubular elements, i.e. stays, of external diameter 45.75 cm and thickness 1.42 cm. The replacing of the cables by the stays, allowed the designer to save money invested in the realization of an *ad hoc* protection system (larch plank and metal cladding) for the two main GLT beams. From geometric point of view the span is about 83 m long and 3.22 m wide; the pillar shown a height of about 15 m and the double-beam deck width is 4 m, of which 3.22 m represents the free crossing width [38]. The whole static scheme sees two pillars located on both sides (Figure 2.3.2), while the resistant scheme of the deck is obtained linking the two main glued laminated timber (GLT) arcuate beams, of rectangular cross-section of 20 by 194.1 cm, by H-shape steel tubular elements (Figure 2.3.3).



Figure 2.3.1. “Trasaghis” footbridge.



Figure 2.3.2. “Trasaghis” footbridge. View of the pillars.



Figure 2.3.3. View from the bottom of the “Trasaghis” footbridge on the left. Zoom on the structural resistant scheme of the deck on the right.

The second footbridge under study, called “Tesa” footbridge, is shown in Figure 2.3.4. It is located in Farra d’Alpago Municipality not far from Belluno city (Figure 2.3.5). The static scheme of the bridge is inspired by the classic cable-stayed solution [39]. Totally 16 steel cables (of diameter 44 mm and 32 mm) are employed to carries the two main curved GLT beams of rectangular cross-section 18 by 123.8 cm. The two antennas are 16 m high. From a geometric point of view, the span length is about 110 m subdivided into three segments of length 22.5 m, 65 m (in the middle) and 22.5 m, respectively; while the width of the deck is about 2.5 m. The resistant scheme of the deck is realize by linking these two main beams with steel tubular elements of high strength, assuming the classical “U-shape” cross-section (Figure 2.3.7).



Figure 2.3.4. General view of the “Tesa” footbridge.



Figure 2.3.5. “Tesa” footbridge. Satellite view of the location.



Figure 2.3.6. View of the pillar on the left; detail of the connection between cable and deck on the right.



Figure 2.3.7. View of the structural scheme of the “Tesa” footbridge deck.

Both the footbridges mentioned above were experimentally and numerically studied in this thesis. In particular:

- “Trasaghis” footbridge: has been subject to an extensive in situ monitoring campaign carried out by the author with the aim to identify its dynamic behaviour, in order to implement, subsequently, different numerical structural control systems as presented in *Chapter 6*;
- “Tesa” footbridge: has been subject to an extensive in situ monitoring campaign. Even if this bridge has been studied from a numerical point of view, in this case study the attention of the author is addressed to the definition, implementation and validation of an alternative model for the pedestrians (crowd) loads based on a stochastic approach, as discussed in section 4.2.

More details about the two structures under study are given in *Appendix A* (section A.1 and section A.2, respectively). For the numerical models and the achieved results the reader is referred to *Chapter 3* from to *Chapter 6*.

To conclude this introduction of timber bridges, in some countries different timber solutions are employed not only for “pedestrian” application but also as classical road bridges. In the following pictures (from Figure 2.3.8 to Figure 2.3.12) a few examples of road timber bridges spread all around the world, are presented. They are taken from the proceeding of the last international conference in timber bridges ICTB2013 held in Las Vegas last October, 2013.

The first one, see Figure 2.3.8, is located in Norway and it is a classical arch bridge [40].



Figure 2.3.8. Tynset bridge, Norway [40].

Another example, see Figure 2.3.9, is represented by the Cosumnes River Bridge located near Sacramento, California (USA). This is a classical truss bridge [41].



Figure 2.3.9. Cosumnes River Bridge, California (USA) [41].

An example of a five-span timber structure is the Goodpasture Covered Bridge (see Figure 2.3.10) crossing the McKenzie River in eastern Lane County, Oregon (USA) [42].



Figure 2.3.10. Goodpasture Covered Bridge. Lane County, Oregon (USA) [42]. a) lateral view; b) frontal view.

Another example, see Figure 2.3.11, of arch timber bridge is here below presented is located close to the town Gislaved (Sweden) and it is one of the infrastructures belonging to Highway 27 [43].



Figure 2.3.11. Goodpasture Covered Bridge. Lane County, Oregon (USA) [43].

To conclude this part in the next picture the oldest road timber bridge in Skelleftea (Sweden), see Figure 2.3.12, completed in 1737 is reported [44].



Figure 2.3.12. Lejonstroms Bridge. Skelleftea, Sweden [44].

2.4 References

- [1] DIN-Fachbericht 102, Betonbrücken. Deutsches Institut für Normung, 2003.
- [2] ENV 1995-2, Eurocode 5 - Design of timber structures – bridges. European Committee for Standardization, 1997.
- [3] C. Adam, P. Salcher, 2011. Assessment of high-speed train-induced bridge vibrations. On the Proceedings of the 8th International Conference on Structural Dynamics, EUROLYN 2011, Leuven, Belgium, 4-6 July 2011.
- [4] Adam, C., Heuer, R., Ziegler, F., 2012. Reliable dynamic analysis of an uncertain compound bridge under traffic loads. *Acta Mechanica*, 223, pp. 1567 - 1581.
- [5] A. Tributsch, C. Adam, 2013. System identification of an old railway bridge in different structural conditions. On the Proceeding of the Vienna Congress on Recent Advances in Earthquake Engineering and Structural Dynamics 2013 (VEESD 2013), Vienna, Austria, 28-30 August 2013.
- [6] F. Ansari; Giacosa L.M.; A. Bassam; A. Tennant; J. Hongqiang; A. De Stefano, 2005. Design of Fiber Optic Based Monitoring Systems for Cable-Stayed Bridges. In: *ISISS'2005*, Nanjing, China.
- [7] Giacosa L.M.; F. Ansari; A. De Stefano, 2005. Development and testing of fiber optic sensors for structural health monitoring of cable-stayed bridges. In: *SHM'05*, Perth, Australia, 12 - 14 December 2005.
- [8] Cimellaro G.P.; Domaneschi M.; Martinelli L.; De Stefano A., 2010. Health monitoring of a smart base isolated benchmark cable-stayed bridge using symptom approach. In: *Fifth International Conference on Bridge Maintenance, Safety and Management (IABMAS10)*, Philadelphia, PA (USA), 11-15 July 2010. p. 321.

- [9] Anil K. Chopra, 1995. Dynamics of Structures, third edition. Prentice Hall, Englewood Cliffs, New Jersey.
- [10] Tom Proulx, 2010. Dynamics of Bridges. Conference Proceeding of the Society for Experimental Mechanics Series – A conference on Structural Dynamics, 28th IMAC.
- [11] H. Max Irvine, 1981. Cable Structures. The MIT Press Series in Structural Mechanics. Cambridge, Massachusetts, and London, England.
- [12] Wenzel H., 2009. Health Monitoring of Bridges. John Wiley & Sons Ltd, The Atrium, Southern Gate, Chichester, West Sussex PO19 8 - SQ, England.
- [13] Wenzel H., Pichler D., 2005. Ambient Vibration Monitoring. John Wiley & Sons Ltd, The Atrium, Southern Gate, Chichester, West Sussex PO19 8SQ, England.
- [14] C.F. Beards, 1996. Structural Vibration: Analysis and Damping. Halsted Press, an imprint of John Wiley & Sons Inc., New York NY.
- [15] Ewins, D.J., 2000. Modal Testing: theory, practice and application, 2nd ed., Research Studies Press.
- [16] Kareem A., Gurley K., 1996. Damping in structures: its evaluation and treatment of uncertainty. Journal of Wind Engineering and Industrial Aerodynamics, 59, pp. 131-157.
- [17] Farrar C. R., Worden K., 2012. Structural Health Monitoring: A Machine Learning Perspective. Fundamental axioms of structural health monitoring. John Wiley & Sons, Chichester, UK, November 22, 2012.
- [18] Casciati F., Faravelli L., 1991. Fragility analysis of complex structural system, Research Studies Press, Taunton.
- [19] Balkaya, C., Bortoluzzi D., Casciati F., Kostopoulou G., Bogonikolos N., 2012. System Architecture For An Interactive Database To Structural Control Of Transport Network Infrastructure: A Case Study Of Railroad Bridge. On the Proceeding of 5th European Conference on Structural Control – EACS2012, Genova, Italy 18-20 June 2012.
- [20] Faravelli L., Bortoluzzi D., Messervey T.B., Sasek L., 2012. Temperature Effects On The Response Of The Bridge “ÖBB Brücke Großhaslau”. Invited contribution - ABC12, Saint Petersburg, Russia, July 1-4, 2012.

- [21] Casciati S., Faravelli L., Bortoluzzi D., 2013. The Effect Of Temperature Variability When Monitoring A Railway Bridge. On the proceeding of 11th International Conference on Recent Advances in Structural Dynamics - RASD2013, Pisa (ITA), 1st – 3rd July 2013.
- [22] Casciati F., Casciati S., Faravelli L., Bortoluzzi D., Masservey T.B., 2013. Estimating Thermal Inertia And Temperature Distribution Consistent With Monitored Data From A Railway Bridge. On the Proceeding of the 4th International Conference on Computational Methods in Structural Dynamics & Earthquake Engineering - COMPDYN2013, Kos Island (GR), 12-14 Jun 2013.
- [23] Bortoluzzi D., Casciati S., Faravelli L., 2013. Modeling The Dependency of Displacement Variability on Thermal Effects. *Journal of Vibration and Control*, vol. 19 (15), pp. 2301-2313.
- [24] Peeters, B., G. De Roeck, 2001. One-year monitoring of the Z24-Bridge: environmental effects versus damage events. *Journal Of Earthquake Engineering And Structural Dynamics*, 30, pp. 149-171.
- [25] Peil U., Mehdiانpour M., Frenz M. and Weilert K., 2006. Life time assessment of bridges In *Bridge Maintenance, Safety, Management, Life-Cycle Performance and Cost*. Ed. Cruz PJ, Frangopol DM and Neves LC.
- [26] Casciati S., Chen Z., 2011. A multi-channel wireless connection system for structural health monitoring applications. *Structural Control and Health Monitoring Journal*, 18 (5), pp. 588–600.
- [27] SAMCO – Guidelines for Structural Control, 2006. www.samco.org
- [28] Oeding, 1961. *Verkehrsanalyse Fußgänger*, Stadt Stuttgart Planungsamt, Abt. Verkehr [in German].
- [29] HiVoSS Design of Footbridges – guideline, 2008. Project: RFS2-CT-2007-00033 – EN02.
- [30] HiVoSS Design of Footbridges – guideline, 2008. Project: RFS2-CT-2007-00033 – EN03.
- [31] Eurocode 0 - Appendix A2, Basis of Structural Design, EN 1990.
- [32] Eurocode 1 - Part 3, Actions on structures. UNI ENV 1991-3, September 1998.
- [33] ISO 10137, Bases for design of structures - Serviceability of buildings and walkways against vibration, 2007.

- [34] BS5400, Part 2, Appendix C, Vibration Serviceability Requirements for Foot and Cycle Track Bridges. British Standards Institution, 1978.
- [35] Guidelines for the design of footbridges. Fib bulletin 32, November 2005.
- [36] Footbridges: assessment of vibrational behaviour of footbridges under pedestrian loading - Technical guide, 2006 – Sétra-AFGC.
- [37] Pisano A., Fuschi P, De Domenico D, 2014. Limit Analysis: A Layered Approach for Composite Laminates , Direct Methods for Limit States in Structures and Materials, Springer Science+Business Media B.V., Dordrecht (DEU), pp. 23-56, ISBN: 978-94-007-6826-0.
- [38] Casciati S., Faravelli L. and Bortoluzzi D., 2013. Pedestrian timber bridges: experimental investigation and modelling. On the Proceeding of the 10th International Conference on Damage Assessment of Structures - DAMAS 2013. Trinity College Dublin Ireland, July 8-10 2013.
- [39] Bortoluzzi D., Casciati S., Faravelli L., 2013. Testing the effects of walking and running on an existing timber pedestrian bridge. On the Proceeding of the 9th International Conference on Structural Dynamics - EURODYN 2014. Porto, Portugal, 30 June – 2 July 2014.
- [40] Malo K.A., Ostrycharczyk A., Barli R., Hakvåg I., 2013. On development of network arch bridges in timber. On the Proceeding of 2nd International Conference on Timber Bridges 2013 – ICTB2013, Las Vegas, Nevada USA, September-October, 2013.
- [41] Gilham P.C., 2013. Stretching the Limits, Four Timber Bridge Case Studies. On the Proceeding of 2nd International Conference on Timber Bridges 2013 – ICTB2013, Las Vegas, Nevada USA, September-October, 2013.
- [42] Ausland G.W., La Morticella. T., 2013. Goodpasture Covered Bridge Rehabilitation. On the Proceeding of 2nd International Conference on Timber Bridges 2013 – ICTB2013, Las Vegas, Nevada USA, September-October, 2013.
- [43] Ekholm, K., Nilsson, P., Johansson, E., 2013. Case Study Of The Longest Single Span Timber Bridge For Highway Loads In Sweden. On the Proceeding of 2nd International Conference on Timber Bridges 2013 – ICTB2013, Las Vegas, Nevada USA, September-October, 2013.
- [44] www.tt-forums.net

Chapter 3 Experimental campaign and numerical modeling

In this chapter the numerical models of the two pedestrian bridges under study (section 2.3) are presented. For more details about the pedestrian bridges the reader is referred to *Appendix A*.

All the structural models are developed within the theory of Finite Element Model (FEM) [1]. The code adopted is developed by MSC Marc software-house. In particular the graphical interface called MENTAT2010 [2] is used. This software allows one a complete solution (pre-processing solution and post-processing solution) for implicit nonlinear Finite Element Analysis (FEA). It allows one to accurately simulate the response of structures under static, dynamic and multi-physics loading scenarios. Marc's versatility in modelling nonlinear material behaviours and transient environmental conditions makes it an efficient tool for the design of structural systems. Moreover it allows the user to define the *ad hoc* functions for boundary conditions, loads configuration and so forth...

3.1 Experimental campaign

In this section the experimental campaigns carried out in situ for the two structures under study are presented. It is worth underlining that these tests are a must in view of defining more realistic numerical models to represent the dynamic behaviour of the footbridges. In particular the calibration and validation of the FE models will be entrusted to the comparison of the responses of the footbridges under wind loads acquired in situ, with the responses achieved by the implemented numerical models. Indeed, in this particular application, the loads associated to the wind can be regarded as "ambient vibration" or "background noise". During the experimental campaigns, long

acquisitions of the structural response of the bridges under “low-wind-velocity” were collected for this purpose.

3.1.1 “Tesa” footbridge experimental campaign

On November 7, 2013 an experimental campaign was performed with the aim of the acquisition of the bridge dynamic response (i.e. the acceleration components of relevant points along the footbridge deck) under different loading conditions [3]-[4].

The data acquisition is tailored to standard tri- and uni- axial *Kinematics EPISENSOR* accelerometer (Figure 3.1.1), while the data transmission is entrusted to wireless transceiver [5] in order to cover all the entire span length of the bridge, without the need for the intermediate storage stations. An example of these devices is reported in Figure 3.1.2.



Figure 3.1.1. Example of the tri-axial accelerometer posed over the deck.



Figure 3.1.2. Example of the wireless station unit (WSU) employed for the data acquisition-transmission.

During the in situ tests, a total of six accelerometers is deployed; in particular:

- two uni-axial accelerometers anchored to the “internal-main” cables, labelled as WSa5_ch1 and WSa5_ch2;
- four tri-axial devices labelled as W*Sa*_{*i*}, *i*=1,...,4, where *i* represents the *i*-th accelerometers, along the centreline of the deck in *ad hoc* positions. More details are shown in Figure 3.1.3.

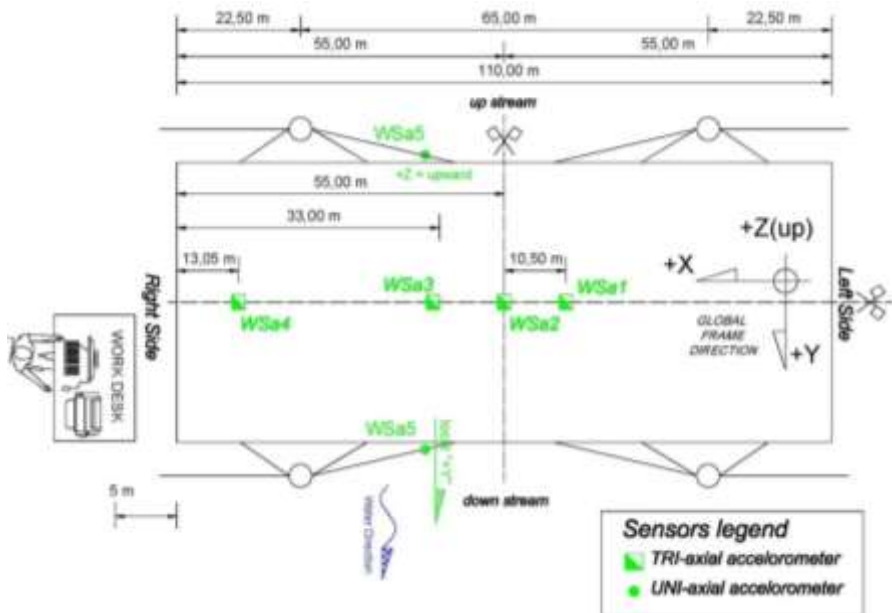


Figure 3.1.3. Sensors equipment configuration during the in situ tests.

Figures 3.14, 3.15 and 3.16 show the positions of the sensors WSa1, WSa2 and WSa3.



Figure 3.1.4. Sensors WSa1 during the in situ tests.

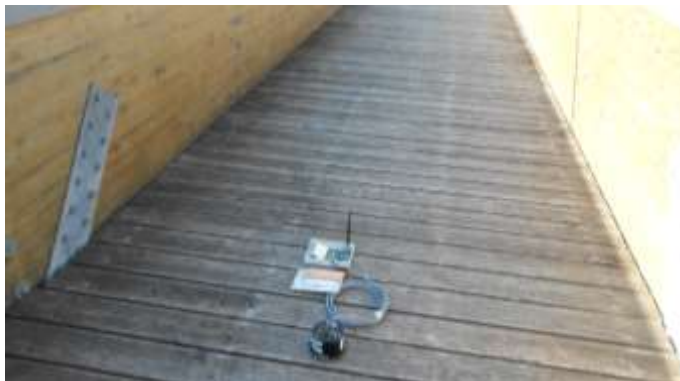


Figure 3.1.5. Sensors WSa2 during the in situ tests.



Figure 3.1.6. Sensors WSa3 during the in situ tests.

Two groups of tests are carried out during the experimental campaign:

- *test A - environmental loads*, i.e. wind (the bridge location is often interested by strong winds) used as “calibration” test for the instrumentations, and for the first “validation/calibration” of the numerical model;
- *test B - running and walking* along the deck. Different schemes of “human induced loads” (HIL) are defined. For the *walking loads*, three different cases are analyzed: a round trip along the bridge of one person (*test B1*), four persons (*test B2* – see Figure 3.1.7) and six persons (*test B3*). For the *running* configuration, the case of a round trip of one person is considered (*test B4*). More details will be presented in section 4.3.2 and in *Appendix D* discussing the validation of the model for the crowd load proposed in this thesis.

All the accelerations are acquired with a sampling frequency of 100 Hz.

An example of the accelerations acquired by WSa2 along the vertical axis Z for *test A* and for *test B2* is reported in Figure 3.1.8 and Figure 3.1.9 respectively.



Figure 3.1.7. “Tesa” footbridge – picture during test B2.

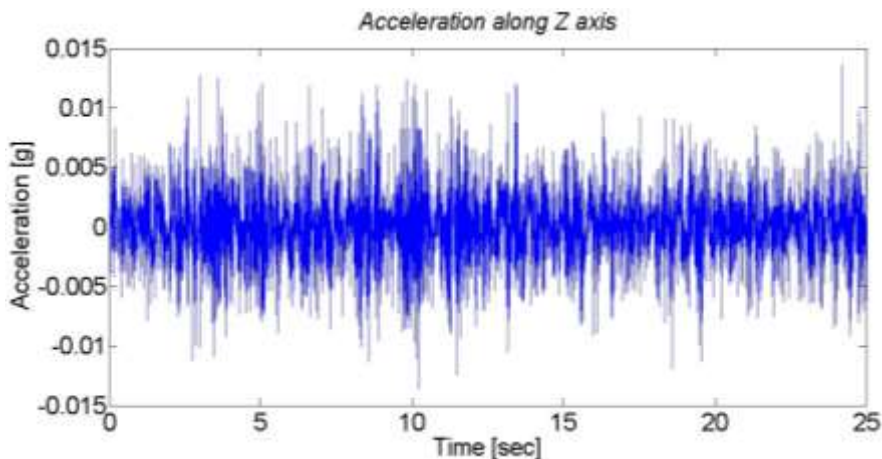


Figure 3.1.8. Acceleration along the Z axis recorded by WSa2 – duration 25 sec – sampling rate 100 Hz – November 7, 2013 @ 2.12 pm – air temperature 15°C.

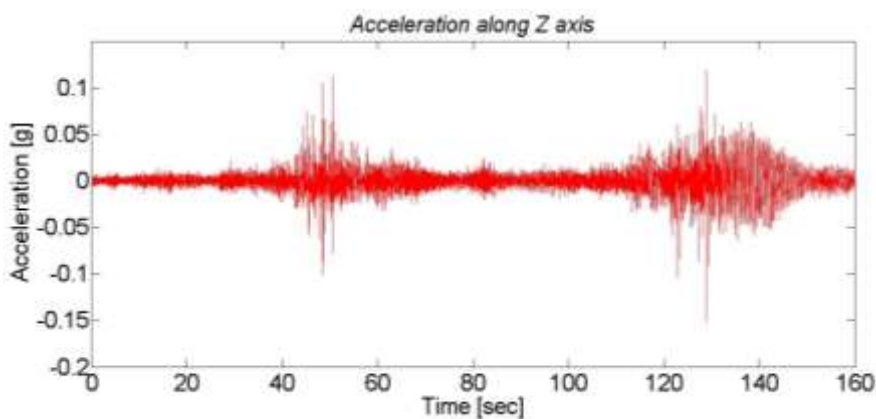


Figure 3.1.9. Acceleration along Z axis recorded (160 sec) by WSa2 – sampling rate 100 Hz – November 7, 2013 @ 2.55 pm – air temperature 15°C.

All the recorded data are analyzed following four different approaches:

- 1) standard Fast Fourier Transform (FFT);
- 2) Short Time Fast Fourier Transform (STFFT) ([6]-[7] among others);
- 3) Wavelet algorithm (WA) ([8]-[9] among others);
- 4) Stochastic Subspace Identification theory (SSI) ([10]-[12] among others).

All the calculations are performed within the MatLAB environment [13]; the SSI analysis is carried out by using the MACEC toolbox of MatLAB [14]. In particular the

methodologies STFFT, WA and SSI were used for better identify the interaction behaviour between the pedestrian and the bridge as better described in *Chapter 4*.

As an example, the results achieved applying the different methodologies described above for the acceleration acquired by WAa1 during the *test A* along *Y* transversal axis are represented from Figure 3.1.10 to Figure 3.1.12. The results are summarized and compared in Table 3.1.1.

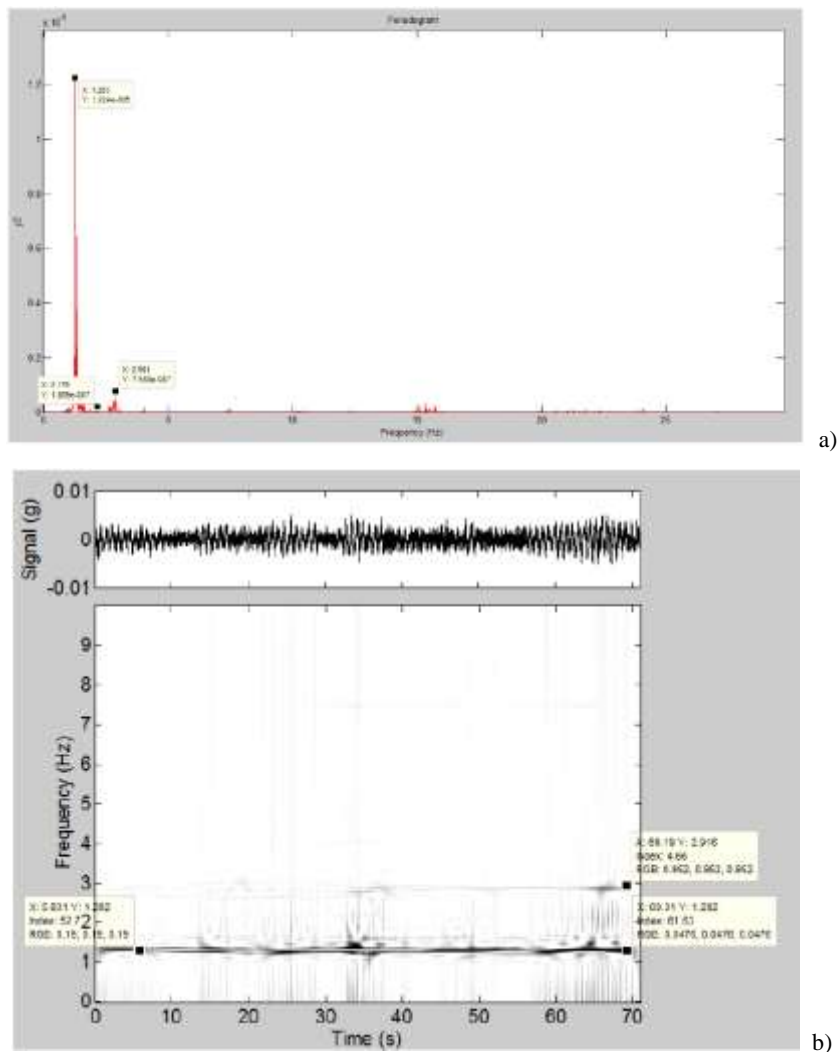
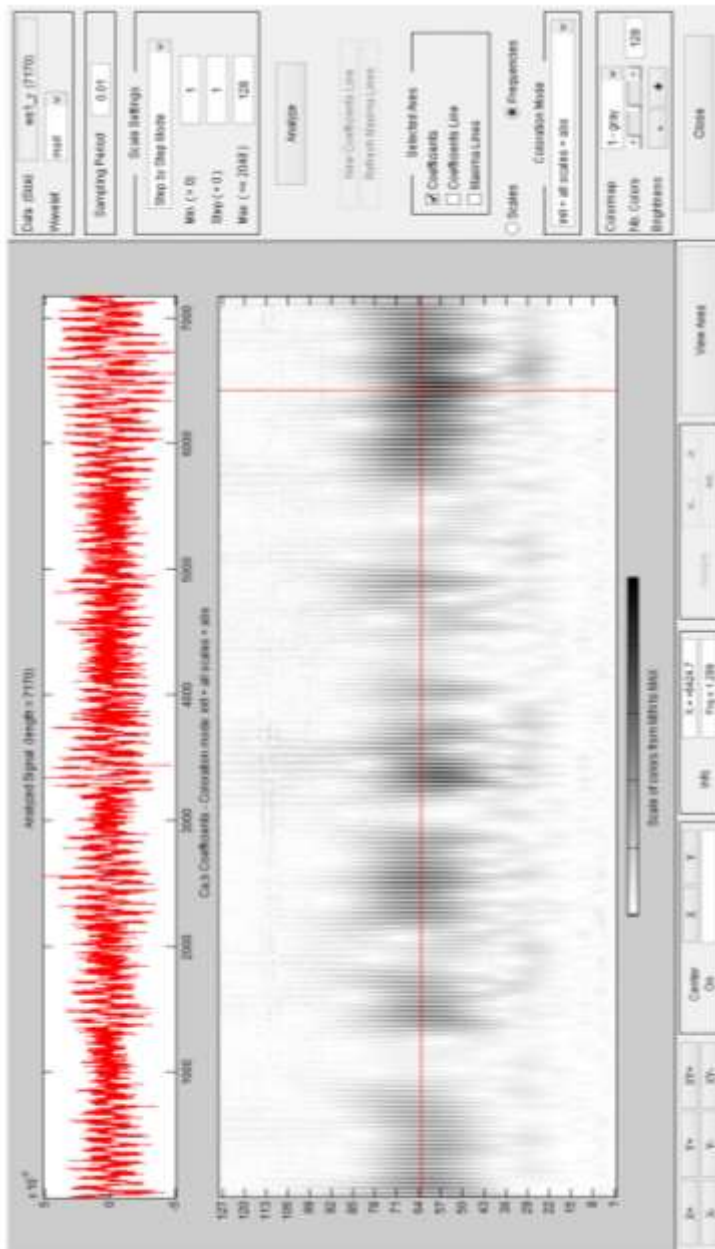


Figure 3.1.10. Data processing – acceleration acquired by WAa1 during the *test A* along *Y* transversal axis. a) FFT; b) STFFT.



a)

Figure 3.1.11. Data processing – acceleration acquired by WAA1 during the test A along Y transversal axis. a) WA.

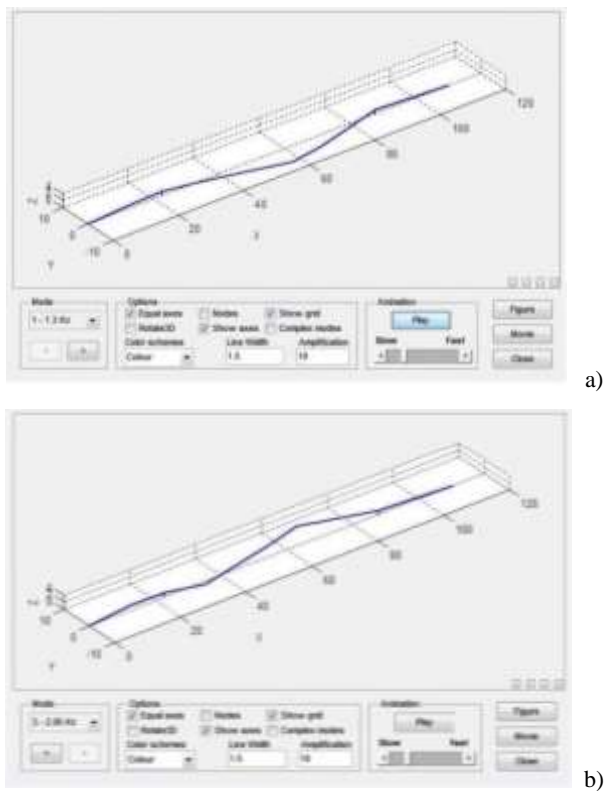


Figure 3.1.12. Data processing by using SSI – acceleration acquired by WAa1 during the *test A* along *Y* transversal axis. a) mode I ($f=1.30$ Hz); b) mode III ($f=2.85$ Hz).

Table 3.1.1. “Tesa” footbridge – frequencies range from data analysis.

Algorithm	Frequency [Hz]	damping [-]
<i>FFT</i>	1.283	-
	2.901	
<i>STFFT</i>	1.300	-
	2.900	
<i>WA</i>	1.300	-
	2.900	
<i>SSI</i>	1.311	1.84 %
	2.850	3.163 %

3.1.2 “Trasaghis” footbridge experimental campaign

Two experimental campaigns were planned. The accelerations in previously selected points of the bridge under environmental loads were collected. Two challenges were met:

- 1) replace the standard wired acquisition system;
- 2) create a database of data to develop a (future) reliable process to clean the effects of current environment conditions, that might afflict different experimental campaigns.

About the first aspect the classical cable solution for the data acquisition is able to cover distance up to about 30 m. Being the span of the bridge about 85 m long, to overcome this experimental gap without use of signal repetition bridge, the transmission of the data was entrusted to a wireless technology (Figure 3.1.13) as illustrated in [5] and [16].



Figure 3.1.13. The tri-axial accelerometer connected with a wireless sensor unit (WSU) posed over the deck.

To acquire the acceleration standard tri- and uni-axial *Kinematics EPISENSOR* accelerometers were employed (Figure 3.1.14). In total six accelerometers were used: four tri-axial and 2 uni-axial.



Figure 3.1.14. Example of the Kinematic EPISENSOR uni- and tri- axial accelerometer employed during the experimental campaigns.

The first set of experiments was carried out on November 30, 2012. The average temperature of the air along the data acquisition was about 10 °C.

The second campaign of experiments was carried out on May 12, 2013. Two sets of data from this test are reported:

- the first one was collected in the morning (9.30 a.m. – temperature of air about 15.5 °C);
- the second one at noon (12:00 a.m. – temperature of the air about 25 °C).

This test repetition was planned for investigating changes in the structure behavior related to environment condition variations.

The configuration of the sensors for both the campaigns is given in Figure 3.1.15.

The acquired data are then elaborated using the standard approach proposed by the classical Fast Fourier Transformation (FFT). The related acceleration periodograms for the components along the transversal (Y) and vertical (Z) axes are given in Figure 3.1.16 and Figure 3.1.17. As an example the data acquired by the device in the position labelled $P\#3$ are reported.

The analysis of these periodograms shows the same ranges for the frequencies. In particular the experimental results confirmed the low sensitivity of the dynamic response to temperature variations, i.e., the prevalence of the steel skeleton on determining the footbridge vibration. A summary is reported in Table 3.1.2.

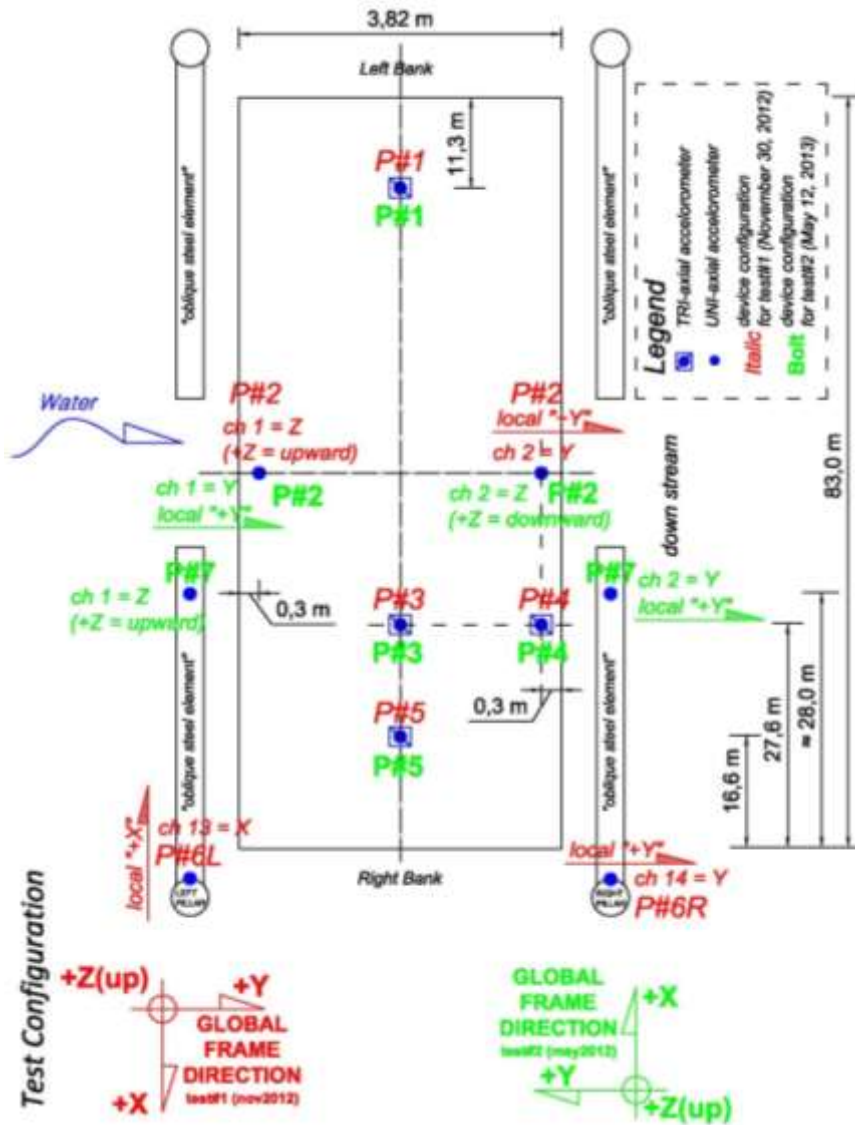


Figure 3.1.15. Sensors configuration for the two experimental campaign (November 30, 2012 and May 12, 2013).

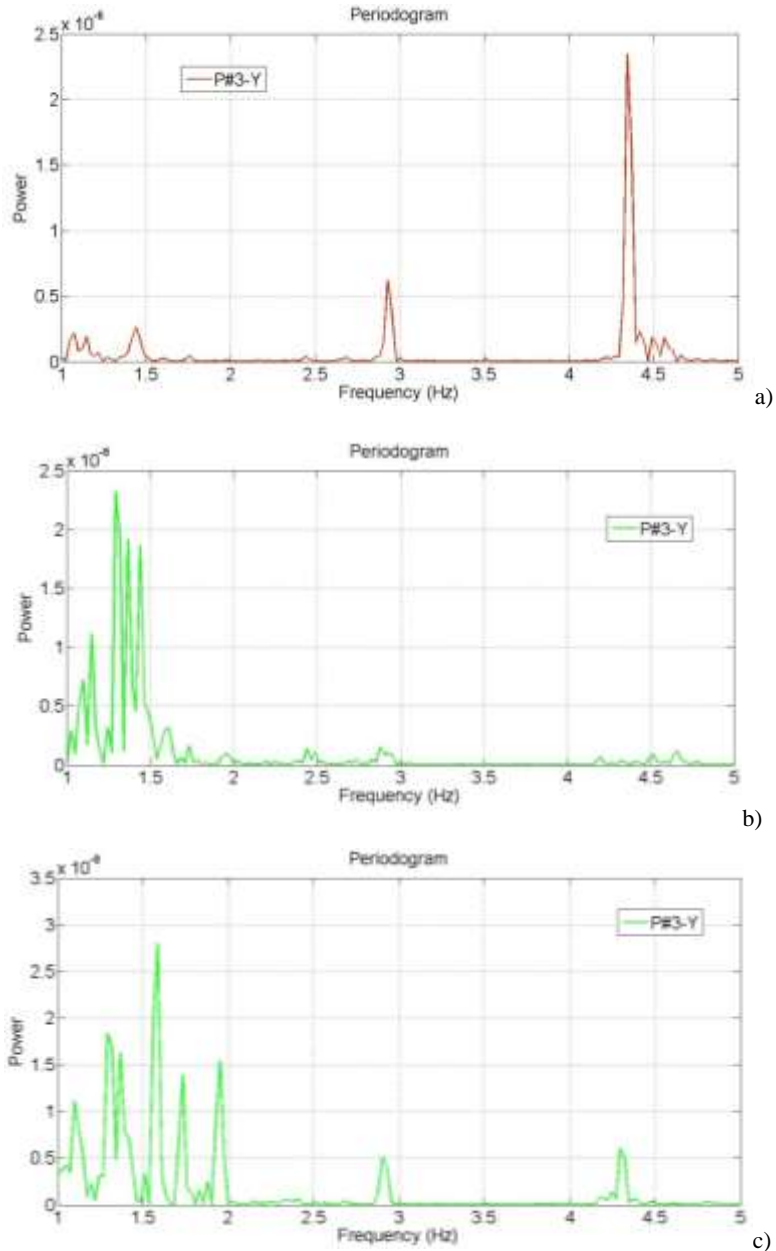


Figure 3.1.16. Periodograms of the signals recorded at position 3 (P#3): from the top to bottom, one sees the elaboration of the signals (along direction Y) collected in November, in the early morning of May 12, 2013 and in the late morning of the same day. The number of points in the temporal window of the signal is 2170.

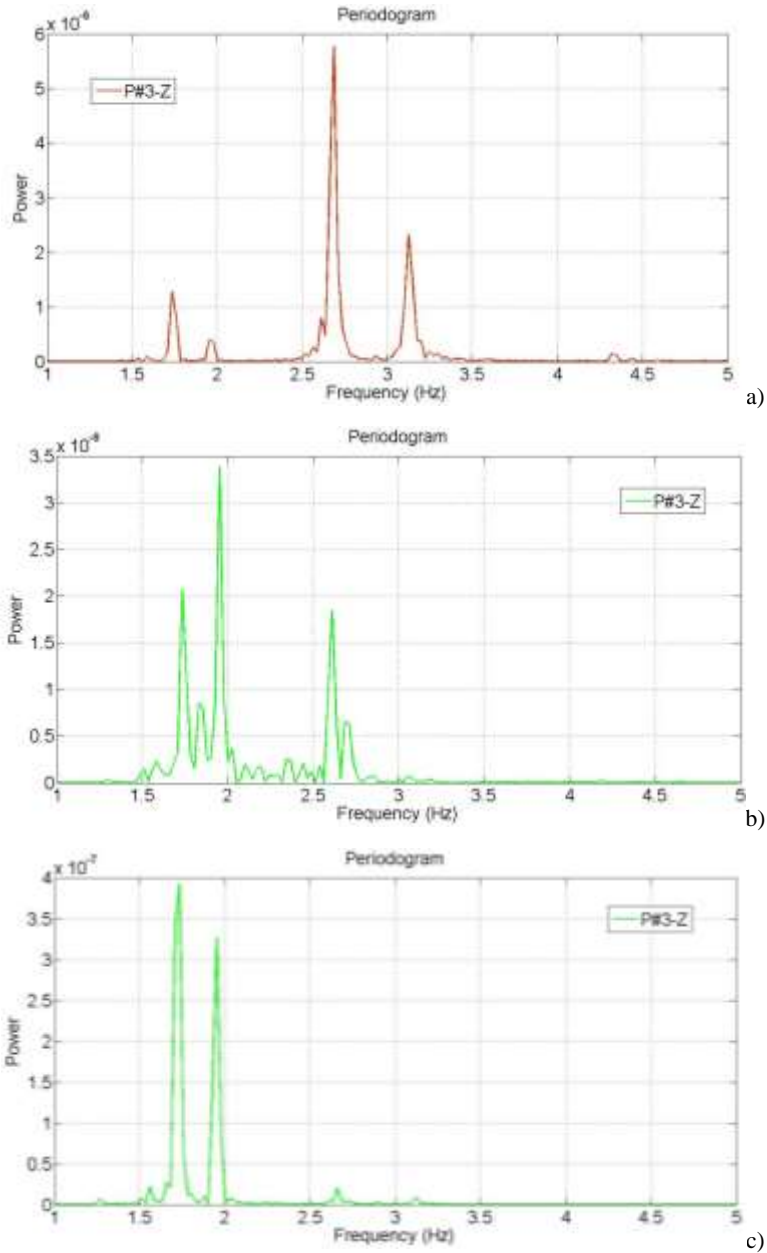


Figure 3.1.17. Periodograms of the signals recorded at position 3 (P#3): from the top to bottom, one sees the elaboration of the signals (along direction Z) collected in November, in the early morning of May 12, 2013 and in the late morning of the same day. The number of points in the temporal window of the signal is 2170.

Table 3.1.2. Frequency ranges “Trasaghis” footbridge – main results.

Set ID	Frequency [Hz]	Oscillation plane
1	1.05	X - Z
2	1.40	X - Y
3	1.75	Z
4	1.96	X - Y & X - Z
5	2.55	Z

From the analysis of the signal recorded during these tests different frequencies peaks appear in the range under about 1.40 ± 1.50 Hz. Numerical investigation and focused analysis on the acquired data on field showed as these frequencies can be associated to the dynamic behaviour of the stay and the deck-stay connection (Figure 3.1.18 and Figure 3.1.19). More details are provided in section 3.3.2.

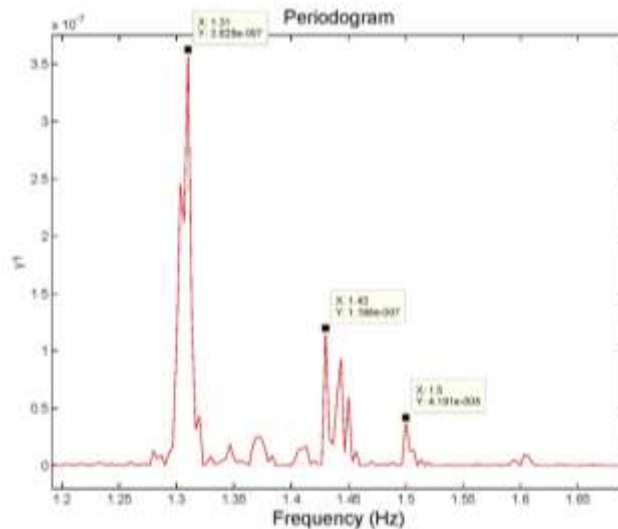


Figure 3.1.18. Periodograms of the signals recorded at position 7 (P#7): FFT along direction Y.

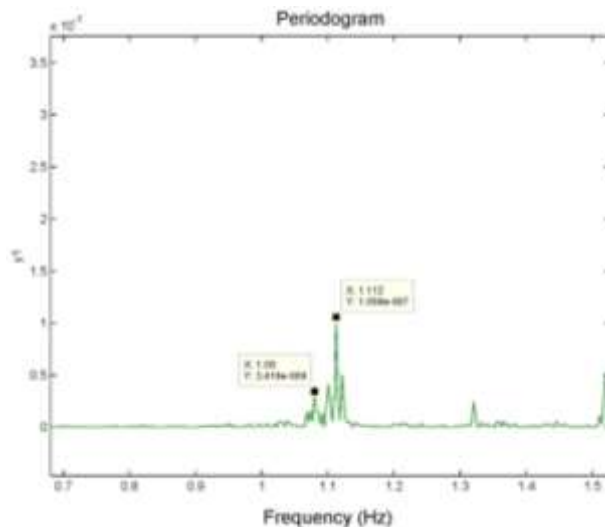


Figure 3.1.19. Periodograms of the signals recorded at position 7 (P#7): FFT along direction Z - data collected in May 12, 2013.

The measurements of the campaign carried out in May, 2013 were collected during two different tests: in the early morning the first, and at noon the second one. These tests are justified by the wish of extracting the variations in the structure performance due to changes in the environment conditions. There are small discrepancies between the values recorded in the early morning and the late morning, but the deviation is within confidence intervals. In other words the second campaign allows one to confirm the ranges of frequency covered by the vibration of the different elements, even if some small deviations associated to the temperature variation, have to be emphasized.

3.2 Cable-stayed system: “Tesa” footbridge FE Model

In this section the description of the “Tesa” footbridge numerical model is given. The model is developed within the Marc-MENTAT2010 software environment [2].

3.2.1 Design data and numerical model definition

The static scheme of the bridge is inspired by the classic cable-stayed solution. Two pillars 16 m height are located on both sides of the bridge. On them sixteen steel cables are hanged to carry the deck. In particular eight “internal-secondary” cables of diameter 32 mm, and other eight “external-main” cables of diameter 44 mm are adopted. From a

geometric point of view, the span length is about 110 m subdivided into three segments of length 22.5m, 65m (in the middle) and 22.5 m, respectively. The free crossing width of the deck is 3.2 m.

Following the technical documents, details, information and so forth... provided by the designer of the footbridge, a first “rough” numerical model is built.

The global reference frame adopted follows the next rule:

- X axis: along the bridge axis, i.e. parallel to the deck;
- Y axis: transversal axis, i.e. orthogonal to the deck;
- Z axis: vertical axis parallel to the gravity axis.

A general view of the model implemented in which is represented in Figure 3.2.1.

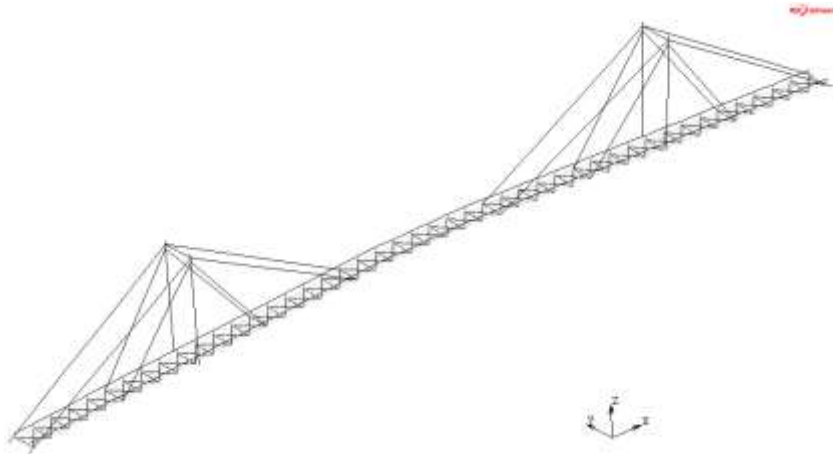


Figure 3.2.1. View of the numerical model implemented in MARC Mentat2010.

The model is defined by using the classical *beam* element. This class of elements is used to model the two mains GLT beams, the horizontal steel tubular element belonging to the U-shape resistant scheme of the deck, the four longitudinal timber beams that support the walking deck, the steel pillars. The cables are modeled using the standard equivalent stiffness technique; that is defining an equivalent value of the Young’s modulus. The walking deck has not been modeled because it represents a non-structural elements. *Ad hoc* rigid links are used to connect the axes of the two main curved beams with the longitudinal beams to model the resistant scheme of the deck.

An overview of the geometry of the structural elements implemented in the FEM is summarized in Table 3.2.1.

Table 3.2.1. “Tesa” footbridge - numerical model: mains features.

ID	<i>element type</i>	<i>size [mm]</i>	<i>note</i>
GLT beam	<i>beam</i>	1238 by 18	solid cross-section
longitudinal timber beam	<i>beam</i>	163 by 100	solid cross-section
steel pillar	<i>beam</i>	radius = 228.6 – th. 12.5	tubular cross-section
cable	-	diameter: 32 and 44	no compression
mains steel braces	<i>beam</i>	diameter: 25	solid cross-section
U-shape steel elements	<i>beam</i>	100 by 200 – th. 5	tubular cross-section

A summary of the model properties is given in Table 3.2.2.

Table 3.2.2. “Tesa” footbridge - numerical model: main features.

ID	<i>TOT [num]</i>
<i>nodes</i>	610
<i>beam</i>	837
<i>rigid link</i>	90

The materials properties are summarized in Table 3.2.3. Due to the complexity of the problem, for all structural elements the standard isotropic behavior is adopted according to the structural code [17].

All the non-structural elements masses have been evaluated following the technical documents and implemented in the numerical model, in order to ensure a consistent dynamic response of the model.

Table 3.2.3. “Tesa” footbridge - numerical model: materials properties.

	Timber – BS14 & BS16	Cable $\phi 32$	Cable $\phi 44$	Steel - S355J0
mass density [Kg/m ³]				
ρ	500.00	5620.00	8260.00	7850.00
Young’s Modulus [N/m ²]				
E	1.10+10	1.65+11	1.65+11	2.06 e+11
Poisson’s Coefficients [-]				
ν	0.10	0.30	0.30	0.30

The following kinematics boundary are introduced:

- for the base of the pillars and for the stays connected with the ground all the degree of freedom are assumed fixed; that is $D_x=D_y=D_z=R_x=R_y=R_z=0$;
- to model the presence of the *neoprene* support below the mains GLT beams the following degree of freedom are assumed fixed; that is $D_y=D_z=R_z=0$.

More details about the kinematics boundary conditions are summarized in Figure 3.2.2 and Figure 3.2.3.

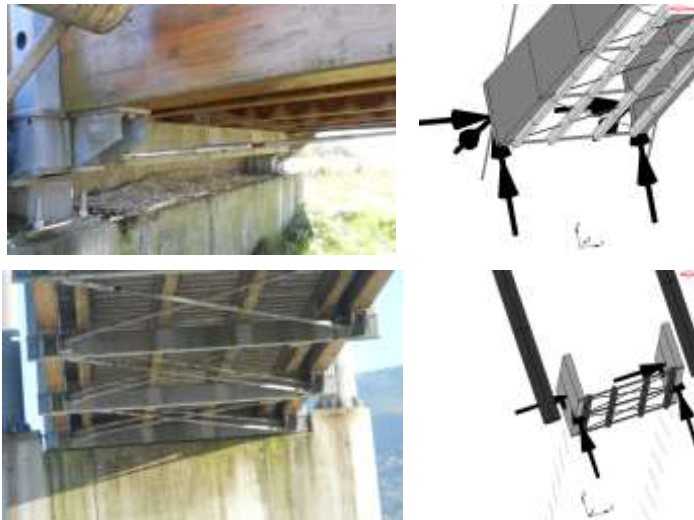


Figure 3.2.2. Detail of the kinematics boundary condition below the mains GLT beams. On the left picture from field; on the right the implemented boundary on the numerical model.



Figure 3.2.3. Detail of the kinematics boundary condition at the base of the pillars. On the left picture from field; on the right the implemented boundary on the numerical model.

Finally an *ad hoc* pre-strain is given to the “external” cables to achieve the final geometrical configuration of the bridge (Figure 3.2.4).

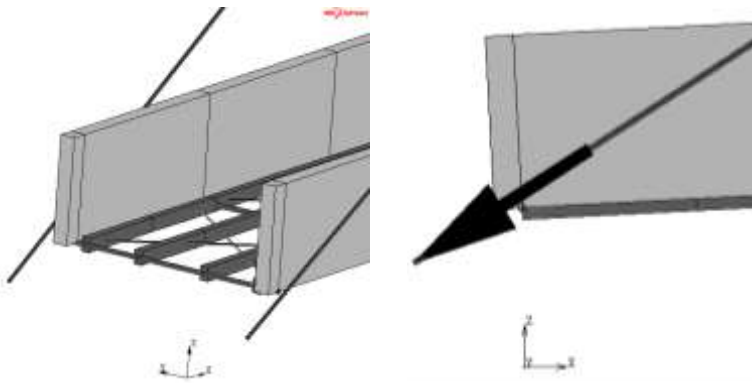


Figure 3.2.4. Detail of the kinematics boundary condition at the base of the pillars. On the left picture from field; on the right the implemented boundary on the numerical model.

To conclude this part, some plots of the FEM are reported in the figures from 3.2.5 to 3.2.8.

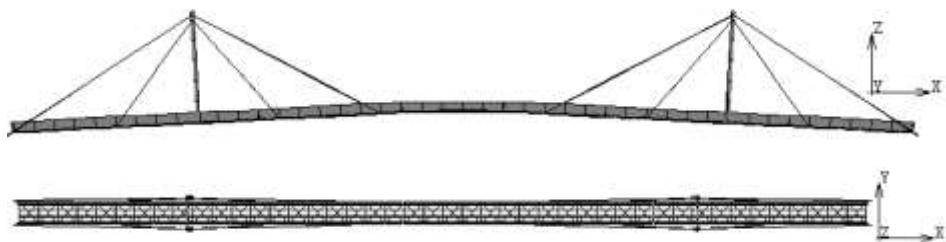


Figure 3.2.5. Above: lateral view of the numerical model; below: view from the above.



Figure 3.2.6. Frontal view of the numerical model.



Figure 3.2.7. 3-D view of the numerical model.

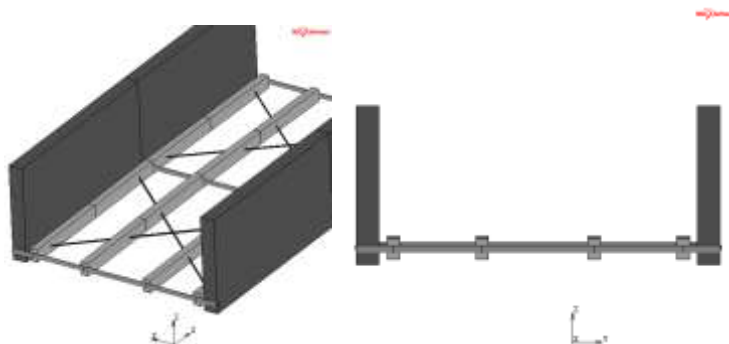


Figure 3.2.8. View of the deck. On the left 3-D view; on the right cross-section view.

In order to take into account the geometric non linearity due to the presence of the cables, the “large strain” option has been activated in the software configuration.

It is worth underlining that, even if the whole general dynamic problems is not linear due to the geometric non linearity introduced by the cables, all the dynamic analysis are conducted within small oscillations around the deformed configuration of equilibrium achieved by the bridge.

3.2.2 FE Model refinement and validation

In order to calibrate and validate the numerical model developed, all the data recorded on the field during *test A* (section 3.1.1) are analyzed following the standard Fast Fourier Transform (FFT) approach.

The results achieved for the acceleration acquired by WAa1 during the *test A* along the Y transversal axis are represented in Figure 3.2.9. The related results are summarized and compared in Table 3.2.4.

Based on the results achieved analysing the data acquired on field, the numerical model previously defined has been refined (e.g. the nodal mass associated to the non-structural elements has been modified) until the dynamic modal analysis associated to the FEM “match well” with the experimental evidence.

The comparison between the analysis of the data coming from the field and the refined numerical model is reported in Figure 3.2.10.

As observed previously even if this bridge has been subject to an extensive study both from the numerical point of view and from the analysis of the data acquired during the in situ monitoring campaign, the attention on the “Tesa” footbridge is mainly addressed to the definition, implementation and validation of a model for the pedestrian loads.

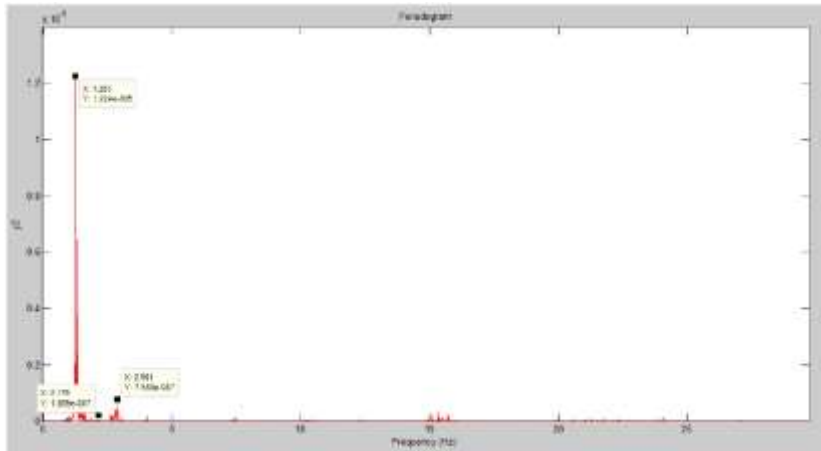


Figure 3.2.9. FFT – acceleration acquired by WAA1 during the *test A* along the *Y* axis.

Table 3.2.4. “Tesa” footbridge – frequencies comparison.

Algorithm	Frequency [Hz]
<i>FFT</i>	1.283
	2.901

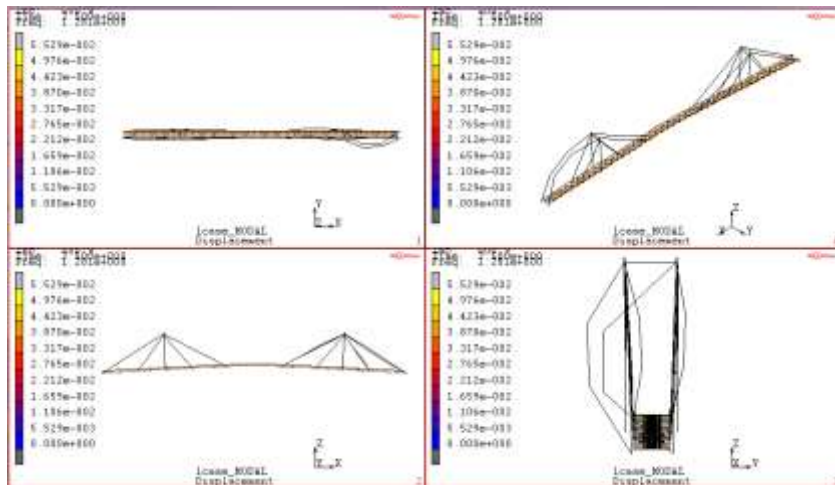


Figure 3.2.10. Mode I – prevalent motion along the transversal direction *Y*. FEM dynamic modal analysis performed in MARC Mentat2010 – $f = 1.28$ Hz.

3.3 FE Model of the “Trasaghis” footbridge

In this section the description of the “Trasaghis” footbridge numerical model is given. The model is developed within the Marc-MENTAT2010 software environment [2].

3.3.1 Project data and numerical model definition

Despite the bridge looks of the cable-stayed type, the static scheme sees a vertical antenna on both sides but the cables are replaced by tubular steel elements. This assumption during the design stage made quite complicated the definition and calibration of the numerical model as described later on in this section.

Starting for the technical documents provided by the designer of the footbridge, a first “rough” numerical model is built following all the design details. In general the span is 83 m and the double beam deck width is 4 m, of which 3.22 m represents the free crossing width for the pedestrians.

The reference global frame has been selected with the:

- *X* axis: along the bridge axis, i.e. parallel to the deck;
- *Y* axis: transversal axis, i.e. orthogonal to the deck;
- *Z* axis: vertical axis parallel to the gravity axis.

A general view of the model implemented in which is represented in Figure 3.3.1.

The model is composed by classical *beam* and *shell* elements. In particular the beam elements are used to model the H-shape steel tubular element of the deck, the five longitudinal timber beams that carry the walking deck, the steel tubular elements of the pillars and oblique stays and the deck braces; while the shell elements are employed to model the two mains GLT beams and walking timber deck. Moreover *ad hoc* rigid links are used to connect the walking deck with the longitudinal beams to model the real space between these elements. An overview of the geometry of the structural elements implemented in the FEM is summarized in Table 3.3.1.

The materials properties are summarized in Table 3.3.2. In particular for the timber elements (according to the structural code [17]), the orthotropic behavior is adopted to represent better their mechanical properties [18].

A summary of the main features of the FE model is given in Table 3.3.3.

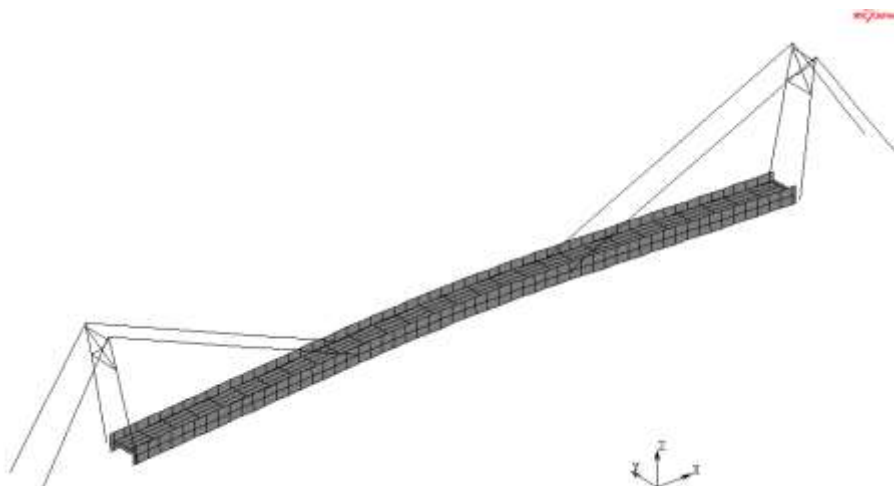


Figure 3.3.1. View of the numerical model implemented in MARC Mentat2010.

Table 3.3.1. “Trasaghis” footbridge - numerical model: geometry of the structural elements.

ID	element type	size [mm]	note
GLT beam	shell	2950 by 1000 – th. 200	-
walking deck	shell	2950 by 725 – th. 63	-
longitudinal timber beam	beam	163 by 120	solid cross-section
steel pillar	beam	radius = 228.6 – th. 16	tubular cross-section
steel stay	beam	radius = 136.5 – th. 8	tubular cross-section
mains steel braces	beam	80 by 10	solid cross-section
H-shape steel elements	beam	1200 by 200 – th. 63	tubular cross-section

Table 3.3.2. “Trasaghis” footbridge - numerical model: materials properties.

	Timber - GL28c	Timber - GL24c	Steel - S355JR
mass density [Kg/m ³]			
ρ	509.68	509.68	7645.26
Young's Modulus [N/m ²]			
E_1	1.26e+10	1.16e+10	2.10e+11
E_2	3.90e+08	3.20e+08	
E_3	3.90e+08	3.20e+08	
Poisson's Coefficients [-]			
ν_1	0.40	0.40	0.30
ν_2	0.40	0.40	
ν_3	0.40	0.40	
Shear's Modulus [N/m ²]			
G_{12}	7.20+08	5.90+08	8.10e+10
G_{23}	7.20+08	5.90+08	
G_{31}	7.20+08	5.90+08	

Table 3.3.3. “Trasaghis” footbridge - numerical model: main features.

ID	TOT [num]
<i>nodes</i>	724
<i>beam</i>	572
<i>shell</i>	352
<i>rigid link</i>	145

For the kinematics boundary conditions the following assumptions are assumed:

- for the base of the pillars and for the stays connected with the ground all the degree of freedom are assumed fixed; that is $D_x=D_y=D_z=R_x=R_y=R_z=0$;
- below each ends of the mains GLT beams a standard abutment is implemented to model the presence of the *neoprene* support;
- to represent the link located to each ends of the GLT beams between the foundation system and the GLT beam, the following kinematic boundary is implemented: $D_x=D_y=D_z=R_y=R_z=0$.

More details on the kinematics boundary conditions are summarized from Figure 3.3.2 to Figure 3.3.4.

Great care was paid to model the mass of all the non-structural elements because of their fundamental importance when performing dynamic analysis; i.e. dynamic modal and dynamic transient analysis. Thus, following the technical documents, all these mass are first valuated and then implemented within the numerical model as “lamped mass” along the deck.

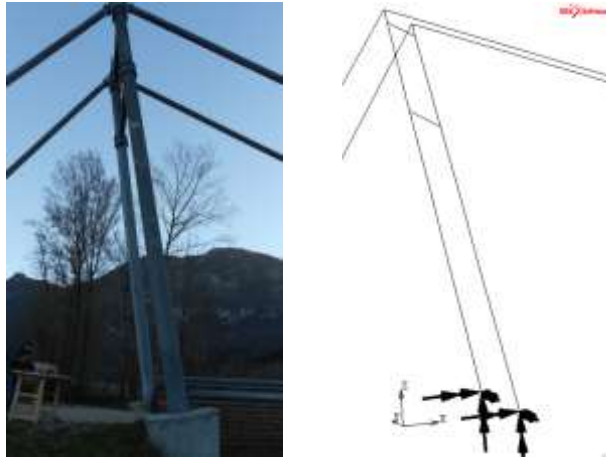


Figure 3.3.2. Detail of the kinematics boundary condition at the base of the pillars. On the left picture from field; on the right the implemented boundary on the numerical model.



Figure 3.3.3. Detail of the kinematics boundary condition at the base of the stays. On the left picture from field; on the right the implemented boundary on the numerical model.

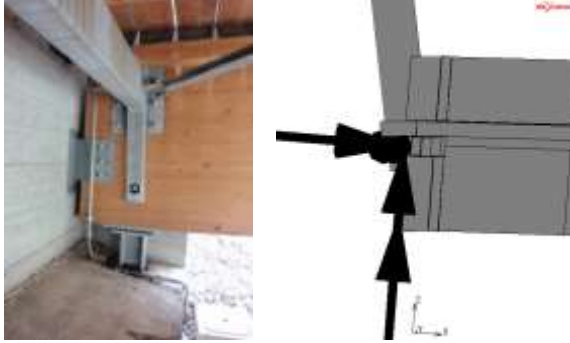


Figure 3.3.4. Detail of the kinematics boundary condition for the GLT beams. On the left picture from field; on the right the implemented boundary on the numerical model.

Great care was paid to model the damping of the structure. In particular the damping properties are fitted by identifying the Rayleigh's coefficients (see equation (2.29)) based on the first experimental campaign carried out in this bridge. The environmental test shown two peaks along Z axis in terms of frequencies; that is $f_1 = 1.75$ Hz and $f_2 = 2.67$ Hz. By applying the bandwidth method presented in section 2.1, the following damping value can be evaluated: $\xi_1 = 0.0092$ and $\xi_2 = 0.0056$ respectively for the frequencies f_1 and f_2 . Thus, the Rayleigh's coefficients can be evaluated as:

$$\left\{ \begin{array}{l} \alpha_1 = \frac{2\omega_1\omega_2(\xi_1\omega_1 - \xi_2\omega_2)}{\omega_1^2 - \omega_2^2} \\ \alpha_2 = \frac{2(\xi_1\omega_1 - \xi_2\omega_2)}{\omega_1^2 - \omega_2^2} \end{array} \right. ; \quad (3.1)$$

where $\omega_1 = 2\pi f_1 = 11.0$ rad/s and $\omega_2 = 2\pi f_2 = 16.7$ rad/s. Substituting these values in the above equation ones obtains $\alpha_1 = 0.1681$ and $\alpha_2 = 11.63e-5$. These parameters are implemented within the code for the element that compose the two main GLT beams. This approach for the estimation of the modal damping properties is an alternative way which is often followed in the modelling process, especially when one preliminarily knows that are the most significant modes.

To verify the goodness of the implemented model, the maximum vertical displacement at the mid-span obtained by the simulation is compared with the one obtained during the loading test. The load test was carried out in order to simulate the uniformly distributed load required by the regulations [17] equal to 400 kg/m^2 (more details are given in section A.1). The result from the numerical analysis differs by about 1.50 cm from the

displacement recorded in field⁹, so the model can be considered validated from the static point of view.

To conclude this part some plots of the FEM are reported in figures 3.3.5 to 3.3.10.

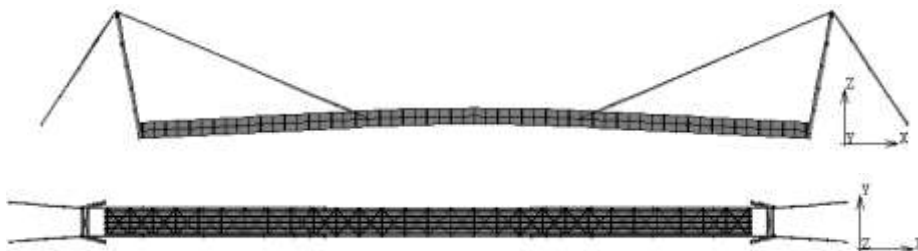


Figure 3.3.5. Above: lateral view of the numerical model; below: view from the above.



Figure 3.3.6. Frontal view of the numerical model.

⁹ About 13.2 cm evaluated by the FEM against 14.5 cm recorded during the loading test.

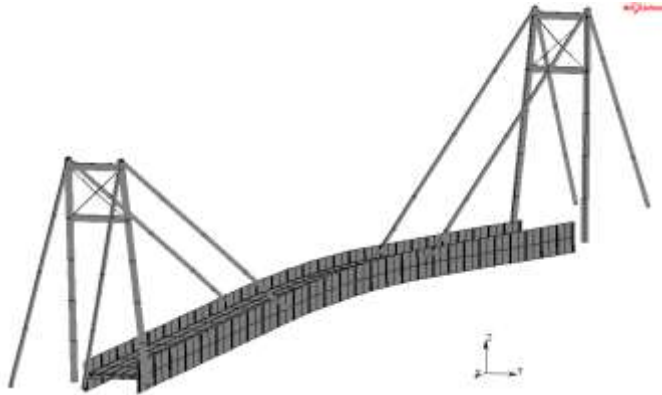


Figure 3.3.7. 3-D view of the numerical model.

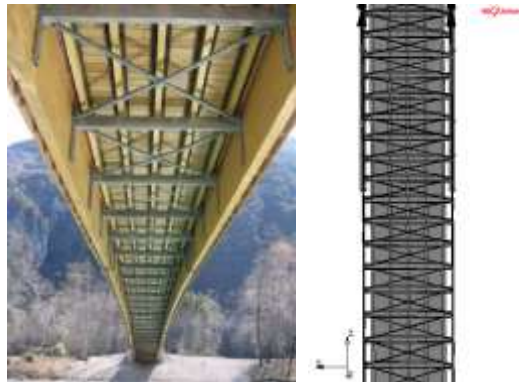


Figure 3.3.8. View from the bottom of the deck. On the left picture from field; on the right the implemented boundary on the numerical model.

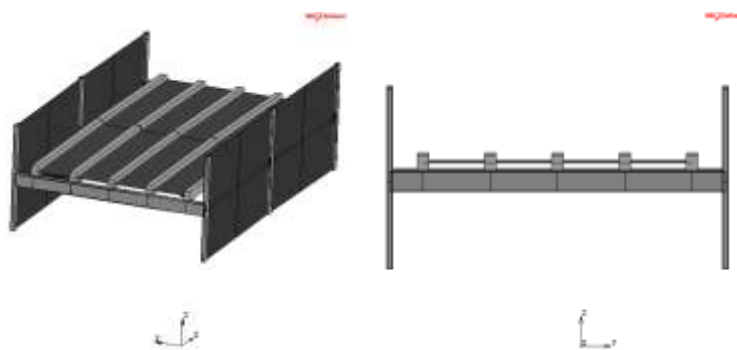


Figure 3.3.9. View of the deck. On the left 3-D view; on the right cross-section view.



Figure 3.3.10. View of the steel pillars and stays systems. On the left 3-D view; on the right cross-section view.

3.3.2 FE Model refinement and validation

Based on the main results of the experimental campaigns, in terms of signal analysis by the standard FFT transform, the numerical model described is then refined, calibrated and validated from dynamic point of view.

The behaviour of the link between the steel stay elements and the deck, and their role with respect to the whole dynamic response of the bridge, is not a priori known. For better investigate this aspect a preliminary numerical model (Figure 3.3.11) of the steel portal is implemented in MARC Mentat2010 [2]. All the elements touching the ground are regarded as fully fixed; that is both translations and rotations are assumed to be zero ([19] and [20]).

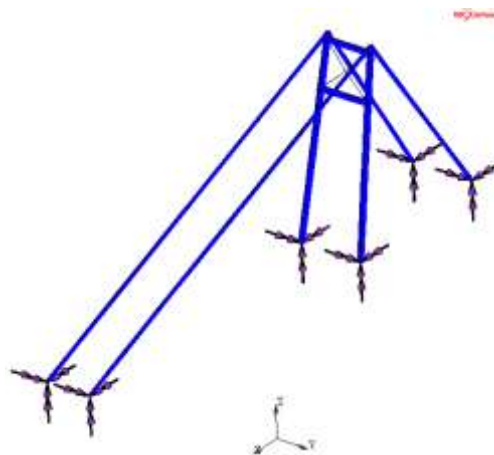


Figure 3.3.11. Partial numerical model of the steel pillars and stays implemented in MARC Mentat2010.

The modal analysis of this partial model provides the range of frequencies that can be associated with the single components of the steel supporting system. Four situations are of interest for this study:

- the vibration of the longest elements (the ones linking the deck with the antenna), the vibration - relevant frequency as f_1 ;
- the vibration associated with an in-plane (transversal to the bridge axis) movement of the single antenna portal - relevant frequency as f_2 ;
- the vibration of the rear oblique elements of the antenna - relevant frequency as f_3 ;
- the vibration of the vertical columns forming the antenna - relevant frequency as f_4 .

Of course, each of the frequency values introduced above, denotes the lower bound of a frequency band where several modes show the vibration of these elements. Indeed the vibration in two parallel elements can occur in different planes (either in-plane or out-of-plane) and can combine with different signs in the structural system giving rise to a multiplicity of modes. The values of f_1, \dots, f_4 , were then also calculated under different constraints at the points where the link with the deck will be realized (Table 3.3.4).

Table 3.3.4. Partial FEM - Frequency ranges for different boundary conditions for the deck-stay link.

<i>Boundary conditions for the deck-stay link</i>	<i>Frequency [Hz]</i>			
	f_1	f_2	f_3	f_4
fixed ends	1.52-1.54	3.43	5.60-6.61	8.73
A - free vertical translation	1.52-1.54	3.43	5.60-6.61	8.73
B - free transversal translation	0.39-2.06	3.43	5.52-6.60	8.66
C - free rotation around the transversal axis	1.07-1.54	3.43	4.25-6.61	8.40
D - free rotation around the vertical axis	1.08-1.54	3.36	4.33-6.56	8.73
A+B	0.39-2.05	3.46	5.52-6.73	8.66
C+D	1.07-1.09	3.36	4.25-6.56	8.40
A+C+D	1.07-1.09	3.35	4.20-6.54	8.37

The recorded signals and the numerical model signals confirm the role of the long tubular stays in determining the vibration of the system at frequencies in the range from 1 to 2 Hz. Within this range, actually, the possible combinations of their vertical (in plane) movements correspond to the lowest frequency value, and those of their horizontal (out-of-plane) movements correspond to an intermediate frequency range, both resulting in modest movements of the deck. This different orthogonal behavior is due to the connections of the stays, which are represented by hinges in the vertical plane, but they can transfer the moments in the orthogonal plane. A further slightly higher frequency shows the movement of all the oblique elements in the same (transversal/out-of-plane) direction resulting in “a torsion” of the central third of the deck. A short summary of the frequencies of interesting for this study is given in Table 3.3.5.

Following the above observations, the numerical model of the whole bridge is so refined (e.g. the nodal mass associated to the non-structural elements has been modified) until the dynamic modal analysis associated to the FEM “match well” with the experimental evidence. An example of the validation is reported from Figure 3.3.12 to Figure 3.3.17. A dynamic modal comparison in terms of frequencies range for the main modes between the results is reported in Table 3.3.6. Some small discrepancies appear but, however, they can be assumed acceptable for the purpose of this work, taking also in account the complexity of the structural scheme of the bridge (i.e. the coupling between steel and wood in the resistant scheme of the deck; the steel stays, and so forth...).

Table 3.3.5. Frequency ranges for the lowest modes of the “Trasaghis” footbridge.

Set ID	Frequency [Hz]	Involved Elements	Oscillation plane
1	1.06	Tubular stay	$X - Z$
2	1.41	Tubular stay	$X - Y$
3	1.96	Tubular stay	$X - Y$ & $X - Z$

Table 3.3.6. Frequencies percentage error. Comparison between “field” and “FEM” results.

ID	$\varepsilon = \left \frac{f_{field} - f_{FEM}}{f_{FEM}} \right \times 100$
mode I	2.3 %
mode II	2.8 %
mode III	5.8 %

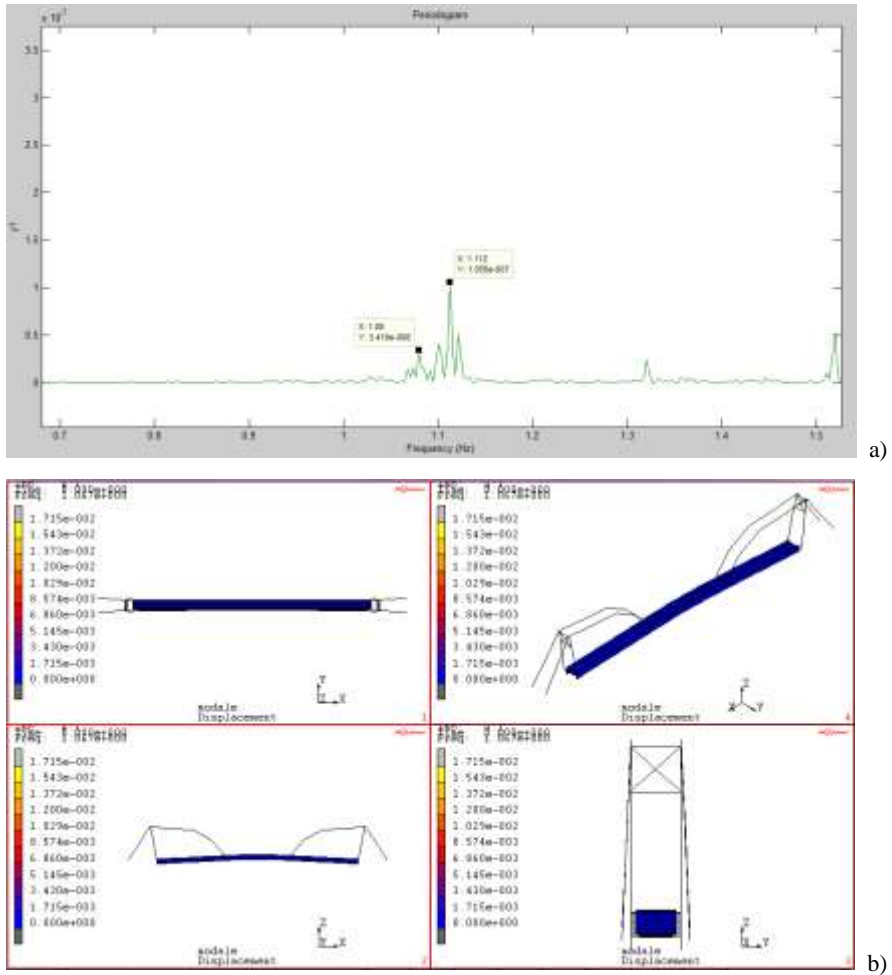


Figure 3.3.12. Mode I – local mode related to the prevalent vertical motion of the stays. a) FFT of the experimental data (Campaign of May, 2013 – position P#7) – $f = 1.08 \pm 1.11$ Hz; b) FEM dynamic modal analysis performed in MARC Mentat2010 – $f = 1.06$ Hz.

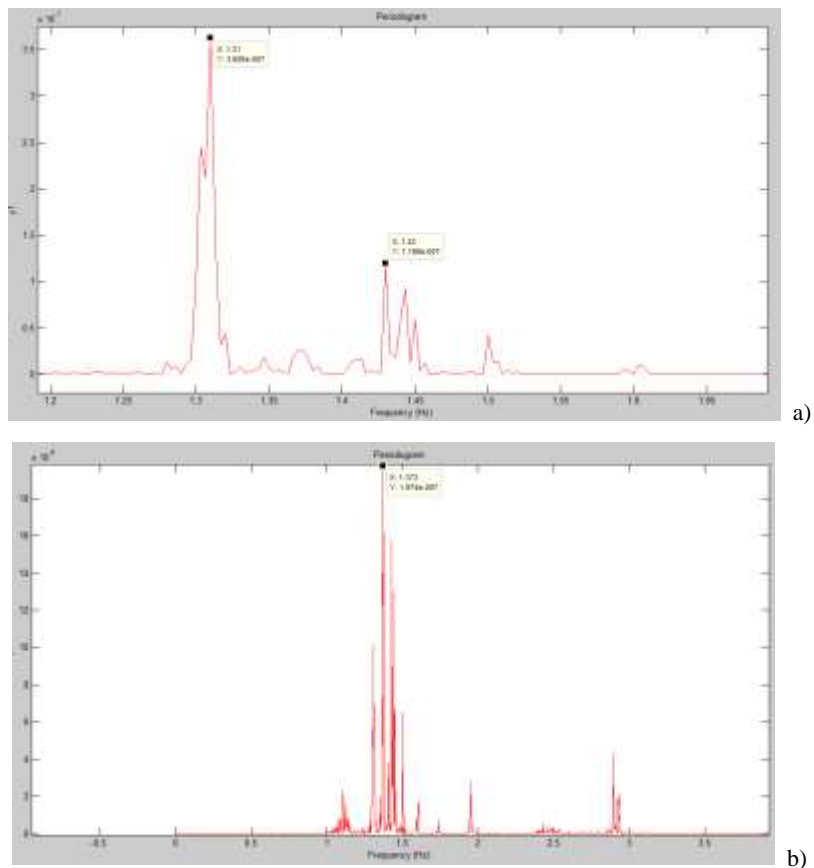


Figure 3.3.13. Mode II – local mode related to the prevalent horizontal/transversal motion of the stays.
 a) FFT of the experimental data along Y (Campaign of May, 2013 – position $P\#7$) – $f = 1.31 \pm 1.43$ Hz; b)
 FFT of the experimental data along Y (Campaign of May, 2013 – position $P\#1$) – $f = 1.37$ Hz.

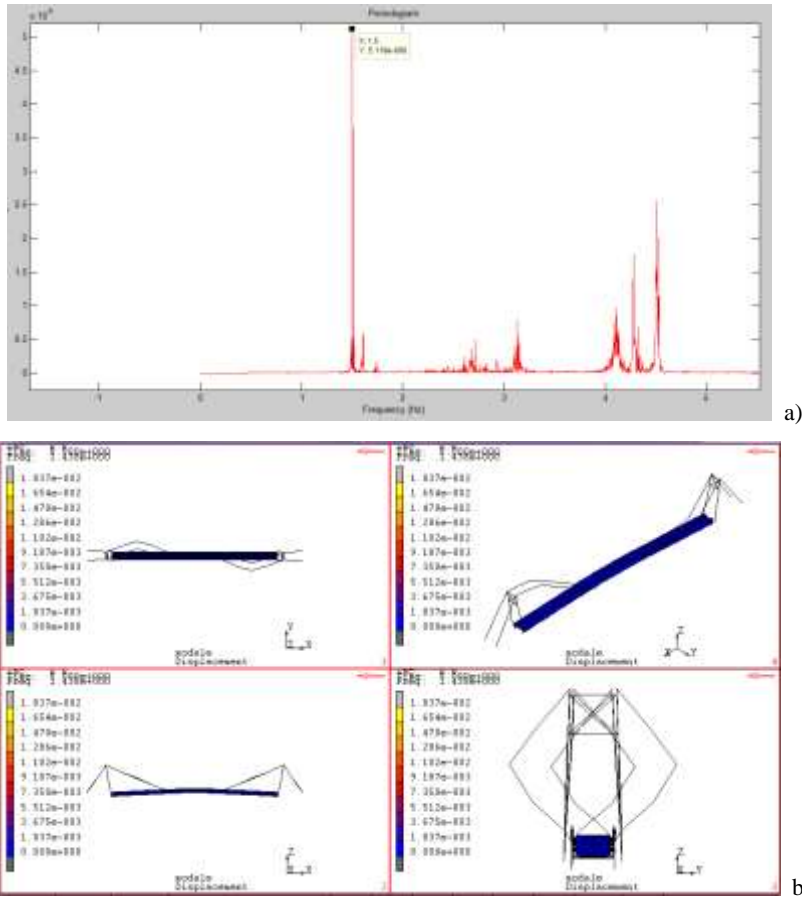


Figure 3.3.14. Mode II – local mode related to the prevalent horizontal/transversal motion of the stays.
 a) FFT of the experimental data along Z (Campaign of May, 2013 – position P#1) – $f = 1.5$ Hz; b) FEM dynamic modal analysis performed in MARC Mentat2010 – $f = 1.41$ Hz.

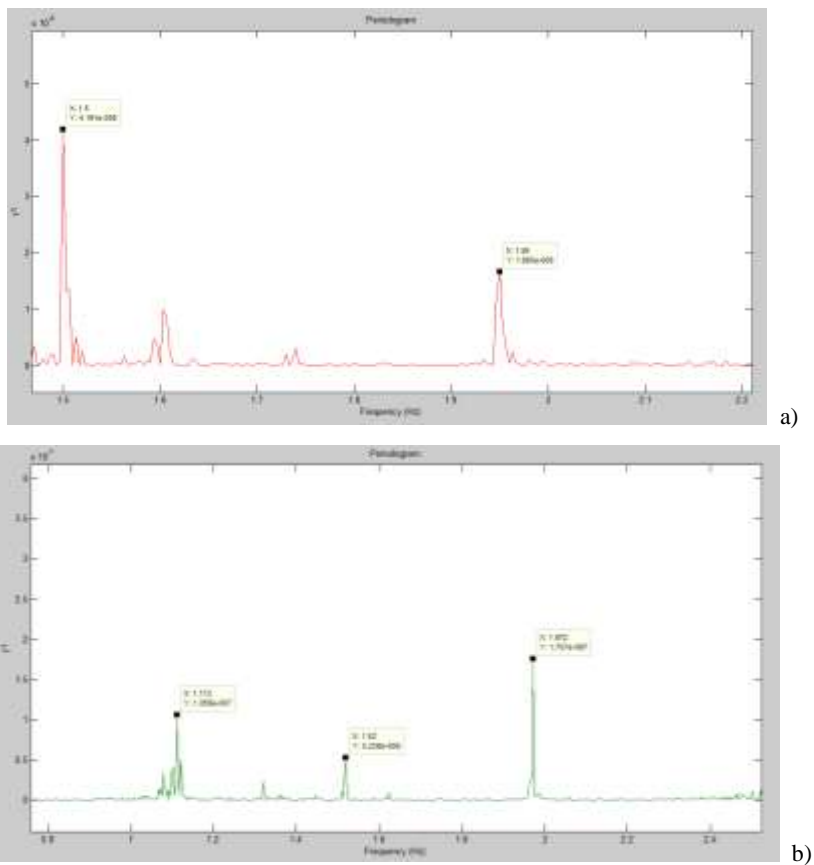


Figure 3.3.15. Mode III – global “pseudo” torsional mode of the deck. a) FFT of the experimental data along Y (Campaign of May, 2013 – position $P\#7$) – $f = 1.95$ Hz; b) FFT of the experimental data along Y (Campaign of May, 2013 – position $P\#1$) – $f = 1.97$ Hz.

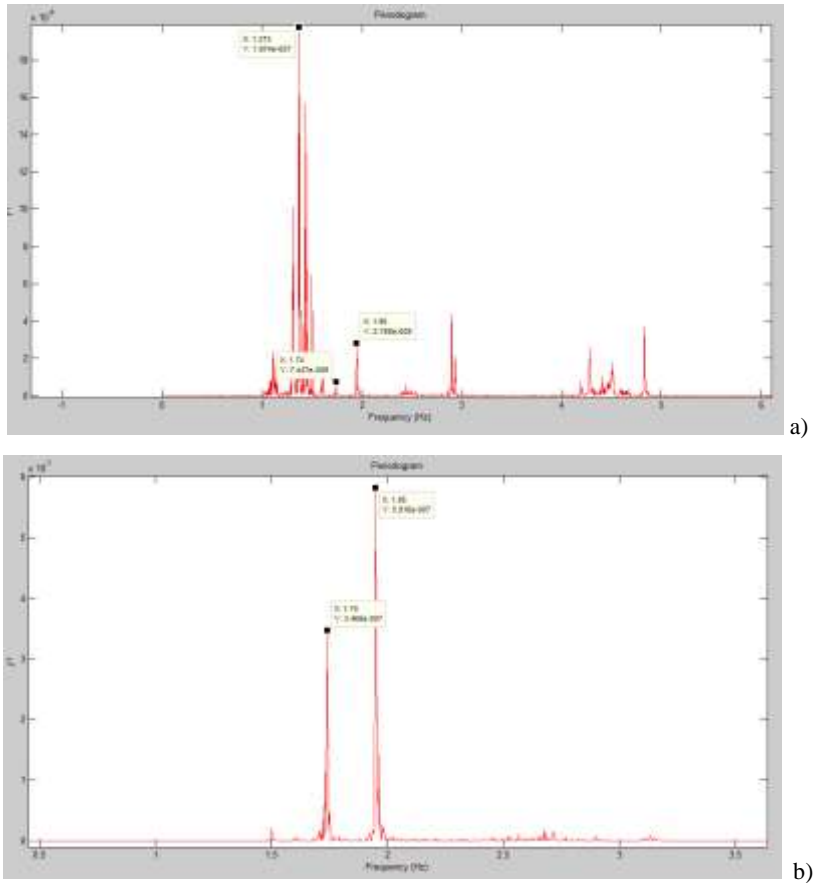


Figure 3.3.16. Mode III – global “pseudo” torsional mode of the deck. a) FFT of the experimental data (Campaign of May, 2013 – position P#3) – $f = 1.74 \pm 1.95$ Hz; b) FFT of the experimental data along Y (Campaign of May, 2013 – position P#3) – $f = 1.74 \pm 1.95$ Hz.

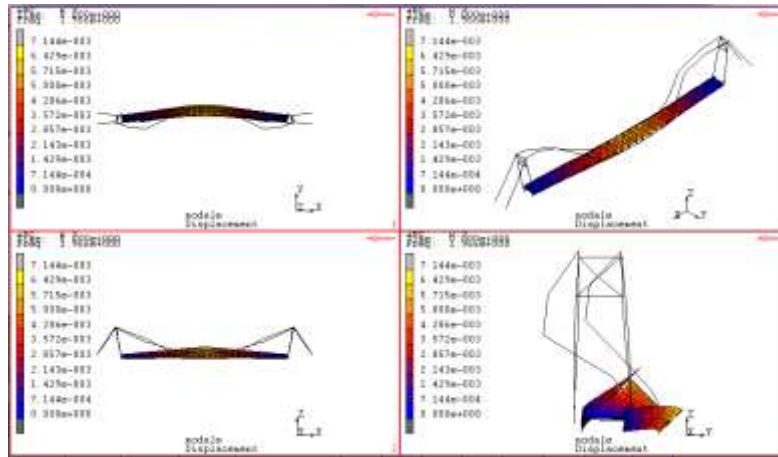


Figure 3.3.17. Mode III – global “pseudo” torsional mode of the deck. FEM dynamic modal analysis performed in MARC Mentat2010 – $f = 1.96$ Hz.

3.4 References

- [1] Zienkiewicz, O.C.; Taylor, R.L.; Zhu, J.Z., 2005. *The Finite Element Method: Its Basis and Fundamentals* (Sixth ed.). Butterworth-Heinemann. ISBN 0750663200.
- [2] www.mscsoftware.com
- [3] Bortoluzzi D., Casciati S., Faravelli L., 2013. Testing the effects of walking and running on an existing timber pedestrian bridge. On the Proceeding of the 9th International Conference on Structural Dynamics - EURO DYN 2014. Porto, Portugal, 30 June – 2 July 2014.
- [4] S. Casciati, F. Casciati, L. Faravelli and D. Bortoluzzi, 2014. Modelling The Human Induced Vibrations In A Cable-Stayed Pedestrian Timber Bridge. On the Proceeding of the 7th European Workshop on Structural Health Monitoring – EWSHM2014, July 8-11, 2014. La Cité, Nantes, France.
- [5] S. Casciati and Z. Chen, 2011. A multi-channel wireless connection system for structural health monitoring applications. *Structural Control and Health Monitoring Journal*, 18 (5), pp. 588–600.
- [6] H.I. Choi and W. Williams, 1989. Improved Time-Frequency Representation of Multicomponent Signals Using Exponential Kernels. *IEE Transactions on acoustic, speech, and signal processing*, vol 37, no. 6, June 1989.

- [7] L. Cohen, 1995. Time-frequency Analysis. Electrical engineering signal processing Prentice Hall Signal Processing series (1st edition - 1995).
- [8] Mallat, S., 1999. A Wavelet Tour of Signal Processing, 2nd edn. London, UK. Academic Press.
- [9] Burrus, C.S., Gopinath, R.A. and Guo, H. Introduction to Wavelets and Wavelet Transforms, 1st edn, Englewood Cliffs,NJ: Prentice Hall Inc.
- [10] B. Peeters and G. De Roeck., 1999. Reference-based stochastic subspace identification for output-only modal analysis. Mechanical Systems and Signal Processing, 13(6):855-878. Theory reference for the SSI method available in MACEC.
- [11] E. Reynders and G. De Roeck., 2008. Reference-based combined deterministic-stochastic subspace identification for experimental and operational modal analysis. Mechanical Systems and Signal Processing, 22(3):617-637. Theory reference for the CSI method available in MACEC.
- [12] E. Reynders, D. Degrauwe, G. De Roeck, F. Magalhães, and E. Caetano., 2010. Combined experimental-operational modal testing of footbridges. ASCE Journal of Engineering Mechanics, 136(6):687-696. Two case studies on the use of OMA and OMAX for footbridge testing, for which MACEC was used.
- [13] www.mathworks.it
- [14] MACEC a MatLAB toolbox - <http://bwk.kuleuven.be/bwm/macec>
- [15] Bortoluzzi D., Casciati F., Casciati S., Faravelli L., Chen Z., 2013. Reporting the results of two experimental campaigns on a pedestrian timber bridge - 9th International Workshop on Structural Health Monitoring 2013 – IWSHM - Stanford University, Stanford, CA – USA, September 10-2, 2013.
- [16] Bortoluzzi D., Casciati F., Casciati S., Faravelli L., 2013. Comparison of accelerometric response records on a timber footbridge. On the Proceeding of 2nd International Conference on Timber Bridges 2013 – ICTB2013, Las Vegas, Nevada USA, September-October, 2013.
- [17] NTC 2008. Norme tecniche per le costruzioni (in Italian) - D.M. 14 Gennaio 2008.
- [18] S. Casciati and M. Domansechi, 2007. Random imperfection fields to model the size effect in laboratory wood specimens, Structural Safety, 29 (4), pp. 308-321.

- [19] Casciati S., Faravelli L. and Bortoluzzi D., 2013. Pedestrian timber bridges: experimental investigation and modelling. On the Proceeding of the 10th International Conference on Damage Assessment of Structures - DAMAS 2013. Trinity College Dublin Ireland, July 8-10 2013.
- [20] Casciati S., Faravelli L., Bortoluzzi D., 2013. Human Induced Vibrations In A Pedestrian Timber Bridge. On the Proceeding of the 4th International Conference on Computational Methods in Structural Dynamics & Earthquake Engineering - COMPDYN2013, Kos Island (GR), 12-14 Jun 2013.

Chapter 4 Modeling the main actions

As already pointed out in *Chapter 2*, when one works with the design and/or control of slender structures as pedestrian bridges, generally the main problems are related with the comfort of the users rather than with the strength of the construction materials. Thus an inaccurate modelling definition of the load(s) at the design stage could result dangerous in term of both resistance and comfort.

Thus, one of the main challenges for the designer is to identify the most suitable model of the *live load(s)*, to be applied on the structure in order to capture/identify the most reliable response of the structure under study. To achieve this purpose a pure theoretical definition of the loads could result unsatisfactory. The best result is achieved merging theoretical aspects with observations made in laboratory and/or in the field on a real case study.

An incorrect definition of the live loads during the design stage can be produces two concatenated effects in terms of comfort; they are:

- 1) an ineffective performance with, in the worst case, a decrease in the achieved comfort level;
- 2) a damage from the economic point of view. In fact, usually, in order to achieve a better level of comfort one needs to install *ad hoc* devices on the structure, i.e. TMDs, dampers and so forth..., that are expensive in term of both installation and maintenance.

In this chapter, models of the main loads to be considered in the design of pedestrian bridges are presented ([1] and [2]) for:

- 1) the wind load;
- 2) the Human Induced Loads (HIL).

For both of them one is looking for models which allows the simulation of time histories of random field realizations.

For the first one the procedure based on a stochastic simulation approach, comes from the literature [9] (see section 4.1). For the case of the human induced vibration a new model for the crowd load is discussed in section 4.2.

4.1 Wind action

In previous chapter, the wind has been introduced as “ambient vibration” (or background noise) and it has been used for the calibration and validation of the numerical models of the two footbridges under study. In this section a more sophisticated mathematical model of the wind is introduced for the purpose of this thesis: i.e. implementation of different control solutions for the mitigation of the footbridge vibrations.

In wind engineering, Monte Carlo simulation is becoming one of the most important tool for the design of wind-excited structures [3]. The following formulas describe the procedure adopted in this work.

The wind velocity is usually idealized as the sum of two components: the first one, the “mean” part (\mathbf{U}), is assumed to be constant along a given time interval; the second component, the “fluctuating” part (\mathbf{u}), represents the atmospheric turbulence. It is usually modelled as a stationary zero mean Gaussian random process. To simulate the fluctuating part the “*weighted amplitude waves superposition*” (WAWS) method is adopted in this thesis [4]-[7].

Let $\{O; x_1, x_2, x_3\}$ be the global Cartesian reference system with O lying on the ground, and the x_3 axis parallel to the gravity direction (Figure 4.1.1). One also assumes, without loss of generality, that \mathbf{U} is parallel to the x_1 axis. Within the above hypotheses one can write:

$$\mathbf{V}(\mathbf{x}, t) = \mathbf{U}(x_3) + \mathbf{u}(\mathbf{x}, t), \quad (4.1)$$

in which,

$$\mathbf{U}(x_3) = \frac{1}{k} u^* \ln \left(\frac{x_3}{z_0} \right), \text{ along } x_1 \text{ axis}, \quad (4.2)$$

where $k=0.41$ is the Von Karman constant [4], z_0 the roughness length and u^* the shear velocity. An example [8] of the mean wind velocity profile with the height is reported in for three different scenario of roughness in Figure 4.1.2.

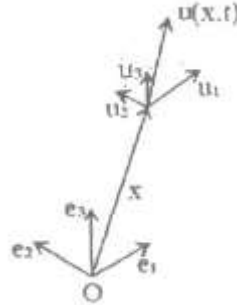


Figure 4.1.1. Global reference frame.

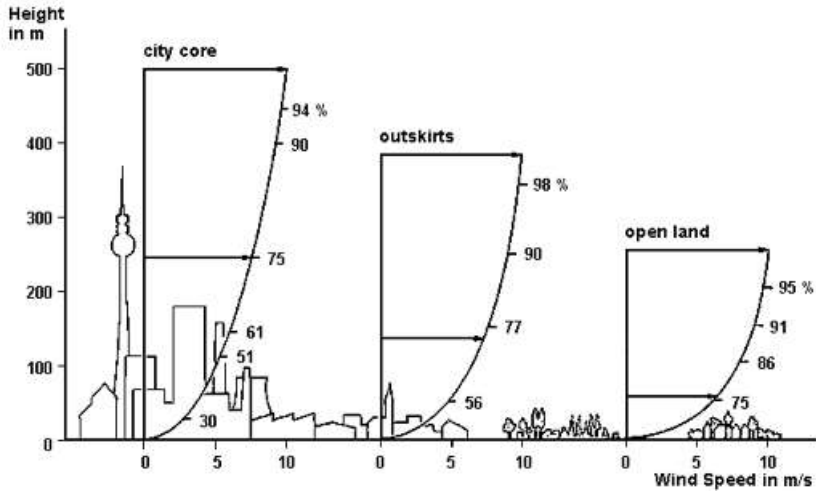


Figure 4.1.2. Example of “mean” wind velocity (U) trend for three different case of roughness [8].

Let $\mathbf{x}=(x_1, x_2, x_3)$ be the vector position of any point P in the above frame, then one can introduce the fluctuating part of the wind velocity as $\mathbf{u}(\mathbf{x}, t)=(u_1, u_2, u_3)$ where u_1, u_2, u_3 are respectively the longitudinal, lateral and vertical components of turbulence as in Figure 4.1.1.

To introduce the turbulence field \mathbf{u} as a zero mean, Gaussian, stationary random field, depending on time, one has to introduce the autocorrelation function $R_{u_i u_j}(\mathbf{x}, \mathbf{x}', t, t')$ for each pair of points P and P' with absolute positions indicated by \mathbf{x} and \mathbf{x}' , respectively, in the above global frame. In particular one has:

$$R_{u_i u_j}(\mathbf{x}, \mathbf{x}', t, t') = \mathbf{E}[u_i(\mathbf{x}, t), u_j(\mathbf{x}', t')], \quad (4.3)$$

where $\mathbf{E}[-]$ is the mean operator.

In the wind engineering field, it is reasonable assume \mathbf{u} as an *ergodic* process; i.e. in other words, the statistical properties of the fluctuating part of the wind velocity could be deduced from a single, sufficiently long, sample of the process. By applying the Fourier transform of the cross power spectral density (CPSD) function between u_i and u_j the autocorrelation function is given as:

$$R_{u_i u_j}(\mathbf{x}, \mathbf{x}', t, t') = \int_{-\infty}^{+\infty} S_{u_i u_j}(\mathbf{x}, \mathbf{x}', \omega) e^{i\omega\tau} d\omega, \quad (4.4)$$

where ω is the circular frequency, $\tau = t - t'$ and i the imaginary unit.

The autocorrelation function depends on τ (i.e. the process stationary in time) and on the positions \mathbf{x} and \mathbf{x}' . As a consequence the random field is not isotropic. Moreover it is important underline as this field is not homogeneous because the autocorrelation function depends separately from the height of the points \mathbf{X}_3 , \mathbf{X}'_3 from the ground (with the zero level assumed as in Figure 4.1.1).

The model adopted in the following work describes the CPSD [6] in term of the auto-spectra $S_{u_i u_j}(\mathbf{x}, n)$, $S_{u_i u_j}(\mathbf{x}', n)$ and coherence function $Coh_{u_i u_j}(\mathbf{x}, \mathbf{x}', n)$, $i, j = 1, 2, 3$, in which $n = \frac{\omega}{2\pi}$ represents the frequency.

Focusing the attention on the simulation of the fluctuating velocity in the plane (x_2, x_3) it is reasonable to neglect the quadrature spectrum related to the imaginary part of the CPSD¹⁰.

By normalizing the auto-spectrum for the turbulence component $u_i(\mathbf{x}, n)$, $S_{u_i u_i}(\mathbf{x}, n)$, one obtains:

$$\sigma_{u_i}^2(\mathbf{x}) = \int_0^{+\infty} S_{u_i u_i}(\mathbf{x}, n) dn, \quad (4.5)$$

in which $\sigma_{u_i}^2(\mathbf{x})$ represents the variance of the component $u_i(\mathbf{x}, n)$.

¹⁰ The quadrature spectrum becomes significant only for point located, far from each-others, along the wind direction x_1 . So this aspect is not relevant for footbridges, and can be neglected without loss of generality.

Following the model proposed in [9] and [10] the auto-spectrum $S_{u_i u_j}(\mathbf{x}, n)$ of the three components of the turbulence can be analytically given as:

$$\frac{nS_{u_i u_j}(\mathbf{x}, n)}{\sigma_{u_i}^2(\mathbf{x})} = \frac{\lambda_j n (L_{u_i}(\mathbf{x}) / \|\mathbf{U}(\mathbf{x})\|)}{(1 + 1.5 \lambda_j n (L_{u_i}(\mathbf{x}) / \|\mathbf{U}(\mathbf{x})\|))^{5/3}}, \quad (j=1, 2, 3), \quad (4.6)$$

where L_{u_i} is the integral length scale of the turbulence component u_j , and $\lambda_1 = 6.868$, $\lambda_2 = 9.434$, $\lambda_3 = 6.103$.

The three components of the turbulence $\mathbf{u}(\mathbf{x}, t) = (u_1, u_2, u_3)$, that are orthogonal to each other, are usually assumed statistically uncorrelated. Vice versa, the dependency of each pairs of parallel turbulence components in two distinct points of the space is described by the coherence function modelled as follows:

$$\begin{aligned} Coh_{u_i(\mathbf{x})u_j(\mathbf{x}')}(\mathbf{x}, \mathbf{x}', n) &= \\ &= \exp \left[- \frac{n \sqrt{[2C_{j1}(x_1 - x'_1)]^2 + [2C_{j2}(x_2 - x'_2)]^2 + [2C_{j3}(x_3 - x'_3)]^2}}{\|\mathbf{U}(\mathbf{x})\| + \|\mathbf{U}(\mathbf{x}')\|} \right], \quad (j=1, 2, 3), \end{aligned} \quad (4.7)$$

where the coefficient C_{js} represents the exponential decay of the component u_j versus the longitudinal ($s=1$), lateral ($s=2$) and vertical ($s=3$) displacements respectively.

Once introduced the problem from a mathematical point of view, in order to obtain a simulated realization of the wind velocity field, one needs to discretize the spatial domain into $k=1, 2, 3, \dots, N$ nodes which usually represent some significant points of the structure under study¹¹. Assuming that $\mathbf{x}^{(k)} = (x_1^{(k)}, x_2^{(k)}, x_3^{(k)})$ represent the position of the generic k -th node of the discretized space, (4.1) can be rewritten simply as:

$$\mathbf{V}^k(t) = \mathbf{V}^k(\mathbf{x}^{(k)}, t) = \mathbf{U}(\mathbf{x}^{(k)}) + \mathbf{u}(\mathbf{x}^{(k)}, t), \quad k=1, 2, 3, \dots, N, \quad (4.8)$$

where u_1^k, u_2^k, u_3^k are, once again, respectively the longitudinal, lateral and vertical components of turbulence in the k -th node of the simulation domain. Following the

¹¹ Usually the same points corresponds to a subset of the nodes used in the numerical model (FEM).

above approach the time-dependent turbulence random field $\mathbf{u}(\mathbf{x}, t) = (u_1, u_2, u_3)$, is transformed into a $3N$ -variate stationary random process $\underline{\mathbf{u}}(t)$, where $\underline{\mathbf{u}}(t)$ is a $3N$ -order vector containing the components $u_1^{(k)}, u_2^{(k)}, u_3^{(k)}$ of the turbulence vector $\mathbf{u}^{(k)}(t)$.

The characterization of the $\underline{\mathbf{u}}(t)$ process is complete introducing the power spectral density matrix (PSD) of order $N \times N$ defined as:

$$S_{\underline{\mathbf{u}}}(\mathbf{n}) = \begin{pmatrix} S_{u^{(1)}u^{(1)}}(\mathbf{n}) & \cdots & S_{u^{(1)}u^{(N)}}(\mathbf{n}) \\ \vdots & \ddots & \vdots \\ S_{u^{(N)}u^{(1)}}(\mathbf{n}) & \cdots & S_{u^{(N)}u^{(N)}}(\mathbf{n}) \end{pmatrix}, \quad (4.9)$$

where each component are defined by a matrix of order 3×3 :

$$S_{u^{(h)}u^{(k)}}(\mathbf{n}) = \begin{pmatrix} S_{u_1^{(h)}u_1^{(k)}}(\mathbf{n}) & S_{u_1^{(h)}u_2^{(k)}}(\mathbf{n}) & S_{u_1^{(h)}u_3^{(k)}}(\mathbf{n}) \\ S_{u_2^{(h)}u_1^{(k)}}(\mathbf{n}) & S_{u_2^{(h)}u_2^{(k)}}(\mathbf{n}) & S_{u_2^{(h)}u_3^{(k)}}(\mathbf{n}) \\ S_{u_3^{(h)}u_1^{(k)}}(\mathbf{n}) & S_{u_3^{(h)}u_2^{(k)}}(\mathbf{n}) & S_{u_3^{(h)}u_3^{(k)}}(\mathbf{n}) \end{pmatrix}, \quad h, k = 1, 2, \dots, N \quad (4.10)$$

The PSD in (4.9) is real¹², symmetric and positive definite at each frequency value \mathbf{n} .

Introduce the two-side power spectral density matrix (2-DPSD) as follows:

$$G_{\underline{\mathbf{u}}}(\mathbf{n}) = \begin{cases} \frac{1}{2\pi} S_{\underline{\mathbf{u}}}(\mathbf{n}) \\ \frac{1}{2\pi} S_{\underline{\mathbf{u}}}(\mathbf{n})^* \end{cases}, \quad (4.11)$$

where the operator * indicates the complex conjugate.

Since $\underline{\mathbf{u}}(t)$ is $3N$ -variate stationary random Gaussian process, it is possible to apply the Priestley spectral approach to generate its representation; that is:

$$\underline{\mathbf{u}}(t) = \int_{-\infty}^{+\infty} e^{i\omega t} d\mathbf{Z}(\omega), \quad (4.12)$$

¹² The PSD is real because the quadrature spectrum has been neglected.

where $\mathbf{Z}(\omega)$ is a zero-mean normal complex random process in which $d\mathbf{Z}(\omega) = \mathbf{Z}(\omega + d\omega) - \mathbf{Z}(\omega)$ that satisfies:

$$\begin{aligned} \mathbf{E}[d\mathbf{Z}(\omega)] &= 0 \quad \forall \omega \\ \mathbf{E}[d\mathbf{Z}(\omega)d\mathbf{Z}^{*T}(\omega')] &= \begin{cases} G_{\underline{\mathbf{u}}}(\omega)d\omega & \text{if } \omega = \omega' \\ 0 & \text{otherwise} \end{cases} \end{aligned} \quad (4.13)$$

Moreover, since the simulated process is a real-value process the Hermitian symmetry is guaranteed; that is $d\mathbf{Z}(\omega) = d\mathbf{Z}^*(-\omega)$.

Introducing now the vector $\mathbf{w}(\omega)$ containing $3N$ complex-value uncorrelated white noise with unit variance and Hermetian symmetry, and an *ad hoc* deterministic matrix $\mathbf{T}(\omega) | G_{\underline{\mathbf{u}}}(\omega) = \mathbf{T}(\omega) \cdot \mathbf{T}^*(\omega)^T$, it is possible to rewrite the increment $d\mathbf{Z}(\omega)$ as follows:

$$d\mathbf{Z}(\omega) = \mathbf{T}(\omega)\mathbf{w}(\omega)\sqrt{d\omega}. \quad (4.14)$$

Substituting (4.14) into (4.12) it is possible to rewrite the random process $\underline{\mathbf{u}}(t)$ as:

$$\underline{\mathbf{u}}(t) = \int_{-\infty}^{+\infty} e^{i\omega t} \mathbf{T}(\omega)\mathbf{w}(\omega)\sqrt{d\omega}, \quad (4.15)$$

It is convenient to apply the decomposition of the 2-DPSD matrix by the Cholesky factorization¹³:

$$\mathbf{T}(\omega) = \begin{pmatrix} T_{11}(\omega) & 0 & \dots & 0 \\ T_{21}(\omega) & T_{22}(\omega) & \dots & 0 \\ \vdots & \vdots & \ddots & \vdots \\ T_{3N1}(\omega) & T_{3N2}(\omega) & \dots & T_{3N3N}(\omega) \end{pmatrix}, \quad (4.16)$$

The discrete version of the equation (4.15) can be written as:

$$\underline{\mathbf{u}}(t) \cong \sum_{-\infty}^{+\infty} e^{i\omega_k t} \mathbf{T}(\omega_k)\mathbf{w}(\omega_k)\sqrt{\Delta\omega}, \quad (4.17)$$

¹³ This approach is not unique. Different factorization/decomposition can be applied.

where the following sequence of uniformly spaced circular frequencies ω_k with step $\Delta\omega$ is considered:

$$\omega_k = \begin{cases} (k-1)\Delta\omega & \text{for } k = 1, \dots, \frac{N_\omega}{2} + 1 \\ -\omega_{N_\omega+2-k} & \text{for } k = \frac{N_\omega}{2} + 2, \dots, N_\omega \end{cases}, \quad (4.18)$$

in which a cut-off circular frequency $\omega_c = \frac{N_\omega}{2\Delta\omega}$ is introduced.

Introducing the decomposition proposed in (4.16) into equation (4.17), the j -th component of the process can be rewritten as:

$$\underline{u}_j(t) \cong \sum_{r=1}^j \sum_{k=1}^{+\infty} e^{i\omega_k t} T_{jr}(\omega_k) w_r(\omega_k) \sqrt{\Delta\omega}, \quad j = 1, 2, \dots, 3N \quad (4.19)$$

and it can be used for the simulation process by truncating the summation to the finite number N_ω of harmonics. The entire simulation of the process $\underline{\mathbf{u}}(t)$ is then generated along a sequence of N_t uniformly spaced time instant defined as:

$$t_j = (j-1)\Delta t, \quad \text{for } j = 1, \dots, N_t. \quad (4.20)$$

Equation (4.19) might be interpreted as a multidimensional Fourier series in which the fundamental circular frequency is represented by $\Delta\omega$, and the corresponding period is defined as $T_p = 2\pi/\Delta\omega$. The simulation represented in (4.19) may be interpreted as a process with periodicity T_p . Therefore, the simulation of the process requires to be satisfied the following condition about its time duration:

$$t_{sample} < T_p. \quad (4.21)$$

More in general, must be satisfied the following conditions:

$$\begin{aligned} \Delta\omega &\leq \frac{2\pi}{N_t \Delta t} \\ \Delta t &\leq \frac{\pi}{4\omega_c} \end{aligned} \quad (4.22)$$

An alternative representation of the equation (4.19) is given in [5]; that is:

$$\underline{u}_j(t) \cong \sum_{r=1}^j \sum_{k=1}^{N\omega} T_{jr}(\omega_k) \cos(\omega'_k t + \phi_{rk}) \sqrt{\Delta\omega}, \quad j = 1, 2, \dots, 3N \quad (4.23)$$

where $\omega'_k = \omega_k + \delta\omega_k$ with $\delta\omega_k$ a small random frequency introduced to avoid the periodicity of the simulated signal, and $\phi_{rk} \in [0, 2\pi]$ are random (independent) phases uniformly distributed.

In design applications the above fields are obtained using *ad hoc* algorithms (an example is represented in Figure 4.1.3). One can refer to [7] among others. Following this approach the only parameters that one needs to set in order to get the wind field simulation are:

- 1) mean velocity of the wind;
- 2) roughness length;
- 3) time step;
- 4) grid of nodes over which the simulation is performed.

Once simulated the wind velocity field, by the Bernoulli's formula, it is possible to evaluate the force field that can be used within the FEM in order to perform a structural analysis of the structure under study; that is:

$$F_i^{(k)}(\mathbf{x}^{(k)}, t) = q_i^{(k)} \Omega = \left(\frac{1}{2} \rho \left[V_i^{(k)}(\mathbf{x}^{(k)}, t) \right]^2 \right) \Omega, \quad i = 1, 2, 3, \dots, 3N, \quad (4.24)$$

where $F_i^{(k)}(\mathbf{x}^{(k)}, t)$ is the i -th component (expressed in N) of the force vector $\mathbf{F}^{(k)}(\mathbf{x}^{(k)}, t)$, $V_i^{(k)}(\mathbf{x}^{(k)}, t)$ is the wind velocity field simulated in (4.8), $\rho = 1,25 \text{ kg/m}^3$ the air mass density, and Ω (expressed in m^2) the impact surface on the structure in which the wind is blowing.

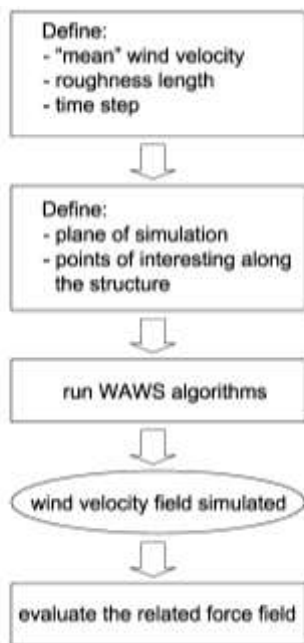


Figure 4.1.3. Flowchart for the wind velocity field simulation.

4.2 Human induced vibration source

Despite several proposals can be found in the literature (and/or guidelines) about the modelling of the load induced by a single pedestrian, no reference seems to be addressed to the common case of groups of walking people.

In this section a model for introducing the crowd loads on a footbridge is discussed. The effects of the simulated realizations are compared with the ones recorded during an experimental campaign carried out on the in-service “Tesa” footbridge (see section 2.3 and section 3.1.1).

The classical dynamic behaviour of a single pedestrian is first considered on the basis of the existing literature (more details are presented in *Appendix B*). A first distinction has to be done about the different dynamic effect of walking and running. Indeed during pedestrian walking there is always one foot in contact with the ground, while during running this disappears and usually only one foot touches the ground in a discontinuous manner. Any person walks with similar step frequencies in the range from 1.25 to 2.3 Hz, due to similar physiological human constitutions, but the step frequencies are

influenced by the purpose of the movement and the intensity of the pedestrian loading [11].

The most common time domain models for these forces scheme can be found in literature and/or in the guidelines (see [11]-[14] among others). They are based on the assumption that both human feet produce the same force. The resulting periodic force is expressed by standard Fourier series as follows:

- vertical (gravity) component:

$$F_v(t) = P \left(1 + \sum_{n=1}^k \alpha_{n,v} \sin(2\pi n f_v t - \varphi_n) \right); \quad (4.25)$$

- lateral (transversal) component:

$$F_{lat}(t) = P \sum_{n=1}^k \alpha_{n,lat} \sin(2\pi n f_{lat} t - \varphi_n); \quad (4.26)$$

The model of the pedestrian running is more complicated because, during the run, there is a so called “lift-off phase”, during which no foot is in contact with the ground. Only the vertical component of these forces is taken into consideration because it has been observed as the horizontal components, both lateral and longitudinal, have a low “impact” on the dynamic response of the bridge [14]. The vertical component is modelled by using the standard Fourier transform as follows:

$$F_{r,vert}(t) = P + \sum_{n=1}^k P_n \sin(2\pi n f_r t) \quad \text{for } (j-1)T_m \leq t \leq \left(j - \frac{1}{2}\right)T_m; \quad (4.27)$$

$$F_{r,vert}(t) = 0 \quad \text{for } \left(j - \frac{1}{2}\right)T_m < t \leq jT_m$$

4.2.1 Crowd Load Model (CLM)

In order to simulate the interaction between the structure and the human induced loads in a realistic manner, a model for the load due to a group of persons is required. In this section a numerical model of the crowd load is discussed. As already observed in section 2.3, the proposed model is validated on the base of the records acquired during the experimental campaign carried out on the “Tesa” footbridge.

A numerical model for the crowd load has to account for several aspects: psychology, motion, individual feeling and so forth... The introduction of the global effects of these aspects by an amplification factor, as suggested in some guidelines (e.g. [14]), could result quite inaccurate.

The main ideas behind the new model for the crowd load can be summarized as follows:

- the load is regarded as the sum of a “*steady/mean*” and a “*fluctuation*” part.
- the spectrum of the fluctuation part fits the one of data recorded during the experimental campaign.

Thus the pedestrian induced force is the sum of two components. Indeed the pedestrian can be seen, from the mechanic point of view, as a moving mass; thus one can identify a steady component related to its weight, and a fluctuation part related to the inertial component of its motion. In other words the fluctuation part takes into account that, during the motion, each pedestrian foot transmits to the structure different values of the force.

The model is referred to only two main directions: transversal axis (Y), and vertical or gravity axis (Z).

Without loss of generality, the procedure is presented with reference for the case of six persons walking along the deck in couples of two.

The first step, for the lead simulation, is to identify the *grid* of $k=1,2,\dots,N$ nodes (Figure 4.2.1) where the generic node has coordinates $P_k = (X_k; Y_k)$.

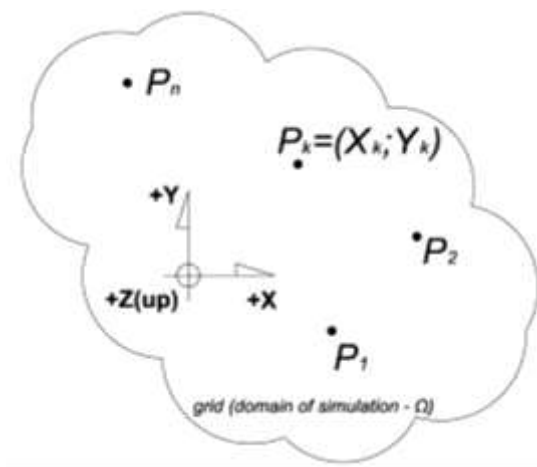


Figure 4.2.1. Grid of nodes for the simulation.

The main hypothesis on which the proposed model is based is the *ergodicity* of the process. Given this assumption, it is possible to define the Cross Power Spectral Density

Function (CPCD) in terms of auto-spectra $S_{f_i f_j}$ and coherence function $Coh_{f_i^{(h)} f_j^{(k)}}$ as follows:

$$\begin{cases} S_{f_i f_j}(x, x'; n) = \sqrt{S_{f_i f_j}(x; n) S_{f_i f_j}(x'; n)} Coh_{f_i f_j}(x, x'; n) \\ Coh_{f_i^{(h)} f_j^{(k)}}(n) = \exp \left[-\frac{n \|(C_j^{(h)} + C_j^{(k)})(x^{(h)} - x^{(k)})\|}{\|F^{(h)}\| + \|F^{(k)}\|} \right] \end{cases} \quad i, j = 1, 2. \quad (4.28)$$

where:

- $F^{(h)}, F^{(k)}$: are the stationary value of the forces (or mass) due to one pedestrian;
- f_i, f_j : any pair forces (or mass) due to the movement of the crowd, simulated by the process, acting along the two main direction above described in any pair of position x, x' ;
- n : the frequency [Hz];
- $C_j^{(k)}$: the second order tensor is defined as follows:

$$C_j^{(k)} = \sum_{s=1}^3 C_{js} f_s^{(k)} \otimes f_s^{(k)}, \quad (4.29)$$

where f_s^k is the s -th component of the local frame defined on the general node $k=1, 2, \dots, N$ (Figure 4.2.2), and the matrix of coefficient C_{js} is assumed equal to:

$$C = \begin{bmatrix} 0 & 0,3 & 0,05 \\ 0 & 0 & 0 \\ 0 & 0,65 & 0,3 \end{bmatrix}. \quad (4.30)$$

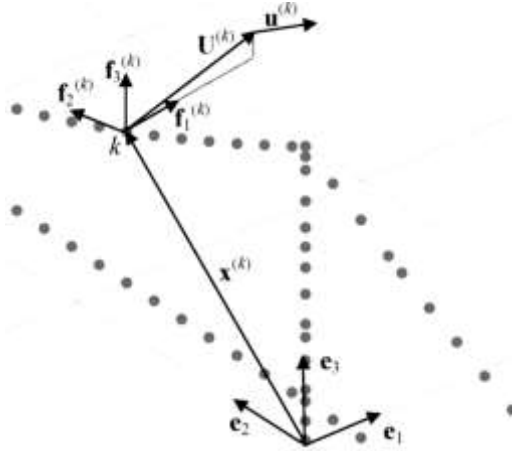


Figure 4.2.2. Local frame system for the k -th node.

Once a realization of the field is simulated by *ad hoc* code in MatLAB [15], a more realistic physical distribution of the above simulated forces is needed. Indeed, as suggested by the experience, the pedestrians during their motion will try to move along the centreline of the deck rather than close to the handrail of the footbridge. Moreover in a crowd situation, all the pedestrians tend to conform their footstep in accordance with the crowd velocity. Thus, a correction function $f_{bd}(X,Y)$ is introduced, where (X,Y) are the planar coordinates of the k -th node of the simulation grid defined above (Figure 4.2.1). In other words the purpose of this function is to decrease the value of the simulated forces belonging to the nodes close to the external side of the pedestrian bridge, where is likely to assume that the pedestrian will avoid to walk, shifting the forces towards the centreline of the deck;

Summarizing, the field forces along Y and Z axes proposed by the above CLM model can be represented as follows:

$$F_{CROWD}(X,Y;t) = (F_{STEADY} + F_{FLUCTATING}(X,Y;t)) * f_{bd}(X,Y). \quad (4.31)$$

It has to be underlined as in this procedure the velocity of the crowd during the crossing of the footbridge is hypothesized constant along all the simulation; in other words the hypothesis of a *uniform linear motion* is assumed. Moreover, from a kinematic point of view it is assumed that each pedestrian will take the place of his/her predecessor (Figure 4.2.3). Furthermore the spatial configuration of the pedestrians is assumed the same along the simulation; that is the distance between two consecutive pedestrian in both the

longitudinal and transversal directions of the deck is fixed and correspond to the dimension of the simulation grid.

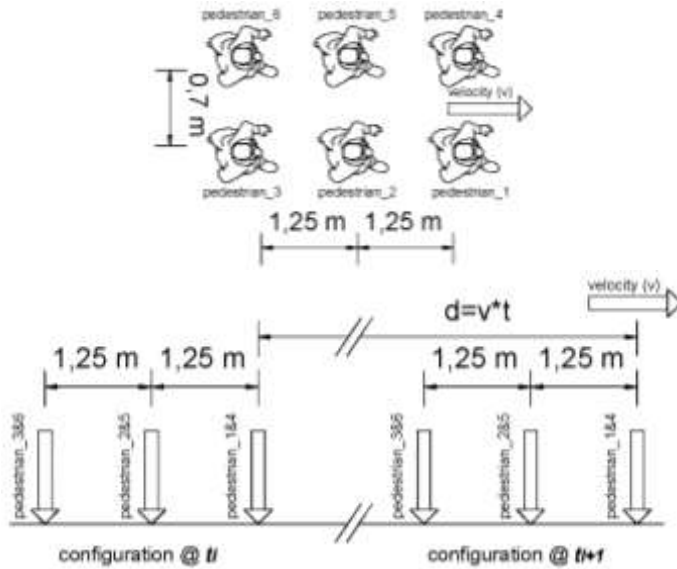


Figure 4.2.3. Spatial configuration of the crowd model implemented.

From another point of view the proposed model can be given in different way idealizing a group of pedestrian as a “rigid” moving body. The model of these loads leads, within the hypothesis of a deterministic approach, to a constant deterministic value at any time in the considered nodes. The loads is simply “translated” along the deck according to the classical relation “*space = velocity -by- time*” but its value (“mean” value) remain the same on time and space (Figure 4.2.4).

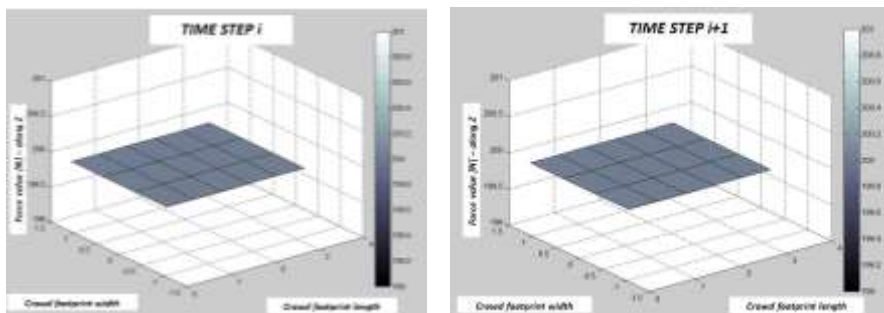


Figure 4.2.4. Classical model of moving loads. Deterministic approach. An example of two consecutive time steps.

In the model presented in this thesis, even if the *uniform linear motion* hypothesis is still adopted, a random process is assumed in order to give fluctuation around the “mean” to the components of the forces (the “fluctuating” part).

The above procedure for load modelling is summarized by the flowchart represented in Figure 4.2.5.

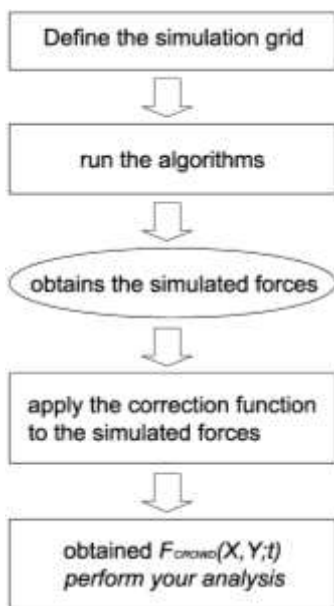


Figure 4.2.5. Flowchart for the CLM simulation.

To calibrate and validate the model the experimental campaign carried out on the “Tesa” footbridge is supported to provide the required information. Figure 4.2.6 and Table 4.2.1 summarize the main aspects of this campaign, already illustrated in section 3.1.1.

More details about the sets of data used for the calibration and validation of the proposed model are reported in *Appendix D*.

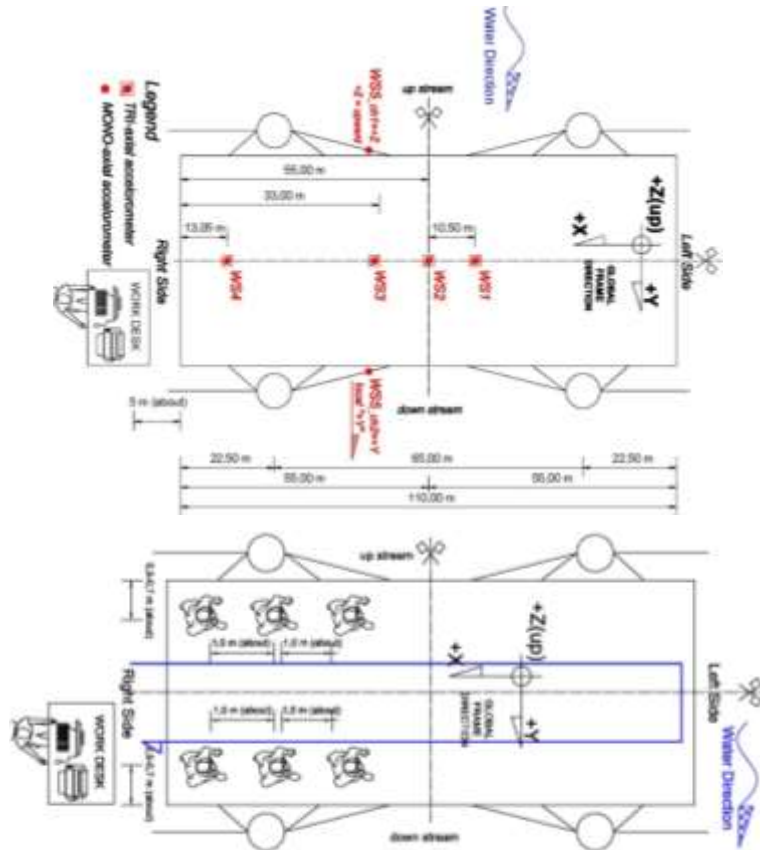


Figure 4.2.6. Above: experimental set-up; below: walking test of six person configuration.

Table 4.2.1. Walking (round trip) of six persons.

Type	ID
Day/Time	November 7, 2013 / 3.00 pm
Test type	walking (round trip)
Air temperature	15°C
Pedestrian(s) num.	6 persons
Total Pedestrian(s) mass	480 Kg
Total time duration	≈2:42 min
Average velocity of the pedestrians	1.35 m/s

4.3 Time-histories simulation

4.3.1 Wind velocity field

Following the procedure for the wind velocity field simulation summarized in section 4.1 one has first to introduce the nodes of interest along the footbridge profile. With reference to the ‘‘Trasaghis’’ footbridge 23 nodes are selected as shown in the simulation grid in Figure 4.3.1. In particular fifteen nodes are equally spaced along the deck, while the remaining eight nodes are located along the pillars and the oblique steel stays (Figure 4.3.1 and Table 4.3.1).

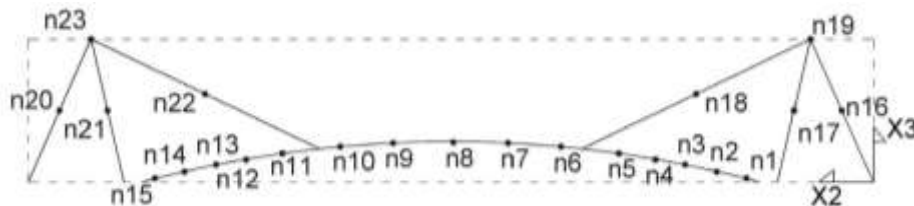


Figure 4.3.1. Grid of nodes for wind velocity field simulation.

Table 4.3.1. Coordinates of the nodes for the simulation grid.

<i>Node ID</i>	x_2 [m]	x_3 [m]	<i>Node ID</i>	x_2 [m]	x_3 [m]
1	12.47	1.79	12	77.07	2.67
2	18.33	2.08	13	82.94	2.38
3	24.20	2.38	14	88.81	2.08
4	30.07	2.67	15	94.67	1.79
5	35.95	2.96	16	4.63	9.39
6	41.82	3.25	17	10.52	9.64
7	47.70	3.45	18	24.81	9.75
8	53.57	3.52	19	9.26	16.28
9	59.44	3.45	20	102.51	9.39
10	65.32	3.25	21	96.62	9.64
11	71.19	2.96	22	82.34	9.75
			23	97.88	16.28

The parameters necessary to perform the simulation are defined below:

- shear velocity of the wind: $u^* = 7$ m/s;
- Von Karman constant: $k = 0.41$;

- roughness length: $z_0 = 0.30$ m according to [16];
- time step: $\Delta t = 0.05$ sec as a compromise between achievable accuracy and required computational effort. The duration of the simulated time history is assigned to be 60 sec in view of the exemplification purpose of these analyses. Of course, in the actual design process, longer durations would be better recommended.

With the above data one achieves an average value of $\mathbf{U}(x_3)$ (see equation (4.2)) equal to about 27 m/s. An example of the simulated velocity fields for the nodes $n1$ and $n19$ belonging respectively to the deck and to the top of the pillar, are shown in Figure 4.3.2.

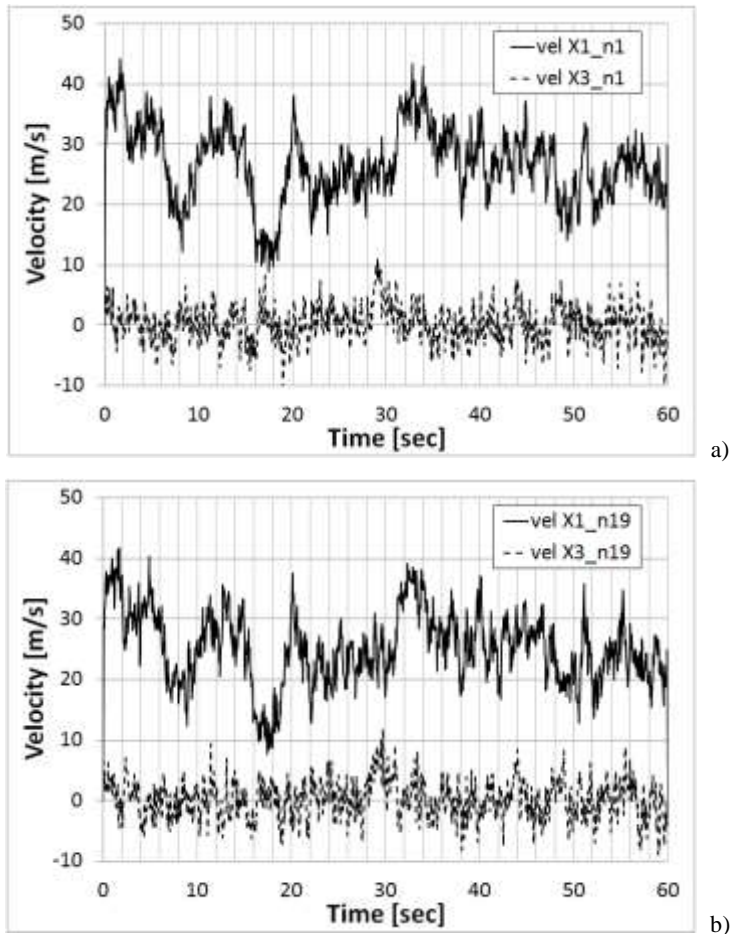


Figure 4.3.2. Wind velocity components along the x_1 and x_3 axes as simulated for node: a) $n1$, b) $n19$.

Once the wind velocity field is obtained, by applying the equation (4.24), the related force field for each node of the grid is calculated. When introducing the time histories as boundary conditions in the finite element analyses, one can either consider them as instantaneously applied (with consequent impact phenomena that can be create several problems during the dynamic analysis), or “smooth” them by applying an initial and a final linear ramp (to avoid the above impact phenomena). The second option is then adopted. As an example in Figure 4.3.3 the time histories of the forces for the nodes $n8$, $n22$ and $n23$ are plotted. For each node the two components along the x_1 and x_3 axes are plotted.

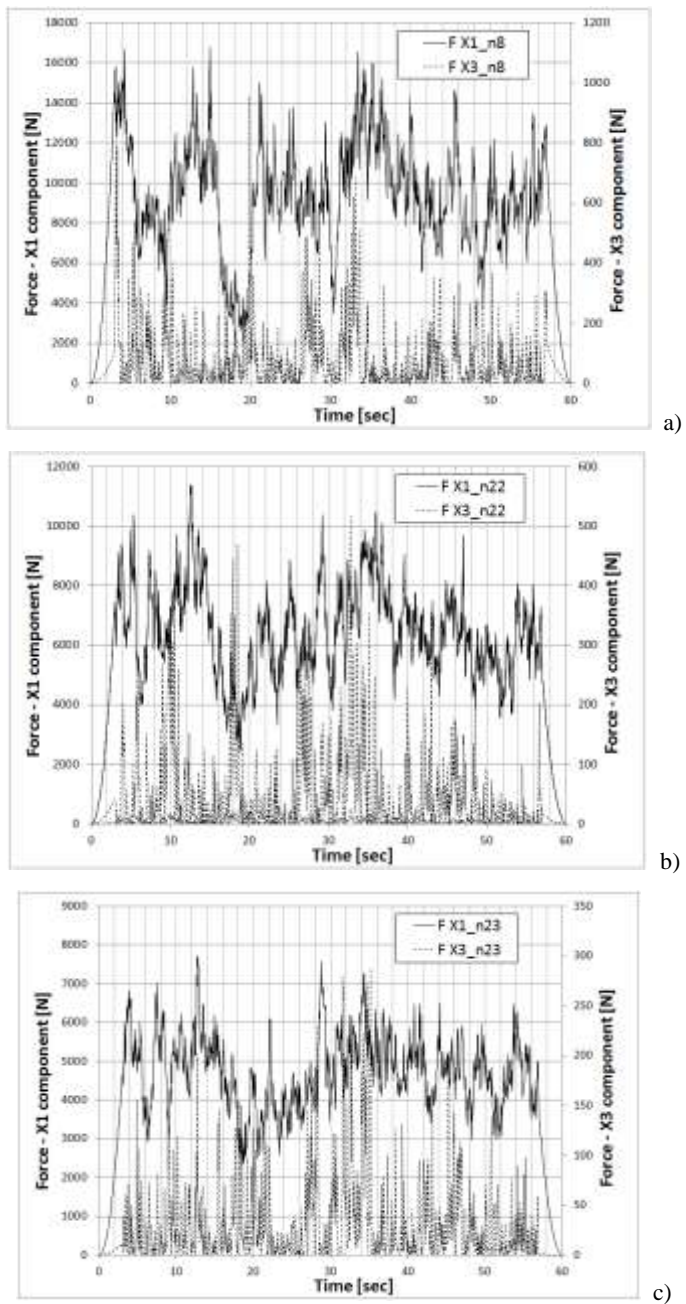


Figure 4.3.3. Force components along the x_1 and x_3 axes for node: a) n_8 , b) n_{22} and c) n_{23} .

4.3.2 Crowd Load Model: numerical simulation and validation

Moving now to the simulation of the crowd load, following the procedure summarized in Figure 4.2.5, the first step is to define the grid over which the algorithm will be applied. For the case study (i.e. “Tesa” footbridge) the grid is made by 24 nodes subdivided in 4 rows (parallel to the longitudinal direction of the deck) and 6 columns (parallel to the transversal direction of the deck) for a global dimension of 2.5 by 3.125 m, in order to be consistent with the mesh of the “Tesa” footbridge deck (Figure 4.3.4). This means that each pedestrian insist, at any instant of the time, on four nodes to represent the possibility of the pedestrian to move “freely” during the motion. The step of the nodes is assumed equal to 0.625 m, in order to simulate an average human footstep. In other words the velocity of the crowd is assumed equal to $v = 0.625$ m/s; i.e. 1 footstep/sec.

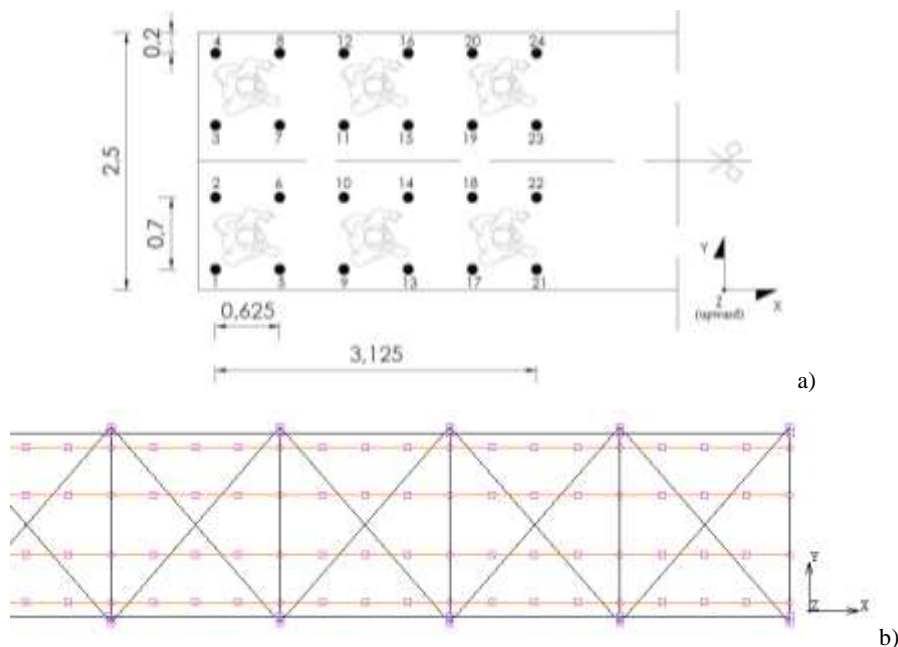


Figure 4.3.4. a) Grid of nodes for the simulation; b) example of the deck nodal grid implemented in MARC Mentat2010.

The steady value of the force (or mass) due to a singular pedestrian is assumed equal to $F_{pedestrian}=800$ N/pedestrian (about 80 Kg/pedestrian). In other words this means that on each nodes of the grid the applied force is equal to $F^{(k)}=200$ N/nodes with $k=1,2,\dots,24$ (Figure 4.3.5).

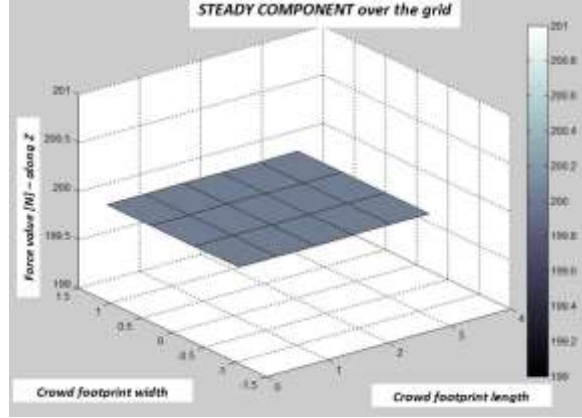


Figure 4.3.5. Steady component of the force over the simulation grid.

The correction function is defined as follows:

$$f_{bd}(X, Y) = (-0.82Y^2 + 1.50) \left(2 \left(0.30 \cos \left(2 \left(\frac{\pi}{l_{grid}/2.5} \right) X \right) + 0.50 \right) \right), \quad (4.32)$$

where (X, Y) are the planar coordinates of the k -th node of the grid, and $l_{grid} = 3.125$ m the length of the grid. In Figure 4.3.6 the 3-D plot of the above function is shown.

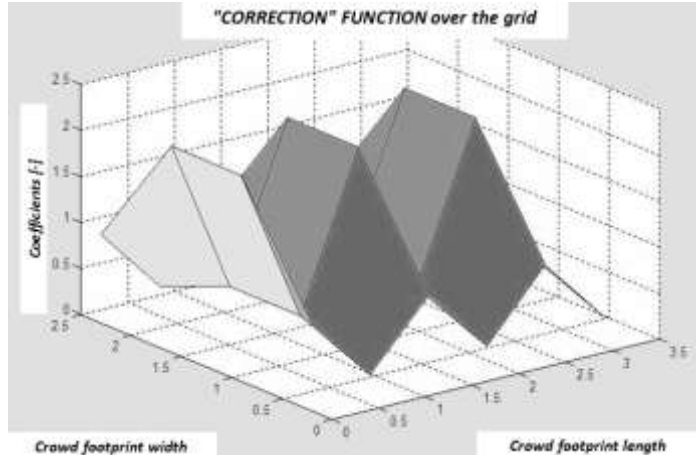


Figure 4.3.6. 3-D plot of the "barrel dented" function over the nodes of the simulation grid.

As an example, from Figure 4.3.7 to Figure 4.3.9, the plots of the simulated forces at three different time steps are represented.

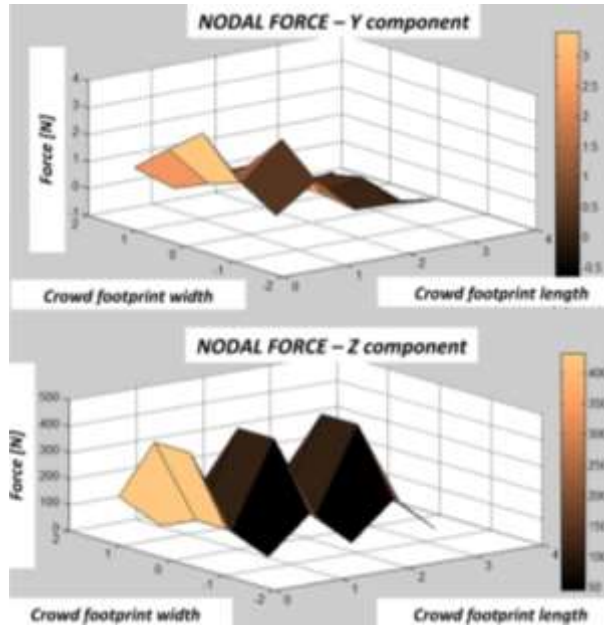


Figure 4.3.7. Step 1 – simulated force files by the proposed CLM model.

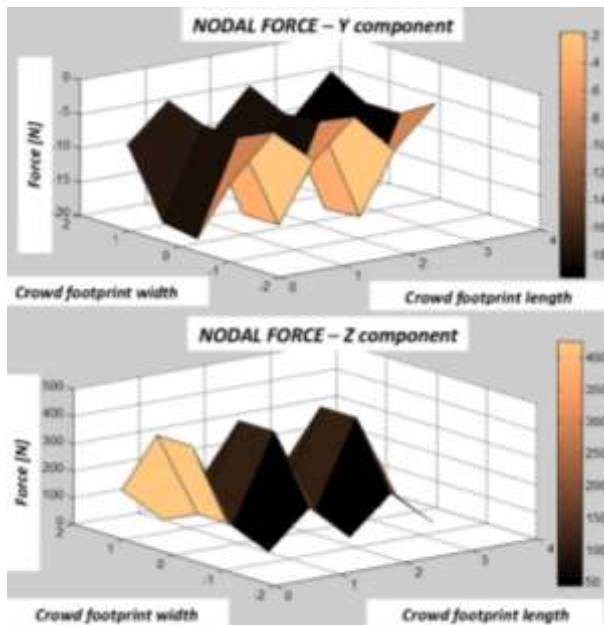


Figure 4.3.8. Step 2 – simulated force files by the proposed CLM model.

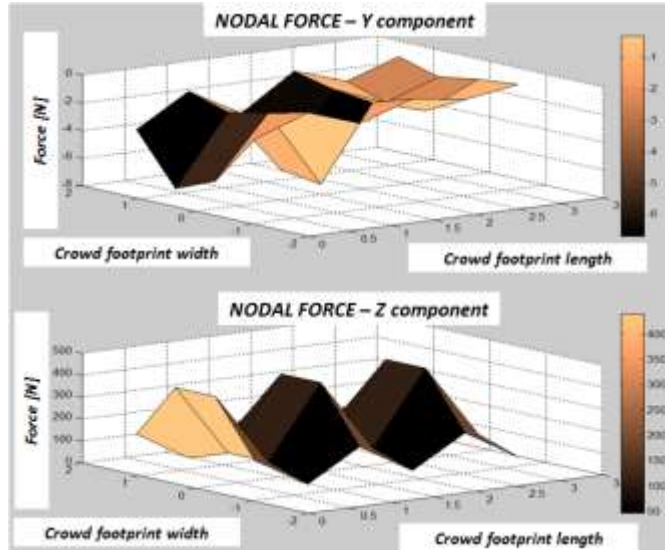


Figure 4.3.9. Step 3 – simulated force files by the proposed CLM model.

Once obtained the above field of forces, in order to evaluate the performance of the proposed CLM model, a dynamic transient analysis is performed based on the numerical model of the footbridge developed in section 3.3. The obtained forces have been implemented as nodal forces within the FEM (Figure 4.3.10), acting along both Y and Z axes in accordance with the CLM model.

Once performed the dynamic transient analysis the nodal accelerations are extrapolated from the results and analyzed following the Short Time Fast Fourier (STFFT) algorithm (see *Appendix D*). In particular the numerical accelerations of the node of the FE model corresponding to the position along the deck of the accelerometer labelled as WSa2 (see Figure 3.1.3) are used.

In Figure 4.3.11 and Figure 4.3.12 the comparisons between the results acquired in situ and the ones obtained from the numerical simulation along Y and Z axes are presented respectively.

It is worth underlining that, for the purpose of this section, the data acquired in situ along Z axis, have been firstly filtered.

More details about the set of data used for the comparison is reported in *Appendix D*.

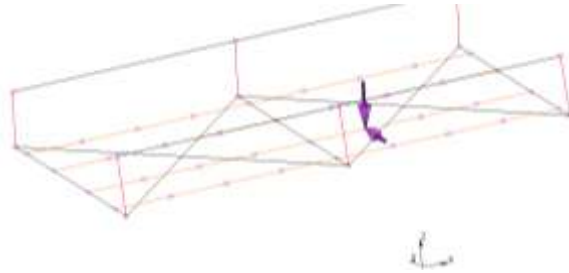


Figure 4.3.10. Example of the simulated forces implemented in MARC Mentat2010.

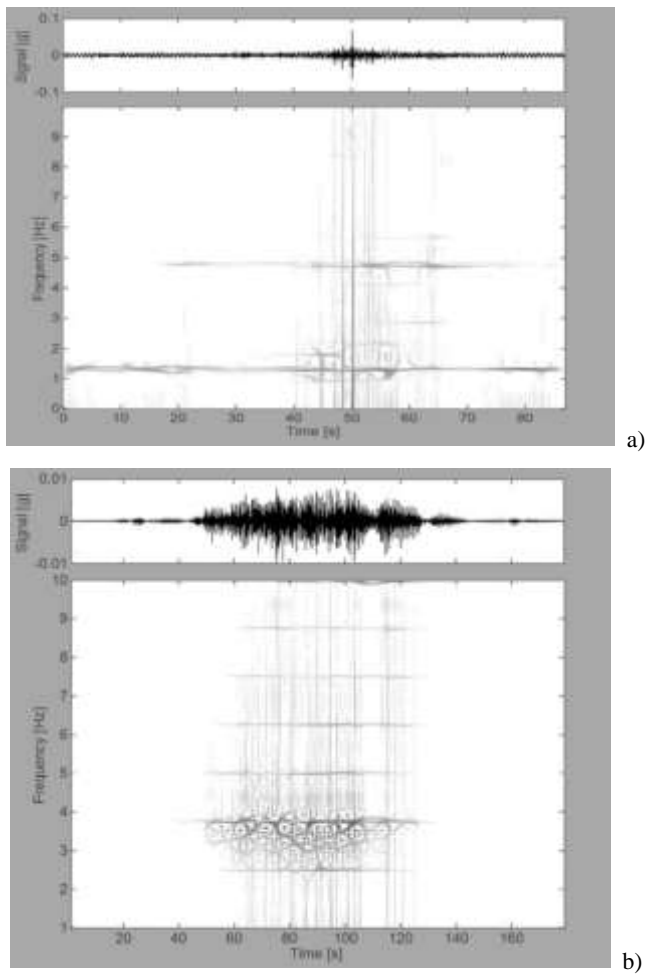


Figure 4.3.11. Time-frequency plots from the data taken by sensor WSa2 along axis Y (transversal).
a) data acquired in situ; b) data from the numerical simulation.

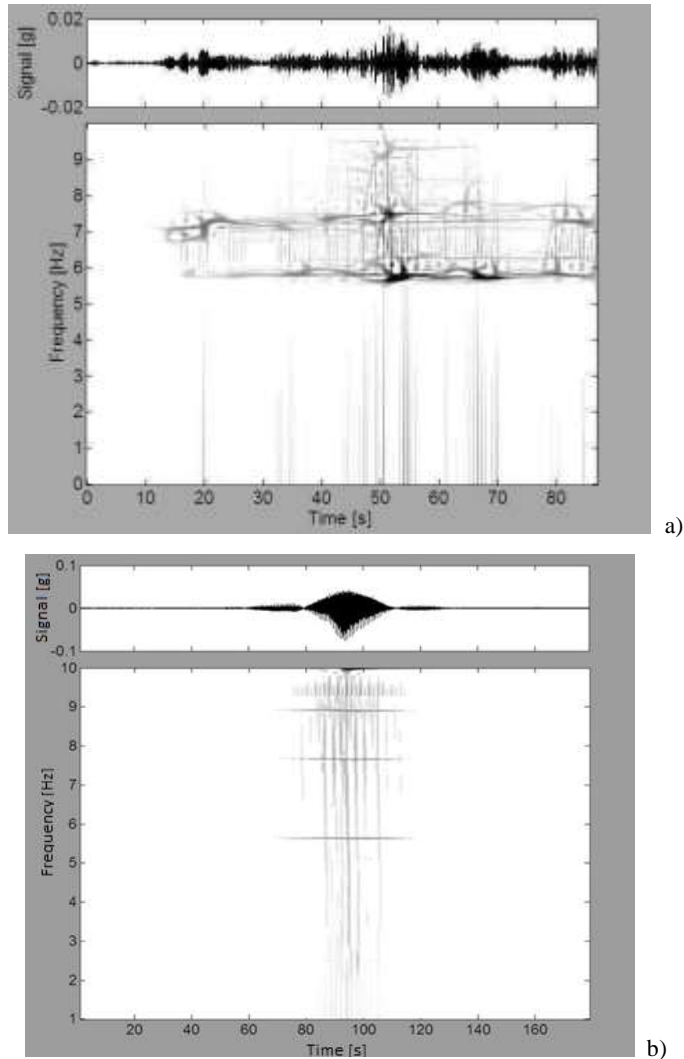


Figure 4.3.12. Time-frequency plots from the data taken by sensor WSa2 along axis Z (gravity)
 a) data acquired in situ and filtered at 2.50 Hz; b) data from the numerical simulation.

The analysis of the results shows as the proposed CLM model is able to capture the main features of the interaction between the pedestrians and the bridge in terms of both range of frequencies and time activation of a particular frequency. About this aspect has to be stressed as the assumption of the velocity of the pedestrian during the simulation about half of that one recorded during the test on field (in order to get equivalence between the simulated footstep and the node of the mesh), “moves” the response of the

model in terms of time activation of the frequencies. By the way this suggests to improve the model in such a way to better represent a more detailed distribution of the pedestrians velocity during the crossing.

The proposed model seems to represent the observed records in a proper manner. Anyway further studies and experimental campaigns are needed to confirm and to improve the proposed CLM model.

4.4 References

- [1] Pisano A., 2001. Modellazione aleatoria delle azioni statiche e delle sollecitazioni, in: Muscolino Giuseppe, *Dinamica delle Strutture*, McGraw Hill, Milano (ITA), pp. 235-242 [In Italian].
- [2] Di Paola M., Pisano A., 2001. Digital Simulation using stochastic differential calculus, International Conference On Monte Carlo Simulation, Monte Carlo, 18-21 Giugno, Monte Carlo Simulation, Shueller&Spanos, pp. 167-174.
- [3] Bortoluzzi, D., Casciati, S., Elia, L., Faravelli, L. 2013. Semi-Active Control for the Mitigation of the Vibration on a Footbridge. On the Proceeding of XXI Congresso dell'Associazione Italiana di Meccanica Teorica ed Applicata – AIMETA2013 – Torino , Italy, September, 17-20, 2013.
- [4] Solari G. et al., 2006. Monte Carlo simulation of wind velocity fields on complex structures, *Journal of Wind Engineering and Industrial Aerodynamics* 94, 323–339.
- [5] Shinozuka M. and Jan, C.-M. 1972. Digital simulation of random processes and its applications, *Journal of Sound and Vibration*, vol. 25, no. 1, pp. 111–128.
- [6] Deodatis, G. 1996. Simulation of ergodic multivariate stochastic processes, *Journal of Engineering Mechanics*, vol. 122, no. 8, pp. 778–787.
- [7] Solari G. and Piccardo, G., 2001. Probabilistic 3-D turbulence modeling for gust buffeting of structures, *Probabilistic Engineering Mechanics*, vol. 16, no. 1, pp. 73–86.
- [8] www.stadtentwicklung.berlin.de
- [9] Ubertini F. et al., 2010. Computer Simulation of Stochastic Wind Velocity Fields for Structural Response Analysis: Comparisons and Applications, Hindawi Publishing Corporation *Advances in Civil Engineering*, Article ID 749578.

- [10] G. Solari, G. Piccardo, 2001. Probabilistic 3D turbulence modeling for gust buffeting of structures, *Prob. Eng. Mech.* (16) pp. 73–86.
- [11] Guidelines for the design of footbridges. *Fib bulletin* 32, November 2005.
- [12] Heinemeyer, C., Butz, C., Keil, A., Mark, S., Goldack, A., Trometer, S., Lukić, M., Chabrolin, B., Lemaire, A., Martin, P., Cunha, Á., Caetano, E., 2009. *Design of Lightweight Footbridges for Human Induced Vibrations*. Background document in support to the implementation, harmonization and further development of the Eurocodes, JRC European Commission, Luxembourg.
- [13] Živanović, S. et al., 2005. Vibration serviceability of footbridges under human induced excitation: a literature review. *Journal of Sound and Vibration* 279, pp. 1-79.
- [14] *Footbridges: assessment of vibrational behaviour of footbridges under pedestrian loading - Technical guide, 2006 – Sétra-AFGC.*
- [15] www.mathworks.it
- [16] NTC 2008. *Norme tecniche per le costruzioni (in Italian) - D.M. 14 Gennaio 2008.*

Chapter 5 Model order reduction (MOR)

Numerical simulations are nowadays in almost all fields of the sciences an important tool to predict the behaviour of the process under study by-passing the direct experimentation on large scale (i.e. laboratory test, field campaign, and so forth...) which are usually quite expensive.

Accurate simulations imply that the errors of the virtual models be small, and that different aspects of the process taken into account.

Although the calculation power is greatly improved over the last decades, in the field of structural engineering, many time one needs to work with dynamic models that may contain a large number of equations. This makes the analysis heavy in terms of calculation time. For this reason one needs to simplify these models in order to achieve lighter models of analysis, by preserving a good approximation of the final results. This means that if one wants to simplify a given problem it has to be sure to represent all the main features of the original problem in order to avoid losses of important information.

The Model Order Reduction (MOR) is the label by which such a problem is denoted. The fundamental methods in the area of Model Order Reduction were published in the eighties and nineties of the last century. In 1981 Moore [1] published the method of Truncated Balanced Realization, in 1984 Glover published his famous paper on the Hankel-norm reduction [2], that are still nowadays the “foundations” of this method. More details will be given in the followings, but in Figure 5.1 the working concept of MOR is introduced in a graphical manner. From this figure it is easy-to-understand how sometimes very little information is required to describe a model. This simple example shown as, even with only a few facets, the rabbit on the right can still be recognized as such.

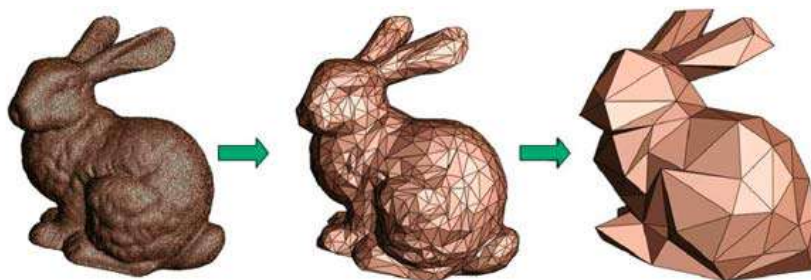


Figure 5.1. MOR: graphical representation [4].

Within the MOR techniques, current research studies are focused on the possibility to “capture” lower order models for nonlinear systems (see [3] among others). Nevertheless, also the correct application of MOR when dealing with linear systems still requires attentions and this is the topic of this chapter.

The MOR technique based on balanced transformation is first described from the mathematical point of view and then applied to the case study. It is worth noting there is no attempt to give a literature “review” in the field of MOR, but one just introduces the applied procedure.

5.1 MOR background

Up to 10-15 years ago, MOR techniques [4], were strictly required in order to solve, due to the low computation hardware capability available, large-size dynamic structural problems. Today the MOR strategy offers a tool that include both low computational costs, and a viable methodology toward the implementation of real time control systems useful for the solution of problems where several repeated analyses must be carried out (i.e. optimization and/or reliability problems [5]).

Within the field of structural engineering, the adopted mathematical models have the classical partial differential equations form, whose spatial derivatives are easily removed, by a finite element process. For a standard dynamic system the problem is therefore rearranged in terms of ordinary differential equations¹⁴ where the second derivative with respect to time appears. In order to introduce the MOR technique for a linear dynamic system, one re-formulates the problem in the **state space**:

¹⁴ The number of equations represents the order of the model, say N .

$$\frac{d\mathbf{x}(t)}{dt} = \mathbf{A}\mathbf{x}(t) + \mathbf{B}\mathbf{u}(t) \quad (5.1)$$

$$\mathbf{y}(t) = \mathbf{C}\mathbf{x}(t) + \mathbf{D}\mathbf{u}(t) \quad (5.2)$$

where \mathbf{u} is the input vector, related so to an external excitations (size p), \mathbf{x} is the vector state variables¹⁵ of size n and \mathbf{y} the response vector of size q . Moreover \mathbf{A} is a square matrix of size n by n , \mathbf{B} a matrix of size n by p , \mathbf{C} a matrix of size q by n and \mathbf{D} a matrix of size q by p .

Assuming now that the response of the system depends only on the state of the system, it is possible to neglect the matrix \mathbf{D} . Introducing the transformation $\mathbf{z}(t) = \mathbf{T}\mathbf{x}(t) | \mathbf{T} \in \mathbb{R}^{q \times n}$ where \mathbf{T} is an invertible matrix but not necessarily the unit matrix, and taking into mind once said above, one has¹⁶:

$$\dot{\mathbf{z}} = \mathbf{T}\mathbf{A}\mathbf{T}^{-1}\mathbf{z} + \mathbf{T}\mathbf{B}\mathbf{u} \quad (5.3)$$

$$\mathbf{y} = \mathbf{C}\mathbf{T}^{-1}\mathbf{z} \quad (5.4)$$

where, as usual, the superposed dot denotes time derivative.

The following steps regard the concepts of **reachability** and **controllability**.

A given system is completely reachable if it is possible to determine an *ad hoc* input signal able to lead, within a finite time interval, the system from the zero state to a predefined state. In other words the reachability represents the measure in which the state of the system can be manipulated by the input $\mathbf{u}(t)$. This concept regards only the state equations [6], so the matrix \mathbf{C} and \mathbf{D} can be neglected. From a mathematical point of view one introduces the matrix of reachability \mathbf{Q}_R as:

$$\mathbf{Q}_R = \left[\mathbf{B} \quad \mathbf{A}\mathbf{B} \quad \mathbf{A}^2\mathbf{B} \dots \mathbf{A}^{n-1}\mathbf{B} \right]^T. \quad (5.5)$$

The system is defined as fully reachable if $\text{rank}(\mathbf{Q}_R) = n$.

In a similar way a given system is controllable if for each possible initial state of the system is possible to introduce an *ad hoc* input signal leads the system to the zero state in a finite time interval.

¹⁵ The state variables are not supposed to have any physical meaning; they have only mathematical quantities.

¹⁶ The dependence over the time is suppressed for sake of simplification.

The matrix of **observability** of the system can be defined as:

$$\mathbf{Q}_o = \begin{bmatrix} \mathbf{C} & \mathbf{C}\mathbf{A} & \mathbf{C}\mathbf{A}^2 & \dots & \mathbf{C}\mathbf{A}^{n-1} \end{bmatrix}^T. \quad (5.6)$$

The system is then defined as fully observable if $\text{rank}(\mathbf{Q}_o) = n$.

The next step is to introduce the concept of **Gramian** [4]. The Gramians are matrices that contain information about the proprieties of the system, let it to be \mathbf{W} :

$$\mathbf{W} = \int_{t_1}^{t_2} \mathbf{G}(\tau) \mathbf{G}^T(\tau) d\tau. \quad (5.7)$$

In the matrix $\mathbf{G}(\tau)$ the columns represent each single response signal due to the generic input signal. It is possible to demonstrate that the above matrix \mathbf{W} is positive semi-definite with eigenvalues $\lambda_1^2 \geq \lambda_2^2 \geq \dots \geq \lambda_n^2 \geq 0$ and the corresponding eigenvectors v_1, v_2, \dots, v_n mutually orthogonal forming a base of orthonormal vectors. Following [1] it is possible to re-write the matrix of the generic Gramian as:

$$\mathbf{W} = \int_{t_1}^{t_2} \mathbf{G}(\tau) \mathbf{G}^T(\tau) d\tau = \mathbf{V} \mathbf{\Lambda}^2 \mathbf{V}^T, \quad (5.8)$$

where $\mathbf{V} = (v_1, v_2, \dots, v_n)$ is the matrix of eigenvectors, and $\mathbf{\Lambda}$ the diagonal matrix.

Then introduces the following quantities [1]:

$$\mathbf{W}_c = \int_0^{\infty} \mathbf{e}^{\tau \mathbf{A}} \mathbf{B} \mathbf{B}^T \mathbf{e}^{\tau \mathbf{A}^T} d\tau, \quad (5.9)$$

$$\mathbf{W}_o = \int_0^{\infty} \mathbf{e}^{\tau \mathbf{A}} \mathbf{C} \mathbf{C}^T \mathbf{e}^{\tau \mathbf{A}^T} d\tau, \quad (5.10)$$

respectively the Gramian matrix of controllability and observability. These matrices satisfy the air of Lyapunov equations [6]-[10]:

$$\mathbf{A} \mathbf{W}_c + \mathbf{W}_c \mathbf{A}^T + \mathbf{B} \mathbf{B}^T = 0, \quad (5.11)$$

$$\mathbf{A}^T \mathbf{W}_o + \mathbf{A} \mathbf{W}_o + \mathbf{C}^T \mathbf{C} = 0. \quad (5.12)$$

Finally the balanced transformation to perform the reduction is achieved by:

1. solving the Lyapunov equations (5.11) and (5.12) find the Gramian matrices of controllability (5.9) and observability (5.10);
2. perform the Cholesky factorizations of the Gramian matrices:

$$\begin{cases} \mathbf{W}_C = \mathbf{L}_C \mathbf{L}_C^T \\ \mathbf{W}_O = \mathbf{L}_O \mathbf{L}_O^T \end{cases} \quad (5.13)$$

3. evaluate the Singular Values Decomposition (SVD) of the Cholesky factors:

$$\mathbf{L}_O^T \mathbf{L}_C = \mathbf{U} \mathbf{\Lambda} \mathbf{V}^T \quad (5.14)$$

where \mathbf{U} is the matrix of the eigenvectors of the matrix in the r.h.s., say \mathbf{Q} , by its transpose, \mathbf{V} is the matrix of the eigenvectors of $\mathbf{Q}^T \mathbf{Q}$ and $\mathbf{\Lambda}$ is the diagonal matrix of the singular values.

4. introduce the balanced transformation [6]:

$$\begin{aligned} \mathbf{T} &= \mathbf{L}_C \mathbf{V} \mathbf{\Lambda}^{-1/2} \\ \mathbf{T}^{-1} &= \mathbf{\Lambda}^{-1/2} \mathbf{U}^T \mathbf{L}_O^T \end{aligned} \quad (5.15)$$

such that $\mathbf{T}^{-1} \mathbf{W}_C \mathbf{T}^{-T} = \mathbf{T}^T \mathbf{W}_O \mathbf{T} = \mathbf{\Lambda}$. Evaluate the space of the balanced matrix as:

$$\begin{aligned} \mathbf{A}_b &= \mathbf{T}^{-1} \mathbf{A} \mathbf{T} = \mathbf{\Lambda}^{-1/2} \mathbf{U}^T \mathbf{L}_O^T \mathbf{A} \mathbf{L}_C \mathbf{V} \mathbf{\Lambda}^{-1/2} \\ \mathbf{B}_b &= \mathbf{T}^{-1} \mathbf{B} = \mathbf{\Lambda}^{-1/2} \mathbf{U}^T \mathbf{L}_O^T \mathbf{B} \\ \mathbf{C}_b &= \mathbf{C} \mathbf{T} = \mathbf{C} \mathbf{L}_C \mathbf{V} \mathbf{\Lambda}^{-1/2} \end{aligned} \quad (5.16)$$

To operate a model reduction the Hankel singular values are then introduced.

A given system is considered as fully balanced within the time interval $[0, T]$ if:

$$\mathbf{W}_C = \mathbf{W}_O = \mathbf{\Lambda}^2, \quad (5.17)$$

where:

$$\mathbf{W}_C = \mathbf{W}_O = \mathbf{\Lambda}^2 = \begin{bmatrix} h_1 & 0 & \cdots & 0 \\ 0 & h_2 & \cdots & \vdots \\ \vdots & \vdots & \ddots & 0 \\ 0 & \cdots & 0 & h_n \end{bmatrix}, \quad (5.18)$$

is a diagonal matrix in which $h_1 \geq h_2 \geq \dots \geq h_n \geq 0$ are the Hankel's singular values. Following [7]-[9] these values can be evaluated by:

$$h_i = \sqrt{\lambda_i (W_c W_o)}. \tag{5.19}$$

Concluding and generalizing the problem, let's consider a generic balanced model described by the matrices A_b , B_b , C_b and D_b with the corresponding Hankel's singular values sorted in descending order. Choose an appropriate truncation r such that h_r is strictly greater than h_{r+1} and define the state vector $x = \{x_1, x_2\}$ where x_1 corresponds to the first r component, while x_2 the remaining $n-r$ components.

A visual representation of the above MOR technique is given in Figure 5.1.1 [11].

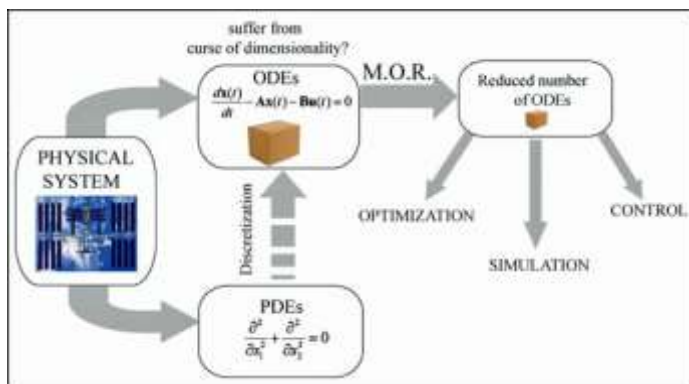


Figure 5.1.1. MOR: visual representation [11].

The concept behind this reduction technique is that the singular values of the corresponding Hankel matrix tend to the second order modes λ_i . Because the number of non-zero singular values of the Hankel matrix determines the order of the system, the reduction consists in neglecting the λ_{k+1} smaller than a fixed value λ_k ; This operation is called truncation.

The balance of the system, instead, is the core of the optimization for the order reduction because the reduced model must retain the properties of controllability and observability. Thanks to the balancing the values are arranged in descending order that give a measure of the controllability and observability of the model. Once balanced, one can proceed with the truncation of the states size in order to exclude the smallest Hankel's singular values to achieve the approximate lower model order.

This truncation technique is called *balanced truncation* and consists in the reduction of the model for elimination of the system's vibration modes less significant. By neglecting the smallest Hankel's values, in other words, one deletes the states that, with difficulty, will be reached and observed by the system.

If are pushed too much the reductions, or if one decides to ignore a large number of λ , there is the risk of losing important information about the model (i.e. the structure under study) analyzed. The result is that the response of the system does not correspond to the results calculated by an exact solution of the model. For this reason it is important make a right decision about the appropriate value of λ from where to truncate the model without compromising the goodness of the final results.

5.2 Structural response

In this section the procedure described in the previous section is applied to the "Trasaghis" footbridge. In order to apply the MOR to the case study a "lighter" numerical model compared with the "full" one described in section 3.2.2, is developed within the MARC Mentat2010 environment [12]. Only *beam* elements are employed as reported in Figure 5.2.1. Also for this model great care is taken for the implementation of the so called non-structural mass as described in section 3.2.2 (e.g. larch cladding, handrail and so forth...) and for the kinematic boundary condition in order to achieve the best representation.

The new model is characterized by 301 beam elements and 208 nodes, and it is able to represent, for the dynamic point of view, the full FEM. A dynamic modal comparison between the "full" and the "light" FEM of the "Trasaghis" footbridge is reported from Figure 5.2.2 to Figure 5.2.6. Some discrepancies appear in terms of frequencies as reported in Table 5.2.1. They could have been reduced by a suitable refinement but this is out from the exemplification nature of the computational reported.

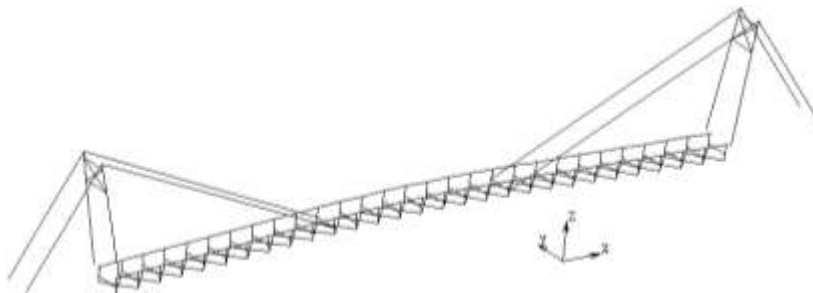


Figure 5.2.1. "Light" FEM implemented in MARC Mentat2010 environment.

Table 5.2.1. Frequencies percentage error. Comparison between “light” and “full” FEM.

ID	$\varepsilon = \left \frac{f_{full} - f_{light}}{f_{light}} \right \times 100$
mode I	13.1 %
mode II	5.7 %
mode III	22.4 %
mode IV	33.9 %
mode V	13.0 %

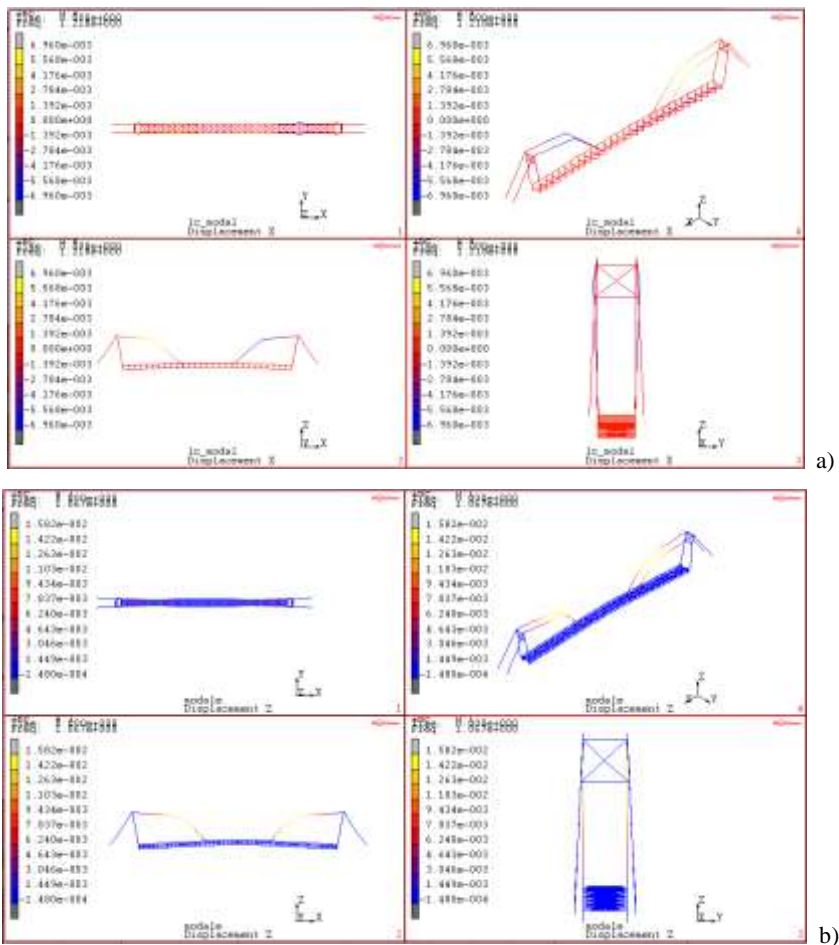


Figure 5.2.2. Dynamic modal comparison of the “Trasaghis” footbridge FEM: mode I. a) “Light” FEM $f = 1.22$ Hz; b) “Full” FEM $f = 1.06$ Hz.

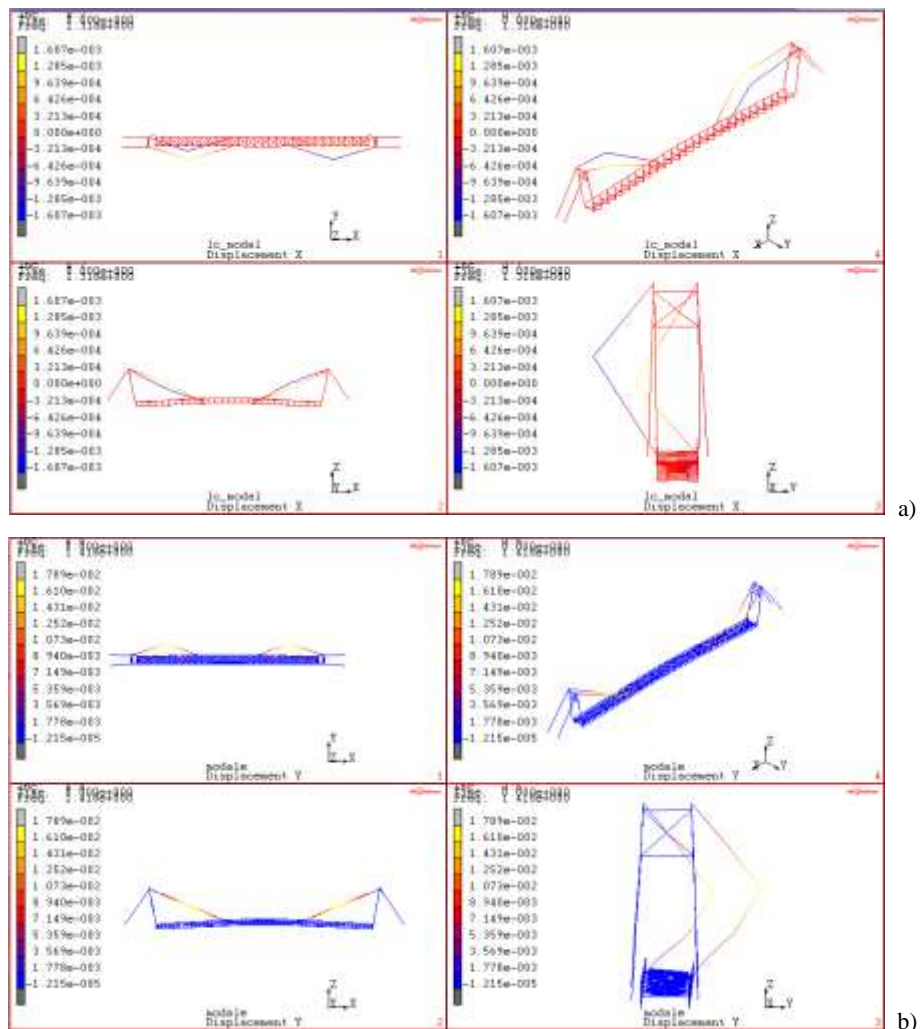


Figure 5.2.3. Dynamic modal comparison of the “Trasaghis” footbridge FEM: mode II. a) “Light” FEM $f = 1.32$ Hz; b) “Full” FEM $f = 1.41$ Hz.

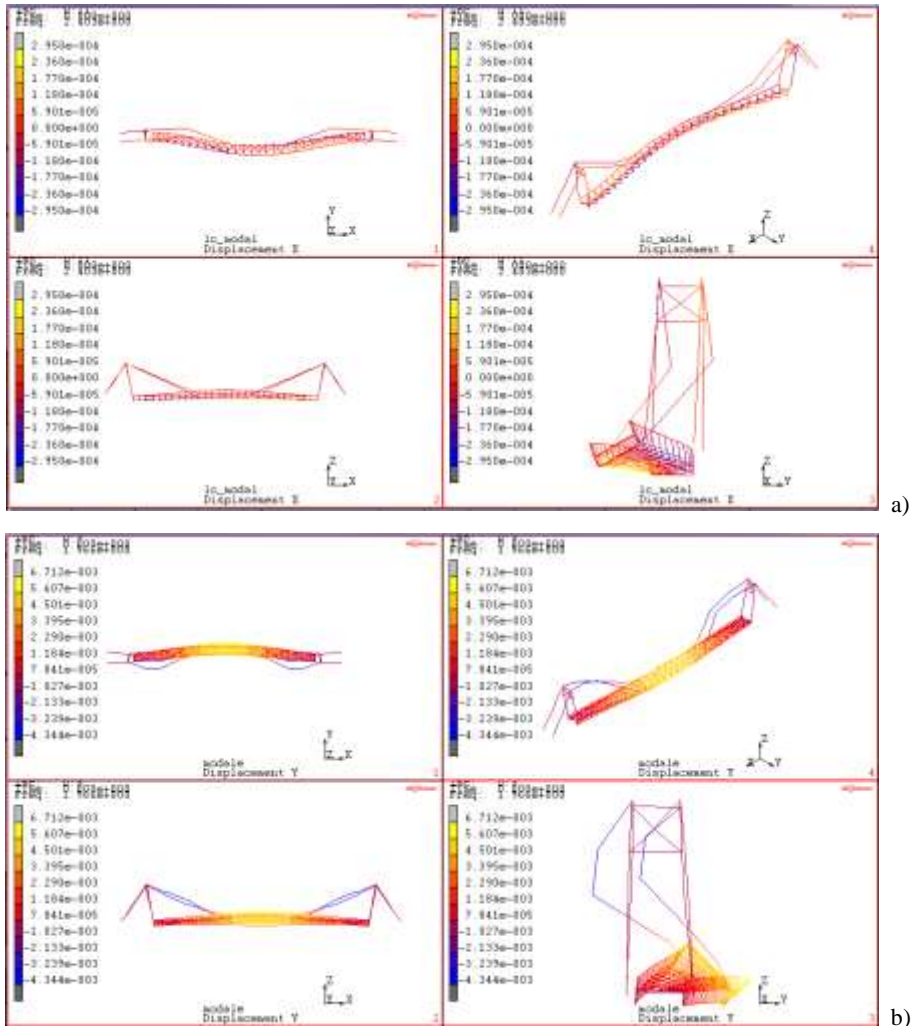


Figure 5.2.4. Dynamic modal comparison of the “Trasaghis” footbridge FEM: mode III. a) “Light” FEM $f = 2.40$ Hz; b) “Full” FEM $f = 1.96$ Hz.

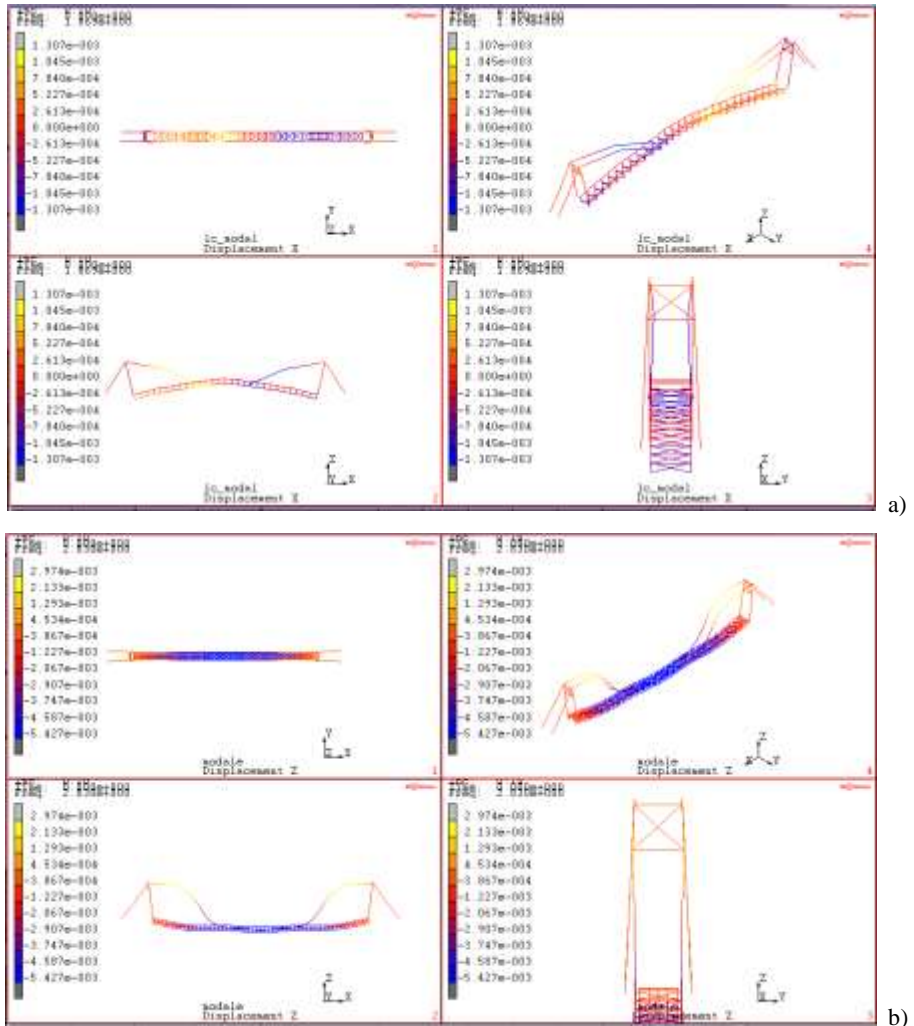


Figure 5.2.5. Dynamic modal comparison of the “Trasaghis” footbridge FEM: mode IV. a) “Light” FEM $f = 1.87$ Hz; b) “Full” FEM $f = 2.83$ Hz.

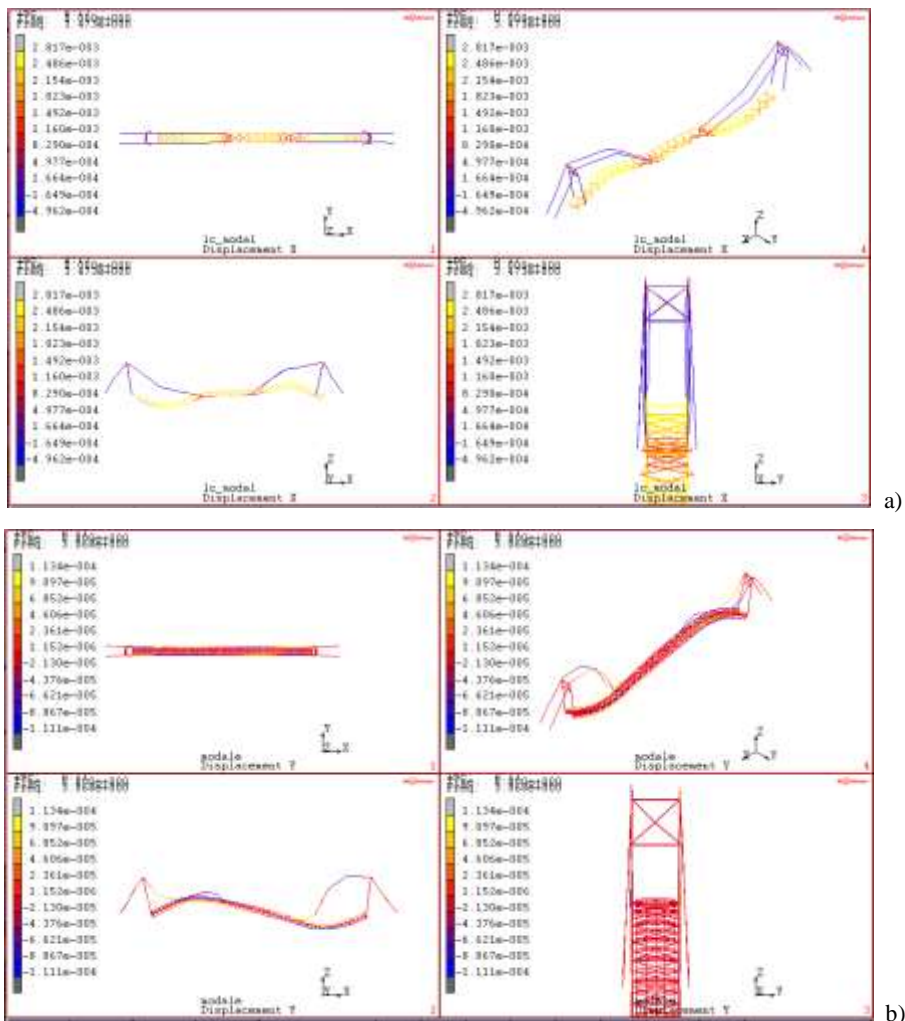


Figure 5.2.6. Dynamic modal comparison of the “Trasaghis” footbridge FEM: mode V. a) “Light” FEM $f = 3.47$ Hz; b) “Full” FEM $f = 3.07$ Hz.

Once defined the “light” FEM, a *Model Order Reduction* (MOR) methodology is applied and developed within MatLAB environment [13]. In particular three stable sets of modes are identified of size *145 states*, *114 states* and *84 states*, respectively, as shown in Figure 5.2.7 [14].

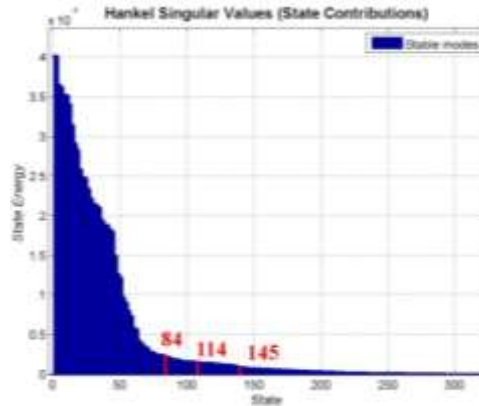


Figure 5.2.7. Hankel Singular Values – State Contributions.

To test the MOR method a dynamic transient analysis under wind loads is performed [15]. Following the simulation procedure proposed in section 4.1 one has to introduce the nodes of interest along the footbridge profile. With reference to the “light” FE Model of the “Trasaghis” footbridge 11 nodes are selected as shown in the simulation grid here below. In particular five nodes are equally spaced along the deck, while the remaining six nodes are located two at the top of the pillars and four along the oblique steel stays (Figure 5.2.8). The others parameters necessary to perform the simulation are:

- shear velocity of the wind: $u^* = 7$ m/s;
- Von Karman constant: $k = 0.41$;
- roughness length: $z_0 = 0.30$ m according to [16];
- time step: $\Delta t = 0.01$ sec to achieve a good compromise between accuracy and required computational effort. The total duration of the simulated time history is assigned to be 60 sec, of which 30 sec are related to the “wind action” while the remaining 30 sec are related to the “structural rest” to capture the bridge response once the wind stops.

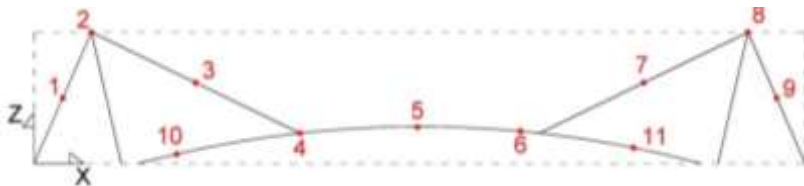


Figure 5.2.8. Gird of nodes for the “light” numerical model of the “Trasaghis” footbridge.

It is worth underlining that in this particular case only the fluctuating part of the wind velocity is considered. Once simulated the wind velocity field, the related force field is evaluated by the Bernoulli's formula. After that these forces are then implemented within the numerical model. As an example in Figure 5.2.9 and Figure 5.2.10 are represented respectively the time histories of the wind velocity and the related wind forces for the node of the grid located in the middle of the span (*node 5*).

Then a dynamic transient analysis is performed: total analysis time 60 sec – time step = 0.01 sec – total steps = 6000; i.e. twice the duration of the wind velocity time history as observed above.

The dynamic response of the numerical model in terms of displacements and accelerations of the node located in the middle of the steel stay (*node 3*) is plotted in Figure 5.2.11 and Figure 5.2.12.

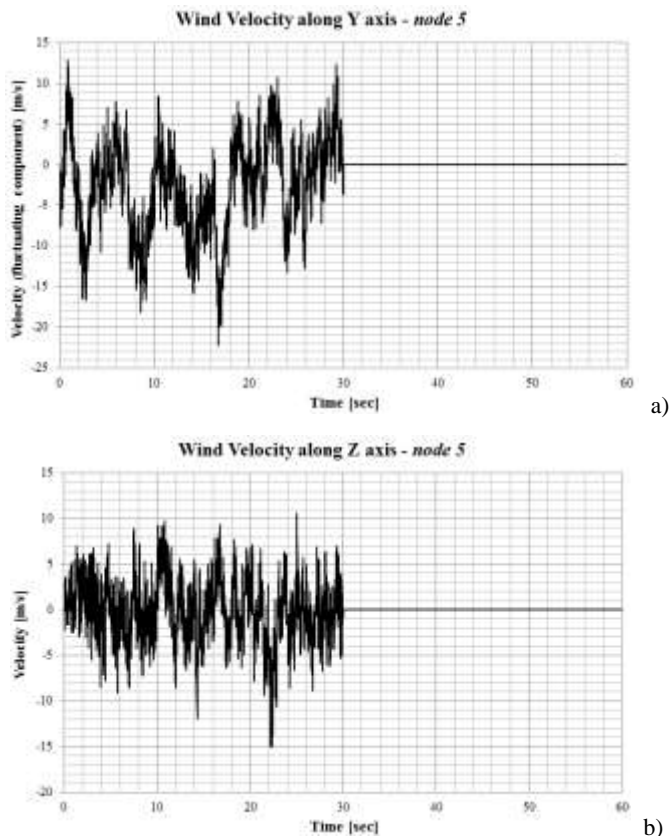


Figure 5.2.9. Fluctuating part of the simulated wind velocity for the *node 5*. a) Y component; b) Z component.

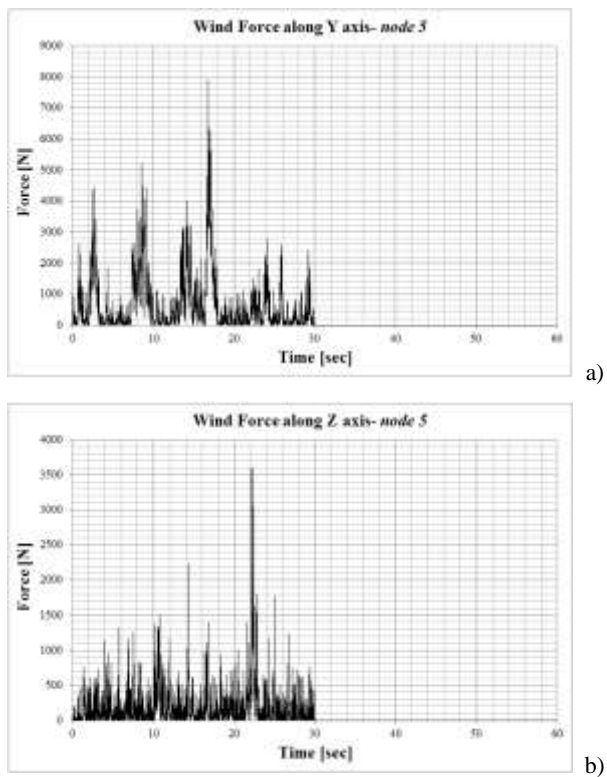


Figure 5.2.10. Wind forces for the *node 5*. a) Y component; b) Z component.

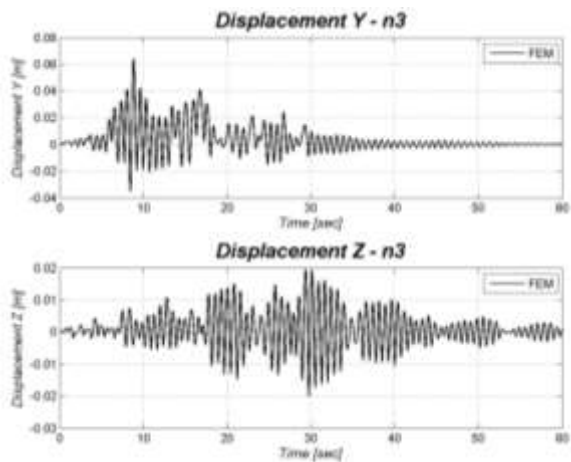


Figure 5.2.11. Dynamic response of the “light” FEM under the simulated wind loads – node 3. Displacement along Y and Z axes.

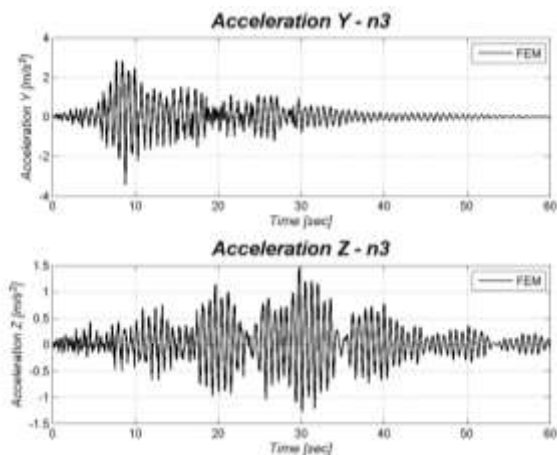


Figure 5.2.12. Dynamic response of the “light” FEM under the simulated wind loads – node 3. Accelerations along Y and Z axes.

5.3 MOR accuracy

The MOR method allows one to obtain a lighter model in terms of computational costs, compared with FEM, but able to catch all the main features in the dynamic response of the pedestrian bridge.

The advantage in terms of “time consuming” of the MOR technique for the analysis carried out as described in the previous section, are summarized in Table 5.3.1. It is worth underlining that all the calculations are performed with a *AMD A4-4355m Processor – RAM 4.00 Gb*.

Table 5.3.1. Time consuming

<i>Model</i>	<i>Time Consuming</i>	<i>Code</i>
FE Model	660.00 sec	MARC Mentat2010
LIGHTER model	about 4 days	MATLab
MOR 145 states	672.65 sec	MATLab
MOR 114 states	287.15 sec	MATLab
MOR 84 states	274.14 sec	MATLab

To verify the accuracy of the above procedure, a comparison in terms of the time histories of the displacements obtained by the “light” FEM and the ones from the three

obtained MOR models are presented here below. In particular, without loss of generality, the results are presented in terms of Y (transversal) and Z (vertical-gravity) axe displacement of the *node 5* (Figure 5.3.2 and Figure 5.3.2).

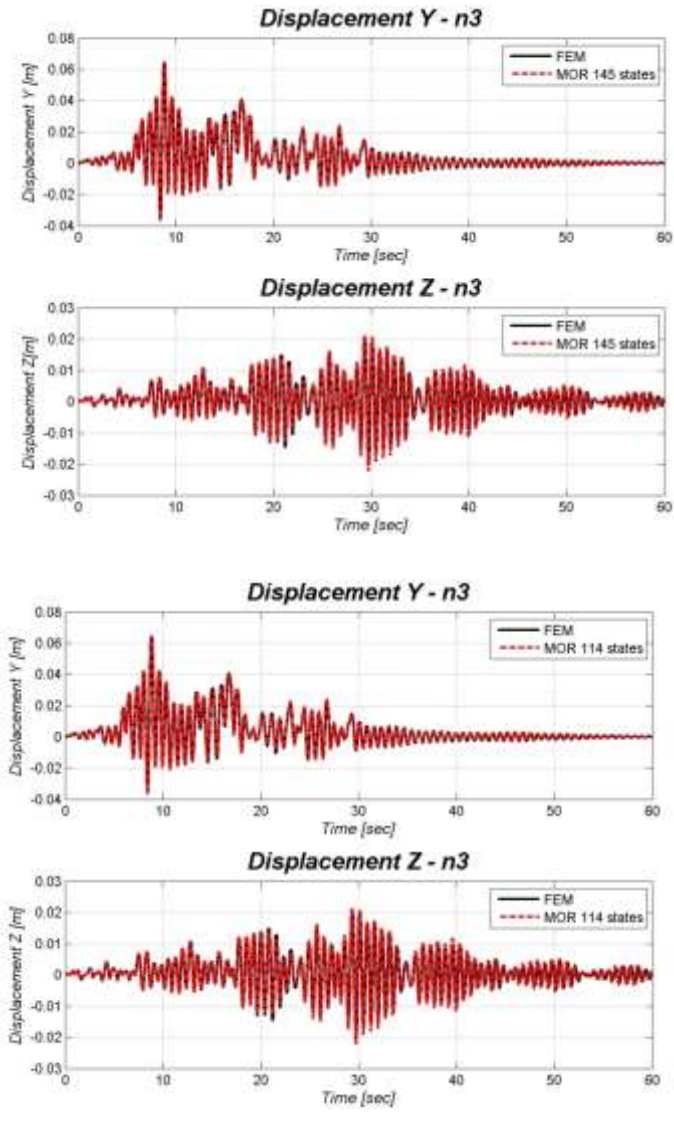


Figure 5.3.1. Comparison among “light” FEM and the implemented MOR models in terms of displacements along Y and Z axes – *node 3*. a) MOR 145 states; b) MOR 114 states.

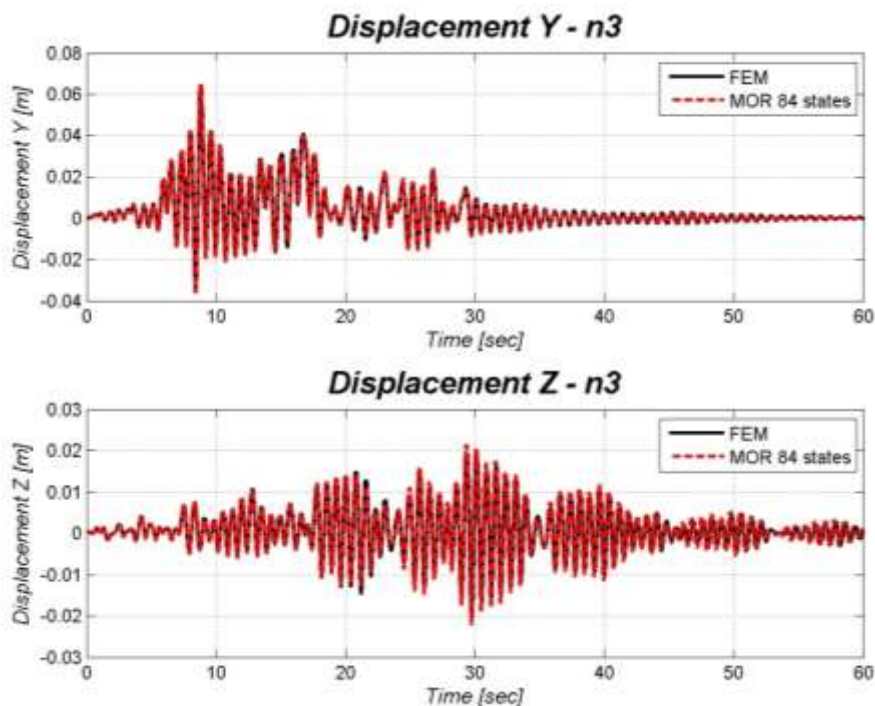


Figure 5.3.2. Comparison among “light” FEM and the implemented MOR models in terms of displacements along Y and Z axes – node 3 - MOR 84 states.

As one can observe from the above plot, the response labelled as “MOR 145 states” well fits with the response achieved by the full FE Model of the footbridge. Moving to schemes including a lower value of states (i.e. MOR 114 and 84 states) some small discrepancies appear, even if compensated by a significant decrease of the calculation time.

5.4 References

- [1] Bruce Moore 1981. Principal Component Analysis in Linear Systems: Controllability, Observability, and Model Reduction. IEEE Transactions on Automatic Control, AC-26(1).

- [2] Glover, K. 1984. All optimal Hankel-norm approximations of linear multivariable systems and their ∞ -error bounds. *Int. J. Control*, 39, pp. 1115–1193.
- [3] Calberg K., Bou Mosleh C., Farhat C. 2011. Efficient non-linear model reduction via a least squares Petrov-Galerkin projection and compressive tensor approximations, *International Journal for numerical methods in engineering*, 86, pp.155-181.
- [4] Schilders W.H.A., van der Vorst H.A., Rommes J. 2008. *Model Order Reduction : Theory, Research Aspects and Applications*, Springer.
- [5] F. Casciati , S. Casciati, L. Faravelli, M. Franchinotti 2012. *Model Order Reduction vs. Structural Monitoring. On the Proceeding of 6th European Workshop on Structural Health Monitoring – EWSHM2012 – Dresden, Germany, July 3-6, 2012.*
- [6] Athanasios C. 2005. *Approximation of large-scale dynamical systems*, Society for Industrial and Applied Mathematics, Philadelphia.
- [7] A.C. Antoulas, 2002. *Lectures on the approximation of large-scale dynamical systems*, Society for Industrial and Applied Mathematics, Philadelphia.
- [8] Antoulas A.C., 2002. *Frequency Domain Representation and Singular Value Decomposition*. Tech. Report, <http://www.ece.rice.edu/~aca/>
- [9] Antoulas A.C., Sorensen D.C. , Zhou Y., 2002. *On the decay rate of Hankel singular values and related issues*. Tech. Report, <http://www.ece.rice.edu/~aca/>
- [10] Antoulas A.C., Sorensen D.C. e Gugercin S., 2001. *A survey of the model reduction methods for large-scale systems*, *Contemporary Mathematics*, vol. 280, pp. 193-219.
- [11] www.elitenetzwerk.beyern.de
- [12] www.mscsoftware.com
- [13] www.mathworks.it
- [14] Casciati S., Faravelli L., 2014. *Quantity vs. Quality in the Model Order Reduction (MOR) of a Linear System* , *Smart Structures and Systems*, 13 (1).
- [15] Bortoluzzi, D., Casciati, F., Faravelli, L. 2014. *Vibration mitigation in a “cable-stayed-like” timber footbridge. On the Proceeding of the 6th World*

Conference on Structural Control and Monitoring - 6WCSCM, Barcellona, Spain, 15-17 July, 2014.

- [16] NTC 2008. Norme tecniche per le costruzioni (in Italian) - D.M. 14 Gennaio 2008.

Chapter 6 Control solutions

Vibration control is a branch of the structural mechanic that study the possibility of mitigate the effects of an “external” input acting on a generic structure (i.e. bridges, buildings and so forth...) by using an *ad hoc* set of technical devices [1].

The vibration control devices are classified into three different sets:

- 1) *passive control* devices have no feedback capability between them, structural elements and the ground;
- 2) *active control* devices incorporate real-time recording instrumentation, input processing equipment and actuators within the structure;
- 3) *hybrid control* devices have combined features of active and passive control systems.

The distinction between passive and active control systems [2] is represented in Figure 6.1 and Figure 6.2.

A passive control system (e.g. energy dissipation system or a dynamic vibration absorber) develops motion control forces at the points of attachment of the system (see [3]-[5] among others). The motion of the points at which these devices are hanged produces the power needed to generate the proper control forces; while the relative motion of these points determine the amplitude and direction of the control forces.

An active control system also develops motion control forces; however the magnitude and direction of these forces are determined by a controller based on the information recorded by sensors throughout a control strategy, i.e. a proper algorithm. These forces are supplied by the active control system. In this solution the forces have to be fully powered by an *ad hoc* “external” power source. The related power, depending on the application and on the structure under study, may be large and require a lot of energy supply. In general an active control system should provide for better or more versatile response control.

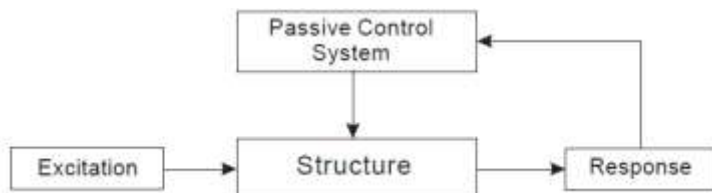


Figure 6.1. Scheme of a Passive Control System [2].

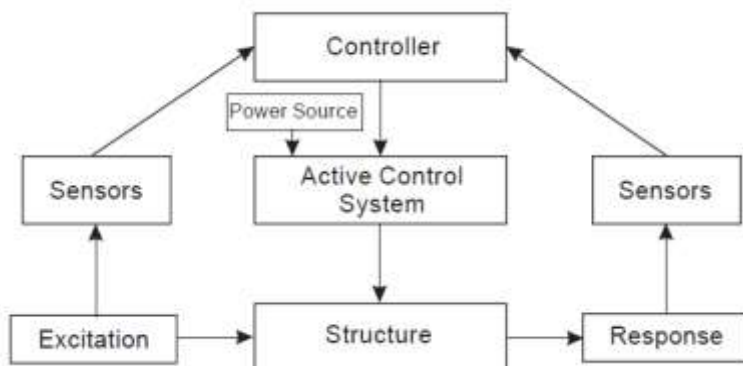


Figure 6.2. Scheme of an Active Control System [2].

Semi-active control systems (see [6] among others) may be deduced starting from a passive control systems which have been modified to allow for adjustment of their mechanical properties [2]. The mechanical properties of semi-active control systems may be adjusted by a controller as for the active control system in Figure 6.2. Nevertheless has to be stressed as in this case the control forces are developed as a result of motion of the structure points at which the semi-active devices (per passive control systems) are attached. Semi-active control systems usually require a low demand of power for the adjustment of the mechanical properties of the system that can be related to the power output of the system.

Different approaches can be used to control a structure in order to smooth the effects of the external actions and to improve the structures' performance. In particular:

- to dissipate the wave energy with properly engineered dampers mounted inside the structure;
- to disperse the wave energy between a wider range of frequencies;
- to absorb the resonant portions of the whole wave frequencies band with the help of so-called mass dampers.

Within the last kind of the above devices one has: the so called TMD (tuned mass dampers – see [4] among others) for the passive control approach, the AMD (active mass dampers) for the active one, and the HMD (hybrid mass dampers) for the hybrid control.

The following control solutions are introduced with reference of the “Trasaghis” footbridge (see section 3.3) for the mitigation of the wind induced vibrations.

6.1 Passive control solutions

The finite element discretization leads one to write the standard dynamics equations in a matrix form (see section 2.1):

$$\mathbf{M}\ddot{\mathbf{x}}(t) + \mathbf{C}\dot{\mathbf{x}}(t) + \mathbf{K}\mathbf{x}(t) = \mathbf{f}(t), \quad (6.1)$$

where, \mathbf{M} , \mathbf{C} and \mathbf{K} are the mass, damping and stiffness matrices respectively, \mathbf{x} are the node generalized displacements, \mathbf{f} are the nodal forces, t denotes the time and a “dot” the time derivative as usual.

The governing relations with tuned mass dampers add forces at given locations [2] as follows:

$$\mathbf{M}\ddot{\mathbf{x}}(t) + \mathbf{C}\dot{\mathbf{x}}(t) + \mathbf{K}\mathbf{x}(t) = \mathbf{f}(t) + \mathbf{T}[\mathbf{c}\dot{\mathbf{z}}(t) + \mathbf{k}\mathbf{z}(t)], \quad (6.2)$$

where \mathbf{T} is a topological matrix while the matrices \mathbf{c} and \mathbf{k} contain, for each TMD, the damping coefficient c and the stiffness k . The variable \mathbf{z} is the relative displacement of the added mass of the single TMD at the anchorage point, so that:

$$m\ddot{\mathbf{z}}(t) + c\dot{\mathbf{z}}(t) + k\mathbf{z}(t) = -m\ddot{\mathbf{x}}(t), \quad (6.3)$$

where m is the added mass and is the displacement of the hanging point in the direction of the TMD degree of freedom z .

The standard design of a single TMD device requires the tuning of the frequency and the added mass, or better the ratio μ between this secondary mass and the primary one, for a 1-DOF system. The damping and stiffness coefficients, c and k in equation (6.3), depend on the ratio μ as reported in [2], [7] and [8]-[11] among others. A first extension to MDOF's primary systems, see [2], was developed for the design of TMD devices in frames with lumped masses at each stories.

Let's consider the case of a N -DOF damped structure. If a single TMD is installed in correspondence to the j -th DOF, the equations of motion can be written as:

$$\mathbf{M}\ddot{\mathbf{x}}(t) + \mathbf{C}\dot{\mathbf{x}}(t) + \mathbf{K}\mathbf{x}(t) = \mathbf{f}(t) + d_j \left[c_j \dot{z}(t) + k_j z(t) \right], \quad (6.4)$$

where δ_j is the standard diagonal matrix of Kronecker indexes. To complete the formulation the above j -th equation have to be coupled with equation (6.3) where all the coefficients come with the index j ; that is:

$$\begin{cases} \mathbf{M}\ddot{\mathbf{x}}(t) + \mathbf{C}\dot{\mathbf{x}}(t) + \mathbf{K}\mathbf{x}(t) = \mathbf{f}(t) + d_j \left[c_j \dot{z}(t) + k_j z(t) \right] \\ m\ddot{z}(t) + c_j \dot{z}(t) + k_j z(t) = -m\ddot{x}(t) \end{cases}. \quad (6.5)$$

If the TMD is to be designed for the i -th structural mode with modal properties M_i , K_i and C_i , the design problem is similar to the design of a TMD device for a 1-DOF structure. Indeed, introducing the modal coordinate $y(t)$, the resulting modal equation can be written as follows:

$$M_i \ddot{y}(t) + C_i \dot{y}(t) + K_i y(t) = \Phi_i^T \{ \mathbf{f}(t) + d_j [c_j \dot{z}(t) + k_j z(t)] \}. \quad (6.6)$$

Two critical problems, not usually considered in the standard design procedure of a TMD(s) device(s), are here discussed:

- 1) when using a commercial software for the finite element analyses (FEA), the modal mass normalization is pursued toward having that matrix built as an identity matrix;
- 2) when the primary system is a bridge, there are longitudinal and transversal symmetries which suggest to hang several identical devices at different points. This is especially true when the vibration to be mitigated give rise to local vibration problems, instead than the case when the vibration problems originates from an oscillation of the whole structural system.

The first aspect requires¹⁷ to obtain from the numerical model the mass, damping and stiffness matrices, and to work directly on them toward the suitable normalization procedure for instance working in the MatLAB environment [12].

Due to the structural, material and geometry symmetry of the ‘‘Trasaghis’’ footbridge, it is reasonable to assume that the vibration of the structural elements occurs in phase or in opposition of phase, as well as in combined modes. Thus, the TMD system becomes a multiple tuned mass damper, with devices hung in several companion points.

Two situations may be identified:

¹⁷ If no specific options are provided in the FEA software options.

- among the modes of interest, there is one of them which sees the mass normalization associated with a selected hanging point to produce unit entries in all the companion points;
- among the modes of interest, there are two modes at the same frequency or at frequencies close to each other which see unit entries of the first eigenvector in one half of the companion points, while the remaining points see the unit entries in the second eigenvector.

For both these cases, the normalized modal mass is easily computed. A suitable per cent of it is then distributed across all the companion positions, and the TMD parameters are accordingly computed, within the hypothesis that these parameters are assumed to be equal for all the devices because of the symmetry hypothesis for the structure given previously.

Usually commercial FEA implement a normalization of the modal masses values, which is useful for the calculation, but that have no scientific meaning. This suggested implementing the following alternative procedure:

- 1) select the mode and the companion TMD hanging position;
- 2) identify and isolate a group of nodes whose masses could influence the single hanging point is. For instance, in the procedure proposed in this thesis, three nodes belonging to the structure are considered for this application; namely, one is the node at which the TMD will be physically hanging, and the other ones are its two adjacent nodes;
- 3) perform a dynamic modal analysis and for each TMD location, collect the modal masses of any single cluster of nodes above selected. In other words, for the procedure proposed, one needs to collect the modal mass of the three nodes;
- 4) the dynamic modal analysis is then repeated with a rigid link connecting the hanging node to an additional node where the given added mass of the TMD device is assigned. This produces a further modal mass, whose ratio-to the sum of the cluster modal masses is computed toward the standard TMD design.

Summarizing in the above proposed procedure, instead of computing as usual the modal mass at the hanging node, and introducing the mass damper as μ times the modal mass, it is considered the ratio μ between the nodal masses as normalized by the FEA code. It is important to underline that, following this procedure, the influence of the mesh discretization on the result needs to be checked by, for example, comparing them with

the ones obtained from a coarser mesh. This because the discretization influences the choice of the cluster of nodes whose masses is influenced by the presence of the TMD.

A real-case exemplification of the proposed method is performed with reference of the “Trasaghis” footbridge (see *Appendix A*, section A.1 for more details about the bridge). A summary of the mains elements masses is given in Table 6.1.1. The performance of the designed TMD passive solution is checked with the reference of the wind loads as expressed in *Chapter 3*. The resulting forces coming from the wind velocity file act on both sides of the footbridge, as prescribed in [13]. Two different numerical analyses are performed:

- structural “static” analysis, from which the baseline for the dynamic vibration is obtained;
- structural “dynamic transient” analysis.

Subtracting the “static” response from the “dynamic” one in terms of displacements, it is possible to isolate the pure dynamic response of the pedestrian bridge. The time duration of the analysis is assigned to be 120 sec; i.e., twice the duration of the wind velocity time history. In this manner, the free vibrations of the system, once the external excitation stops, are also simulated.

As described in section 3.2.2 the role of the steel skeleton of the deck is dominant on the dynamic response of the bridge. The recorded signals from the in situ campaigns confirmed the role of the long tubular stays in determining the vibration of the system at frequencies in the range from 1 to 2 Hz. Actually, as a result of the modal analysis carried out on the numerical model (Figure 6.1.1) developed within Marc MENTAT2010 environment [14] (see section 3.2.2 for further information), the possible combinations of their vertical (in plane) movements correspond to the lowest frequency value, and those of their horizontal (out-of-plane) movements correspond to an intermediate frequency range, both resulting in modest movements of the deck. This different orthogonal behavior is due to the connections of the stays, which are represented by hinges in the vertical plane, but can transfer the moments in the orthogonal plane. A further slightly higher frequency show the movement of all the oblique elements in the same (transversal/out-of-plane) direction resulting in torsion of the central third of the deck. A summary of the frequencies range is given in Table 6.1.2.

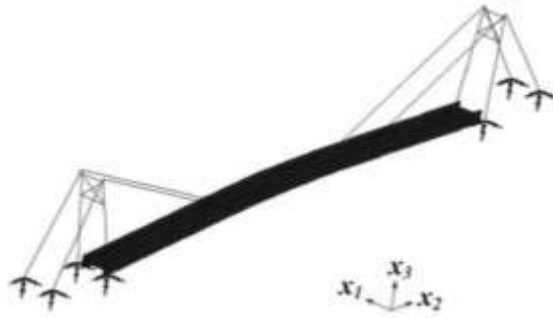


Figure 6.1.1. 3-D view of the numerical model of the “Trasaghis” footbridge implemented in Marc MENTAT2010.

Table 6.1.1. Masses of the structural and non-structural elements for the “Trasaghis” footbridge.

<i>System component</i>	<i>Single element mass[kg]</i>	<i>Number of elements</i>	<i>Mass [kg]</i>
Larch revetment	-	-	11051
GLT main longitudinal beams	16140	2	32880
Wooden walking surface	-	-	7730
Timber beams under the walking surface	828	5	4140
“Internal” tubular steel stays	1760	4	7040
“External” tubular steel stays	845	4	3380
Steel pillars	6270	2	12540
Steel railing	-	-	1200
Steel bracings	-	-	3365
Steel transversal beams	169.7	30	5090
TOTAL			88416

Table 6.1.2. Frequency ranges for the lowest modes of the “Trasaghis” footbridge.

Set ID	Frequency [Hz]	Involved Elements	Oscillation plane
1	1.06	Tubular stay	$x_2 - x_3$
2	1.41	Tubular stay	$x_2 - x_1$
3	1.96	Tubular stay	$x_2 - x_1$ & $x_2 - x_3$

In the case of “Trasaghis” footbridge the deck results quite stiff while the steel supporting skeleton is rather flexible. In particular the values around 1 ± 1.50 Hz of the frequencies of the modes along x_3 and x_1 are associated to all the central nodes of the

stays, which move in a synchronous manner as reported in Table 6.1.2. This fact suggests to append the TMD directly to the tubular steel stays as reported in Figure 6.1.2.

The selected tuning frequencies for the design are:

- 1.05 Hz for the motion along the x_3 (gravity) axis;
- 1.40 Hz for the motion along the x_1 (transversal to the deck) axis.

The small discrepancies of the frequencies values with the values reported in Table 6.1.2 are due to the presence of the mass of the TMDs within the numerical model.

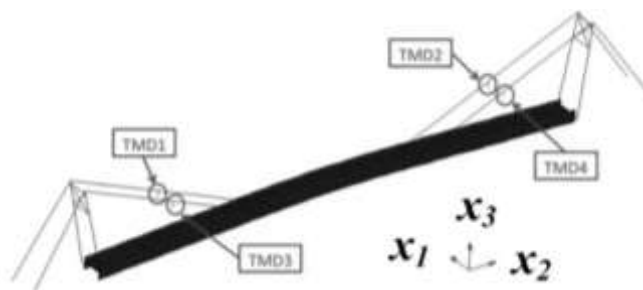


Figure 6.1.2. View of the implemented TMDs solution on “Trasaghis” footbridge. In particular TMD1 and TMD3 hung on the tubular elements in the l.h.s. of the footbridge, while TMD2 and TMD4 are hanged on the tubular elements in the r.h.s.

After having created a model of only 200 nodes, instead of the 500 nodes charactering the full scheme of Figure 6.1.1, the corresponding structural matrices are derived and further elaborated using MatLAB. The modal mass associated to the vertical mode is found to be 4000 kg, with 1000 kg in each of the four stay central nodes. For $\mu=0.05$, the added mass would then be 50 kg per stay. For the mode in the horizontal direction, the reduced model yields to a decoupling of two very close frequency values, so that only two nodes move synchronously (with unity displacement). In this case, a modal mass of 1800 kg is found and must be divided by the number of synchronous nodes (i.e., by 2^{18}), leading to 900 kg each. For $\mu=0.05$, the added mass would then be 45 kg. The final TMD mass is then assumed to be 50 kg and is applied at each stay central node, having set $\mu=0.0556$ for the mode in the horizontal direction.

Adopting the table for the design of the TMD devices given by [15] and summarized in Table 6.1.3, one enters with the selected μ value and a very low damping of the primary

¹⁸ Because two are the nodes that are moving synchronously.

system (of about 1%, which represents a conservative value of damping for wood structures) and obtains the optimum absorber parameters that are:

$$\begin{aligned}\alpha_{opt} &\simeq 0.95 \\ \zeta_{opt} &\simeq 10\%\end{aligned}\quad (6.7)$$

Thus optimum stiffness and damping of the TMDs may be evaluated as:

$$\begin{aligned}k_{opt} &= 4\pi^2 (f \alpha_{opt})^2 M_{TMD} \\ c_{opt} &= 2\zeta_{opt} \sqrt{M_{TMD} k_{opt}}\end{aligned}\quad (6.8)$$

Table 6.1.3. Optimum absorber parameters for TMD design [15].

μ	ζ_s	R_{opt}	α_s	ζ_{opt}
0.01	0	10.138	0.9876	0.04981
	0.01	7.743	0.9859	0.04981
	0.02	6.205	0.9819	0.04981
	0.05	3.798	0.9704	0.04982
	0.1	2.249	0.9436	0.04982
0.03	0	6.058	0.9636	0.08566
	0.01	5.110	0.9592	0.08566
	0.02	4.424	0.9545	0.08566
	0.05	3.109	0.9380	0.08567
	0.1	2.036	0.9032	0.08569
0.1	0	3.602	0.8861	0.1527
	0.01	3.285	0.8789	0.1527
	0.02	3.014	0.8714	0.1528
	0.05	2.399	0.8468	0.1529
	0.1	1.765	0.7991	0.1531
0.2	0	2.865	0.7906	0.2097
	0.01	2.680	0.7815	0.2098
	0.02	2.516	0.7721	0.2099
	0.05	2.113	0.7421	0.2103
	0.1	1.649	0.6862	0.2112

Then assuming $M_{TMD} = 50$ Kg as evaluated above one achieves:

- for the motions along x_3 characterized by a frequency $f = 1.05$ Hz \rightarrow

$$\begin{aligned}k_{opt} &= 4\pi^2 (1.05 * 0.95)^2 50 = 1950 N / m \\ c_{opt} &= 2 * 0.1 \sqrt{50 * 1950} = 60 Ns / m\end{aligned};$$

- for the motion along x_1 characterized by a frequency $f = 1.40$ Hz \rightarrow

$$\begin{aligned}k_{opt} &= 4\pi^2 (1.40 * 0.95)^2 50 = 3400 N / m \\ c_{opt} &= 2 * 0.1 \sqrt{50 * 3400} = 80 Ns / m\end{aligned}$$

Summarizing, for this proposed TMD system, called TMD_A, the main features are collected in Table 6.1.4

Table 6.1.4. Main features of the TMD_A solution.

ID	Value
mass M_{TMD}	50 Kg each TMD
stiffness k_{x1}	3400 N/m
damping c_{x1}	80 Ns/m
stiffness k_{x3}	1950 N/m
damping c_{x3}	60 Ns/m

The alternative design approach consists of the following steps:

- 1) identify the sub-system whose vibrations have to be mitigated. In the considered case study, it is represented by the four tubular stays of total mass 1760 Kg (Table 6.1.1). Each stay is discretized into four hollow elements leading to a nodal mass of 440 kg per node. For further calculations, the attention is focused on the three internal nodes.
- 2) when considering the mode at 1.05 Hz and a rigid link to the added mass, the modal analysis provides the following (dimensionless) modal masses as provided by the FEA coded employed [14]: 3.22, 6.55 and 4.52 for the three internal nodes, and 0.77 for the added mass. These values correspond to $\mu=5.39\%$; the error is 7% with respect to the “lightest” FE mesh, and it will be seen to be dependent on the discretization.
- 3) for the mode at 1.40 Hz and a rigid link to the added mass, the modal analysis provides the following (dimensionless) modal masses: 4.09, 7.31 and 4.12 for the three internal nodes, and 0.87 for the added mass. The resulting value of μ is 5.61%, with an even lower error with respect to the “lightest” FE mesh.

Thus, it is seen that the alternative approach leads to consistent results within a suitable degree of approximation. If the reasoning is repeated with a model in which the stays are just discretized into two elements, one obtains higher over-estimations of the values of μ ; namely, 0.75 and 0.76 in the two directions x_3 and x_1 , respectively.

The design of the implemented TMD’s solution is summarized in Figure 6.1.3. Each TMD are realized by a steel hollow cylinder of radius $R = 35$ cm, thickness $t = 4$ mm and length $l = 64$ cm. The design choices allow to fit well with both aesthetics and structural aspects; in fact it is hanged in the hinge located in the middle of the stay.

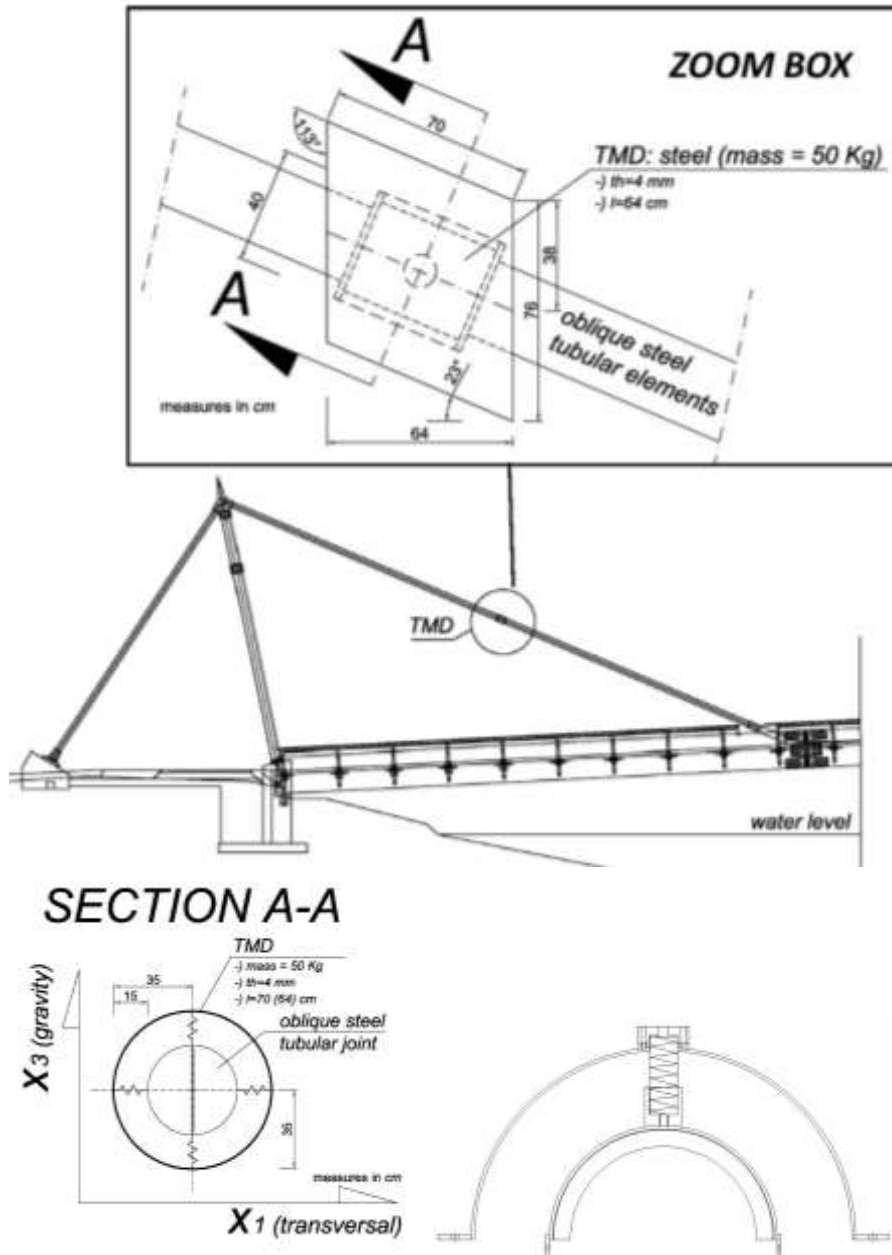


Figure 6.1.3. Above: Lateral view of the location of the i -th TMD. Below: cross-section of the i -th TMD.

The performance of the proposed TMD system (TMD_A), is evaluated by computing the root-mean-square values of the acceleration and displacement time histories obtained at nodes $n8$ and $n22$ in the two directions x_1, x_3 respectively located at the mid span of the deck, and the mid length of the oblique steel stay (Figure 6.1.4). The calculations are carried out by considering both the whole duration of these signals and only their tails (after the 60 sec. of wind excitation); the results are reported in Table 6.1.5 and Table 6.1.6, respectively. An example of the analyzed time histories results is plotted from Figure 6.1.5 to Figure 6.1.7 for the accelerations and displacements respectively for the selected nodes.

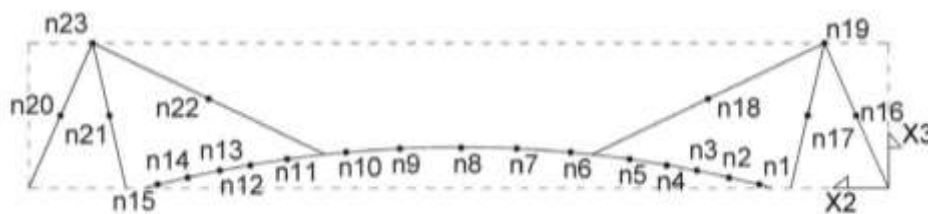


Figure 6.1.4. Grid of nodes.

Table 6.1.5. Root-mean-square values computed on the whole duration (120 sec) of the acceleration and displacement time histories obtained from the numerical analyses. The peak values are also reported in *italic*, and they are expressed in m/s^2 for the accelerations, and in mm for the displacements.

node n8				
	<i>acceleration [m/s²]</i>		<i>displacement [mm]</i>	
	x_1	x_3	x_1	x_3
No TMD	0.1348	0.0665	1.2015	0.5593
	<i>0.6079</i>	<i>0.3503</i>	<i>5.8083</i>	<i>2.7658</i>
TMD_A	0.1335	0.0659	1.1754	0.5467
	<i>0.6217</i>	<i>0.3571</i>	<i>5.9399</i>	<i>2.8283</i>

node n22				
	<i>acceleration [m/s²]</i>		<i>displacement [mm]</i>	
	x_1	x_3	x_1	x_3
No TMD	1.089	0.1605	15.8961	3.8396
	<i>4.8971</i>	<i>0.7539</i>	<i>73.4899</i>	<i>19.8873</i>
TMD_A	0.8296	0.0822	12.7703	1.9309
	<i>3.6528</i>	<i>0.5396</i>	<i>58.4994</i>	<i>14.0121</i>

Table 6.1.6. Root- mean-square values computed on the tails (the first 15 sec after the event) of the of the response time histories obtained from the numerical analyses. The peak values are also reported in italic, and they are expressed in m/s^2 for the accelerations, and in mm for the displacements.

node n8					
		<i>acceleration [m/s^2]</i>		<i>displacement [mm]</i>	
		<i>x1</i>	<i>x3</i>	<i>x1</i>	<i>x3</i>
No TMD		0.0108	0.1174	0.1405	0.0669
		<i>-0.0121</i>	<i>0.0896</i>	<i>0.1686</i>	<i>0.0580</i>
TMD_A		0.0058	0.0597	0.0513	0.0239
		<i>0.0011</i>	<i>-0.2571</i>	<i>0.1547</i>	<i>0.0735</i>

node n22					
		<i>acceleration [m/s^2]</i>		<i>displacement [mm]</i>	
		<i>x1</i>	<i>x3</i>	<i>x1</i>	<i>x3</i>
No TMD		0.0051	0.1014	1.5997	2.4365
		<i>-0.0059</i>	<i>0.0883</i>	<i>0.6423</i>	<i>0.2851</i>
TMD_A		0.0027	0.0113	0.9543	0.2498
		<i>0.0012</i>	<i>0.0275</i>	<i>0.2421</i>	<i>0.1143</i>

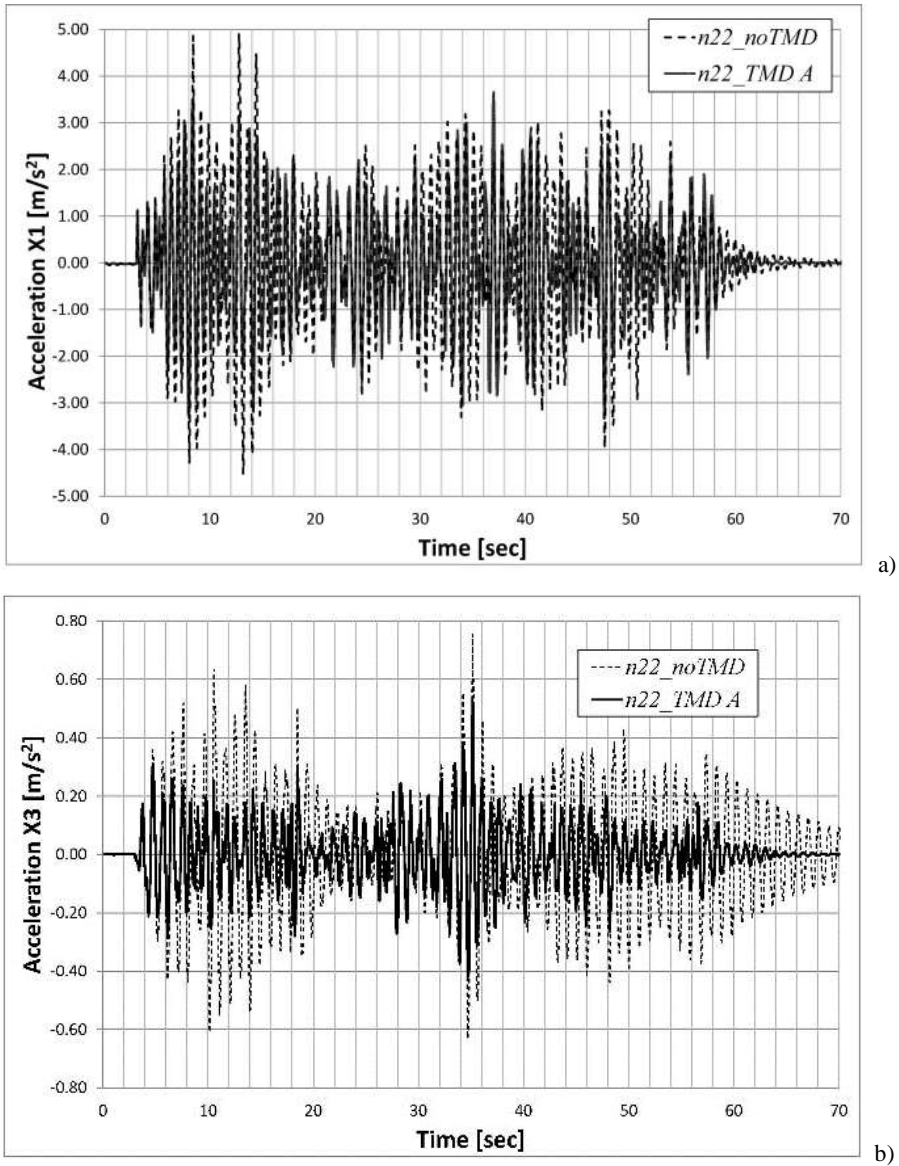


Figure 6.1.5. Time histories response before and after mounting the passive control system (“TMD_A”) designed. Acceleration responses for the node n22 along x1 (a) and x3 (b), respectively.

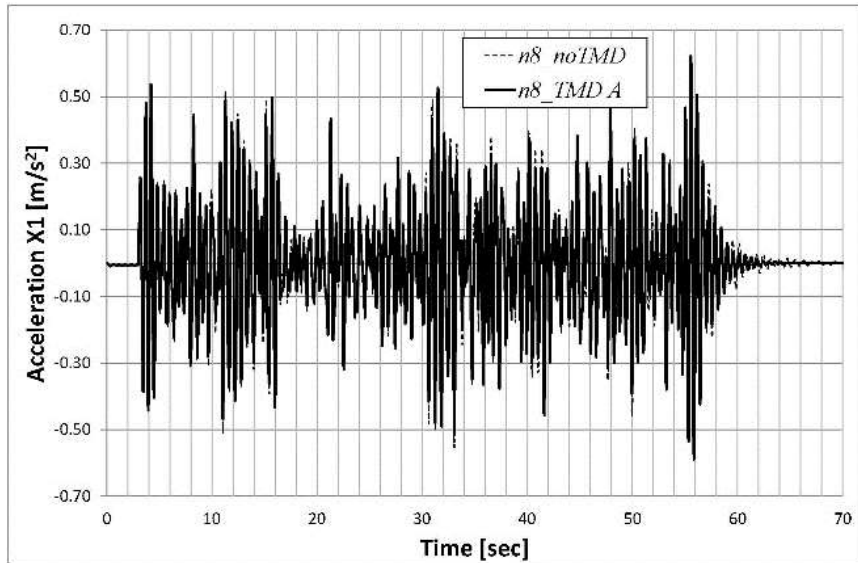


Figure 6.1.6. Time histories response before and after mounting the passive control system (“TMD_A”) designed. Acceleration responses along x_1 at the node n8.

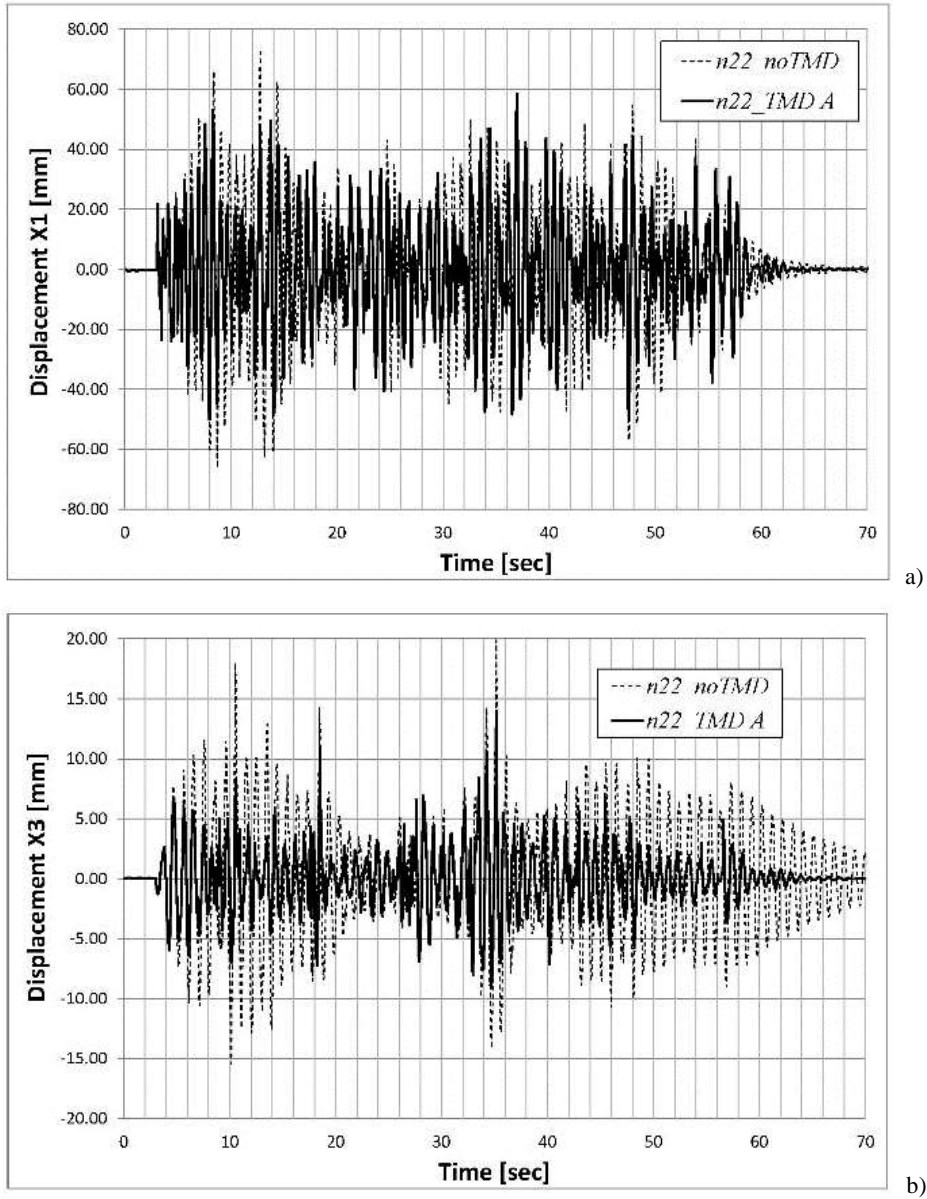


Figure 6.1.7. Time histories response before and after mounting the passive control system (“TMD_A”) designed. Displacement responses for the node n22 along x1 (a) and x3 (b), respectively. The response of the node n8 is meaningful due to the stiffness of the deck.

A significant mitigation of the vibrations is achieved at the central node, $n22$, of the l.h.s. stay, whereas at the deck node, $n8$, only the free response seems to be reduced because of the deck stiffness. Indeed, when the whole duration of the signals at node $n8$ is considered in the calculations of the root-means-square, the devices seem to be only able to reduce the peaks in terms of both acceleration and displacement, not the root-mean-square values.

A further understanding of the implemented passive solution is achieved analyzing the results within the frequency domain as reported in Figure 6.1.8 and Figure 6.1.9. These results confirm the observations about the TMD's effect in terms of vibrations mitigation. In fact, by looking at the frequencies considered in the design of the TMD(s), i.e. 1.05 and 1.40 Hz, it is clear that the designed architecture is able to smooth the peaks of the spectra, obtained from the numerical simulations under wind loads for the "Trasaghis" footbridge, for both the accelerations and displacements. As already observed for the response in terms of standard accelerations and displacements, the effects of the implemented solution are clearly evident for the central node, $n22$, of the l.h.s. stay, whereas the TMD's effects are not so significant as expected.

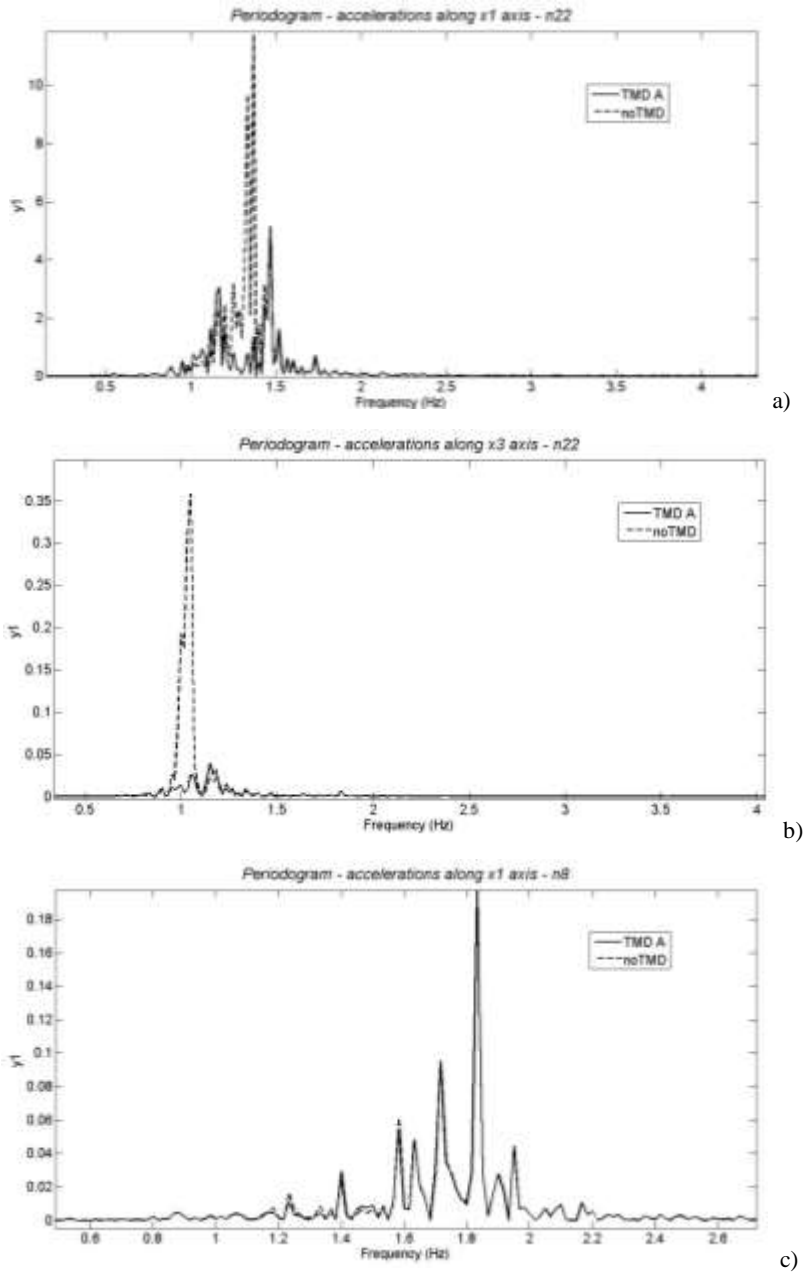


Figure 6.1.8. Response spectra as obtained from the acceleration responses along x_1 (a) and x_3 (b) at the node n22; and (c) from the acceleration response along x_1 at the node n8, before and after the installation of the passive control system (TMD_A).

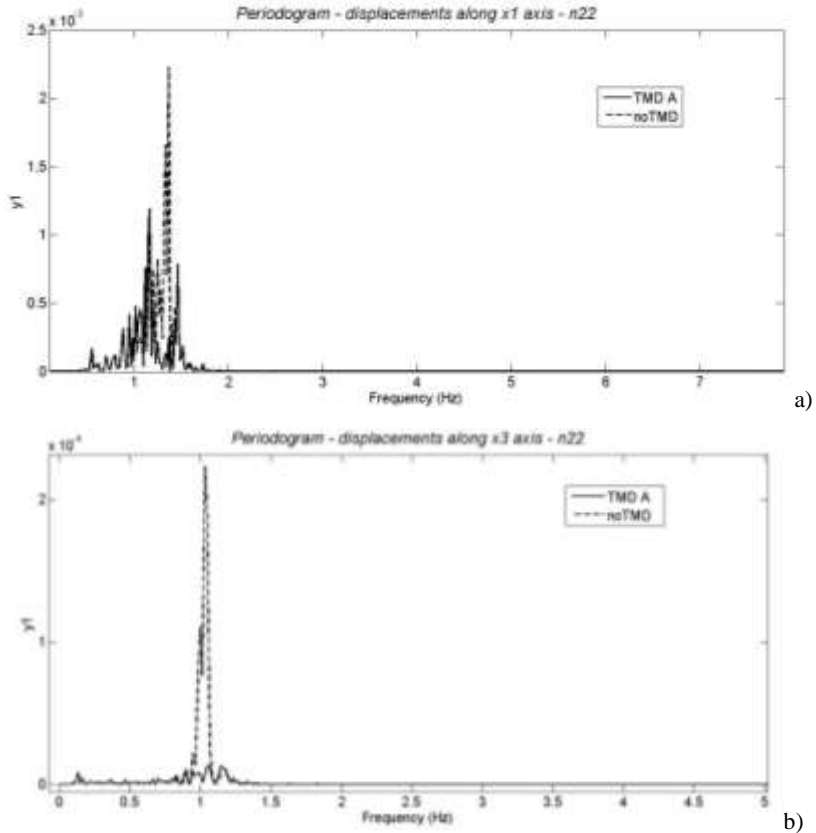


Figure 6.1.9. Response spectra as obtained from the acceleration responses along x_1 (a) and x_3 (b) at the node n22, before and after the installation of the passive control system (TMD_A).

6.2 Semiactive control solutions

In this section the possibility of introducing a control law to improve the vibration mitigation, induced by the wind action on the “Trasaghis footbridge”, achieved by passive devices is discussed. In particular a semiactive strategy is adopted.

The basic idea behind the semiactive control solution is to change some parameters of the structural system to optimize the behaviour of the system with respect to a control criterion. In this approach the only energy necessary here is the energy for regulating the devices which modify the parameters of the system [16]. A semiactive control system varies the values of the stiffness and/or the damping. Recalling for simplicity

and without loss of generality the equation of motion for a I -DOF system (see equation (2.3)), this can be represented simply as:

$$\ddot{x}(t) + 2\xi\omega_0\dot{x}(t) + \omega_0^2x(t) = \frac{F(t)}{m} + f_C, \quad (6.9)$$

where the control force is defined as:

$$f_C = -[2\xi\omega_0\alpha_C(t)]\dot{x}(t) - [\omega_0^2\alpha_K(t)]x(t), \quad (6.10)$$

in which $\alpha_C(t)$ and $\alpha_K(t)$ are functions of time. Control systems where parameters of the system can be varied are called variable structure systems.

This implementation is mainly motivated by the fact that the good performance of the passive solutions, as observed in section 6.1 is restricted to a narrow window around the tuning frequency chosen during the device design [7].

Nevertheless, the global cost of the footbridge suggests to restrict the investigation within very simple technological solutions. Thus, first of all a limitation is set on the available feedback; the relative displacement z and velocity \dot{z} between the anchorage point and the secondary mass seems to be a suitable solution. A second limitation concerns the simplicity of the control law, which is generally made of a premise (IF) and a consequence (THEN). In this way a good compromise between the cost and efficacy of the solution can be achieved.

One assumes that, at each time step, the premise relies on the instantaneous values of the relative displacement and velocity introduced above, while the consequence is on the value of the device output force. In particular the simple “bang-bang control” is adopted [16].

Bang-bang control provides a simple and yet often effective approach. It is usually applied for dissipative devices in order to increase their capabilities in dissipating energy with respect to a classical passive device. The working principle of this control, approach can so summarized:

- when the relative displacement and the relative velocity of the two ends of the damping device are in the same direction, bang-bang control acts in the direction of increasing the forces in the device to a maximum value;
- vice-versa when the relative displacement and the relative velocity of the ends of the device are in opposite directions, the control law decreases the value of the forces to a minimum in order to make the device movement as easy as possible.

Thus, the maximum value of the forces is obtained when the control signal reach its maximum, and the minimum when the control signal reach its minimum. In other words the general representation of the control law can be written as:

$$\begin{cases} F_C(t) = F_{MAX} & \text{if } \text{sign}(\dot{x}) = -\text{sign}(x) \\ F_C(t) = F_{MIN} & \text{if } \text{sign}(\dot{x}) = \text{sign}(x) \end{cases} \quad (6.11)$$

Then it is clear as the minimum value of the control parameter should be set at as small a level as possible, to reduce the dissipative forces to a minimum, while the maximum value of the control parameter should be at the optimal value, that is a value which provides the maximum energy dissipation.

The advantage of this control approach, is that it is easy to implement the “bang-bang” strategy in a real-time algorithm to achieve the structural control purpose. In fact the control signal switches between two values and only the relative displacement needs to be measured by a sensor and fed back to the control signal. Thus, the function $\text{sign}(x)$ can be obtained simply by the relative displacement evaluated by the recorded signal and there is no need to measure the velocity.

More in details for the case study of the “Trasaghis” footbridge the control force is given different values according to the sign of the product $\dot{z}z$. In particular one writes:

$$\begin{cases} F(t) = F_1 & \text{if } \dot{z}z > 0 \\ F(t) = F_2 & \text{if } \dot{z}z < 0 \end{cases} \quad (6.12)$$

where F_1 and F_2 are the maximum and minimum levels, respectively, and they are assigned as functions of the feedback. Note that without an accelerometer one cannot estimate the inertial force of the TMD, whereas the corresponding damping force and the elastic one can be directly calculated based on the available feedback, \dot{z} and z , respectively. An example of the relative displacement along x_1 and x_3 direction is reported in Figure 6.2.1.

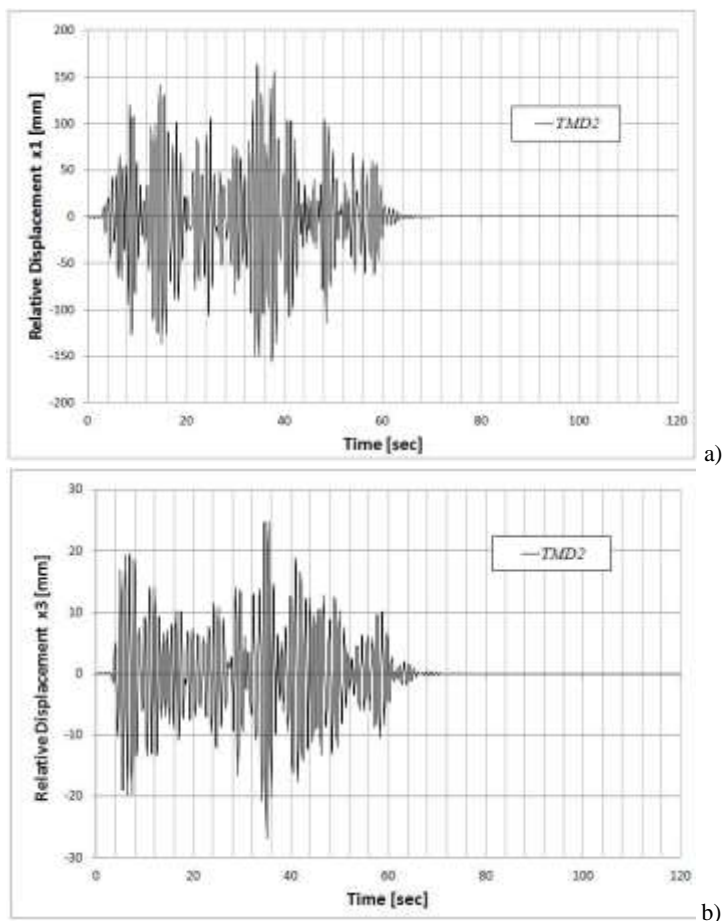


Figure 6.2.1. Time history of the relative displacement for the node of TMD2 along x_1 direction a), and x_3 direction b).

The inertial term is accounted by artificially augmenting the sum of the last two terms in the l.h.s. of equation (6.3) when the maximum control force is calculated at each step of the analysis. The simplest option consists of introducing an amplification factor of 1.8 when assigning the F_2 value in equation (6.12), whereas a de-amplification factor of 0.6 is set to effectively reduce the required minimum control force F_1 . Such a control scheme is denoted as “s1”. Two more control policies are investigated:

- scheme denoted as “s2”: the factors are progressively varied based on the feedback;

- scheme denoted as “s3”: a contribution which replaces the inertia term by an estimate is added.

To check the performance of the semiactive solution, three different configurations for the TMDs are considered:

- 1) the first one is the TMD_A solution as evaluated in section 6.1 (see Table 6.1.4 for the main features of this solution);
- 2) the second one, called TMD_B solution, is obtained tuning the TMD at the frequency $f = 1.96$ Hz (that regards both the motion along x_1 and x_3 as from Table 6.1.2). Following the standard design of the TMD described in section 6.1 and given by [15], assuming a mass of the singular TMD equal to $M_{TMD} = 50$ Kg the stiffness of the TMD may be evaluated as: $f = 1.96$ Hz $\rightarrow k_{opt} = 4\pi^2 (1.96 * 0.95)^2 50 = 6727 N/m$ for both x_1 and x_3 directions. The damping is assumed conservatively equal to case TMD_A along x_1 , that is $c_{opt} = 480 Ns/m$, for both the direction x_1 and x_3 ;
- 3) the third architecture, called TMD_C solution, is obtained mixing the two previous solutions. It mounts the devices of TMD_A in the positions denoted as TMD1 and TMD4 in Figure 6.1.2 and the devices of TMD B in the other two locations (Figure 6.2.2).

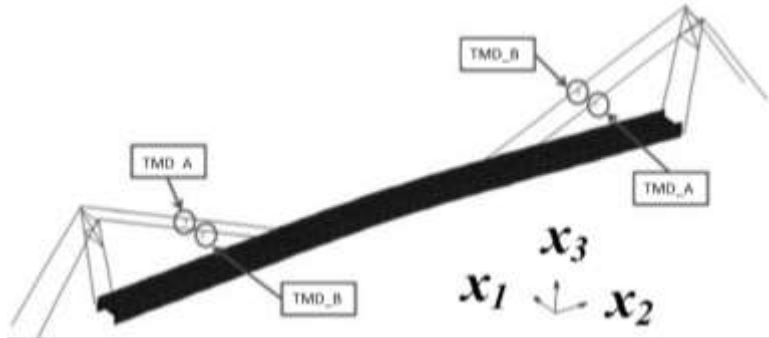


Figure 6.2.2. View of the TMD_C of the “Trasaghis” footbridge.

The main results achieved by the semiactive architecture above described are summarized here below. In particular the results are represented in terms of the root-mean-square for the whole signal (Table 6.2.1) of accelerations and displacements, and in terms of the root-mean-square of the first 15 sec after the event (Table 6.2.2) for both the signal of accelerations and displacements. The control solutions are denoted by the same acronym as the corresponding strategies adopted; i.e. “s_i, i=1,2,3”.

The results shown as the semiactive implementation based on the stiffness and damping coefficients of TMD_A is unable to improve the passive performance, while this occurs for TMD B. In other words a semiactive approach allows the designer to tune the device on a frequency higher than the first one so that a similar effectiveness can be achieved in a more robust manner. It is worth noticing that, from Tables 5 and 6, the least sophisticated control scheme denoted as “TMS_Bs1” results to be the most effective one, with a performance which is very similar (sometimes better) to that of the TMD_A passive configuration, with the difference that the latter one is tuned (in the two directions x_1 and x_3) on a single frequency $f = 1.96$ Hz. Examples of the controlled acceleration are given from Figure 6.2.3 to Figure 6.2.10.

Table 6.2.1. Root-mean-squares on the whole duration (120 sec) of the response time histories computed from the numerical analyses carried out in a semi-active environment. The value in italic in each cell gives the peak value (with its sign) expressed as m/s^2 for the accelerations, and as mm for the displacements.

node n22				
	<i>acceleration [m/s^2]</i>		<i>displacement [mm]</i>	
	x_1	x_3	x_1	x_3
No TMD	1.089	0.1605	15.8961	3.8396
	<i>4.8971</i>	<i>0.7539</i>	<i>73.4899</i>	<i>19.8873</i>
TMD_As1	0.8365	0.0866	12.3125	2.1739
	<i>3.9462</i>	<i>0.4949</i>	<i>54.4649</i>	<i>14.2123</i>
TMD_As2	0.9215	0.0833	13.1832	2.0563
	<i>4.4611</i>	<i>0.5003</i>	<i>59.4422</i>	<i>13.4807</i>
TMD_As3	0.8923	0.0908	12.4023	2.2441
	<i>4.2431</i>	<i>0.5171</i>	<i>56.3241</i>	<i>14.2929</i>
TMD_Bs1	0.9861	0.1415	15.5892	3.5921
	<i>-4.6187</i>	<i>-0.6132</i>	<i>-74.6187</i>	<i>17.4190</i>
TMD_Bs2	1.0143	<i>0.1605</i>	16.3107	3.5868
	<i>5.0301</i>	<i>0.7539</i>	<i>-81.9679</i>	<i>17.7537</i>
TMD_Bs3	0.9715	0.1391	15.3339	3.5241
	<i>-4.4669</i>	<i>0.6060</i>	<i>-70.3799</i>	<i>17.2960</i>
TMD-Cs1	0.9858	0.1414	15.5890	3.5919
	<i>-4.6184</i>	<i>-0.6130</i>	<i>-74.6185</i>	<i>17.4188</i>
TMD-Cs2	0.9937	0.1401	15.7661	3.5537
	<i>4.6502</i>	<i>-0.6104</i>	<i>-75.6504</i>	<i>17.4577</i>
TMD-Cs3	0.9714	0.1390	15.3338	3.5240
	<i>-4.4668</i>	<i>0.6059</i>	<i>-70.3798</i>	<i>17.2959</i>

Table 6.2.2. Root-mean-squares on the tail (the first 15 sec after the event) of the time histories computed as response from the numerical analyses carried out. The value in italic in each cell gives the starting point (with its sign) of the decay, expressed as m/s^2 for the accelerations, and as mm for the displacements.

node n22					
		<i>acceleration [m/s^2]</i>		<i>displacement [mm]</i>	
		<i>x_1</i>	<i>x_3</i>	<i>x_1</i>	<i>x_3</i>
No TMD		0.0051	0.1014	1.5997	2.4365
		<i>-0.0059</i>	<i>0.0883</i>	<i>0.6423</i>	<i>0.2851</i>
TMD_As1		0.0434	0.0117	0.5778	0.3039
		<i>0.0412</i>	<i>-0.0396</i>	<i>0.3939</i>	<i>0.1873</i>
TMD_As2		0.0555	0.0103	0.7216	0.3955
		<i>0.0989</i>	<i>-0.0312</i>	<i>0.5412</i>	<i>0.1930</i>
TMD_As3		0.0393	0.0150	0.5420	0.4022
		<i>-0.1015</i>	<i>-0.0475</i>	<i>0.3979</i>	<i>0.1903</i>
TMD_Bs1		0.1659	0.0917	2.5431	2.3284
		<i>0.6093</i>	<i>-0.2043</i>	<i>0.2570</i>	<i>0.1410</i>
TMD_Bs2		0.1970	<i>0.0914</i>	3.0474	2.3191
		<i>0.7351</i>	<i>-0.2033</i>	<i>0.1992</i>	<i>0.1126</i>
TMD_Bs3		0.1450	0.0897	2.2009	2.2747
		<i>0.5368</i>	<i>-0.1997</i>	<i>0.2547</i>	<i>0.1394</i>
TMD-Cs1		0.1659	0.0917	2.5430	2.3282
		<i>0.6093</i>	<i>-0.2043</i>	<i>0.2568</i>	<i>0.1408</i>
TMD-Cs2		0.1656	0.0913	2.5307	2.3143
		<i>0.6084</i>	<i>-0.1988</i>	<i>0.2610</i>	<i>0.1426</i>
TMD-Cs3		0.1449	0.0896	2.2008	2.2746
		<i>0.5367</i>	<i>-0.1996</i>	<i>0.2546</i>	<i>0.1393</i>

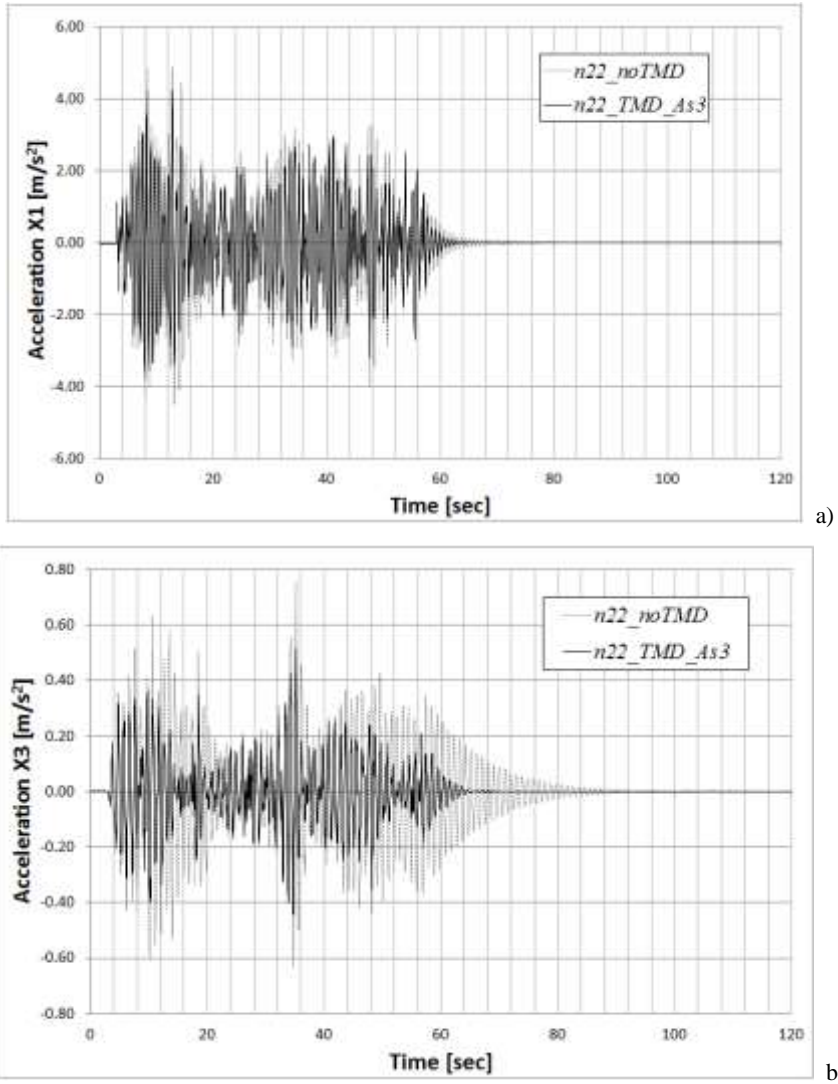


Figure 6.2.3. Time histories of the accelerations (a) along direction x_1 and (b) along direction x_3 obtained for node n22 under the semiactive control scheme TMD_A3.

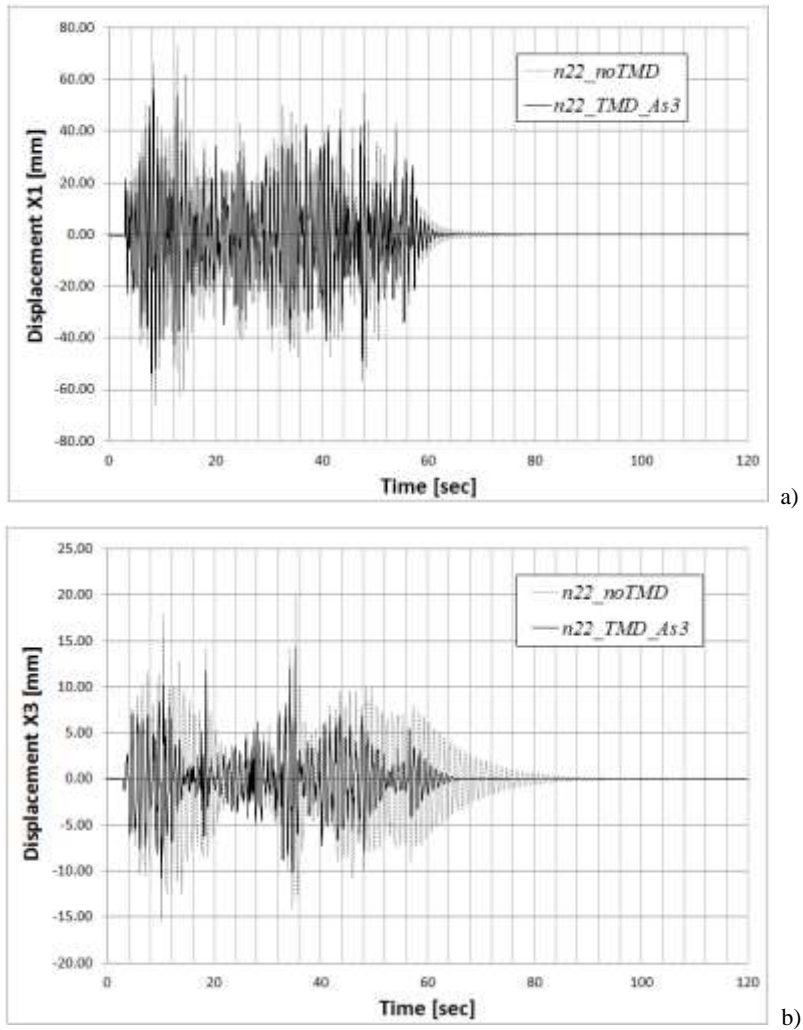
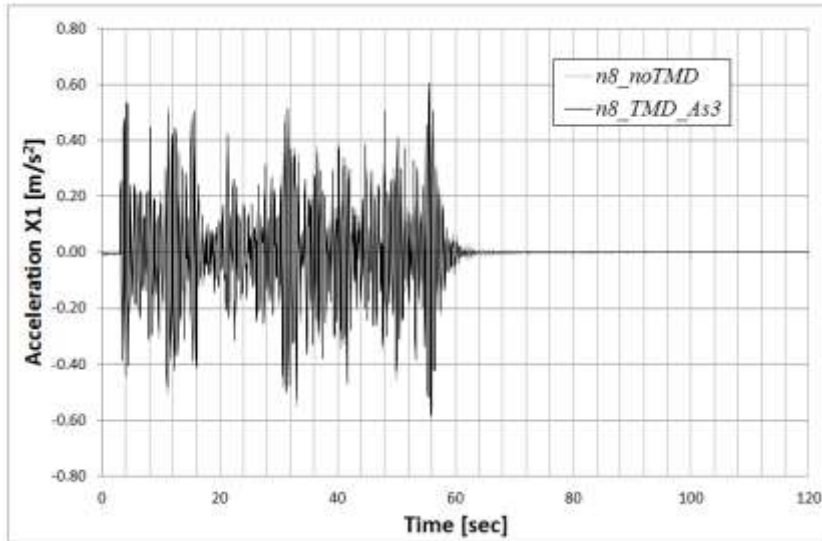
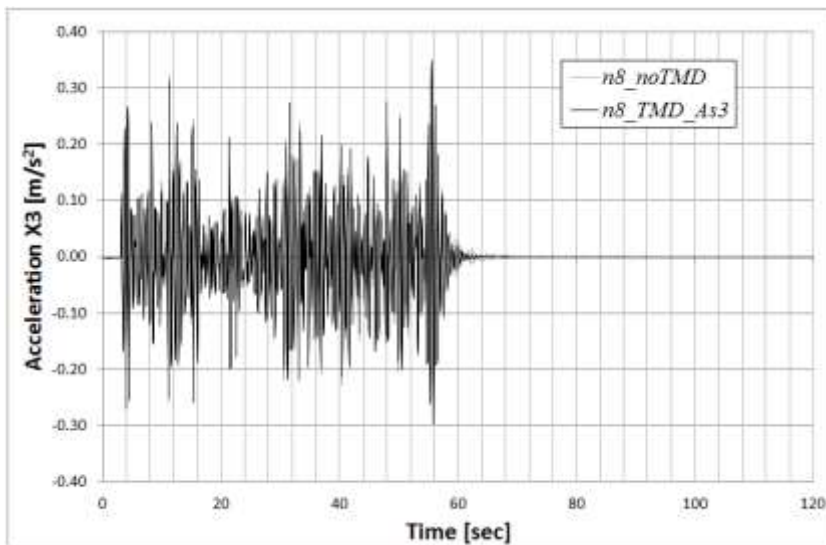


Figure 6.2.4. Time histories of the displacements (a) along direction x_1 and (b) along direction x_3 obtained for node n22 under the semiactive control scheme TMD_As3.



a)



b)

Figure 6.2.5. Time histories of the accelerations (a) along direction x_1 and (b) along direction x_3 obtained for node n8 under the semiactive control scheme TMD_A53.

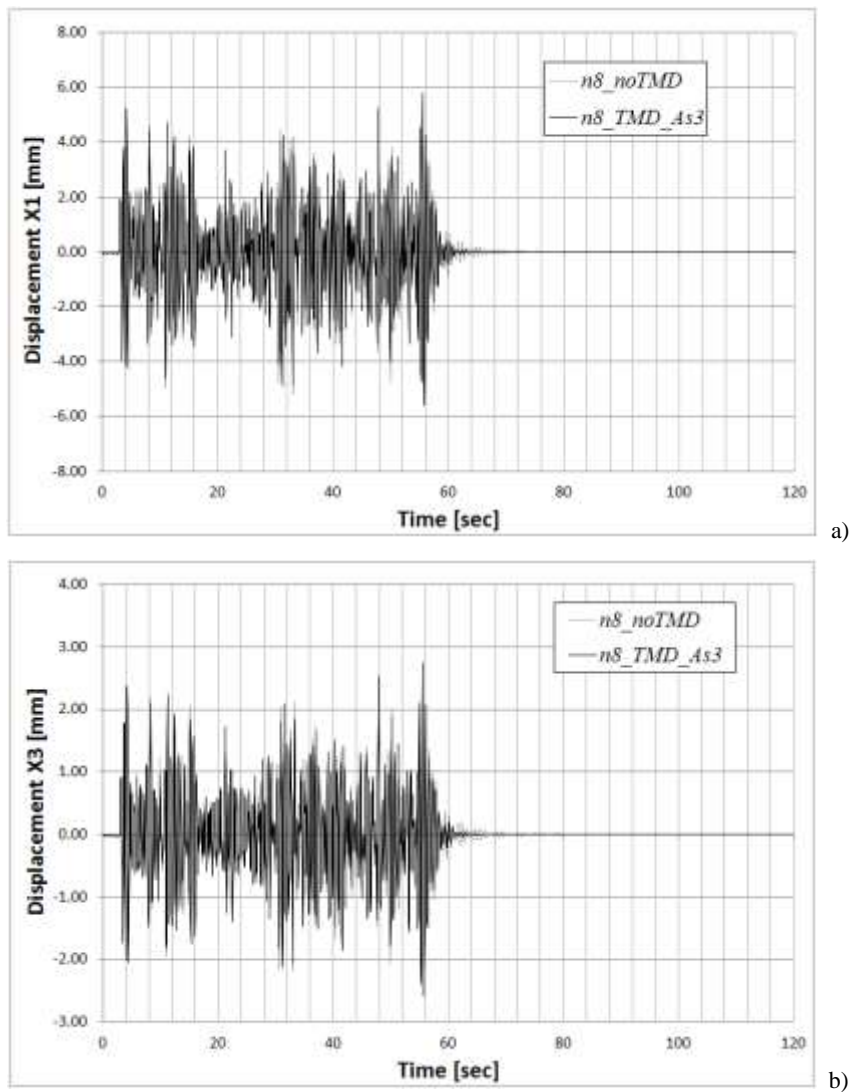
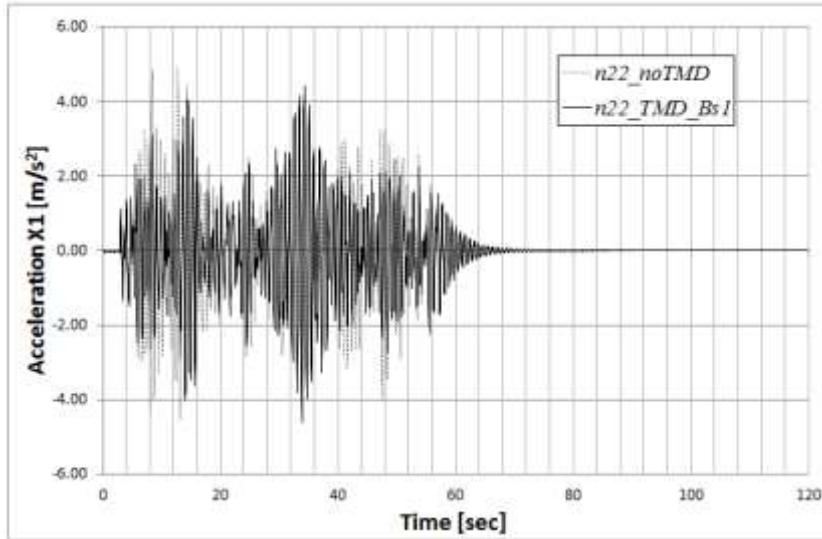
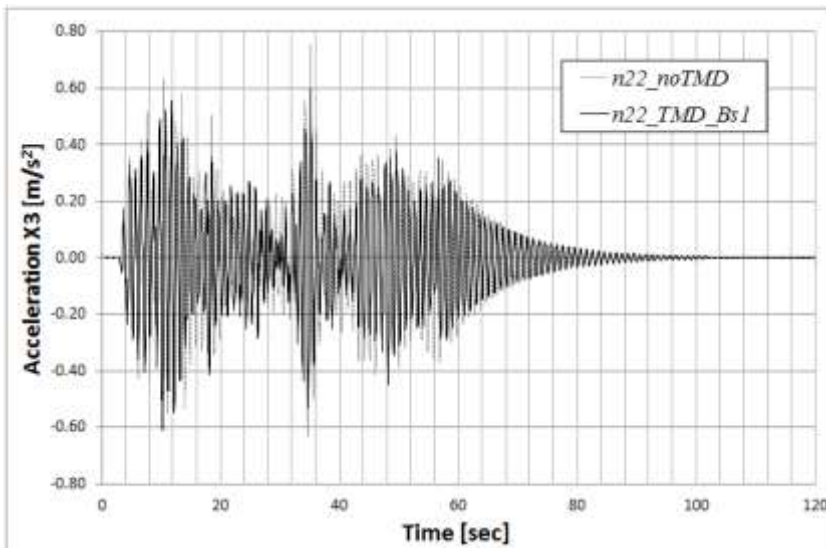


Figure 6.2.6. Time histories of the displacements (a) along direction x_1 and (b) along direction x_3 obtained for node n8 under the semiactive control scheme TMD_A53.



a)



b)

Figure 6.2.7. Time histories of the accelerations (a) along direction x_1 and (b) along direction x_3 obtained for node n22 under the semiactive control scheme TMD_Bs1.

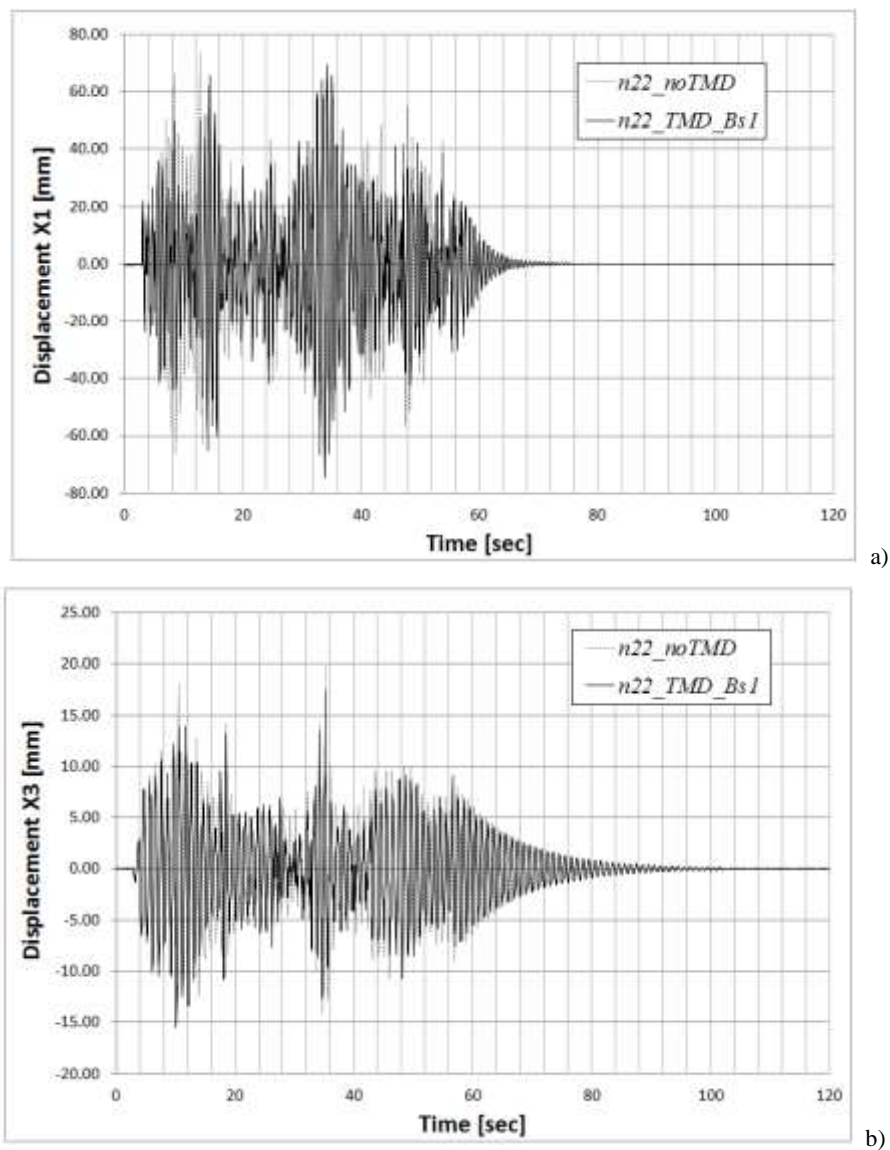


Figure 6.2.8. Time histories of the displacements (a) along direction x_1 and (b) along direction x_3 obtained for node n22 under the semiactive control scheme TMD_Bs1.

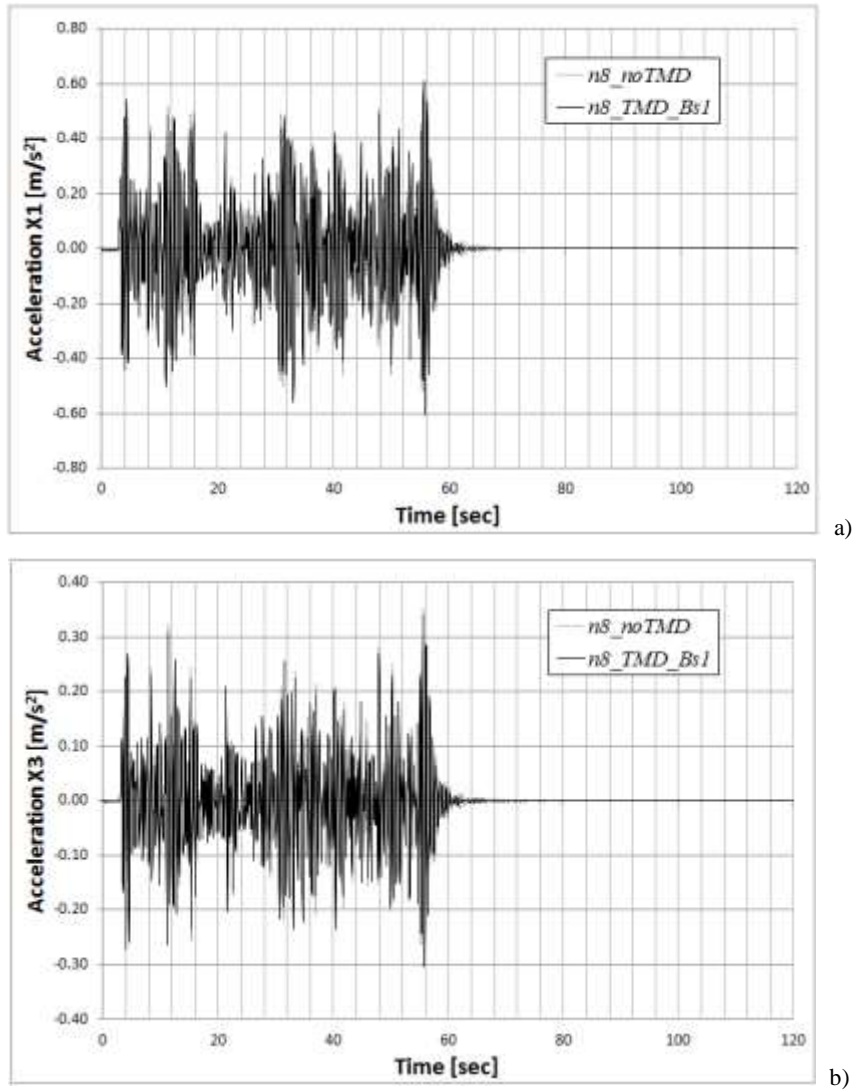


Figure 6.2.9. Time histories of the accelerations (a) along direction x_1 and (b) along direction x_3 obtained for node n8 under the semiactive control scheme TMD_Bs1.

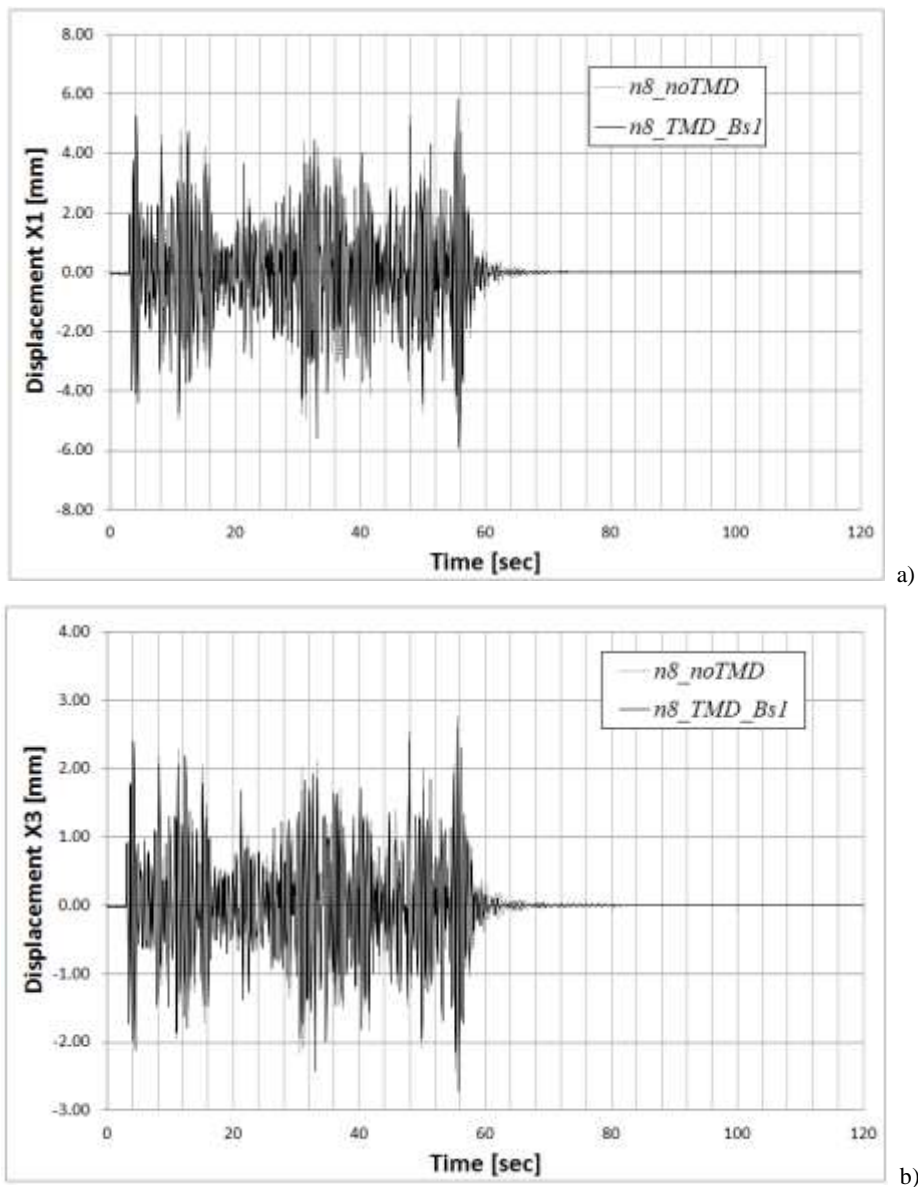


Figure 6.2.10. Time histories of the displacements (a) along direction x_1 and (b) along direction x_3 obtained for node n8 under the semiactive control scheme TMD_Bs1.

6.3 Active control solutions

Once achieved the reduction of the FEM for the “Trasaghis” footbridge (see section 5.2), a structural control is implemented within the MatLAB environment in order to mitigate the vibration induced by wind loads (see section 5.2 and section 5.3).

The implemented active control strategy, or in other words the control forced introduced within the model in order to achieve the purpose of the control, is based on the Linear Quadratic Regulator (LQR) theory. This theory belong to the more general field of the theory of optimal control that concern with the possibility to manage a given dynamic system at its minimum “cost”. In all those cases where the dynamic of the system is described by a set of linear differential equations and the cost may be described by a quadratic function, a feedback control can be achieved by applying the LQR strategy as follows described ([1] and [17]).

Let’s consider a linear dynamic system expressed in state variable form as:

$$\dot{x}(t) = \mathbf{A}x(t) + \mathbf{B}u(t), \quad (6.13)$$

where $x(t) \in \mathbb{R}^n$, $u(t) \in \mathbb{R}^m$ are respectively the states and input vectors, and the initial conditions are assumed to be $x(0) = x_0$.

The LQR strategy problem can be presented as follows: “*find a state-variable feedback (SVFB) control that gives desirable closed-loop properties, such that:*”

$$u(t) = -\mathbf{K}x(t) + v(t). \quad (6.14)$$

where \mathbf{K} is unknown matrix to be found and $v(t)$ the new command input.

Substituting equation (6.14) in (6.13) the problem becomes:

$$\dot{x}(t) = (\mathbf{A} - \mathbf{BK})x(t) + \mathbf{B}v(t) = \mathbf{A}_c x(t) + \mathbf{B}v(t), \quad (6.15)$$

where $\mathbf{A}_c = \mathbf{A} - \mathbf{BK}$ represents the closed-loop plant matrix.

It is reasonable now to design an optimal SVFB control. Thus, let’s introduce the *performance index (PI)* as:

$$J \triangleq \frac{1}{2} \int_0^{\infty} (x^T \mathbf{Q}x + u^T \mathbf{R}u) dt, \quad (6.16)$$

where $\mathbf{Q} = \begin{bmatrix} \mathbf{Q}_{1n} & \cdots & 0 \\ \vdots & \mathbf{Q}_{ii} & \vdots \\ 0 & \cdots & \mathbf{Q}_{mn} \end{bmatrix}$ and $\mathbf{R} = [r_i \delta_{ij}]$, $i, j = 1, 2, \dots, m$ are the so called weighting

square diagonal matrices. The performance index J can be interpreted as an energy function.

Since the only concerns are the internal stability properties of the closed-loop system, it is reasonable to assume $v(t) = 0$. Thus, substituting equation (6.14) into (6.16) we obtain:

$$J \triangleq \frac{1}{2} \int_0^{\infty} [x^T (\mathbf{Q} + \mathbf{K}^T \mathbf{R} \mathbf{K}) x] dt. \quad (6.17)$$

Then the optimal SVFB design can be written as:

$$\text{find } \mathbf{K} \text{ such that } J = \min(J); \quad (6.18)$$

that is in other words, the optimal design concerns the search for the minimum of the energy function J . Since the plant matrix is linear and the PI is quadratic, the problem to minimize J is called the *Linear Quadratic Regulator (LQR)* where the word 'regulator' refers to the fact that the function of this feedback is to regulate the states to zero (see section 5.1). Depending on the parameters selected for the weighted matrices \mathbf{Q} and \mathbf{R} during the design of the control law, the closed-loop system will exhibit a different response.

It is important to observe that since $x(t)$ and $u(t)$ are weighted in J , in order to minimize the function J neither $x(t)$ nor $u(t)$ can be too large. Note that if J is minimized, then it is for sure finite quantity, and since by definition it is an infinite integral of $x(t)$, then one can said that $x(t)$ goes to zero as time t goes to infinity. This in other words guarantees that the closed-loop system will be stable.

Assuming that the closed-loop system is stable so that $x(t)$ goes to zero as time t goes to infinity, it can be shown as the function J is a constant that depends only on a new auxiliary matrix \mathbf{P} and the initial conditions, and it is independent from \mathbf{K} . Then the optimal feedback \mathbf{K} can be evaluated as follows:

$$\mathbf{K} = \mathbf{R}^{-1} \mathbf{B}^T \mathbf{P}, \quad (6.19)$$

where \mathbf{P} is a constant auxiliary matrix that can be evaluated solving the following continuous time *algebraic Riccati equation (ARE)*:

$$\mathbf{A}^T \mathbf{P} + \mathbf{P} \mathbf{A} - \mathbf{P} \mathbf{B} \mathbf{R}^{-1} \mathbf{B}^T \mathbf{P} + \mathbf{Q} = 0. \quad (6.20)$$

This means in other words that the minimum of J can be evaluated solving equation (6.19) which only depends on the initial condition. Thus, the “cost” of the SVFB strategy can be computed knowing only the initial conditions, and so before the control law is applied to the system.

It is worth underlining that the LQR design procedure is guaranteed to produce a feedback that stabilizes the system if two basic properties hold:

- **Theorem 1.** Let the system (A, B) be reachable (see section 5.1). Let R be positive definite and Q be positive definite. Then the closed loop system $(A - BK)$ is asymptotically stable;
- **Theorem 2.** Let the system (A, B) be stabilizable. Let R be positive definite, Q be positive semi definite, and (A, Q) be observable (see section 5.1). Then the closed loop system $(A - BK)$ is asymptotically stable [18].

Summarizing, the above strategy to design the LQR feedback K can be represented by the following flowchart:

- 1) select design parameter matrices Q and R ;
- 2) find P by solving equation (6.20);
- 3) find the SVFB K by solving equation (6.19).

Concluding this introduction about LQR approach, this control strategy to feedback design it is characterized by:

- selecting some design matrices Q and R that are tied to the desired closed-loop performance;
- introducing an intermediate quantity P ;
- solving a matrix design equation;
- obtaining a guaranteed solution that stabilizes the system;
- obtaining very little insight into the robustness or structure of the closed-loop system.

Following the LQR control law strategy above introduced, the proposed active structural control is then achieved by introducing four forces F_Y acting along the Y direction (i.e. transversal to the deck), and applied in the middle of the four oblique steel stays (Figure 6.3.1). In Figure 6.3.2 the time history of the obtained control forces implemented for the three MOR models are shown. The choice to introduce the control forces only along Y direction is due to the fact that, as shown in section 5.2 and section

5.3, the displacements, and also the related accelerations, under wind load are about ten times bigger than the associated ones along the vertical (gravity) Z direction.

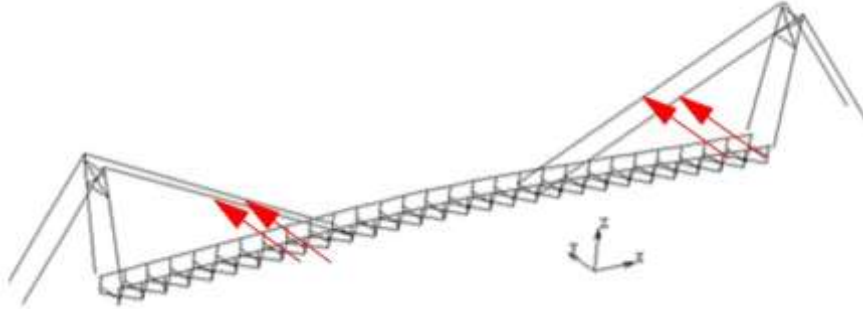
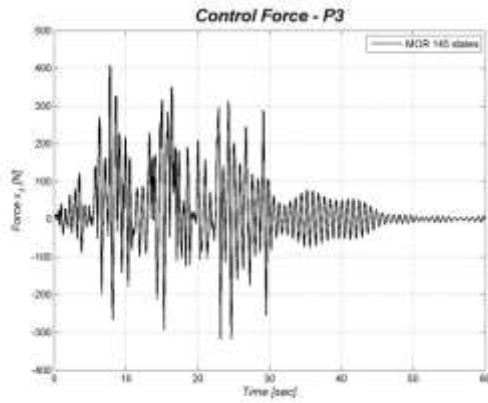
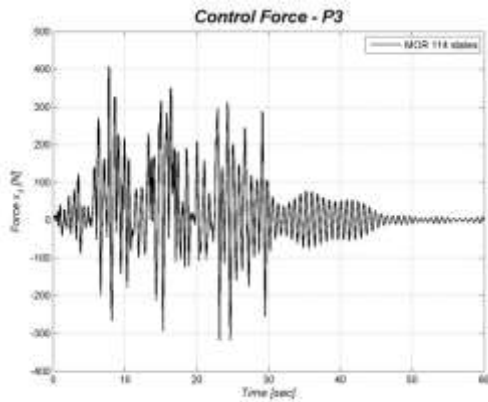


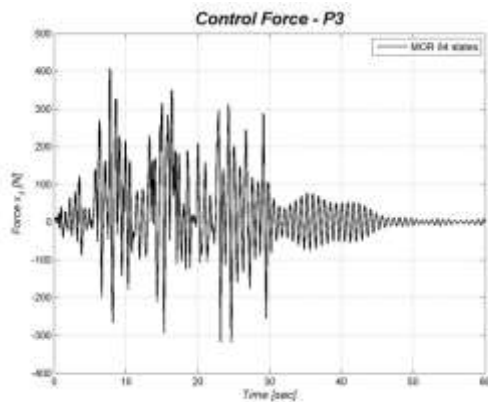
Figure 6.3.1. Scheme of the control forces implemented for the “Trasaghis” footbridge.



a)



b)



c)

Figure 6.3.2. Time history of the control forces – node 3. a) MOR 145 states; b) MOR 114 states; c) MOR 84 states.

In the following figures (from Figure 6.3.3 to Figure 6.3.8) the results in terms of displacements and accelerations along Y and Z axes for the case identified as respectively “MOR 145 states”, “MOR 114 states” and “MOR 84 states”, obtained from the above active control strategy, are compared with the related uncontrolled cases.

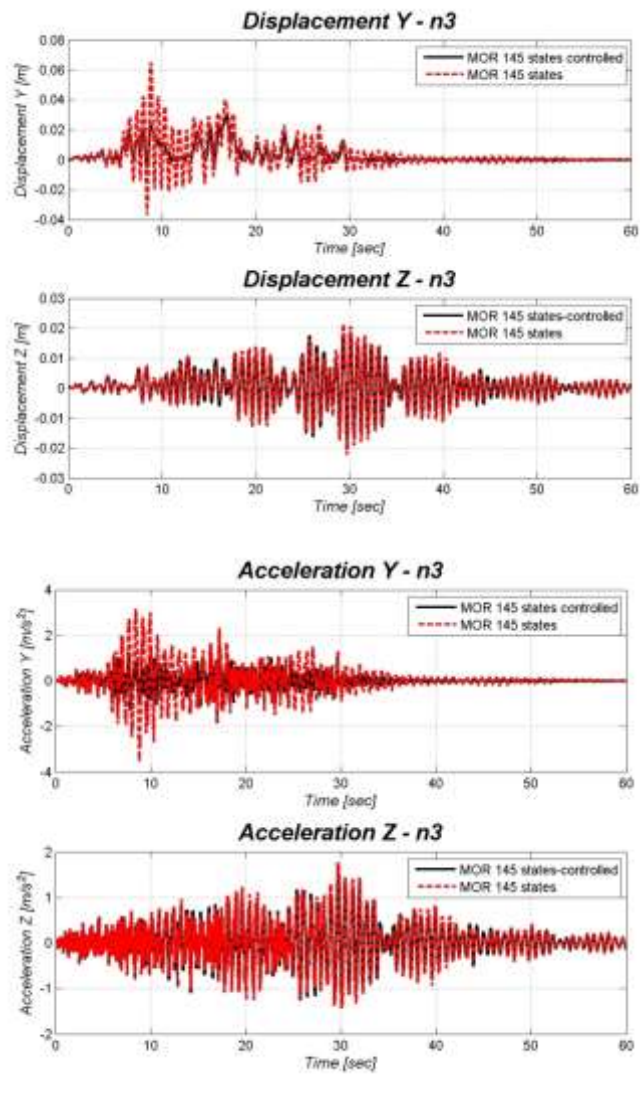


Figure 6.3.3. Active control solution for the “Trasaghis” footbridge - model MOR 145 states: comparison of uncontrolled vs. controlled. Response of: a) Displacements along Y and Z axes – node 3; b) Accelerations along Y and Z axes (zoom between 10 to 20 sec) – node 3.

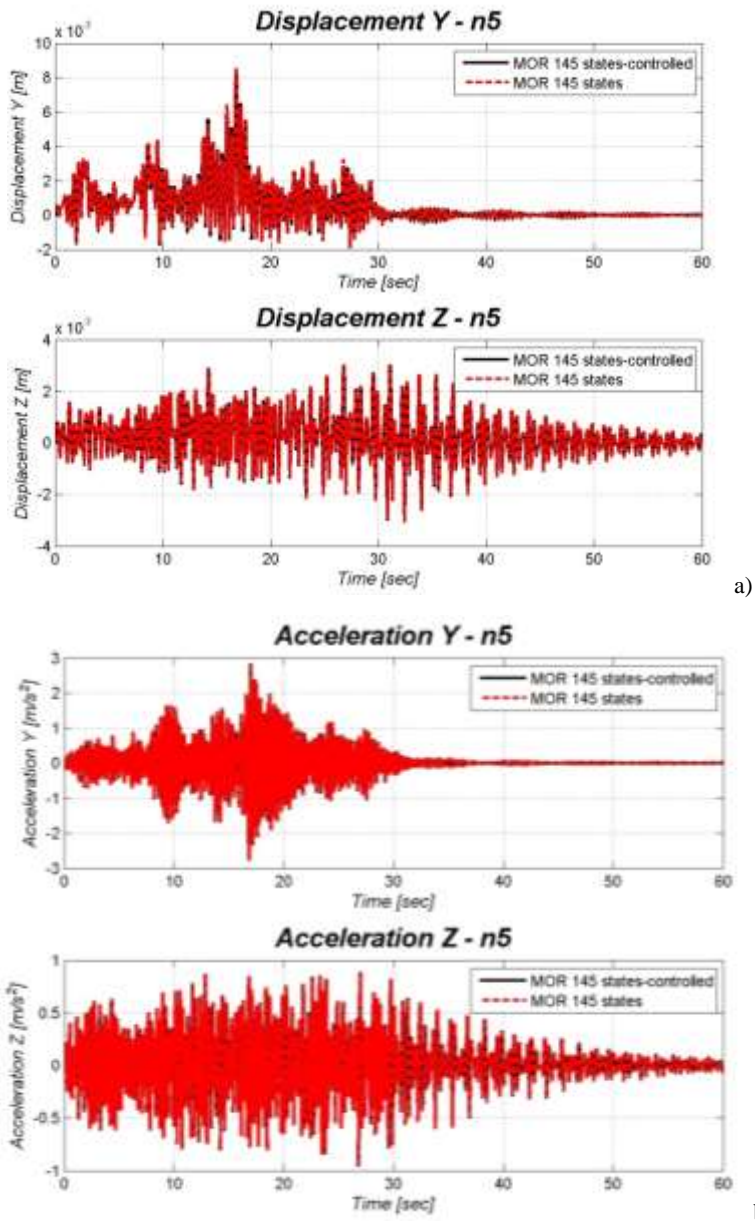


Figure 6.3.4. Active control solution for the “Trasaghis” footbridge - model MOR 145 states: comparison of uncontrolled vs. controlled. Response of: a) Displacements along Y and Z axes – node 5; b) Accelerations along Y and Z axes (zoom between 10 to 20 sec) – node 5.

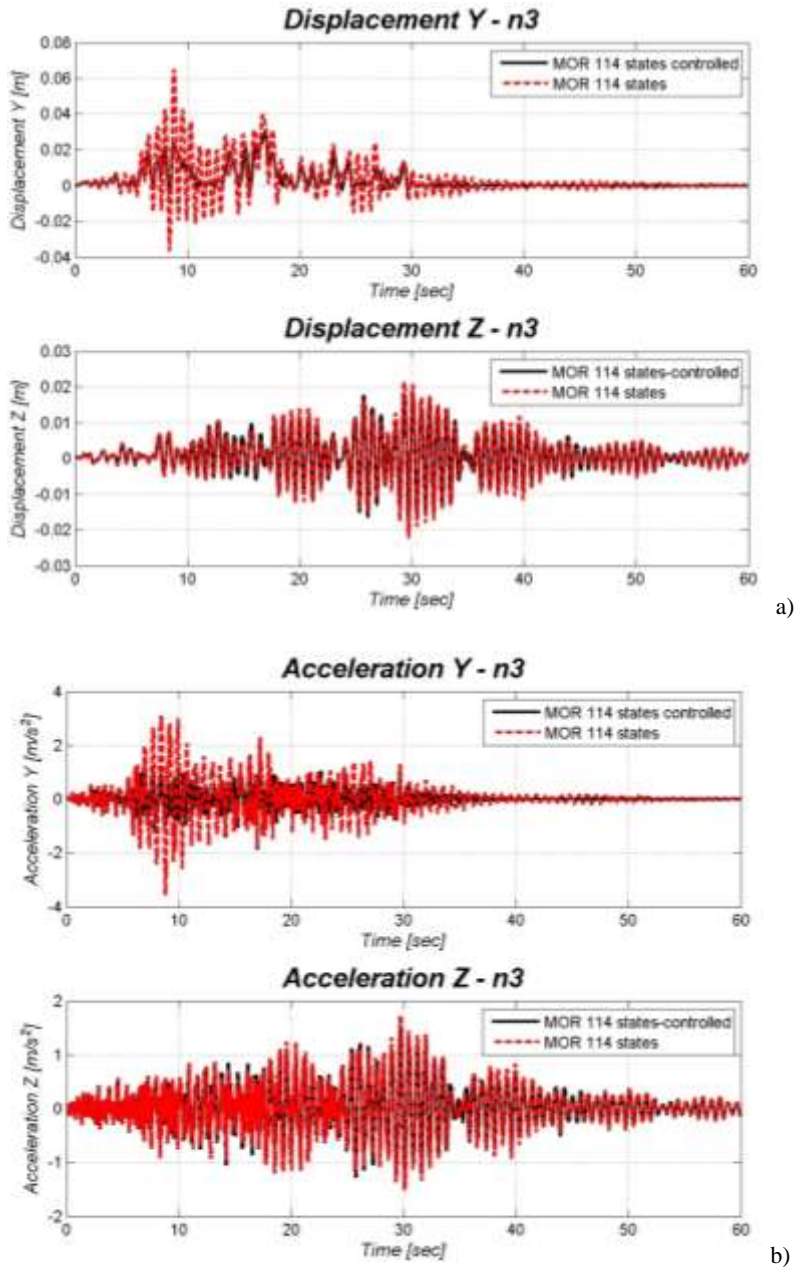


Figure 6.3.5. Active control solution for the “Trasaghis” footbridge - model MOR 114 states: comparison of uncontrolled vs. controlled. Response of: a) Displacements along Y and Z axes – node 3; b) Accelerations along Y and Z axes (zoom between 10 to 20 sec) – node 3.

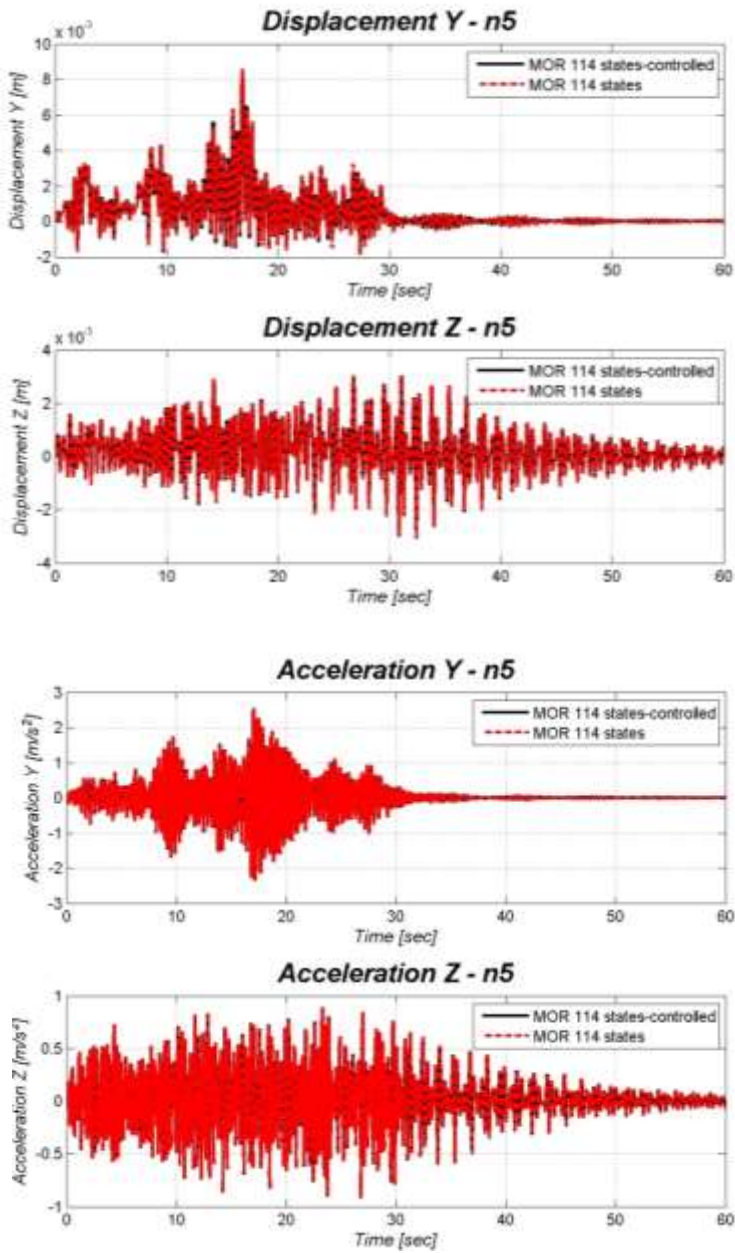


Figure 6.3.6. Active control solution for the “Trasaghis” footbridge - model MOR 114 states: comparison of uncontrolled vs. controlled. Response of: a) Displacements along Y and Z axes – node 5; b) Accelerations along Y and Z axes (zoom between 10 to 20 sec) – node 5.

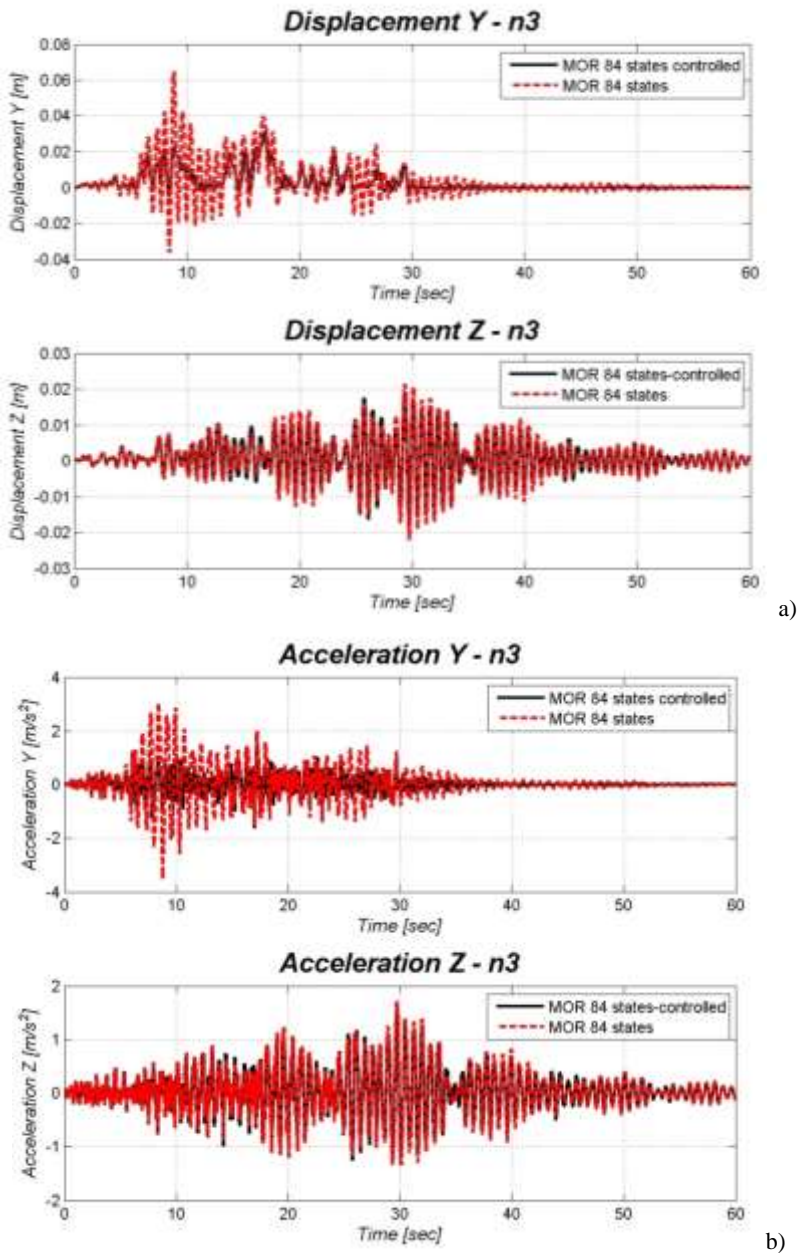


Figure 6.3.7. Active control solution for the “Trasaghis” footbridge - model MOR 84 states: comparison of uncontrolled vs. controlled. Response of: a) Displacements along Y and Z axes – node 3; b) Accelerations along Y and Z axes (zoom between 10 to 20 sec) – node 3.

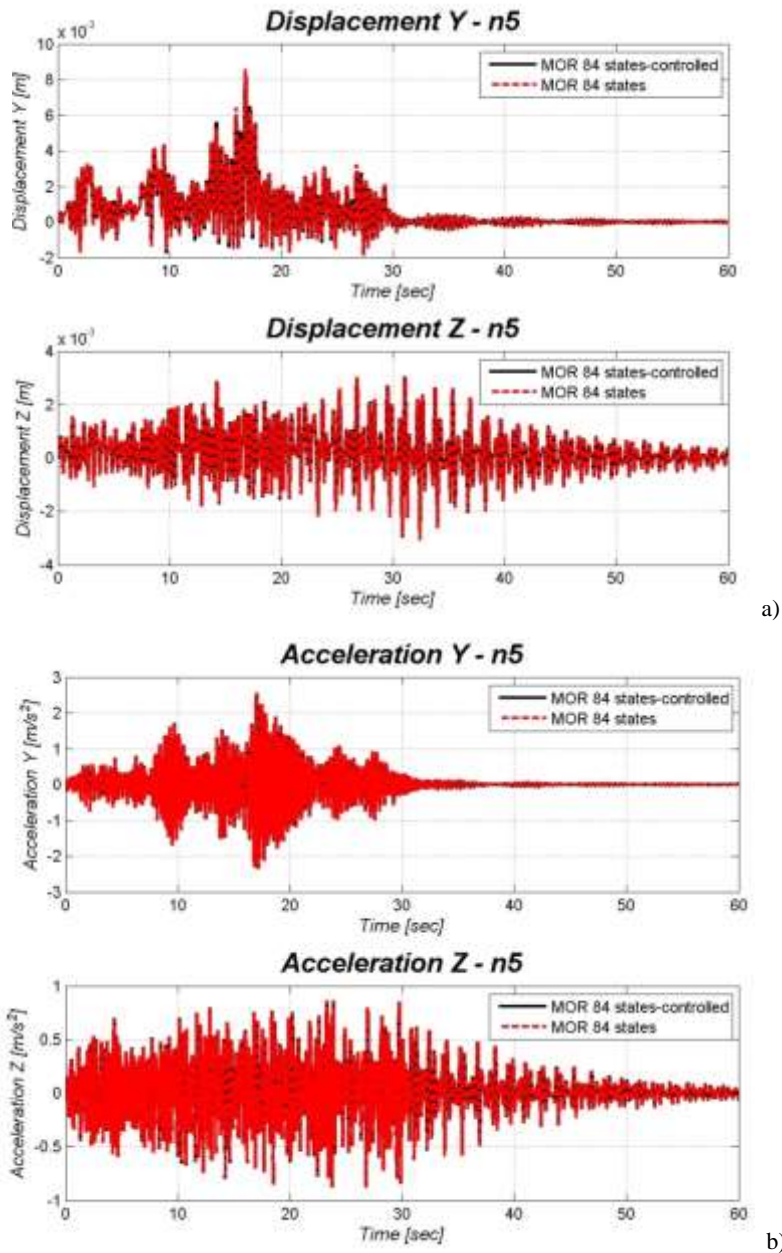


Figure 6.3.8. Active control solution for the “Trasaghis” footbridge - model MOR 84 states: comparison of uncontrolled vs. controlled. Response of: a) Displacements along Y and Z axes – node 5; b) Accelerations along Y and Z axes (zoom between 10 to 20 sec) – node 5.

Concluding, the active proposed structural control implemented for the wind vibration control of the “Trasaghis” footbridge seems to be consistent in terms both of quality and quantity of the vibrations reduction. The better results, due to the design choices about the control forces, are achieved for the reduction of the vibration along the transversal Y axis; while small advantage seems to appear along Z direction. Moreover the results shown, as expected, that the implementation of an active control solution allows to achieve better results in terms of vibrations mitigation compared with the other solutions previously analyzed [19].

6.4 References

- [1] Chu, S.Y.; Soong, T.T.; Reinhorn, A.M., 2005. Active, Hybrid and Semi-Active Structural Control. John Wiley & Sons. ISBN 0-470-01352-4.
- [2] Soong T.T., Dargush G.F., 2007. Passive Energy Dissipation Systems in Structural Engineering, John Wiley & Sons, Chichester, UK.
- [3] Bursi, O. S. , Bonelli A., Ceravolo R., Tondini N., Ussia A., 2011. Dynamic and Aeroelastic Behavior of a Twin Deck Curved Cable-Stayed Footbridge Equipped with Passive Devices. On the Proceedings of the Engineering Mechanics Institute 2011 Conference EMI 2011, Boston, USA, June 2-4, 2011, 366-379.
- [4] A. Tributsch and C. Adam, 2012. Evaluation and analytical approximation of Tuned Mass Damper performance in an earthquake environment. Smart Structures and Systems, Vol. 10, No. 2 (2012) 155-179.
- [5] Schmelzer, B., Oberguggenberger, M., Adam, C., 2010. Performance of Tuned Mass Dampers with uncertain parameters under stochastic excitation. On the Proceedings of the Institution of Mechanical Engineers, Part O: Journal of Risk and Reliability, 224, 4, pp. 298 - 308.
- [6] Ussia A., Bursi, O. S. , Bonelli A., 2012. Optimal Semi Active MR Control Strategies of a Footbridge Endowed with TMDs, smart structures, On the Proceedings of the 5th European Conference on Structural Control, EACS 2012, Genoa, Italy, June 18-20, 2012.
- [7] Casciati F. and Giuliano F., 2009. Performance of Multi-TMD in the Towers of Suspension Bridges, Journal of Vibration and Control, 15 (6), pp. 821-847.
- [8] Rana R. and Soong T.T., 1998. Parametric study and simplified design of tuned mass dampers, Engineering Structures, 20, pp. 193-204.

- [9] Abe, M. and Fujino, Y., 1994. Dynamic Characterization of Multiple Tuned Mass Dampers and Some Design Formulas. *Earthquake Engineering and Structural Dynamics*, 23, pp. 813-835.
- [10] Abe, M. and Igusa, T., 1995. Tuned Mass Dampers with Closely Spaced Natural Frequencies. *Earthquake Engineering and Structural Dynamics*, 24 , pp. 247-261.
- [11] Bandivadekar T.P, Jangid R.S., 2012. Mass distribution of multiple tuned mass dampers for vibration control of Structures. *International Journal Of Civil And Structural Engineering*, 3 (1).
- [12] www.mathworks.it
- [13] NTC 2008. Norme tecniche per le costruzioni (in Italian) - D.M. 14 Gennaio 2008.
- [14] www.mscsoftware.com
- [15] Warburton, G. B., 1982. Optimal Absorber Parameters for Various Combinations of Response and Excitation Parameters. *Earthquake Engineering and Structural Dynamics*, Vol. 10, pp. 381-401.
- [16] Casciati F, Magonette G. and Marazzi F., 2007. *Technology of Semiactive Devices and Applications in Vibration Mitigation*, John Wiley & Sons, Chichester, UK.
- [17] A. Preumont, 2004. *Vibration Control of Active Structures. An Introduction*, 2nd edition. Kluwer Academic Publishers. New York, Boston, Dordrecht, London, Moscow. ISBN: 1-4020-0496-6.
- [18] Schilders W.H.A., van der Vorst H.A., Rommes J. 2008. *Model Order Reduction: Theory, Research Aspects and Applications*, Springer.
- [19] C.M. Casado, I.M. Diaz, J. de Sebastian, A.V. Poncela and A. Lorenzana, Implementation of Passive and Active Vibration Control on an In-service Footbridge, *Structural Control and Health Monitoring*, 20,2013, pp. 70-87.

Chapter 7 Conclusions

In this thesis some control solutions for the vibrations mitigation of pedestrian timber bridges are studied and analyzed.

The main motivations of this thesis are:

- 1) the research in this field is still in progress and several researches all around the world are addressing the study of comfort problems, vibrations control, and so forth... in the area of pedestrian bridges;
- 2) the design process of the footbridge should include the effects of the so called Human Induced Loads (HIL) which are presently under investigation in view of an accurate modelling.

After a state of the art focused on contributions to international conferences held in 2014 on this theme and on existing codes and recommendations, two chapters are devoted to the numerical modelling of the structural system and of the actions, respectively.

Model Order Reduction is discussed in the fifth chapter, while the last chapter before these conclusions summarises the proposed passive and active control solutions conceived and designed within this work of thesis.

Two case studies have supported the numerical investigations. Their importance relies on the fact that those structural systems were fully identified by “*in situ*” experimental campaigns, designed and carried out by the author. Those structural systems were designed respectful of a structural code which only prescribes a static design for them. As a result control schemes are quite desirable in view of ensuring (enhancing) the comfort of the crossing persons (serviceability limit state).

In this thesis, however, there is also an effort to build a design procedure accounting for the induced vibrations which should be able to avoid control correction once the footbridge is put in service.

Appendix A: Technical details for the two footbridges used as case studies

In this chapter some technical details concerning the two footbridges used as case studies are discussed. In particular information on dimensions, materials, constructions techniques and stages, and so forth...are summarized.

In the first section the pedestrian bridge located, in the Trasaghis Municipality and labelled as “Trasaghis footbridge”, is reported. In the second session the pedestrian bridge, located in Farra d’Alpago Municipality and labelled as “Tesa footbridge”, is discussed.

A.1 Trasaghis footbridge

In the North-Eastern Italian region of Friuli, there is a mountain area (Gemona Municipality) which became world-wide famous in 1976 when shaken by a strong earthquake in the spring. The event was followed by a further significant shake in the late summer of the same year. Nevertheless, that area recovered from those catastrophic events and its economy is now strong with an important source coming from the tourism.

The local largest natural lake is called the “Lake of the three municipalities” (or the “Cavazzo Lake” – see the red circle in Figure A.1.1) with an emissary channel which was a barrier for the jogging activity across the surrounding park.

Thus, the designer in accordance with the owner authority, decided to link the two side of the outlet channel with a pedestrian bridge (Figure A.1.2). In particular, for both economical and environmental reasons, only eco-friendly materials (i.e. steel and timber) were adopted to harmonize the structure with the surrounding environment. Indeed, as explained later on, the use of reinforced concrete was limited only to the foundation components.

From the geometric point of view the span is about 83 m and the double- beam deck width is 4 m, of which 3.22 m represents the free crossing width (Figure A.1.3).

Two main materials were adopted for this structure:

- 1) glued laminated timber (GLT) element of high strength: according to DIN1052 code [1];
- 2) steel elements of high strength: according to UNI EN10025 code [2].



Figure A.1.1. Chorography at scale 1:25000: the map shows the lake and the emissary channel. The red circle indicates the bridge location.



Figure A.1.2. A general view of the "Trasaghis footbridge".

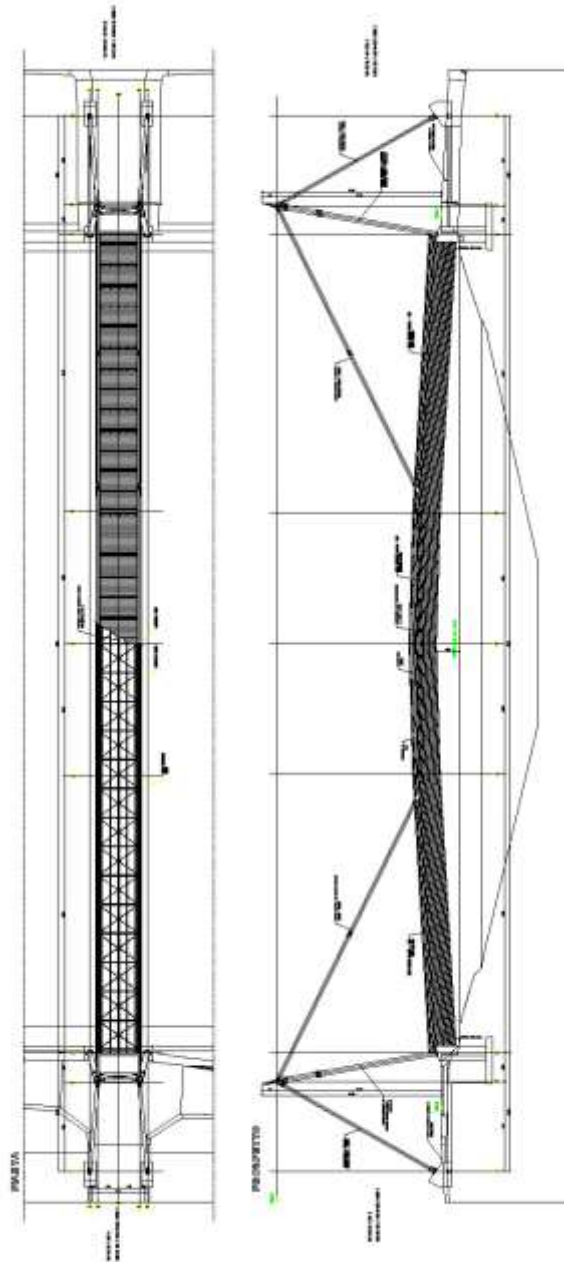


Figure A.1.3. Technical drawings of the footbridge.

Despite the bridge looks of the cable-stayed type (Figure A.1.2), the static scheme sees a vertical antenna on both sides but the usual cables are replaced by tubular steel elements.

The resistant scheme of the deck is made by two lateral main curved GLT beams, of cross-section 20 by 19.41 cm (Figure A.1.4), linked by a sequence of H shape¹⁹ transversal tubular steel elements of type S355JR. The transversal elements that realize the above H shape steel elements are 3.64 m long; each pair of them is braced with *ad hoc* steel elements to ensure the lateral stiffness of the footbridge. Moreover they support five longitudinal timber beams, of cross-section 12 by 16.30 cm, on which the walking tables made by GLT elements, 6.20 cm thick, are mounted and fixed by high-strength screws. More details are represented from Figure A.1.5 to Figure A.1.7.

About the timber materials, glued laminated timber of high strength GL28c is adopted for all structural elements, except for the walking deck made by glued laminated timber of type GL24c (see Figure A.1.6).



Figure A.1.4. Details of the main GLT beams: a) view during the construction stage; b) details of the joint connection.

¹⁹ Steel reinforcement: cross-section 22x12x0.63 cm gives the section of the transversal element.

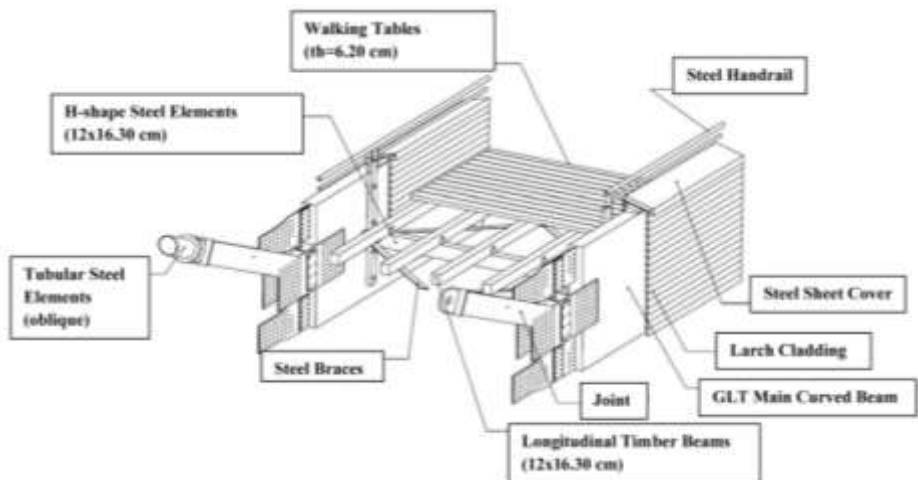


Figure A.1.5. Details of the deck cross-section resistant scheme.



Figure A.1.6. View from above of the structural scheme of the deck.



Figure A.1.7. Detail of the walking table during the construction stage.

For transportation and construction needs, the entire length of the footbridge is subdivided in three sections, each of about 25 m long. *Ad hoc* structural joint connection (Figure A.1.9) were designed and realized at each end of these three parts to allow the final “structural connection” once mounted. They also permit the connection with the steel oblique elements as described later on. It is worth underlining that all these structural elements were realized in factory and mounted *in situ*, limiting in this way the activity on the field, thus making the construction process more automatized (Figure A.1.10).

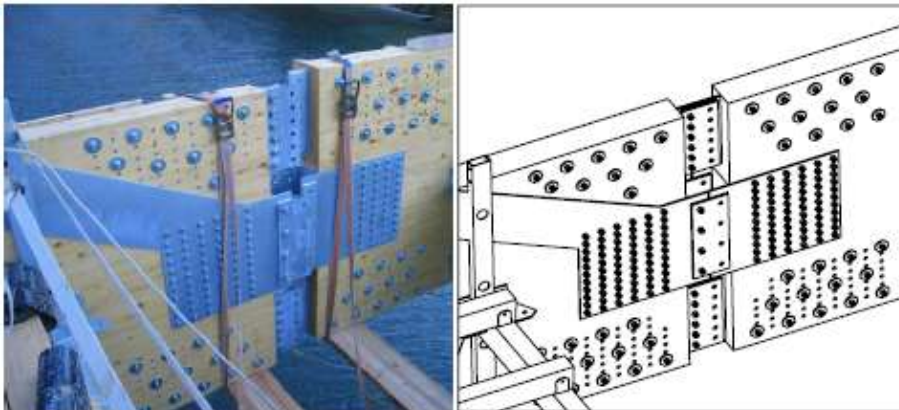


Figure A.1.8. Example of the structural joint connection: detail of the joint.



Figure A.1.9. Example of the structural joint connection: connection of the lateral section in correspondence of the steel oblique tubular element.



a)



b)

Figure A.1.10. Construction stage: assembling the central section of the footbridge. a) before the assembly; b) during the stage.

The two main GLT curved beams are anchored at the thirds (i.e. in correspondence of one of the structural joints described above) to the steel antennas on the two sides. The height of the antennas is about 15 m, and they are made by elements of tubular steel section of external diameter 45.75 cm and thickness 1.42 cm. The link

antenna-beam is made by elements of tubular steel section of external diameter 27.30 cm and thickness 8 mm (Figure A.1.11).

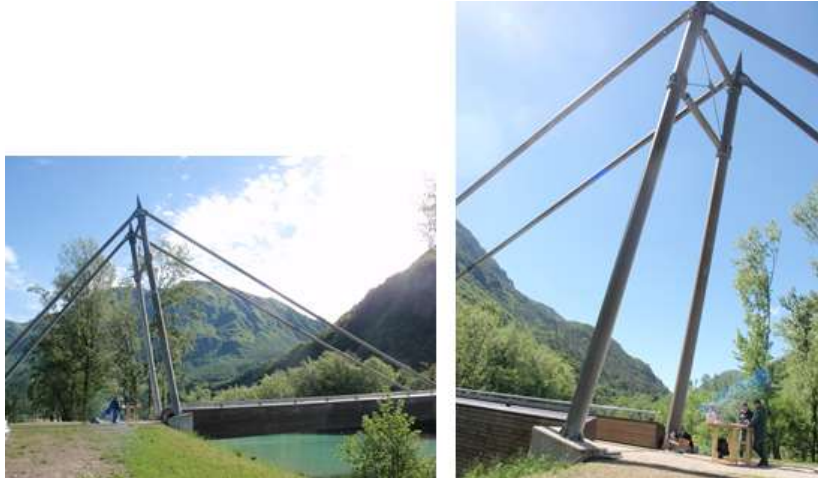


Figure A.1.11. A detail of the tubular steel oblique elements (left). A lateral view of the antenna (right).

Great importance has been given to the durability of the timber elements of this footbridge, especially against environmental, mold and so forth... attach. In fact, as one can see in Figure A.1.12, the external surface of the two main timber beams, are covered by a cladding made by larch planks. Moreover, in its upper side there is a layer of steel material used as water proof system against the rain.

The structural scheme is completed by the *neoprene* supports posed below each ends of the two main curved GLT beam. They allow the thermal deformation of the footbridge. An example of these supports is presented in Figure A.1.13.



Figure A.1.12. View of the upper protection system of the beam made by copper (left). A detail of the external larch cladding (right).



Figure A.1.13. View of the neoprene support.

From the prescriptive point of view, the pedestrian bridge is regarded as category 3 according with the Italian code [3]-[4]. This means that during the design stage beyond the usual “dead” loads, other two “live” loads have to be considered in a static configuration; in particular:

- 1) $q_{1,d}$ = isolated load of 10 kN over an area of 70 by 70 cm;
- 2) $q_{1,e}$ = distributed load of 4.0 kN/m² resulting from a dense people gathering.

In addition²⁰ to the above loads, the effects of snow, wind and earthquake were taken into account by the designer.

Once finished the construction stage, the static *proof test* required by the Italian regulation [3]-[4] was carried out. In addition to the dead loads due to the structural and non-structural elements of the footbridge, an additional loads provided by *ad hoc* devices was added (Figure A.1.14) up to the value suggested by the regulation: $q_{1,e} = 4.0$ kN/m². Once loaded the deck, the measurement of the vertical displacement of sensitive points along the footbridge due to the above loads (Figure A.1.15) was carried out. The maximum vertical displacement measured in the middle of the span was 14.5 cm.

²⁰ It is worth noting that for this structure no particular analysis/assessment of comfort was required during the design stage.

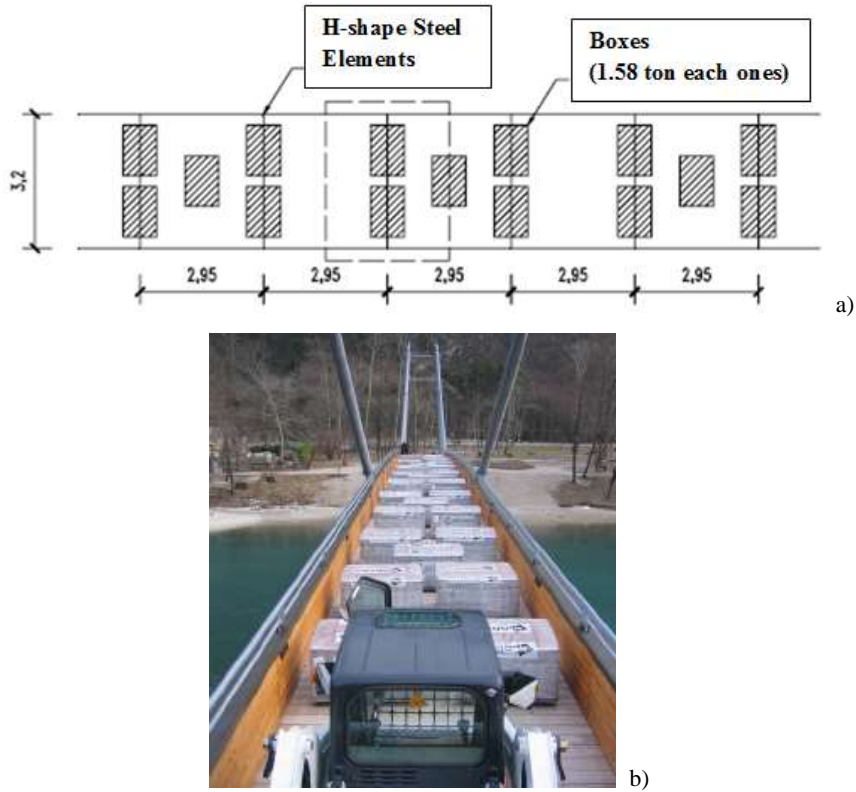


Figure A.1.14. Load test stage. a) Load configuration (measure in m); b) during the test (below).



Figure A.1.15. Measurement during the load test stage carried out.

To conclude the description of the “Trasaghis footbridge” some photographs are incorporated (from Figure A.1.16 to Figure A.1.21) to show the current state of the manufact.



Figure A.1.16. Lateral view of the Trasaghis footbridge.



Figure A.1.17. Frontal view of the Trasaghis footbridge.



Figure A.1.18. Detail of the structural joint between the GLT curved beam and the oblique steel tubular element.



Figure A.1.19. View of the reinforced concrete foundation system.



Figure A.1.20. View from above of the walkway. Detail of the H-shape steel element connection with the GLT curved beam.



Figure A.1.21. Detail of the connection between the GLT curved beam and the concrete foundation system.

A.2 Tesa footbridge

The footbridge reported in this section is located in Farra d'Alpago, an Alpine village close to the town of Belluno (Figure A.2.1). The bridge, built in 2005, connects the two sides of the outlet channel of the “Santa Croce” Lake, where a naturalist area is realized for jogging activities and so forth.



Figure A.2.1. a) Map of the location. The red circle indicates the bridge location. b) Satellite view of the area where the footbridge is located. The red line indicates the footbridge.

Again, to harmonize the structure with the surrounding naturalistic area, only eco-friendly materials (i.e. wood and steel) were adopted during the design stage, limiting the use of reinforced concrete only to the foundations (Figure A.2.2).



Figure A.2.2. Lateral view of the timber footbridge

From the geometric point of view the span is about 110 m and the double-beam deck shows a width of 3.20 m for the free crossing of the pedestrians (Figure A.2.3).

Two main materials are adopted for this structure:

- 1) glued laminated timber (GLT) element of high strength: according to DIN1052 code [1];
- 2) steel elements of high strength: according to UNI EN10025 code [2].

As one can see from Figure A.2.2, the static scheme of the bridge is the classic cable-stayed solution. In total, sixteen steel cables are adopted; in particular, eight “internal-secondary” cables of diameter 32 mm, and other eight “external-main” cables of diameter 44 mm (Figure A.2.4 clarifies the meaning of “internal” and “external”).

The two antennas, located on both sides of the footbridge, are about 16 m high and realized by steel tubular elements of diameter 45.72 cm and thickness 1.25 cm. Particular care was paid to the design of the connection between the cables and the deck and the antennas (Figure A.2.5).

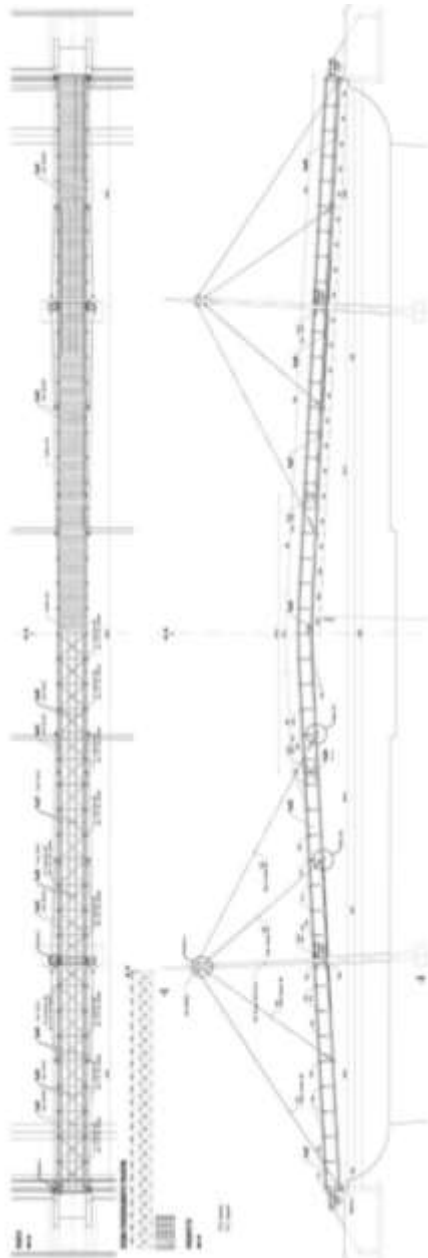


Figure A.2.3. Technical drawings of the footbridge.

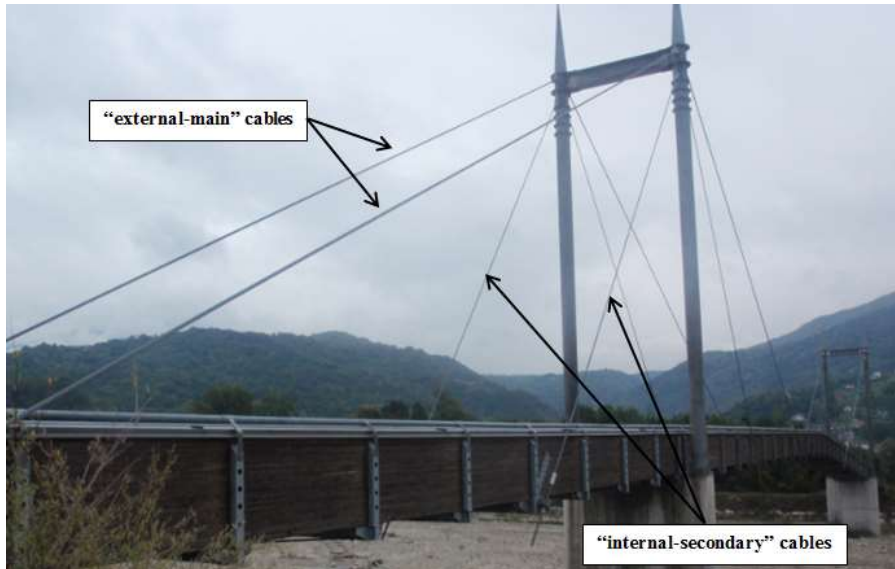


Figure A.2.4. Steel cables.



Figure A.2.5. Detail of the joint connection with the steel cables. Connection with antenna (left); connection with the deck (right).

From the static point of view the deck shows the classical “U-shape” cross section (Figure A.2.6). It is realized by linking two main curved GLT beams, located on the external side of the section, with transversal U-shape steel tubular elements (the vertical ones of dimension 100x120x5 mm, while the horizontal one 100x200x5 mm) of high strength S355J0 according to [2]. Moreover, these elements are connected by steel braces of circular cross-section that provide the lateral stiffness. The structural scheme

is completed mounting, on the “U-shape” elements, four longitudinal GLT rectangular beams (cross section 10x16.3 cm), used to carry the walking deck made of larch planking (thickness 4 cm). More details are reported in Figure A.2.7.

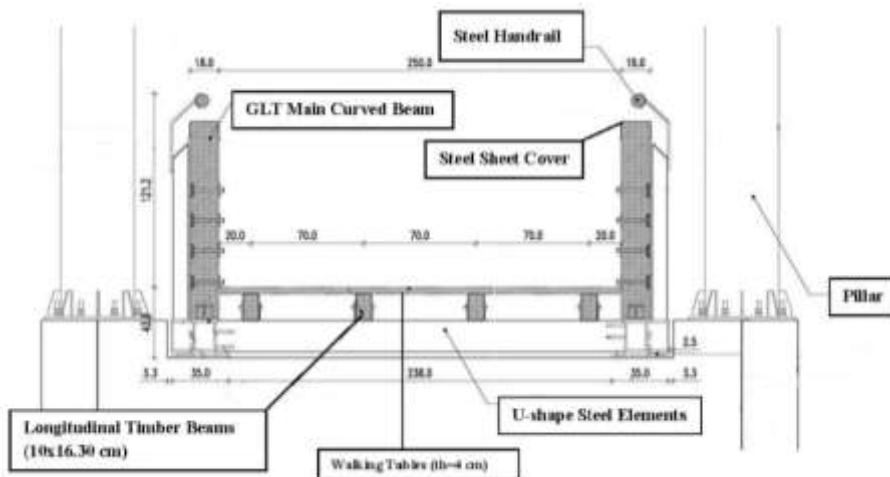


Figure A.2.6. Details of the deck cross-section resistant scheme.



Figure A.2.7. View from the bottom of the deck.

In order to guarantee the thermal deformation of the footbridge, at each ends of the two main GLT beam, *ad hoc* neoprene supports are posed (Figure A.2.8).



Figure A.2.8. Detail of the neoprene support.

The span length can be subdivided into three segments (each of them made of curved GLT-BS14 and GLT-BS16 beams – according to [1]) of length 22.5m, 65m (in the middle) and 22.5 m, respectively. *Ad hoc* structural joint connection (Figure A.2.9) were designed and realized at each ends of these parts to allow the final “structural connection” on field.



Figure A.2.9. Detail of the joints connection.

All these structural elements were realized in factory and mounted *in situ*, limiting in this way the activity on the field, i.e. making the construction process more automatized as possible (Figure A.2.10).



Figure A.2.10. Construction stage: assembling the central section of the footbridge. a) Before the assembly; b) during the stage.

Particular care was finally paid to the protection of the wood specimens; in particular *ad hoc* protective treatments against the attack of environmental agents (i.e. rain, snow, fungus, molds, and so forth) were used.

From the prescriptive point of view, the pedestrian bridge is regarded as category 3 according with the Italian code [3]-[4]. This means that during the design stage beyond the usual “dead” loads, other two “live” loads have to be considered in a static configuration; in particular:

- 3) $q_{1,d}$ = isolated load of 10 kN over an area of 70 by 70 cm;
- 4) $q_{1,e}$ = distributed load of 4.0 kN/m² resulting from a dense people gathering.

In addition²¹ to the above loads, the effects of snow, wind and earthquake were taken into account by the designer as prescribed by the design code.

Once was finished the construction stage the static *proof test* required by the Italian regulation [3]-[4] was carried out. In addition to the dead loads due to the structural and non-structural elements of the footbridge, an additional loads provided by *ad hoc* devices was added until to reach the load provided by the regulations: $q_{1,e} = 4.0 \text{ kN/m}^2$. Once loaded the deck, the measurement of the vertical displacement of sensitive points along the footbridge due to the above loads was carried out. The maximum vertical displacement measured in the middle of the span was 14.5 cm (Figure A.2.11).



Figure A.2.11. Survey operations during the load test.

²¹ It is worth underlining that for this structure no particular analysis/assessment of comfort were required during the design stage.

To conclude the description of the “Tesa footbridge” some photographs are incorporated (from Figure A.2.12 to Figure A.2.18) to show the current state of the footbridge.



Figure A.2.12. Lateral view of the footbridge.



Figure A.2.13. Frontal view of the footbridge.



Figure A.2.14. Detail of the upper protection of the main GLT arcuate beams.



Figure A.2.15. Detail of the internal support made by reinforced concrete.



Figure A.2.16. Cross-section of the deck.



Figure A.2.17. Detail of the connection of the cable with the ground.



Figure A.2.18. View of the walking deck.

A.3 References

- [1] DIN 1052: Design, Analysis and design of timber structures
- [2] UNI EN 10025: Hot rolled products of non-alloy steel for structural applications. Technical delivery conditions.
- [3] D.M. 16 gennaio 1996 – Norme tecniche per le costruzioni in zona sismica [In Italian].
- [4] Norme tecniche per le costruzioni - D.M. 14 Gennaio 2008 (NTC2008) [In Italian].

Appendix B: A standard model for the single pedestrian walking and running

In this chapter a standard model, proposed in the literature for the dynamic behaviour of a single pedestrian walking or running, is presented.

B.1 Dynamic behaviour of a single pedestrian

Different dynamic effects are induced by walking and running respectively. Indeed when the pedestrian is walking there is always one foot in contact with the ground, while during a running there is no contact between the alternate successive touching of one of the two feet (Figure B.1.1). Different persons walk with similar step frequencies [1], into the range 1.25 to 2.3 Hz, due to their similar physiological human constitution, but the step frequencies are influenced by the purpose of the movement and the traffic intensity (Table B.1.1).

The dynamic force induced, by a single pedestrian, can be represented by forces, due to the body mass movement, whose components in the three directions are denoted as put-down, rolling and push-off of the feet. The magnitudes of these forces depend on the step frequency and on the body weight. The lateral component is caused by the movement of the centre of gravity from one foot to the other. This kind of oscillation of the centre of gravity [2] introduces a dynamic force with half the walking frequency (Figure B.1.2). The longitudinal force (along the deck axis) characterises the retarding and the pushing walking period.

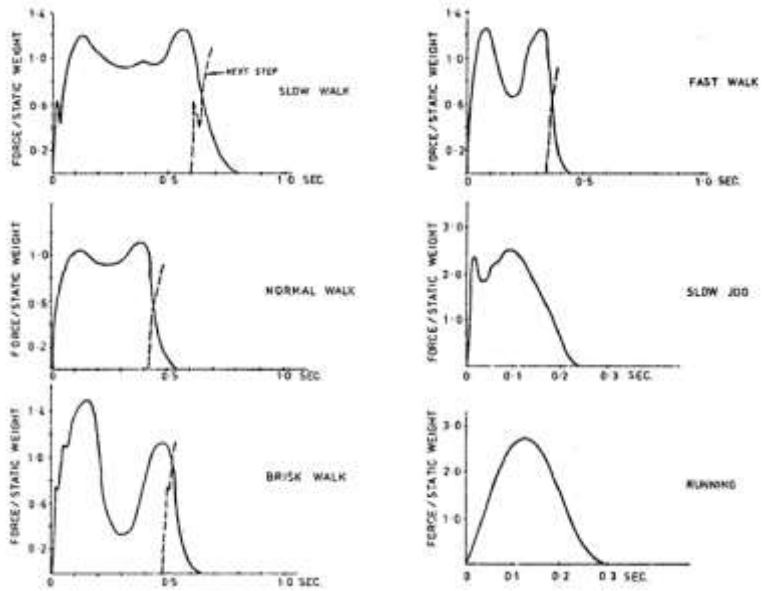


Figure B.1.1. Force trend due to different types of step [1].

Table B.1.1. Range of activities (top table). Typical values for step frequency (f_s), velocity (v_s) and step length (l_s) (bottom table) [1].

Activity	Group Size N ^o of people	Range of activity rate, Hz (Footsteps/s)	
		Normal Range	Measured Range
Pedestrian Movements			
Walking	1, 2 and 4	1.6 – 2.2	1.0 – 3.0
Jogging	1, 2 and 4	2.2 – 3.2	1.6 – 4.0
Rhythmic Exercises			
Jumping	1, 4 and 8	2.0 – 3.0	1.4 – 4.0
Stride Jumps	1, 2 and 4	2.0 – 2.6	1.6 – 3.4
Running-on-the-spot	1, 2 and 4	2.2 – 3.2	1.4 – 4.0

	f_s	v_s	l_s
	[Hz]	[m/s]	[m]
slow walking	1.7	1.0	0.60
normal walking	2.0	1.5	0.75
fast walking	2.3	2.3	1.00
normal running	2.5	3.1	1.25
fast running	>3.2	5.5	1.75

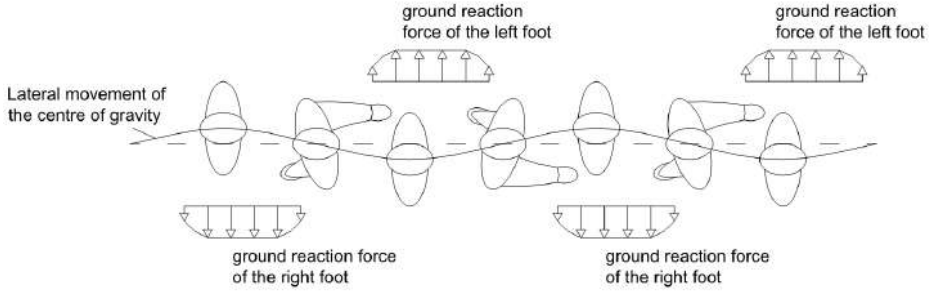


Figure B.1.2. Schematic representation of the lateral forces during the motion [2].

Time domain models are usually adopted for these forces [3]. One assumes that both human feet produce the same forces. The resulting periodic forces are represented by Fourier series as follows:

- vertical (gravity) direction (Figure B.1.3):

$$F_v(t) = P \left(1 + \sum_{n=1}^k \alpha_{n,v} \sin(2\pi n f_v t - \varphi_n) \right); \tag{B.1}$$

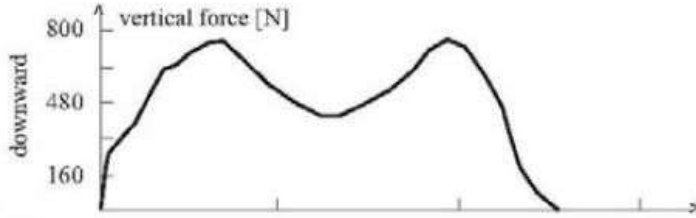


Figure B.1.3. Time history of the human induced force: vertical component [3].

- lateral (transversal) direction (Figure B.1.4):

$$F_{lat}(t) = P \sum_{n=1}^k \alpha_{n,lat} \sin(2\pi n f_{lat} t - \varphi_n); \tag{B.2}$$

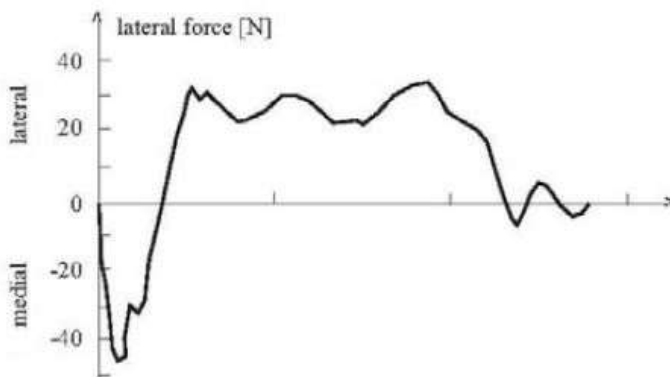


Figure B.1.4. Time history of the human induced force: lateral component [3].

- longitudinal (concordant to the deck axis) direction (Figure B.1.5):

$$F_{long}(t) = P \sum_{n=1}^k \alpha_{n,long} \sin(2\pi n f_{long} t - \varphi_n); \quad (\text{B.3})$$

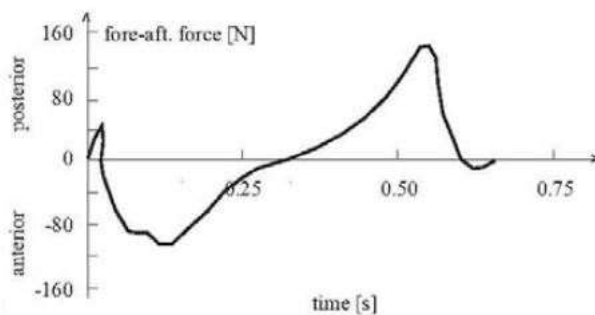


Figure B.1.5. Time history of the human induced force: longitudinal component [3].

where:

- $\alpha_{n,v}$, $\alpha_{n,lat}$, $\alpha_{n,long}$: numerical coefficients corresponding to the n th harmonic for vertical, lateral and longitudinal direction respectively;
- P : static load of the pedestrian;
- f : frequency component of repetitive loading (i.e. frequency of the motion);
- φ_n : phase angle of the n th harmonic;

- k : number of harmonics that characterize the forcing function in the frequency range of interest.

The usual value for the static load of the pedestrian is $P = 700$ N, while the number of the harmonics to be accounted depends on the forces under study. For the vertical component it is reasonable to assume $k = 1$ (Figure B.1.6), whereas for the two horizontal components it is better to consider $k = 3$ or 4 (Figure B.1.7).

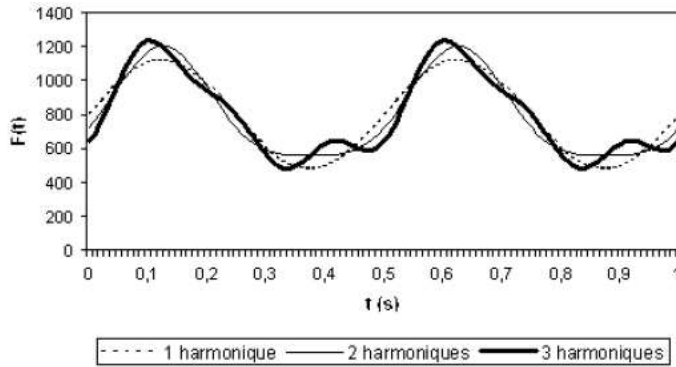
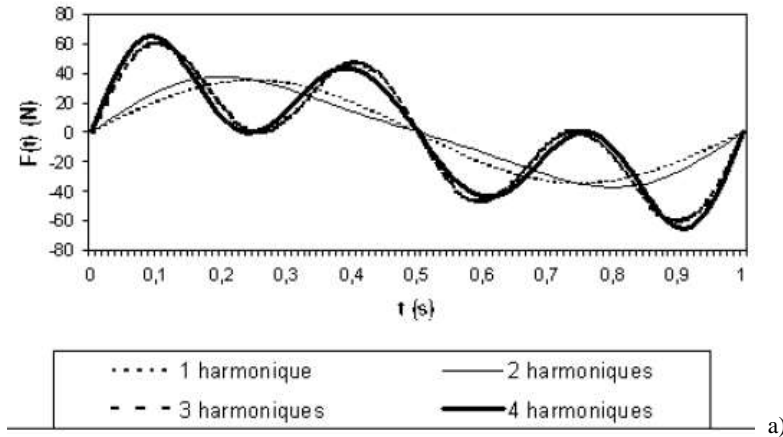


Figure B.1.6. Walking force: vertical component. Differences between three harmonics representation for walking step frequency $f=2\text{Hz}$ [3].



a)

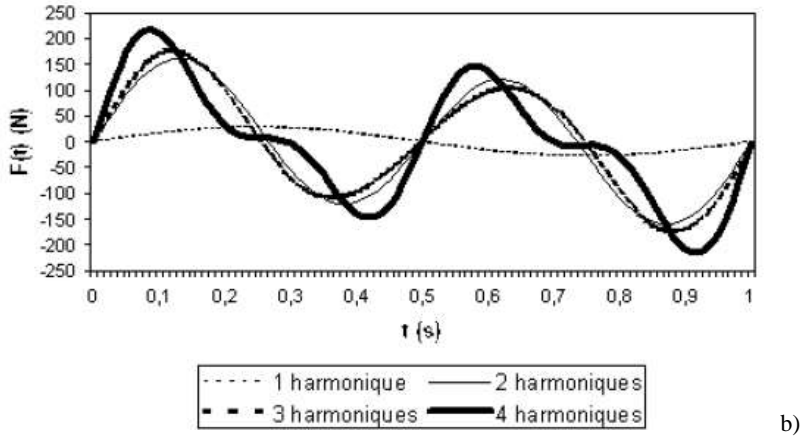


Figure B.1.7. Walking force. a) lateral component; b) longitudinal component. Differences between four harmonics representation for walking step frequency $f=2\text{Hz}$ [3].

The model of the pedestrian running is more complicated because the running depends more on the individual way of running and the type of shoes. These forces are characterised by a lift-off phase, during which no foot is in contact with the ground. Usually only the vertical component is taken into consideration because it has been observed as the horizontal components, both lateral and longitudinal, have a low “impact” on the dynamic response of the bridge when compared with the vertical one [3].

The vertical component is then modelled by Fourier transform as follows:

$$\begin{aligned}
 F_{r,vert}(t) &= P + \sum_{n=1}^k P_n \sin(2\pi n f_r t) \quad \text{for } (j-1)T_m \leq t \leq \left(j - \frac{1}{2}\right)T_m \\
 F_{r,vert}(t) &= 0 \quad \text{for } \left(j - \frac{1}{2}\right)T_m < t \leq jT_m
 \end{aligned}
 \quad ; \quad (\text{B.4})$$

where:

- P : static load of the pedestrian;
- j : the step number, $j=1,2,\dots, m$;
- f_r : running frequency;
- $T_m = \frac{1}{f_r}$: running period.

In this case, the phase shifts are assumed to be negligible. Three harmonics are usually adopted for the load representation (Figure B.1.8) and the amplitudes of the these harmonics are assumed as follows: $P_1 = 1.6 P_0$; $P_2 = 0.7 P_0$; $P_3 = 0.2 P_0$.

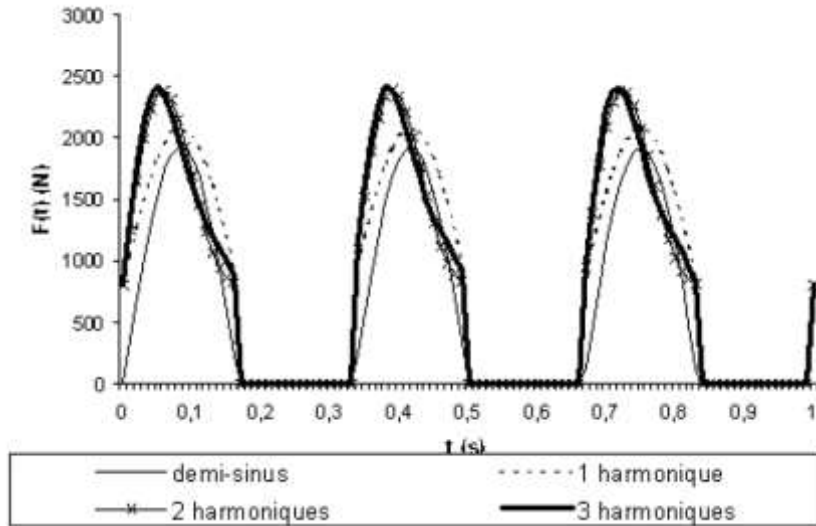


Figure B.1.8. Running force, vertical component. Differences between three harmonics representation for running step frequency $f=3\text{Hz}$ [3].

Different value of the Fourier coefficients for walking and running have been proposed by various authors and a review is presented in Table B.1.2 [4].

Table B.1.2. Different Fourier coefficients for walking and running [4].

Author(s)	Fourier coefficients / Phase angles	Comment	Type of activity and load direction
Blanchard et al.	$a_1 = 0,257$		Walking - vertical
Bachmann & Ammann	$a_1 = 0,4 - 0,5; a_2 = a_3 = 0,1$	for $f_p = 2,0 - 2,4$ Hz	Walking - vertical
Schulze	$a_1 = 0,37; a_2 = 0,10; a_3 = 0,12; a_4 = 0,04; a_5 = 0,015$	for $f_p = 2,0$ Hz	Walking - vertical
Bachmann et al.	$a_1 = 0,4/0,5; a_2 = a_3 = 0,1$	$f_p = 2,0/2,4$ Hz	Walking - vertical
	$a_1 = a_2 = a_3 = 0,1$	$f_p = 2,0$ Hz	Walking - lateral
	$a_{1/2} = 0,1; a_1 = 0,2; a_2 = 0,1$	$f_p = 2,0$ Hz	Walking - longitudinal
	$a_1 = 1,6; a_2 = 0,7; a_3 = 0,3$	$f_p = 2,0 - 3,0$ Hz	Running - vertical
	$\varphi_2 = \varphi_3 = \pi/2$		Walking - vertical & lateral
Kerr	$a_1, a_2 = 0,07; a_3 = 0,2$	a_1 is frequency dependant	Walking - vertical
Young	$a_1 = 0,37 (f_p - 0,95) \leq 0,5$ $a_2 = 0,054 + 0,0088 f_p$ $a_3 = 0,026 + 0,015 f_p$ $a_4 = 0,01 + 0,0204 f_p$	Mean values for Fourier coefficients	Walking - vertical
Charles & Hoorpah	$a_1 = 0,4$		Walking - vertical
	$a_1 = 0,05$		Walking - lateral
	$a_1 = 0,2$		Walking - longitudinal
ECS, DIN1074	$a_1 = 0,4; a_2 = 0,2$		Walking - vertical
	$a_1 = a_2 = 0,1$		Walking - lateral
	$a_1 = 1,2$		Jogging - vertical
Synpex findings	$a_1 = 0,0115f_s^2 + 0,2803 f_s - 0,2902$ $\varphi_1 = 0$ $a_2 = 0,0669f_s^2 + 0,1067 f_s - 0,0417$ $\varphi_2 = -99,76f_s^2 + 478,92 f_s - 387,8$ [°] $a_3 = 0,0247 f_s^2 + 0,1149 f_s - 0,1518$ If $f_s < 2,0$ Hz $\varphi_3 = -150,88 f_s^3 + 819,65 f_s^2 - 1431,35 f_s + 811,93$ [°] If $f_s \geq 2,0$ Hz $\varphi_3 = 813,12 f_s^3 - 5357,6 f_s^2 + 11726 f_s - 8505,9$ [°] $a_4 = -0,0039 f_s^2 + 0,0285 f_s - 0,0082$ $\varphi_4 = 34,19 f_s - 65,14$ [°]	Fourier coefficients and phase angles of step-by-step load model which represents mean human ground reaction forces	Walking - vertical

B.2 References

- [1] Guidelines for the design of footbridges. Fib bulletin 32, November 2005.
- [2] Heinemeyer, C., Butz, C., Keil, A., Mark, S., Goldack, A., Trometer, S., Lukić, M., Chabrolin, B., Lemaire, A., Martin, P., Cunha, Á., Caetano, E., 2009. Design of Lightweight Footbridges for Human Induced Vibrations. Background document in support to the implementation, harmonization and further development of the Eurocodes, JRC European Commission, Luxembourg.
- [3] Footbridges: assessment of vibrational behaviour of footbridges under pedestrian loading - Technical guide, 2006 – Sétra-AFGC.
- [4] Živanović, S. et al., 2005. Vibration serviceability of footbridges under humaninduced excitation: a literature review. *Journal of Sound and Vibration* 279, pp. 1-79.

Appendix C: Overview of some existing codes and guidelines

In this chapter more details on the guidelines introduced in *Chapter 2* about the comfort evaluation of footbridges are given.

C.1 ISO 10137

ISO 10137 [1] provides a series of principles for the prediction of the vibrational characteristics of a structure during the design stage. To assess the effects of the vibrations, it is important to specify to the type of vibration source, its location and the receiving element. The assessment of the response is evaluated by a numerical model. The document gives the designer the choice of the comfort of level to be considered, but states that pedestrian bridges must be so that the amplitude of the vibrations do not cause discomfort to users. In the absence of more definitive data, the code suggests the following maximum levels of vibration:

- in the vertical direction (z-axis): the vibrations should not exceed those obtained by a multiplicative factor of 60 in the selected reference system to the relevant base curve represented in Figure C.1.1. When one or more persons are at rest on the walkway the multiplicative factor of 30 should be applied.
- horizontal vibrations induced by pedestrian traffic or wind should not exceed 60 times the base curve for the horizontal direction (x and y- axis), see Figure C.1.2.

For the calculation of root-mean-square values of the acceleration, an averaging time of 1 s is recommended. Furthermore the following scenarios have to be considered during the calculation:

- one person walking across the walkway and another (the receiver) standing at mid-span;

- an average pedestrian flow based on a daily occurrence rate, e.g. a group size of 8 to 15 people, depending on the length and the width of the walkway;
- the presence of streams of pedestrians (significantly more than 15 persons);
- occasional festive or choreographic events (when relevant).

The document also suggests the dynamic forces produced by the pedestrians that has to be accounted in the design phase. The load induced by a singular pedestrian can be evaluated as:

- vertical direction: $F_v(t) = Q \left(1 + \sum_{n=1}^k \alpha_{n,v} \sin(2\pi n f_v t + \varphi_{n,v}) \right)$, (C.1)

- transversal direction: $F_h(t) = Q \left(1 + \sum_{n=1}^k \alpha_{n,h} \sin(2\pi n f_h t + \varphi_{n,h}) \right)$. (C.2)

The dynamic action of a group of N people is evaluated simply multiplying the above forces by the coefficient $C(N)$ (see Table C.1.1); that is:

$$F_N(t) = F(t) * C(N). \tag{C.3}$$

The details about the above formulas, coefficients and so forth... are not here reported for brevity.

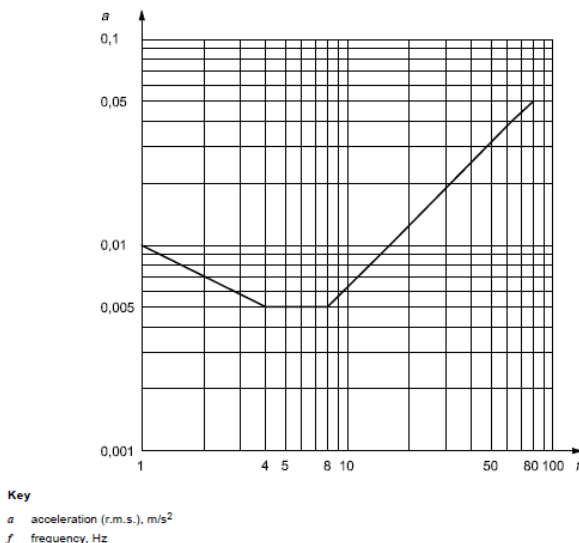


Figure C.1.1. Building vibration z-axis base curve for acceleration (foot-to-head vibration direction) [1].

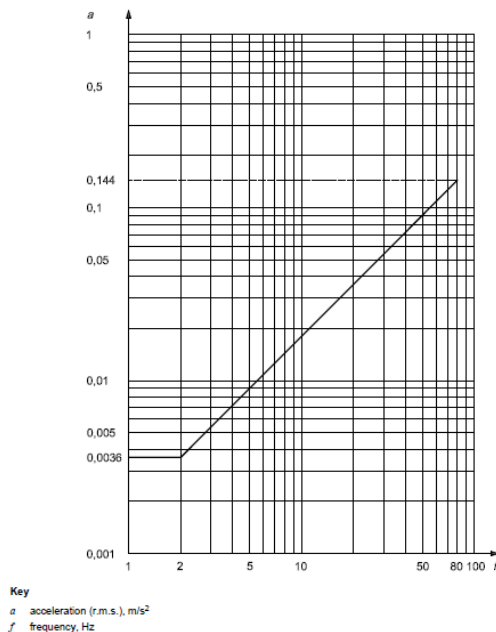


Figure C.1.2. Building vibration x- and y-axis base curve for acceleration (side-to-side and back-to-chest vibration direction) [1].

Table C.1.1. Coordination factor *C(N)* suggested by ISO 10137 [1].

Coordination	1st harmonic	2nd harmonic	3rd harmonic
high	0,80	0,67	0,50
medium	0,67	0,50	0,40
low	0,50	0,40	0,30

NOTE: These values of *C(N)* apply only to the serviceability limit state.

C.2 Fib-buletin 32

The guidelines [2] provide an available tool for the design of the footbridges, in particular with reference to the assessment of the maximum acceleration to be compared with the comfort limit value. For the dynamic analysis it is important to define the density of pedestrians (expressed as [pers/m²], which in turn influences the speed of pedestrians. Based on these guidelines the density is calculated as:

$$q = \frac{\lambda}{v_s \cdot b_{eff}}, \tag{C.4}$$

$$q = \frac{N_r}{L \cdot b_{eff}}, \tag{C.5}$$

where λ is the rate of pedestrian arrival [pers/s], v_s the velocity of pace [m/s], b_{eff} the effective width [m], N_r the number of pedestrians on bridge deck and L the length of bridge [m]. It was observed in [3] that in a pedestrian flow with a density varying between 0.3 and 0.6 pers/m², pedestrians are able to move undisturbed (Figure C.2.1). If the density increases, the single pedestrian is no longer able to move undisturbed but she/he is forced to modify her/his frequency and speed. In general the speed decreases with increasing density as reported in Figure C.2.2.

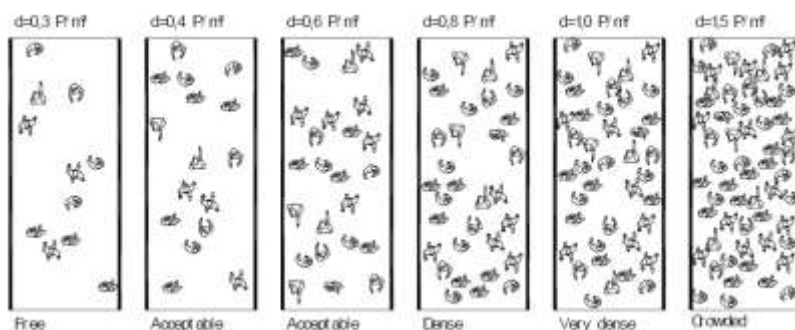


Figure C.2.1. Different scenarios of pedestrian densities [2].

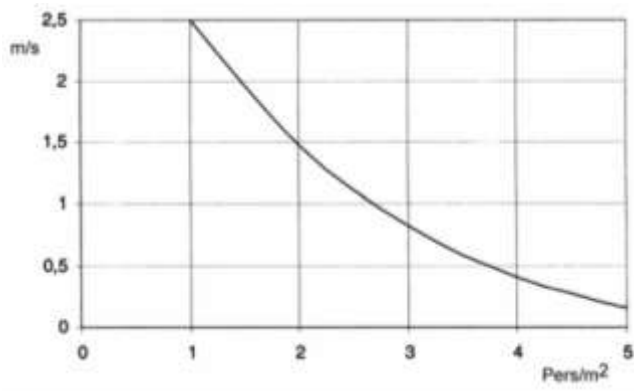


Figure C.2.2. Velocity versus density of pedestrian [2].

The first calculation method proposed by [4] and reported within this guideline is based on the resonant response of a 1-DOF oscillator, and determines the maximum vertical acceleration resulting from the passage of a pedestrian who walks or runs with a

frequency equal to the natural frequency of the bridge. The maximum acceleration can be evaluated as:

$$a = \phi(4\pi^2 f^2 y \alpha), \quad (\text{C.6})$$

where f is the vertical natural frequency of the bridge [Hz], y the static deflection at mid-span for a force of 700 N [m], α the Fourier coefficient of the relevant harmonic of the walking or running rate, ϕ the dynamic amplification factor (Figure C.2.3).

Another model is based on the experience by [5]. The working hypothesis of this method are:

- 1) single-degree-of-freedom (SDF) oscillator with stationary excitation;
- 2) step frequency $f_s =$ natural frequency of the bridge f ;
- 3) coefficient 0.6 due to changing excitation point.

In the above assumptions the maximum acceleration in [m/s^2] is defined as:

$$a = 0.6 \frac{\alpha G}{0.5M} \frac{\pi}{\delta} (1 - e^{-n\delta}), \quad (\text{C.7})$$

where G is the dead load of an ideal pedestrian (0.7 kN), M the mass in [t] of the equivalent 1-DOF oscillator for single span, δ the logarithmic decrement and n the number of cycles per span (span over step length).

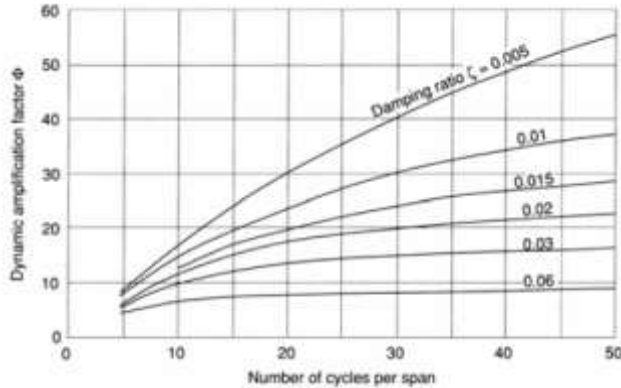


Figure C.2.3. Dynamic amplification factor for resonant response due to sinusoidal force moving across simple span [2].

The guidelines give moreover indications about vandalism loading, or repetitive jumping in order to excite the natural frequency of a bridge, can lead to very high values

of acceleration. Are suggested maximum limit of acceleration for footbridges of 0.7 g to 0.8 g. As already observed in section 1.2 this acceleration should be used during the design stage of the structure but not as a threshold for comfort. To prevent the lock-in effects the guideline suggests a threshold in lateral accelerations of 0.08 m/s^2 for a frequency of 1 Hz.

C.3 BS 5400

The British Standard BS5400, BD 29/04 and BD 37/01 [6] state that all the footbridges should satisfy the following minimum requirements:

- in the vertical direction the natural frequencies of the structure must have a value greater than 5 Hz;
- in the transverse horizontal direction the minimum frequency is fixed at 1.5 Hz.

If the fundamental frequency of vertical vibration, said f_0 , however, is less than or equal to 5 Hz, the maximum vertical acceleration a_v (expressed as m/s^2) of any part of the bridge has to be limited to:

$$a_v \leq 0.5\sqrt{f_0}. \quad (\text{C.8})$$

The maximum vertical acceleration may be calculated either by simplified method or by rigorous method. For complex structures, the maximum vertical acceleration must be calculated assuming that the dynamic load induced by a single pedestrian is that due to a concentrated force F , which moves through the span of the bridge at a constant speed $v_t = 0.9f_0$ [m/s], where:

$$F = 180\sin(2\pi f_0 t). \quad (\text{C.9})$$

If the fundamental frequency of the horizontal vibration is less than 1.5 Hz, great attention has to be paid to avoid the possibility to activate the lateral movement of the deck (the so called *lock-in* effects). The codes, however, do not propose any method to evaluate the maximum horizontal (transversal) acceleration.

C.4 Sétra-AFGC

These guidelines [7] present the main aspects that one has to consider during the design of the footbridge to avoid resonant phenomena in order to improve, or guarantee, an adequate level of comfort. Moreover these guidelines can be used in order to evaluate the comfort of existing bridges. The methodology of working is summarized in the flowchart in Figure C.3.1.

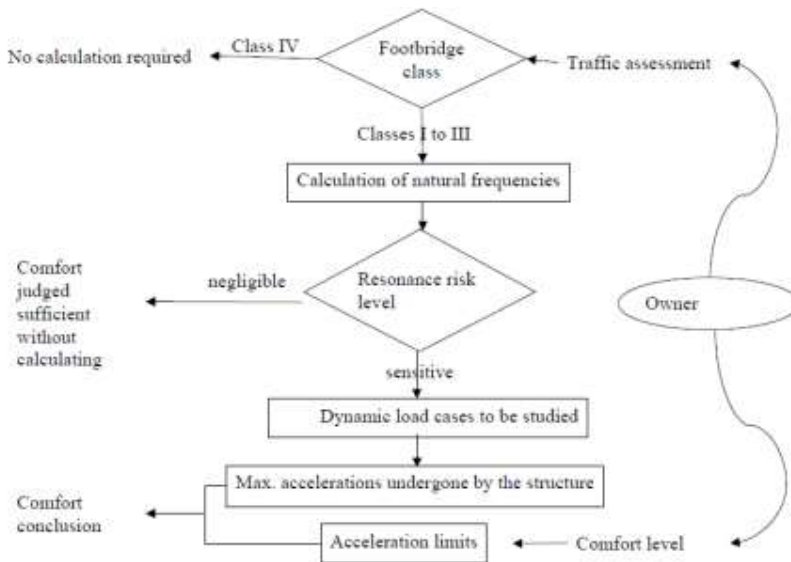


Figure C.3.1. Methodology flowchart proposed by Sétra-AFGC [7].

Operationally the proposed method can be summarized in the following five steps:

- 6) *step 1*: determination of the footbridge class;
- 7) *step 2*: choice of comfort level;
- 8) *step 3*: evaluation of the dynamic footbridge properties (if needed);
- 9) *step 4*: dynamic evaluation (if needed);
- 10) *step 5*: modification of the structural design to fulfil the comfort requirement (if needed).

About the classification of the footbridges, based on the expected (or measured) level of pedestrian traffic, it is possible to determine four classes:

- Class IV: seldom used footbridge, built to link sparsely populated areas or to ensure continuity of the pedestrian footpath across motorway or express lane areas.
- Class III: footbridge for standard use, that may occasionally be crossed by large groups of people but that will never be loaded throughout its bearing area.
- Class II: urban footbridge linking up populated areas, subjected to heavy traffic and that may occasionally be loaded throughout its bearing area.
- Class I: urban footbridge linking up high pedestrian density areas (for instance, nearby presence of a rail or underground station) or that is frequently used by dense crowds (demonstrations, tourists, etc.), subjected to very heavy traffic.

The owner has to determine the footbridge class. It is always possible to select a higher class to ensure/increase the comfort when needed. Class IV footbridges are considered not to require any calculation to check the comfort performance. Anyway for very light footbridges belonging to Class IV, at least Class III should be considered to ensure a minimum level of comfort for the users.

The three levels of comfort can be defined as follows:

- *maximum comfort*: accelerations are “imperceptible” to the users;
- *average comfort*: accelerations are merely perceptible to the users;
- *minimum comfort*: under seldom loading configurations, the accelerations undergone are perceived by the users, but do not become intolerable.

The choice of the comfort level is normally influenced by the attitude of the persons²² using the footbridge and by its level of importance according to *step 1*. The level of comfort is evaluated in reference to the acceleration undergone by the bridge using different dynamic load cases. Due to the subjective nature of the comfort concept, the guidelines present the comfortable limits in terms of four acceleration thresholds, see Table C.3.1 and Table C.3.2, for vertical and horizontal accelerations respectively. The first three ranges correspond to the maximum, mean and minimum comfort levels described in the previous section; while the 4th range corresponds to an uncomfortable situation.

²² In this choice the designer should be more demanding on behalf of particularly sensitive users as schoolchildren, disabled people and so forth..., and more tolerant in case of all those footbridges rarely used by pedestrians.

For the footbridges belonging to the Class as from I to III it is necessary to evaluate the dynamic features of the bridge (i.e. natural vibration frequency). These frequencies for the vertical, transverse horizontal and longitudinal horizontal direction, have to be determined in two different cases: empty footbridge (no pedestrian over the deck) and footbridge loaded by pedestrians (700 N/m²) throughout its bearing area. The ranges in which these frequencies are situated, see Table C.3.3 and Table C.3.4, make possible the assessment of resonance risk. Four ranges can be established: range 1 corresponds to the maximum risk of resonance, while range 4 corresponds to a negligible risk of resonance. In cases where the risk of resonance is considered negligible after the above check, comfort level is automatically considered sufficient.

Table C.3.1. Acceleration ranges (in m/s²) for vertical vibrations proposed by Sétra-AFGC [7].

Acceleration ranges	0	0.5	1	2.5
Range 1	Max			
Range 2		Mean		
Range 3			Min	
Range 4				

Table C.3.2. Acceleration ranges (in m/s²) for horizontal vibrations proposed by Sétra-AFGC. The acceleration is limited in any case to 0.10 m/s² to avoid lock-in effect [7].

Acceleration ranges	0	0.1	0.15	0.3	0.8
Range 1	Max				
Range 2			Mean		
Range 3				Min	
Range 4					

Table C.3.3. Frequency ranges (Hz) of the vertical and longitudinal vibrations [7][36].

Frequency	0	1	1.7	2.1	2.6	5
Range 1						
Range 2						
Range 3						
Range 4						

Table C.3.4. Frequency ranges (Hz) of the transversal vibrations [7].

Frequency	0	0.3	0.5	1.1	1.3	2.5
Range 1						
Range 2						
Range 3						
Range 4						

If the above evaluation shows the possibility of resonance risk a more detailed analysis must be carried out (*step 4*). In this case three different cases of dynamic loads have to be considered:

- **Case 1: sparse and dense crowds.**

This case regards the study of the pedestrian bridges belonging to Class II and III. The number of pedestrians involved, within the hypothesis crowd uniformly distributed over the deck, is equal to:

$$N = S * d , \tag{C.10}$$

in which S indicates the deck area, and d pedestrian density. For Class III footbridges the density d of pedestrian must be taken equal to 0.5 pedestrians/m²; while $d = 0.8$ pedestrians/m² for Class II footbridges. The equivalent number of pedestrians N_{eq} (all in phase and at the same frequency) able to produce the same effects on structure as random pedestrian is:

$$N_{eq} = 10.8 \sqrt{N \xi} , \tag{C.11}$$

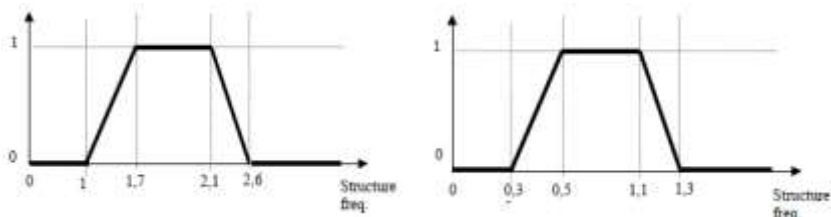
where ξ is the critical damping ratio (Table C.3.5).

Table C.3.5. Typical critical damping ratio [7].

Type	Critical damping ratio
Reinforced concrete	1.3%
Pre-stressed concrete	1%
Mixed	0.6%
Steel	0.4%
Timber	1%

Table C.3.6. Case 1 - Loads per unit of area proposed by Sétra-AFGC. Below: factor ψ for vertical and longitudinal vibrations on the left, and for lateral vibrations on the right [7].

Direction	Load per m ²
Vertical (v)	$d \times (280N) \times \cos(2\pi f_i t) \times 10.8 \times (\xi/n)^{1/2} \times \psi$
Longitudinal (l)	$d \times (140N) \times \cos(2\pi f_i t) \times 10.8 \times (\xi/n)^{1/2} \times \psi$
Transversal (t)	$d \times (35N) \times \cos(2\pi f_i t) \times 10.8 \times (\xi/n)^{1/2} \times \psi$



The loads summarized in Table C.3.6, have to be applied to the whole of footbridge, and the direction of the loads must agree with the direction of the mode under study in order to maximize the response in terms of vibration/accelerations of the bridge (Figure C.3.2).

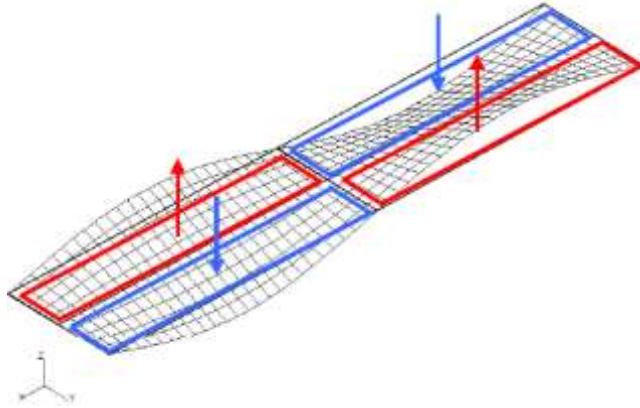


Figure C.3.2. Example of loads application: mode shape versus load direction [7].

- **Case 2: very dense crowds.**

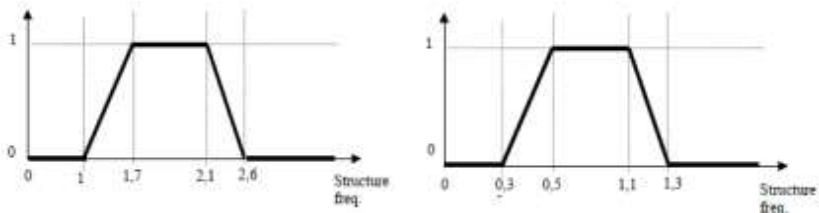
This case regards the study of Class I footbridges. In this application the density of pedestrian is assumed to be $d = 1.0$ pedestrians/m². The equivalent number of pedestrians N_{eq} is:

$$N_{eq} = 1.85\sqrt{N} . \tag{C.12}$$

The forces per unit of area to be applied in this situation are summarized in Table C.3.7.

Table C.3.7. Case 2 - Loads per unit of area proposed by S etra-AFGC. Below: factor ψ for vertical and longitudinal vibrations on the left, and for lateral vibrations on the right [7].

Direction	Load per m ²
Vertical (v)	$1.0 \times (280\text{N}) \times \cos(2\pi f_n t) \times 1.85 (1/n)^{1/2} \times \psi$
Longitudinal (l)	$1.0 \times (140\text{N}) \times \cos(2\pi f_n t) \times 1.85 (1/n)^{1/2} \times \psi$
Transversal (t)	$1.0 \times (35\text{N}) \times \cos(2\pi f_n t) \times 1.85 (1/n)^{1/2} \times \psi$



- **Case 3: effect of the second harmonic of the crowd.**

This case has to be taken into account only for Class I and II footbridges. It is similar to the two cases just presented, but in this case the second harmonic of the stresses caused by the pedestrian walking must also be accounted. The pedestrian density is assumed $d = 1.0$ pedestrians/m² and $d = 0.8$ pedestrians/m² for Class I and II respectively. Once again the crowd is considered to be uniformly distributed, but the individual force exerted by a pedestrian is reduced to 70N vertically, 7N transversally and 35N longitudinally. The correction factor ψ is presented in Figure C.3.3.

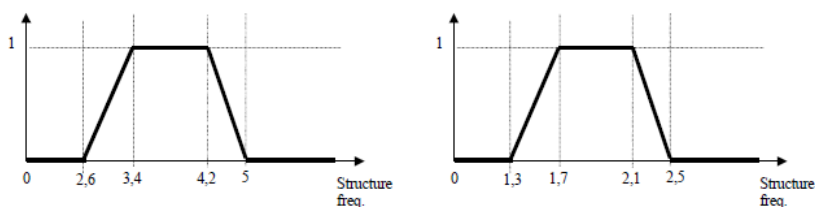


Figure C.3.3. factor ψ for vertical and longitudinal vibrations on the left, and for lateral vibrations on the right [7].

If the above calculation shows that the comfort level are not fulfilled, it is necessary to review the design of the footbridge (changing the natural frequency of the structure, or its stiffness), if we are in the design stage, or introducing *ad hoc* devices to reduce the vibration.

C.5 The comfort level in existing recommendations

To conclude this part related to the comfort for the footbridges (and civil structures in general), in Table C.3.1, Table C.3.2 and Figure C.3.1 a summary of the recommendations provided by the main international codes in terms of frequencies and acceleration limits, respectively, are presented. The synthesis is taken from reference [7].

Table C.3.1. Overview of the limit value of the acceleration according to the main international codes [7].

Vertical acceleration: $a_{v, \text{max}}$ [m/s ²]		
ISO 2631	$1.9 \cdot \sqrt{f_1}$	f_1 = fundamental natural frequency of the bridge
AISC Guide 11	0.5	
Eurocode 1	$\min \begin{cases} 0.50 \sqrt{f_b} \\ 0.70 \end{cases}$	for $f = 1$ to 3 Hz for $f = 3$ -5 Hz: check dependent on case from $f = 5$ Hz: no check necessary
DIN Fachbericht 102	$0.5 \cdot \sqrt{f_1} \cdot \text{vel.}$	for $f \leq 5$ Hz; f_1 = fundamental natural frequency of the unloaded bridge
VCI 2057	$0.6 \cdot \sqrt{f_1} \cdot \text{vel.}$ $0.214 \cdot \text{vel.}$	f_1 = fundamental natural frequency of the bridge
SBA	0.39	
BS 5400	$0.5 \cdot \sqrt{f_1}$	f_1 = fundamental natural frequency of the bridge
Ontario Bridge Code OH783	$0.25 \cdot f_1^{-0.5}$	f_1 = fundamental natural frequency of the bridge
Eurocode 5 (EN 1995-2)	0.7	
Bachmann [40]	0.5 - 1.0	
Japanese Footbridge Design Code (1979)	1.0	
Lateral acceleration: $a_{l, \text{max}}$ [m/s ²]		
Eurocode 1	$\min \begin{cases} 0.14 \sqrt{f_b} \\ 0.15 \end{cases}$	for $f = 0.5$ to 1.5 Hz for $f = 1.5$ -2.5 Hz: check dependent on case from $f = 2.5$ Hz: no check necessary
Eurocode 5 (EN 1995-2)	0.2	for $f = 2.5$ Hz (for the standing individuals)

Table C.3.2. Overview of the critical frequencies according to the main international codes [7].

Code Standard	Limit values	
	Vertical	Horizontal
American Guide Spec	< 3 Hz	
Eurocode 2 (ENV 1992-2)	1.6 Hz - 2.4 Hz	0.8 Hz - 1.2 Hz
DIN Fachbericht 102	1.6 Hz - 2.4 Hz, 3.5 Hz - 4.5 Hz	
Eurocode 5 (ENV 1995-2)	< 9 Hz	< 2.5 Hz
SBA (former East Germany)	1.0 Hz - 3 Hz	
QA 260 (Switzerland)	1.8 Hz - 4.5 Hz	= 1.3 transverse = 2.5 longitudinal
BS 5400 (Great Britain)	< 5 Hz	
Austrroads (Australia)	1.5 Hz - 3 Hz	
Japanese Footbridge Design Code (1978)	1.5 Hz - 2.3 Hz	

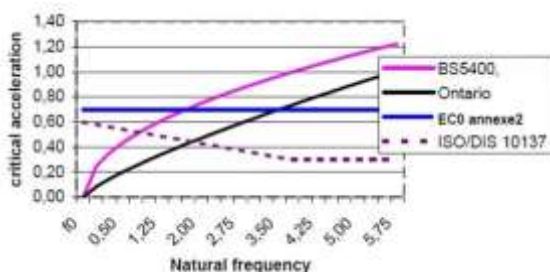


Figure C.3.1. Vertical critical accelerations (m/s^2) versus natural frequency (Hz) by various codes [7].

C.6 References

- [1] ISO 10137, Bases for design of structures - Serviceability of buildings and walkways against vibration, 2007.
- [2] Guidelines for the design of footbridges. Fib bulletin 32, November 2005.
- [3] Oeding, 1961. Verkehrsanalyse Fußgänger, Stadt Stuttgart Planungsamt, Abt. Verkehr (in German).
- [4] Rainer, J. H., Pernica, G. and Allen, D.E., 1987. Dynamic loading and response of footbridges. Structures Section, Institute for Research in Construction, National Research Council of Canada, Ottawa.
- [5] Grundmann H., Kreuzinger H., Schneider M., 1993. Schwingungsuntersuchungen für Fußgängerbrücken, Der Bauingenieur 68 (in German).

- [6] BS5400, Part 2, Appendix C, Vibration Serviceability Requirements for Foot and Cycle Track Bridges. British Standards Institution, 1978.
- [7] Footbridges: assessment of vibrational behaviour of footbridges under pedestrian loading - Technical guide, 2006 – Sétra-AFGC.

Appendix D: Crowd Load Model (CLM): experimental data set

In this chapter more details about the experimental data used for the validation of the crowd load model (see section 4.2) are given.

D.1 Time-Frequency analysis of the signals: theoretical background

The experimental campaign carried out on the “Tesa” footbridge (see section 3.1.1) is supported to provide the required information for the CLM model validation.

To better represent the data in order to reach a better resolution in terms of robustness and efficiency, the analysis is performed following the time-frequency procedure (the so called Short Time Fast Fourier Transform – STFFT) proposed by Choi-Williams (CW) [1]. This choice allows to identify the frequency variation over the time that can be associated to the interaction between the users (i.e. pedestrians motion over the deck) and the footbridge. From another point of view this approach identifies exactly the time at which one particular mode/frequency is activated. Furthermore, it is able to show visually the shift of the frequencies from lower to higher values; that is the transfer of energy from lower to higher modes, can be detected.

Following the procedure proposed by Cohen [2], let t denote the time and ω the pulsation, the time-frequency distribution can be written as:

$$P(t, \omega) = \frac{1}{4\pi^2} \iint \int_{-\infty}^{+\infty} \left[e^{-i\theta(t-u)} \Phi(\theta, \tau) \right] e^{-i\tau\omega} R_{t,1}(t, \tau) du d\tau d\theta \quad (D.1)$$

where:

- u and τ replace t , θ replace ω when integrating;
- $\Phi(\theta, \tau) = e^{-\frac{\theta^2 \tau^2}{s}}$ with $(s \in R)$, is the kernel function of CW distribution;

- $R_{t,1}(t, \tau) = x(u + \tau/2)x^*(u - \tau/2)$ is the autocorrelation function in which $x(t)$ is the input signal, t the time and $u = t + \tau/2$.

Introducing now the Fourier transform $W(t-u)$ for the above kernel function in equation (D.1):

$$P(t, \omega) = \frac{1}{4\pi^2} \int \int_{-\infty}^{+\infty} W(t-u) e^{-i\tau\omega} R_{t,1}(t, \tau) du d\tau; \quad (D.2)$$

As an example the time-frequency analysis is performed for the test carried out on “Tesa2 footbridge, and labelled as *test B3* (see section 3.1.1). The main results for the data acquired by sensor WSa2 (see Figure 3.1.3) along the transversal (Y) and gravity (Z) axis are summarized in Figure D.1.1 and Figure D.1.2 respectively.

During this test, only one frequency clearly appears at 1.35 Hz, and it is constant over the entire duration of the data acquisition. Another frequency appears at 5.00 Hz in the time period between 50 and 70 sec for the right-to-left crossing, and in the time period from 100 to 160 sec for the left-to-right crossing. This plot shows many vertical lines; in particular, one can observe that in the time period between 125 and 140 sec, there is a consistent frequency shift, due to the overlapping of the waves associated to the movement of the pedestrians from the sides toward the mid-span. Also along the Z axis only one frequency clearly appears at 2.00 Hz, and it is activated in the time period between 50 and 80 sec for the right-to-left crossing, and between 100 and 160 sec for the left-to-right crossing. Moreover one more frequency of 6.00 Hz seems to be “slightly” activated between 50 and 70 sec for the right-to-left crossing, and between 130 and 150 sec for the left-to-right crossing.

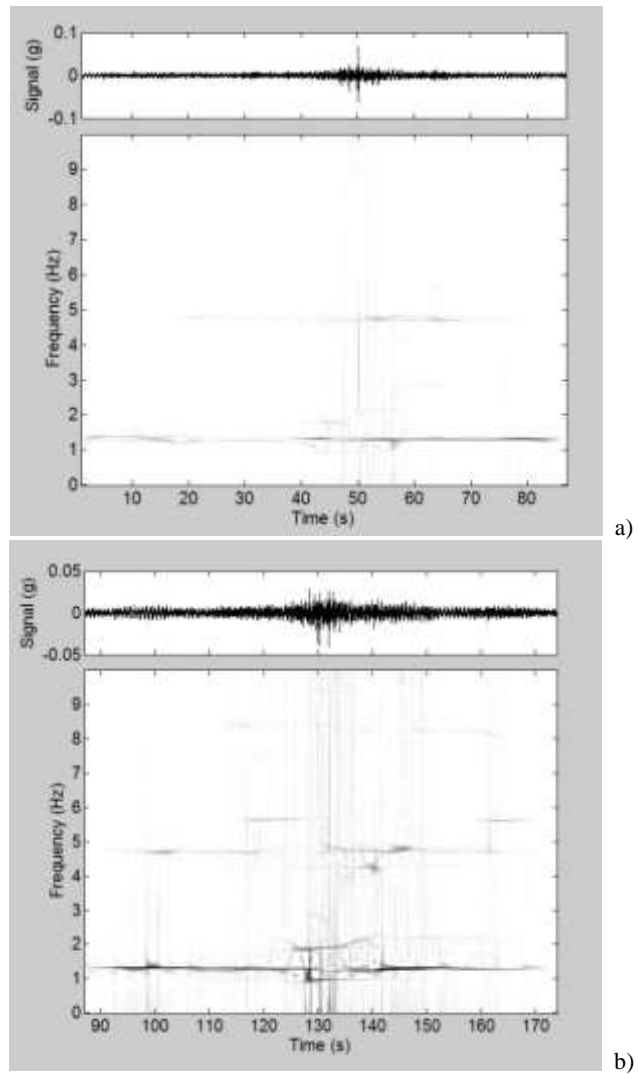


Figure D.1.1. Six persons walking. Time-frequency plots from the data recorded by sensor WSa2 along transversal (Y) axis. a) data from right-to-left crossing; b) data from left-to-right crossing.

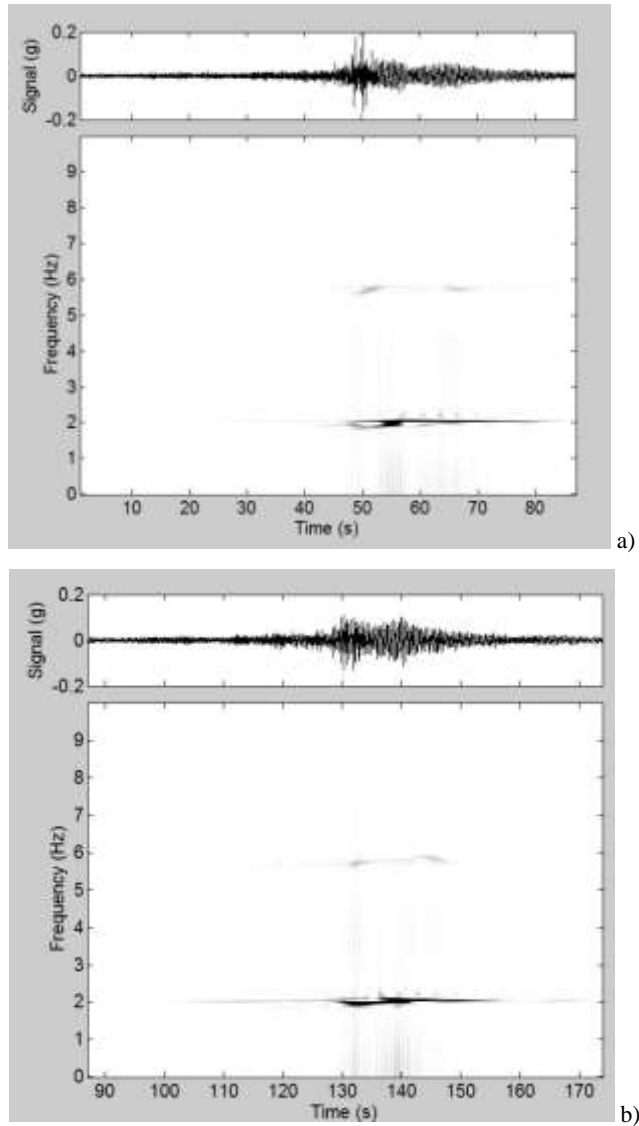


Figure D.1.2. Six persons walking. Time-frequency plots from the data recorded by sensor WSa2 along gravity (Z) axis. a) data from right-to-left crossing; b) data from left-to-right crossing.

D.2 Experimental data analysis

To validate the proposed CLM model, it is necessary to identify a set of experimental data that will be compared with the numerical simulation. By the way, in this section, the data acquired during the *tests B* presented in section 3.1.1 are analyzed and discussed. To give an easier interpretation of these data, each record is classified into two different sets: crossing from the right to the left side of the footbridge (labelled as *RtoL*), and from the left to the right side (labelled as *LtoR*) ([3] and [4]).

To have a clear idea about the acquired data, the numerical analysis of the data are performed following the time-frequency technique (STFFT) presented in the previous section.

Here below the results achieved by the analysis are discussed.

- *test B1*

This test consists of collecting records of the accelerations of the footbridge due to a round trip along the deck. The mass of the person is 85 Kg. Further details about this test are summarized in Table D.2.1. The results achieved for the measurements taken by sensor WSa2 along the transversal *Y* and vertical (gravity) *Z* axes are plotted in Figure D.2.1 and Figure D.2.2 respectively.

Table D.2.1. Walking (round trip) of one person.

<i>Type</i>	<i>ID</i>
Day/Time	November 7, 2013 / 2.48 pm
Test type	walking (round trip)
Air temperature	15°C
Pedestrian(s) num.	1 person
Total Pedestrian(s) mass	85 Kg
Total time duration	≈2:30 min
<i>RtoL</i> time duration	≈1:15 min
<i>LtoR</i> time duration	≈1:15 min
Average velocity of the pedestrian(s)	1.45 m/s

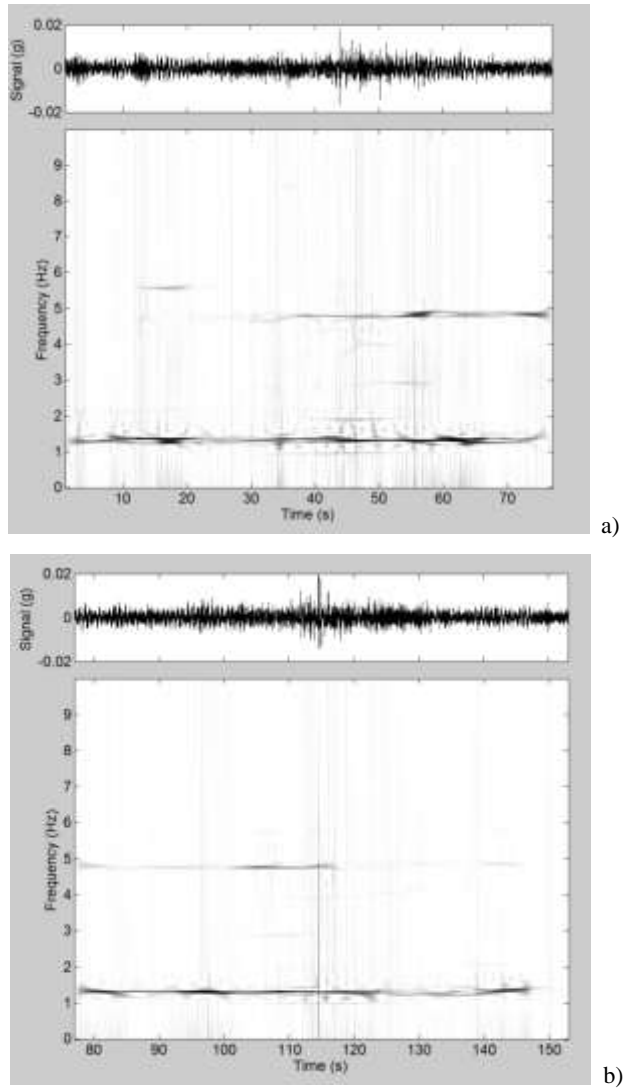


Figure D.2.1. Time-frequency plot from the data taken by sensorWSa2 along Y transversal axis during *test Ia*. a) *RtoL* data ; b) *LoR* data

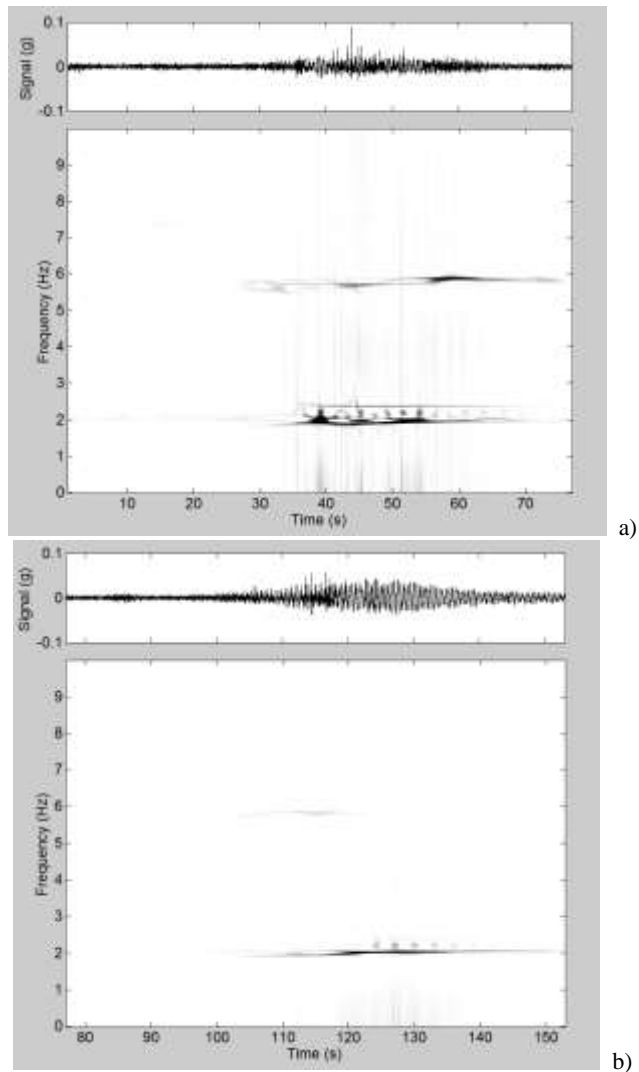


Figure D.2.2. Time-frequency plots from the data taken by sensor W Sa2 along Z gravity axis during *test Ia*. a) *RtoL* data ; b) *LtoR* data

The following three main frequencies (average values) appear along Y axis:

- 1.35 Hz: constant over the time;
- 5.00 Hz: it activates only during the time period from 30 to 70 sec for the *RtoL*, and from 80 to 120 sec for the *LtoR*. This means that this particular

frequency is detected when the pedestrian is located about 15-20 m before the position of the sensor WSa2;

- 5.80 Hz: it activates only during the time period from 10 to 32 sec for the *RtoL*.

Several vertical lines (mostly located between 35 and 60 sec), that represent the shifts in terms of frequencies, appear during the *RtoL* crossing, while they disappear during the *LtoR* crossing. These shifts can be related to noise into the signal due to the overlapping of the waves associated to the movement of the pedestrian from the sides towards the mid-span.

Instead, along *Z* axis two main frequencies (average values) appear:

- 2.00 Hz: it activates during the time periods from 35 to 70 sec for the *RtoL*, and from 105 to 150 sec for the *LtoR*. This means that this particular frequency is detected while the pedestrian is located about 10 m before the position the sensor WSa2 and about 40 m after it;
- 6.00 Hz: it activates only during the time period from 30 to 70 sec for the *RtoL*. Once again, this means that this particular frequency is detected while the pedestrian is located about 10 m before the position the sensor WSa2, and about 40 m after it. During the *LtoR* crossing, this frequency almost disappears.

One can observe that, also for the results along the *Z* axis, the time-frequency plot for the *LtoR* crossing is more “clear/clean” with respect to the *RtoL* crossing. Moreover, the time-frequency plots along the *Z* axis show, in general, a clear trend compared with the ones along the transversal *Y* axis.

- **test B2**

The records of a round trip of four persons along the deck are considered. The average mass is 75 Kg. The pedestrians proceed in pairs by keeping a distance of 1 m between each other in the longitudinal direction of the footbridge, and a distance of about 0.5-0.7 from the closest lateral edge of the footbridge (Figure D.2.3). More details are summarized in Table D.2.2.

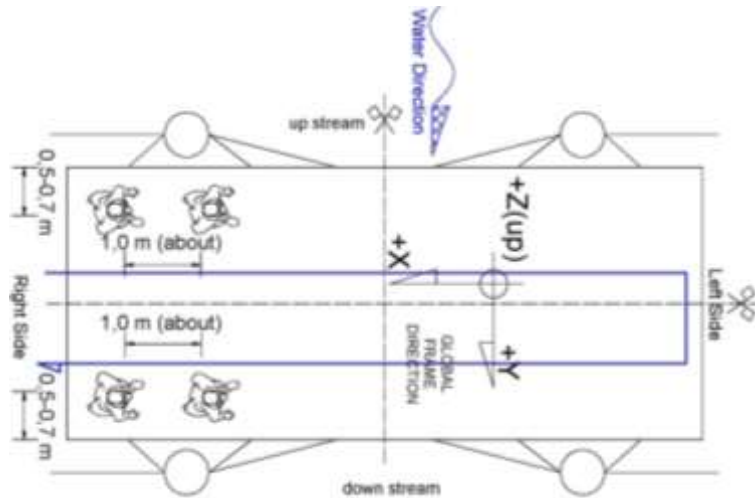


Figure D.2.3. Configuration of the walking test B2.

Table D.2.2. Walking (round trip) of four persons.

Type	ID
Day/Time	November 7,2013 / 2.55 pm
Test type	walking (round trip)
Air temperature	15°C
Pedestrian(s) num.	4 persons
Total Pedestrian(s) mass	300 Kg
Total time duration	≈2:45 min
RtoL time duration	≈1:23 min
LtoR time duration	≈1:20 min
Average velocity of the pedestrian(s)	1.33 m/s

The results achieved for the measurements taken by sensor WSa2 along the transversal Y and vertical (gravity) Z axes are plotted in Figure D.2.4 and Figure D.2.5 respectively.

Along Y axis two main frequencies (average values) appear:

- 1.35 Hz: constant over the time;
- 5.00 Hz: it activates during the time period from 40 to 70 sec for the $RtoL$, and from 80 to 140 sec for the $LtoR$. This means that this particular frequency is

detected when the pedestrian is located about 15-20 m before the position of the sensor WSa2.

One can observe, moreover, that several vertical lines (mostly located between 46 and 60 sec and between 120 and 130 sec), which represent the frequency shifts, appear during both the *RtoL* and the *LtoR* crossings. Furthermore one more frequency of about 2.00 Hz appears at about 130 sec up to the end of the record. All these facts can be related, as previously observed, to the overlapping of the waves associated to the movement of the pedestrians from the sides towards the mid-span of the bridge.

Along *Z* axis the results appear are more “clear/clean”, and in particular only two main frequencies (average values) are highlighted:

- 2.00 Hz: it activates during the time period from 35 to 70 sec for the *RtoL*; and from 110 to 160 sec for the *LtoR*. This means that this particular frequency is detected while the pedestrian is located about 10 m before the position of sensor WSa2, and about 40 m after it;
- 6.00 Hz: it activates during the time period from 30 to 70 sec for the *RtoL* only. This means that this particular frequency is detected while the pedestrian is located about 10 m before the position of sensor WSa2, and about 40 m after it. During the *LtoR* crossing this frequency almost disappears.

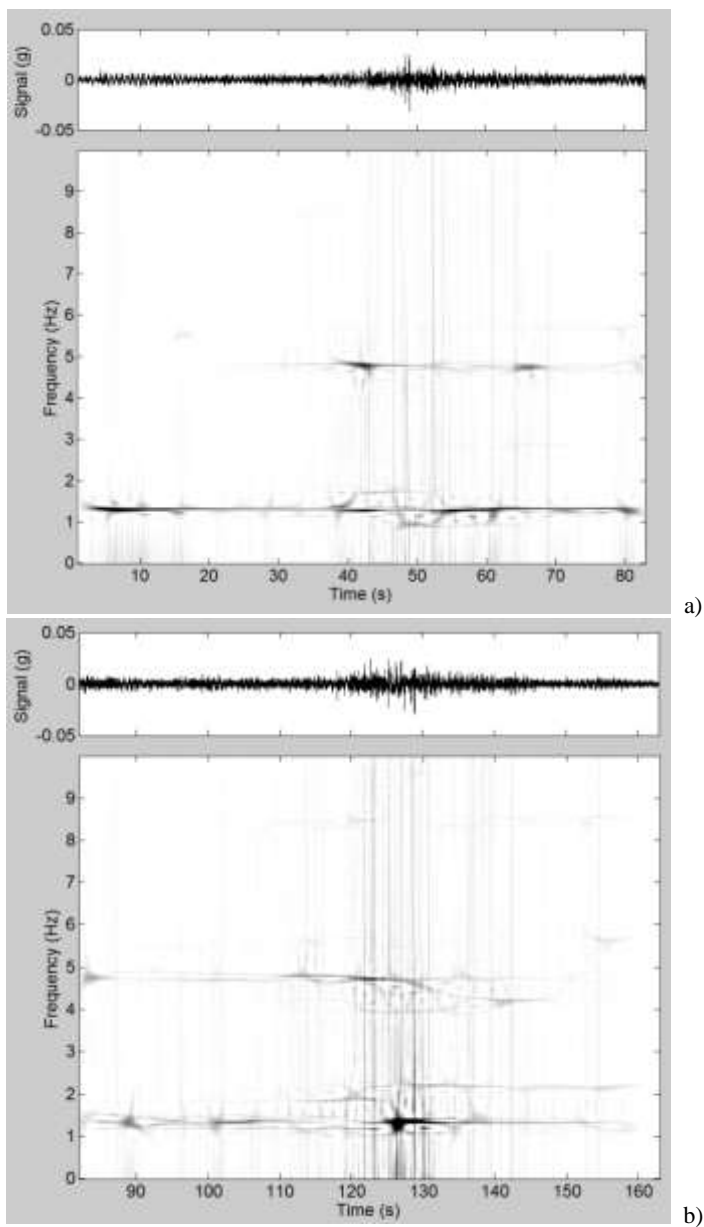


Figure D.2.4. Time-frequency plots from the data recorded by sensor WSa2 along the Y transversal axis during *test Ib*. a) *RtoL* data ; b) *LtoR* data.

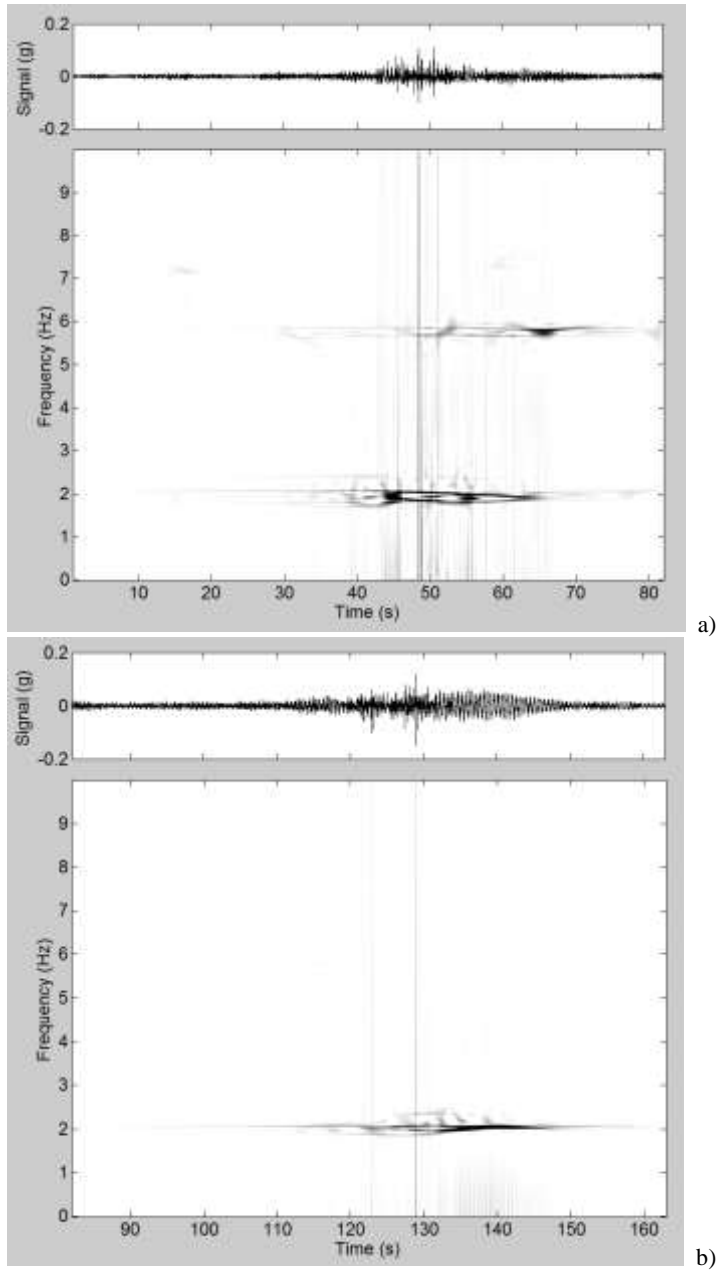


Figure D.2.5. Time-frequency plots from the data recorded by sensor WSa2 along Z gravity axis during test Ib. a) RtoL data ; b) LtoR data.

- **test B3**

In this test, the records of a round trip along the deck of six persons are considered. The average mass is 80 Kg. The pedestrians proceed in pairs by keeping a distance of 1 m between each other in the longitudinal direction of the footbridge, and a distance of about 0.5-0.7 from the closest lateral edge of the footbridge (Figure D.2.6). Further details about this test are summarized in Table D.2.3.

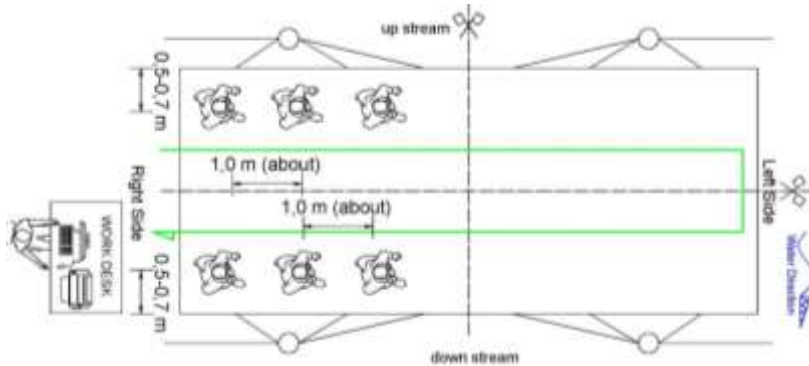


Figure D.2.6. Configuration of the walking *test B3*.

Table D.2.3. Walking (round trip) of six persons.

<i>Type</i>	<i>ID</i>
Day/Time	November 7,2013 / 3.00 pm
Test type	walking (round trip)
Air temperature	15°C
Pedestrian(s) num.	6 persons
Total Pedestrian(s) mass	480 Kg
Total time duration	≈2:42 min
<i>RtoL</i> time duration	≈1:21 min
<i>LtoR</i> time duration	≈1:21 min
Average velocity of the pedestrian(s)	1.35 m/s

During this test, only one frequency clearly appears at 1.35 Hz along *Y*, and it is constant over the entire duration of the data acquisition. Another frequency appears at 5.00 Hz in the time period between 50 and 70 sec for the *RtoL* crossing, and in the time period from 100 to 160 sec for the *LtoR* crossing. Once again, the *LtoR* plot shows many vertical lines; in particular, one can observe that in the time period between 125 and 140

sec, there is a consistent frequency shift, due to the overlapping of the waves associated to the movement of the pedestrians from the sides toward the mid-span (Figure D.2.7). Also along the Z axis only one frequency clearly appears at 2.00 Hz, and it is activated in the time period between 50 and 80 sec for the *RtoL* crossing, and between 100 and 160 sec for the *LtoR* crossing. Moreover one more frequency of 6.00 Hz seems to be “slightly” activated between 50 and 70 sec for the *RtoL* crossing, and between 130 and 150 sec for the *LtoR* crossing (Figure D.2.8).

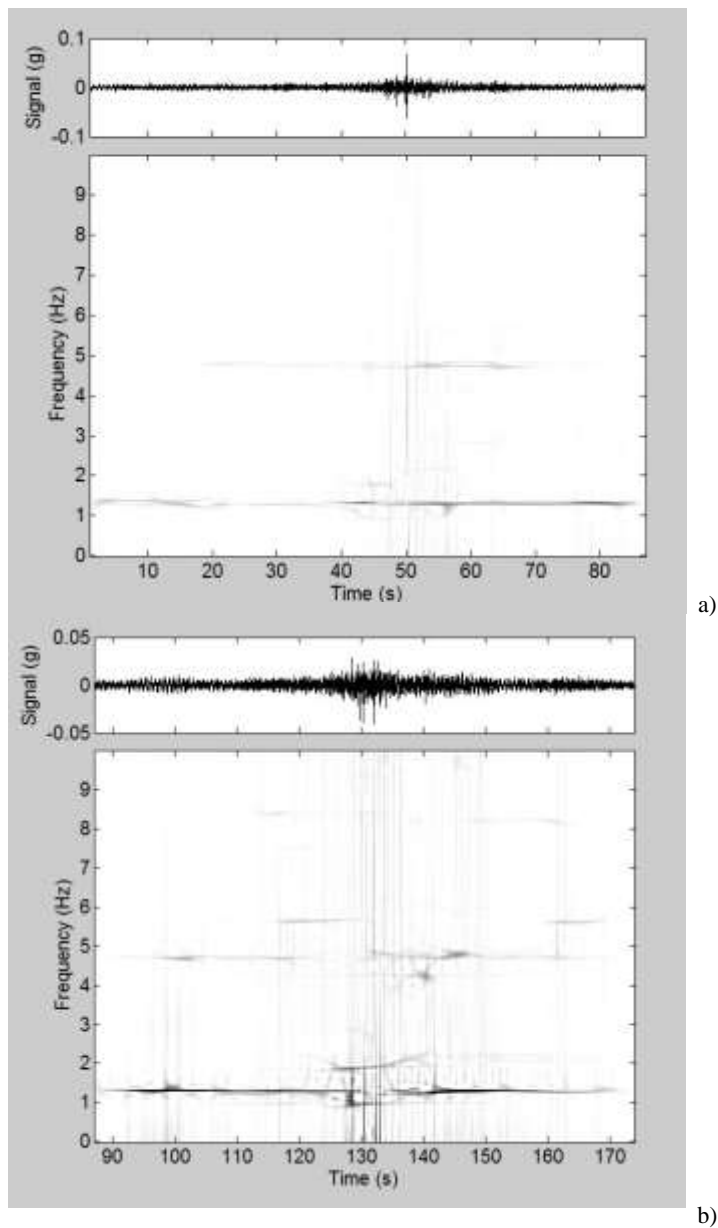


Figure D.2.7. Time-frequency plots from the data recorded by sensor WSA2 along Y transversal axis during test Ic. a) *RtoL* data ; b) *LtoR* data.

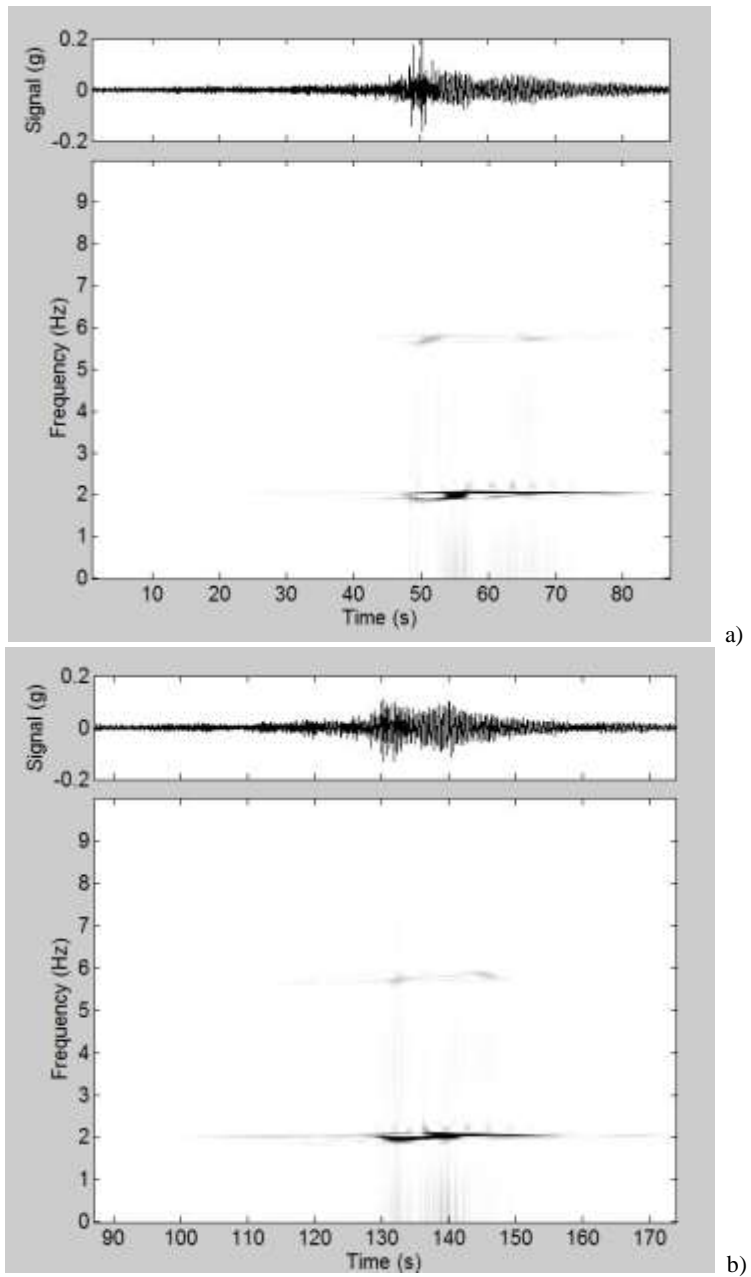


Figure D.2.8. Time-frequency plots from the data recorded by sensor WSa2 along Z gravity axis during test Ic. a) *RtoL* data ; b) *LtoR* data.

- **test B4**

During this test, the footbridge response under a running person along the deck (round trip) is recorded. The average mass is 85 Kg. Further details about this test are summarized in Table D.2.4.

Table D.2.4. Running (round trip) of one person.

<i>Type</i>	<i>ID</i>
Day/Time	November 7,2013 / 3.15 pm
Test type	running (round trip)
Air temperature	15°C
Pedestrian(s) num.	1 person
Total Pedestrian(s) mass	85 Kg
Total time duration	≈0:46 min
<i>RtoL</i> time duration	≈0:23 min
<i>LtoR</i> time duration	≈0:23 min
Average velocity of the pedestrian(s)	4.78 m/s

In Figure D.2.9, the time-frequency plots from the data acquired by sensor WSa2 along the transversal *Y* axis are reported. In this test, only one frequency clearly appears at 1.35 Hz during the *LtoR* crossing. During the *RtoL* crossing, only one vertical line appears at about 35 sec, and it can be associated to one “jump” of the pedestrian in the proximity of sensor WSa2. Moreover, one can observe that during the *LtoR* crossing some frequency shifts appear between 70 and 85 sec. Once again, these shifts are associated to the overlapping of the waves associated with the motion of the pedestrian.

In Figure D.2.10, the plot for the data acquired by WSa2 along the vertical (gravity) *Z* axis is reported. Also in this direction only one frequency clearly appears at 2.00 Hz during the *LtoR* crossing. During the *RtoL* crossing a frequency shift appears at about 35 sec, and can be associated to one “jump” of the pedestrian in the proximity of sensor WSa2, as observed for the *Y* axis.

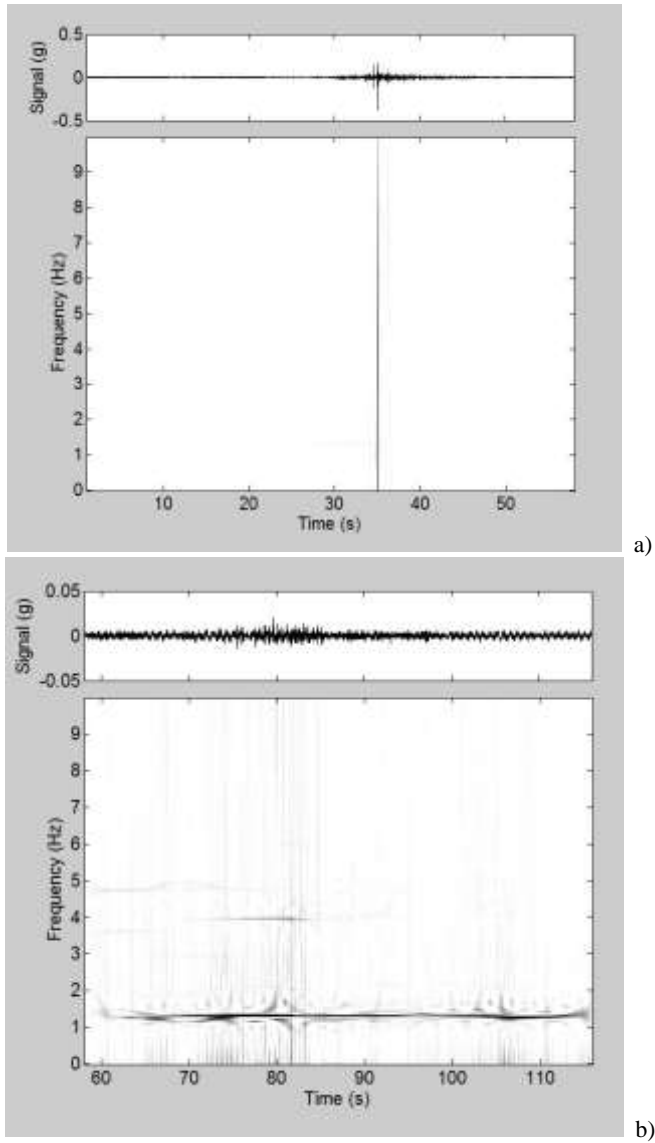


Figure D.2.9. Time-frequency plots from the data recorded by sensor WSa2 along Y transversal axis during *test II*. a) *RtoL* data ; b) *LtoR* data.

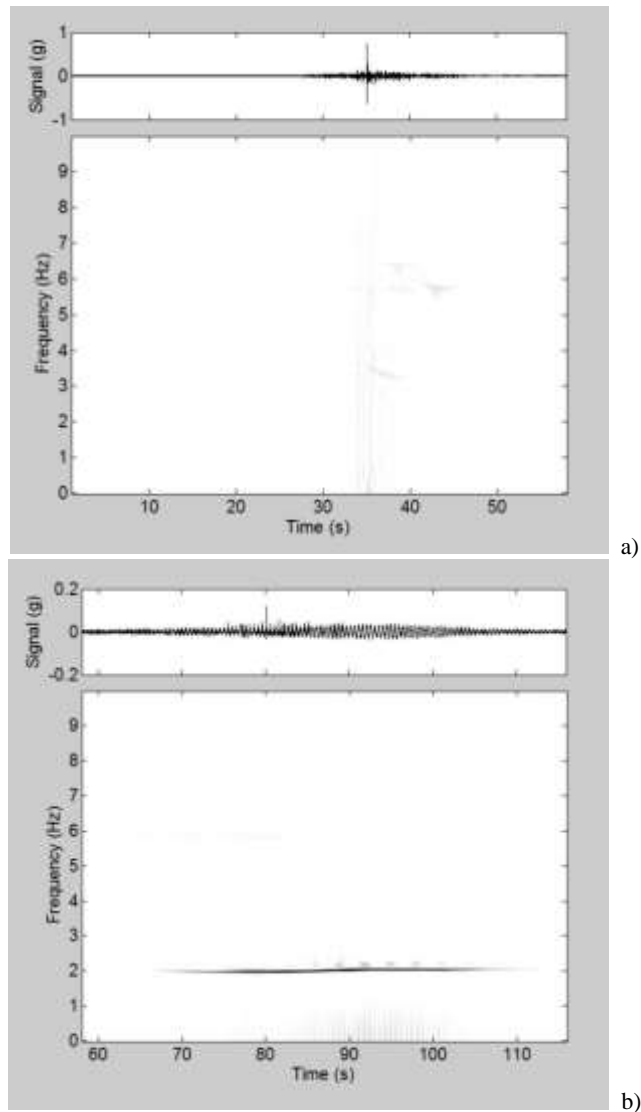


Figure D.2.10. Time-frequency plot - WSA2 along Z gravity axis - test II. a) *RtoL* data ; b) *LtoR* data.

As a general remark of these analysis, it appears as for the data along Y show several frequencies are highlighted compared to the signal along Z axis. Another aspect that can be highlighted is this: during the *LtoR* walking “some” frequencies shifts in Y and in Z directions disappear.

Further investigation regards the singular value decomposition (SVD) of the spectral density matrix. The results are shown in Figure D.2.11; in particular a zoom between 1.00 Hz and 5.00 Hz is plotted.

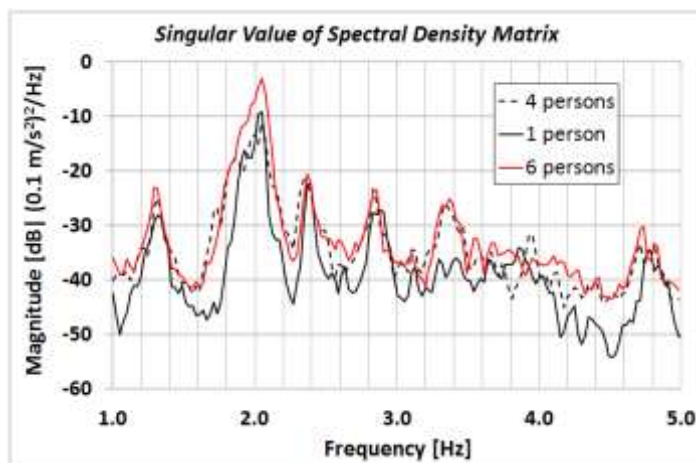


Figure D.2.11. Zoom between 1.00 Hz and 5.00 Hz of the singular value of spectral density matrix. Comparison between acquisitions along transversal Y axis from WSa1 during the test B1 (solid black line) and test B2 (dashed black line) and test B3 (solid red line).

One can see that the trend of the singular value (SV) related to the *test B3* is (almost) always “higher” than the one related to the *test B1* and *test B2*. Higher values of SV indicate that many frequencies can be activated, and so it will be more difficult to identify the real value of the frequency.

D.3 References

- [1] H.I. Choi and W. Williams, 1989. Improved Time-Frequency Representation of Multicomponent Signals Using Exponential Kernels. IEE Transactions on acoustic, speech, and signal processing, vol. 37, no. 6, June 1989.
- [2] L. Cohen, 1995. Time-frequency Analysis. Electrical engineering signal processing Prentice Hall Signal Processing series (1st edition - 1995).
- [3] Bortoluzzi D., Casciati S., Faravelli L., 2014. Testing the effects of walking and running on an existing timber pedestrian bridge. On the Proceeding of the 9th International Conference on Structural Dynamics, EURODYN 2014 Porto, Portugal, 30 June - 2 July 2014.

- [4] S. Casciati, F. Casciati, L. Faravelli and D. Bortoluzzi, 2014. Modelling The Human Induced Vibrations In A Cable-Stayed Pedestrian Timber Bridge. On the Proceeding of the 7th European Workshop on Structural Health Monitoring – EWSHM2014, July 8-11, 2014. La Cité, Nantes, France.

Acknowledgements

Mi sembra doveroso, arrivato a questo punto, fare alcuni ringraziamenti. Innanzitutto vorrei ringraziare la Prof.ssa Faravelli Lucia, il Prof. Fabio Casciati, la Prof. Sara Casciati, l'Ing. Tom Messervey per la disponibilità e l'interesse dimostrati in queste tematiche di ricerca. Inoltre hanno creduto in me e nelle mie capacità, dandomi la possibilità di crescere sia come ingegnere ma soprattutto come persona.

Ringrazio poi l'Ing. Stefano Boranga e tutto lo staff del suo studio, la ditta Holzbau, il comune di Farra d'Alpago, la Comunità Montana dell'Alpago, il comune di Trasaghis e lo studio dell'Arch. Lio Parcianello, per aver dimostrato interesse in questo lavoro.

Un particolare pensiero va poi ai miei genitori mamma Maddalena e papà Antonio che mi hanno sostenuto in tutto e per tutto sia nei momenti belli, che in quelli meno belli, credendo in me e nelle mie capacità, alla mia ragazza Lara, ai miei zii e cugini e amici di famiglia vari.

Un sentito ringraziamento va poi a tutti gli amici di sempre: Ugo, Elia, Ilaria, Necca, Celo, Max, Frostian, Tona, Gellio, ecc..., gli amici di Bologna Paola, Piero e Clara, e ai nuovi amici incontrati a Pavia; Zhicong, Lijun, Ale, Umut, Lorenzo, Michele, tutti i colleghi del dottorato, i compagni di appartamento, i tesisti vari e il personale della segreteria del DICAr.

Infine un doveroso pensiero va ai miei compagni, o meglio "fratelli" dei Formato Standard, e agli amici dei FS: Matteo (il Nippon), Francesco (W), GiaMpaolo (Uomo), Simone (Papi), Mattia (Musso), Nicola (Menellotron Satanvs), Mary (DB), Mary (Mami), Letizia (Ker) ed Adriano. E proprio ad Adriano, che il destino ha voluto con sé troppo presto, va un saluto particolare...*e comunque 5 son troppi!!!...sempre con noi amico!!!*

Grazie a tutti.

Valdenogher, dicembre 2014.

Daniele Bortoluzzi

"Without deviation from the norm, progress is not possible."

(Frank Zappa)